

# ABERRATIONS OF ATOMIC DIFFRACTION

FROM ULTRACOLD ATOMS TO HOT IONS



TECHNISCHE  
UNIVERSITÄT  
DARMSTADT

Vom Fachbereich Physik  
der Technischen Universität Darmstadt

zur Erlangung des Grades  
eines Doktors der Naturwissenschaften (Dr. rer. nat.)

genehmigte Dissertation von  
ANTJE NEUMANN

Erstgutachter: Prof. Dr. Reinhold Walser  
Zweitgutachter: Prof. Dr. Enno Giese

Darmstadt 2021  
D 17

*'Life is not easy for any of us. But what of that? We must have perseverance and above all confidence in ourselves. We must believe that we are gifted for something, and that this thing, at whatever cost, must be attained.'*

- Marie Curie -

ANTJE NEUMANN:

*Aberrations of atomic diffraction - From ultracold atoms to hot ions*

ERSTGUTACHTER: Prof. Dr. Reinhold Walser

ZWEITGUTACHTER: Prof. Dr. Enno Giese

TAG DER EINREICHUNG: 7. Mai 2021

TAG DER PRÜFUNG: 28. Juni 2021

DARMSTADT, Technische Universität Darmstadt

Jahr der Veröffentlichung der Dissertation auf TUpriints: 2021

URN: urn:nbn:de:tuda-tupriints-191391

URI: <https://tupriints.ulb.tu-darmstadt.de/id/eprint/19139>

Veröffentlicht unter CC BY-NC-ND 4.0 International

Namensnennung - nicht kommerziell - keine Bearbeitung

<https://creativecommons.org/licenses/>



---

## ABSTRACT

---

Atomic diffraction is the central concept of matter-wave interferometers, which provide the opportunity of high-precision rotation and acceleration sensing. Ultracold atoms are the ultimate quantum sensors for this purpose. Transferring photon momentum from two counterpropagating laser beams to atomic wavepackets prepares coherent superpositions in the momentum space, realising atomic beamsplitters and mirrors.

Like classical optical systems, these matter-wave devices require exact specifications and ubiquitous imperfections need to be quantified. Therefore, in this thesis, the performance of (3+1)D atomic beamsplitters in the quasi-Bragg regime is studied numerically as well as analytically and is confirmed by experimental data [1]. Ideally, the incoming wavepacket can be split exactly into two parts or reflected perfectly with unit response, independent of its spatial and velocity distribution. However, the velocity selectivity of the Bragg diffraction, as well as losses into undesired diffraction orders in the quasi-Bragg regime, constitute aberrations, which cannot be neglected. The non-ideal behaviour due to spatial variations of the laser beam profiles and wavefront curvatures, regarding realistic Laguerre-Gaussian laser beams instead of ideal plane waves, reduces the diffraction efficiency and leads to rogue momentum components, just like misaligned lasers. In contrast, smooth temporal envelopes improve the beamsplitter performance. Different pulse shapes are taken into account, where some are amenable for closed analytical solutions.

The *realistic* modelling and exhausting aberration studies characterises in detail atomic Bragg beamsplitters and demonstrate pathways for improvements, both required by challenging experiments.

For hot ions in accelerator beams the atomic diffraction is used contrary to generate a velocity filter. Two counterpropagating far-detuned lasers transfer a narrow velocity class of ions from an initially broad distribution via a stimulated Raman transition between the ground states of a  $\Lambda$ -system. This colder subensemble prepares optimal initial conditions for precision collinear laser spectroscopy on fast ion beams. The efficiency of the filter is diminished by aberrations like the spontaneous emission from the two single-photon resonances, as well as the ground-state decoherence induced by laser noise. Spatial intensity variations of the ion and laser beams are considered, whereas wavefront curvature is negligible. A comprehensive master equation leads to conditions for the optimal frequency pair of lasers. The time-resolved population transfer characterises the filter performance and is evaluated numerically as well as analytically. Derived models match the numerical results, keeping the computational effort small.

Taking into account the mentioned aberrations, the possible use of Raman transition as velocity filter for hot ions is demonstrated. Velocity classes with widths as low as 0.2 m/s can be transferred, achieving a significant population proportion from per mill to percent. Applying the analysis to current  $^{40}\text{Ca}^+$  ion experiments, a sensitivity for measuring high ion acceleration voltages on the ppm level or below is substantiated.

---

## ZUSAMMENFASSUNG

---

Atombeugung ist das zentrale Konzept von Materiewelleninterferometern, die das Potenzial für hochpräzise Rotations- und Beschleunigungsmessungen bieten. Dafür sind ultrakalte Atome die ultimativen Quantensensoren. Indem der Impuls zweier Photonen aus gegenläufigen Laserstrahlen auf atomare Wellenpakete übertragen wird, entsteht eine kohärente Überlagerung im Impulsraum, wodurch atomare Strahlteiler und Spiegel realisiert werden.

Genauso wie klassische optische Systeme erfordern diese Materiewellenelemente genaueste Spezifikationen und allgegenwärtige Imperfektionen müssen quantifiziert werden. Daher wird in dieser Arbeit die Performance von (3+1)D Atomstrahlteilern im Quasi-Bragg-Regime sowohl numerisch als auch analytisch untersucht und durch experimentelle Daten bestätigt [1]. Idealerweise wird das einlaufende Wellenpaket in zwei gleichgroße Teile aufgespalten oder perfekt reflektiert, unabhängig von seiner räumlichen und seiner Geschwindigkeitsverteilung. Die im Quasi-Bragg-Regime auftretende Geschwindigkeitsselektivität sowie Verluste in unerwünschte Beugungsordnungen stellen jedoch nicht zu vernachlässigende Aberrationen dar. Im Gegensatz zu idealen ebenen Wellen, führen räumliche Variationen und Wellenfrontkrümmung von realistischen Lauguerre-Gauß Laserstrahlprofilen, genauso wie unzulänglich ausgerichtete Laser, zu einer Verringerung der Beugungseffizienz und unerwünschten Impulskomponenten. Zeitlich glatte Pulseinhüllende verbessern dahingegen die Strahlteilereffizienz. Hier werden verschiedene Pulsformen berücksichtigt, wobei für einige geschlossene analytische Lösungen zugänglich sind.

Die *realistischen* Modellierungen und umfangreichen Aberrationsstudien charakterisieren die Atomstrahlteiler detailreich und zeigen Optimierungsmöglichkeiten, wobei beides für anspruchsvolle Experimente erforderlich ist.

Für heiße Ionen in Beschleunigerstrahlen wird die Atombeugung konträr zur Erzeugung eines Geschwindigkeitsfilters verwendet. Zwei gegenläufige, weit verstimmte Laser filtern eine enge Geschwindigkeitsklasse aus einer anfänglich breiten Ionenverteilung heraus. Dafür wird ein stimulierter Raman-Übergang zwischen den Grundzuständen eines  $\Lambda$ -Systems verwendet. Dieses kältere Subensemble stellt optimale Anfangsbedingungen für präzise kollineare Laserspektroskopie von schnellen Ionenstrahlen dar. Die Effizienz des Filters wird durch Aberrationen, wie spontane Emission der beiden Einzelphotonenresonanzen, sowie durch Laserrauschen induzierte Dekohärenz des Grundzustands, verringert. Räumliche Intensitätsschwankungen der Ionen- und Laserstrahlen werden berücksichtigt, während die Wellenfrontkrümmung vernachlässigbar ist. Eine umfassende Mastergleichung führt zu Bedingungen an das optimale Laserfrequenzpaar. Die Filterperformance wird charakterisiert durch den, sowohl numerisch als auch analytisch ausgewerteten, zeitaufgelösten Populationstransfer. Dabei bestätigen die analytische Modelle die numerischen Ergebnisse und verringern den Rechenaufwand.

Unter Berücksichtigung der genannten Aberrationen wird die Verwendung des Raman-Übergangs als Geschwindigkeitsfilter für heiße Ionen demonstriert. Dabei können sehr schmale Geschwindigkeitsklassen mit Breiten von 0,2 m/s übertragen werden, wobei gleichzeitig eine signifikante Population im Promille- bis Prozentbereich erreicht wird. In Bezug auf aktuelle  $^{40}\text{Ca}^+$ -Ionenexperimente begründet dies für die Messung hoher Ionenbeschleunigungsspannungen eine Sensitivität auf ppm-Niveau oder darunter.



---

# CONTENTS

---

1	INTRODUCTION	1
1.1	Three types of atomic diffraction	1
1.2	From ultracold atoms to hot ions (or vice versa)	2
1.3	Beamsplitter for ultracold atoms	3
1.3.1	Matter-wave interferometry	3
1.3.2	Quantum gases in microgravity: the QUANTUS project	4
1.3.3	Quasi-Bragg diffraction	5
1.3.4	Sources of aberrations	6
1.4	Velocity filter for fast and hot ions	6
1.4.1	Collinear laser spectroscopy	6
1.4.2	Raman diffraction	7
1.4.3	Sources of aberrations	8
1.5	Structure of the thesis	8
I	FUNDAMENTAL CONCEPTS AND METHODS	
2	CONCEPTS OF LIGHT-MATTER INTERACTION	13
2.1	Cold atoms interacting with laser light	13
2.1.1	Interaction Hamilton operator	13
2.1.2	Rotating-wave approximation	15
2.1.3	Rabi frequency	15
2.2	Spatial modes of the electromagnetic field	16
2.2.1	Plane waves	16
2.2.2	Laguerre-Gaussian beams	16
2.3	Spatial modes of matter waves	17
2.3.1	Single-particle systems	17
2.3.2	Many-particle systems	18
2.3.3	Plane waves	21
2.3.4	Coherent states	21
2.3.5	Bose-Einstein condensates	23
2.3.6	Thermal clouds	26
2.3.7	Partially condensed clouds	27
2.4	Hot alkali-like ions interacting with laser light	28
3	TIME EVOLUTION OF LIGHT-MATTER INTERACTION	31
3.1	Schrödinger equation	31
3.1.1	Symplectic integration	32
3.1.2	Disentangling an exponential sum	33
3.2	Von-Neumann equation	34
3.3	Master equation	34
3.3.1	Quantum Monte Carlo wavefunction method	35
3.4	Coordinate transformations	38
3.4.1	Moving frames: Galilean transformation	38
3.4.2	Static frame transformations	39

## II DIFFRACTION OF ULTRACOLD ATOMS

4	DIFFRACTION WITH RESONANT LIGHT	43
4.1	Interaction energy	43
4.2	Local Rabi oscillations	44
4.3	Atom moving in a plane laser wave	45
4.4	Conclusion	50
5	CONCEPTS OF BRAGG DIFFRACTION	51
5.1	Conservation laws	51
5.1.1	On-resonance response	53
5.1.2	Off-resonance response	53
5.2	Counterpropagating bichromatic fields	54
5.3	Interaction energy	55
5.3.1	Comoving, rotating frame	55
5.3.2	Time evolution	57
5.4	Ideal Bragg beamsplitter and mirror	57
5.5	Plane-wave approximation	58
5.5.1	Adiabatic elimination of the excited state	58
5.5.2	Bloch-wave ansatz	59
5.5.3	Ad-hoc ansatz	61
6	(1+1)D BRAGG DIFFRACTION: TEMPORAL PULSES	63
6.1	Pulse shapes	63
6.2	Diffraction with rectangular pulses	64
6.2.1	Velocity selective Pendellösung	64
6.2.2	Losses into higher diffraction orders: Kato solution	66
6.3	Diffraction with hyperbolic secant pulses	71
6.3.1	Velocity selective Demkov-Kunike Pendellösung	72
6.3.2	Losses into higher diffraction orders: extended DK-model	73
6.4	Diffraction with Gaussian pulses	75
6.5	Comparison of the diffraction for all pulse shapes	76
6.6	Proving the Demkov-Kunike model experimentally	78
6.6.1	Experimental scenario	78
6.6.2	Measured observable: normalised diffraction efficiency	78
6.6.3	Results	82
7	(3+1)D BRAGG DIFFRACTION: SPATIAL ENVELOPES	85
7.1	Spatial profile of two counterpropagating Gauss-Laguerre laser beams	86
7.1.1	Local plane-wave approximation	86
7.2	3D Beamsplitter in position and momentum space	87
7.3	Radiative force	90
7.3.1	Radiation pressure due to wavefront curvature	91
7.3.2	Dipole force due to intensity variations	93
7.4	Reduced beamsplitting performance	99
7.5	Misalignment	102
7.5.1	Spatial profile of misaligned laser beams	102
7.5.2	Aberrations due to misalignment	105
7.5.3	Comparison with on-ground experiments	107
8	(3+1)D BRAGG DIFFRACTION: SPONTANEOUS EMISSION	111
8.1	Resonant diffraction with spontaneous emission	111
8.2	Bragg diffraction with spontaneous emission	113

9	SUMMARY OF THE ABERRATIONS OF ATOMIC BRAGG DIFFRACTION	115
9.1	Quantify aberrations with susceptibilities	115
9.2	Minimising aberrations of Bragg diffraction	118
<b>III RAMAN VELOCITY FILTER FOR HOT IONS</b>		
10	RAMAN VELOCITY FILTER	121
10.1	Raman filter as tool to measure high voltages	121
10.1.1	Present spectroscopic high-voltage measurements	121
10.1.2	Raman velocimetry	122
10.2	Experimental conditions	123
10.2.1	Ionic velocity distribution	123
10.2.2	Spatial inhomogeneities	124
10.2.3	Parameters	124
10.3	Theoretical model	126
10.3.1	Ion-field interaction	126
10.3.2	Optical Bloch equations	128
11	RESONANCES IN THE FREQUENCY DOMAIN	129
11.1	Resonance conditions	129
11.2	Contributions of the resonances	130
11.3	Isolating resonances	132
12	TIME RESOLVED POPULATION TRANSFER	135
12.1	Stimulated Raman transition	135
12.1.1	Coherent dynamics	136
12.1.2	Finite laser linewidths	138
12.2	Spontaneous Raman transition	140
12.3	Maximising the population transfer	141
12.3.1	Vanishing laser linewidths	141
12.3.2	Finite laser linewidths	143
12.3.3	Spatial intensity variations	146
<b>IV CONCLUSION</b>		
13	SUMMARY AND OUTLOOK	151
13.1	Raman velocity filter	151
13.2	Atomic Bragg diffraction	153
<b>V APPENDIX</b>		
A	FUNDAMENTAL PARAMETERS	157
A.1	Atomic Bragg diffraction	157
A.2	Raman velocity filter	158
B	NUMERICAL METHODS	159
B.1	Discrete Fourier transform on periodic lattices	159
B.1.1	Wavefunctions	159
B.1.2	Expectation values	160
B.1.3	Conserved quantities	161
B.2	Number of simulation timesteps	161
B.3	Scaling of the numerical simulations	162
C	DISENTANGLING AN EXPONENTIAL: SU(2) ALGEBRA	165

D	MODELS FOR (1+1)D ATOMIC BRAGG DIFFRACTION	167
D.1	Kato model . . . . .	167
D.2	Demkov-Kunike model . . . . .	167
D.2.1	Demkov-Kunike propagator . . . . .	167
D.2.2	Extended Demkov-Kunike model . . . . .	169
E	COMPARISON WITH EXPERIMENTS	171
E.1	Verification of the Demkov-Kunike model . . . . .	171
E.1.1	Expansion of the thermal cloud . . . . .	171
E.1.2	Location of the atoms . . . . .	171
E.2	Laser misalignment . . . . .	174
E.2.1	Expansion of the thermal cloud . . . . .	174
E.2.2	Location of the atoms . . . . .	174
F	RAMAN VELOCITY FILTER	175
F.1	Perturbative metastable state population . . . . .	175
F.2	Full solution of the population transfer via the Raman transition . . . . .	176
	 BIBLIOGRAPHY	 177
	 LIST OF PUBLICATIONS	 189
	 CONFERENCE CONTRIBUTIONS	 190
	 DANKSAGUNG	 191
	 ERKLÄRUNG	 192

---

## INTRODUCTION

---

The physics of ultracold atomic gases has achieved spectacular successes in recent years. One milestone in the history of physical achievements was the generation of the first Bose-Einstein condensates (BECs) [2–4] by E. Cornell, C. Wieman and W. Ketterle in 1995, 71 years after the theoretical prediction by Albert Einstein [5, 6]. This was awarded with the Nobel prize in 2001 [7, 8]. The development of modern lasers since the 1960s represents an additional breakthrough. Several pioneering contributions to the field of laser physics were also awarded with the Nobel prize [9–13]. The combination of both groundbreaking achievements establishes the conditions for precisely controllable driven matter-laser interactions, including atomic diffraction processes. While the theoretical description of these interactions for ultracold atoms at nanokelvins to hot alkali-like ions at Kelvin temperatures are based on the same fundamental concepts, their applications are diverse.

The well-defined properties of ultracold (nK) atomic test masses and their precise control by laser light (cf. Sec. 1.3) are utilised for matter-wave interferometers [14–18], which are the state-of-the-art instruments for high-precision measurements of rotation and acceleration. Applications range from tests of fundamental physics, like the equivalence principle [19–27] or quantum electrodynamics [28–30], to inertial sensing [31–36]. As for all imaging systems, atom optics suffer from imperfections and an accurate characterisation is required in order to rectify them. This is particularly relevant for high precision experiments, like gravimetry [37] and extended free-fall experiments in micro-gravity and space [30, 38–45]. Such challenging experiments require realistic modelling and aberration studies, as presented in this thesis, ideally hinting towards rectification.

At the hot side of the temperature scale (K), the use of Raman diffraction within this thesis is extended to a velocity filter (cf. Sec. 1.4) for precision collinear laser spectroscopy [46–48] on fast ion beams with several keV kinetic energy. Chandrasekhara Raman himself attributes ‘*the wonderful blue opalescence of the Mediterranean Sea*’ as one of the phenomena to the effect he discovered [49–51] a century ago. Inelastic two-photon scattering, as known today, has found innumerable applications from solid-state spectroscopy and enhanced microscopic imaging [52] to actively cooling atoms with velocity selective coherent population trapping [53].

### 1.1 THREE TYPES OF ATOMIC DIFFRACTION

The basic mechanism of atomic diffraction is the stimulated absorption (and emission) of photons from laser beams. Therefore, transferring photon momenta from a laser to the atom can split (beamsplitter) and reverse (mirror) the atomic motion, or slice a narrow contribution out of it (filter). The photon momentum  $p = \hbar k$  and the laser frequency  $\omega$  are coupled with the wavenumber  $k$ , the reduced Planck constant  $\hbar$ , and the speed of light  $c$  by the vacuum dispersion relation  $\omega = c k$ .

There are three types of atomic diffraction with the possibility to generate an atomic beam-splitter, mirror, or filter, described in the following and depicted in Fig. 1.1.

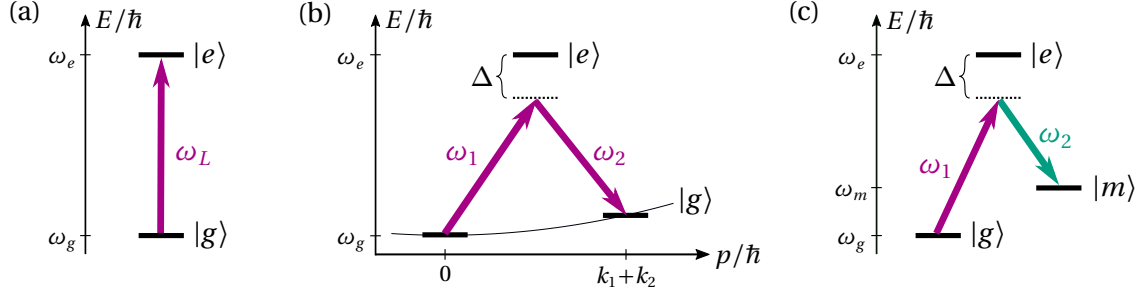


Figure 1.1: Energy diagrams of atomic diffraction: (a) with one on-resonant laser, (b) Bragg diffraction between momentum  $p = \hbar k$  states, and (c) Raman diffraction. The atomic internal states  $|\sigma\rangle$ ,  $\sigma \in \{g, e, m\}$  of energy  $\hbar\omega_\sigma$  are coupled with laser(s) of frequency  $\omega_L$  ( $\omega_1, \omega_2$ ) and a detuning  $\Delta$  to the atomic resonance.

**DIFFRACTION WITH RESONANT LIGHT** Resonant coupling of a two-level system with laser light can generate an absorptive grating. After the stimulated absorption of one laser photon, the atoms in the excited state carry the additional photon momentum in contrast to the ground state. However, this scheme can be used only, if the spontaneous decay of the excited state proceeds mainly to an internal state, which is not detected. The decay back to the ground state produces decoherence, which diminishes the diffraction efficiency.

**BRAGG DIFFRACTION** The moving standing light field, generated by two far-detuned counterpropagating laser beams, builds an optical grating. Therefore, different momentum ground states are coupled without populating the excited state. The transferred momentum is the sum of the single photon momentum of each laser. Due to the coupling within one internal state, the diffracted parts are distinguishable only by carrying different momenta. Therefore, they need to be well localised in the momentum space with momentum widths much smaller than the transferred photon momenta  $\hbar(k_1 + k_2)$ , which is provided by ultracold atoms.

**RAMAN DIFFRACTION** For Raman diffraction, the interaction with two far-detuned laser beams couples two different internal ground states with one excited state. Again, the excited state stays ideally unpopulated. For the purpose of a filter, from an initially hot ensemble with wide momentum distribution only those velocity classes, respectively momenta, are transferred, which match the resonance condition of the Doppler shifted laser frequencies.

## 1.2 FROM ULTRACOLD ATOMS TO HOT IONS (OR VICE VERSA)

In the classical limit of hot ensembles, the quantum mechanical properties of the external motion of the quasi point particles do not matter. Therefore, a non-interacting ensemble of hot ions is an incoherent mixture, distributed according to the Maxwell-Boltzmann distribution, with an extremely large momentum expansion, as visualised with a sketch of the phase-space distribution in Fig. 1.2 (a). The momentum width is defined by the thermal velocity  $v_t \propto \sqrt{T}$  for temperatures in the Kelvin regime. In general, these thermal clouds are an incoherent mixture of coherent states. In case of bosons, their energy distribution follows the Bose-Einstein statistic. However, even for small temperatures, they have a wide velocity spread [cf. Fig. 1.2 (b)] in comparison to Bose-Einstein condensates. The condensation starts at temperatures below the finite phase-transition temperature  $T_c$  in the range of nanokelvins.

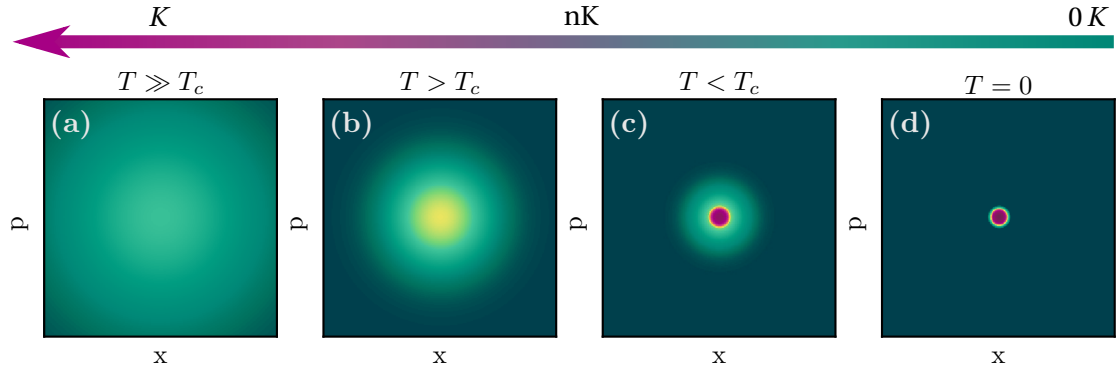


Figure 1.2: Sketch of the phase-space distributions from hot ions (left) to ultracold atoms (right). According to the Nernst heat theorem the absolute zero  $T = 0$  is not reachable but real temperatures indefinite close to  $T=0$  can be realised [54].

Here, the thermal de Broglie wavelength  $\lambda_{\text{dB}} \propto 1/\sqrt{T}$  covers the mean particle distance and the atomic wavepackets of the bosonic ensemble start to overlap. However, in Fig. 1.2 (c), a remaining thermal background with its broader expansion, is distinguishable from the narrower Bose-condensed subensemble. This characterises partially condensed clouds in the crossover from incoherent to coherent states. At zero temperature<sup>1</sup>, a collection of bosonic atoms occupies only one quantum state. This macroscopic quantum state can be described with one single wavefunction. Pure Bose-Einstein condensates are the optimal initial states for matter-wave interferometers based on Bragg diffraction, because these are ultracold fully coherent states, providing required properties of suitable test states, like a narrow velocity spread, as sketched in Fig. 1.2 (d).

### 1.3 BEAMSPLITTER FOR ULTRACOLD ATOMS

Atoms are the ultimate *abrasion free* quantum sensors for electro-magnetic fields and gravitational forces. By a feat of nature, they occur with bosonic or fermionic attributes, but were produced otherwise identically without *manufacturing tolerance*. A beamsplitter prepares superpositions of matter-wave packets by transferring photon momentum from a laser to an atomic wave, while a mirror reverses the atomic motion. These devices are the central components of a matter-wave interferometer.

#### 1.3.1 Matter-wave interferometry

Atom interferometers use the wave properties of particles, introduced by Louis-Victor de Broglie in 1924 [55] (awarded with the Nobel prize in 1929 [56]), with assigning a wavelength  $\lambda = h/p$  to every particle with momentum  $p$ . Therefore, the role of light and matter is reversed compared to optical interferometers. A Mach-Zehnder type atom interferometer is depicted in Fig. 1.3. An incoming wavepacket is split into two parts applying a beamsplitter  $\pi/2$ -pulse with two counterpropagating laser beams. With this atomic diffraction the two wavepackets carry momenta in different directions and therefore they separate in space in the following free propagation of time  $T$ . An atomic mirror, realised with a  $\pi$ -pulse, reflects the atomic motion. After the second interrogation time  $T$  the two paths are closing again in position space. Applying a second beamsplitter, the resulting interference pattern, depending on the evolution

<sup>1</sup> According to the Nernst heat theorem the absolute zero  $T = 0$  is not reachable but real temperatures indefinite close to  $T=0$  can be realised [54].

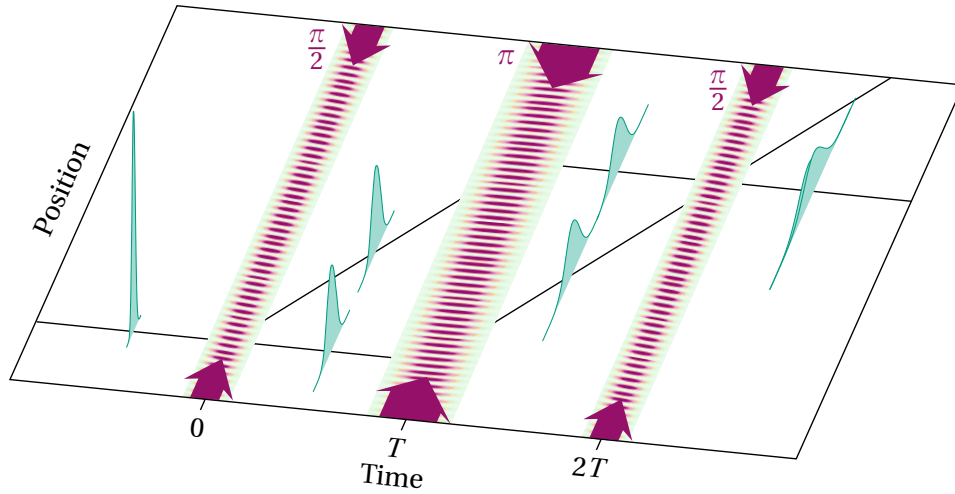


Figure 1.3: Time evolution of an incoming wavepacket (green) in a Mach-Zehnder type matter-wave interferometer. A beamsplitter  $\pi/2$ -pulse, generated by two counterpropagating lasers (magenta), splits the spreading wavepacket into two parts, moving in different directions. After a free propagation time  $T$  a mirror  $\pi$ -pulse inverts these directions. Finally, the two wavepackets are recombined with a second beamsplitter pulse after an additional time of free propagation.

of the atomic wavefunction, provides insight into the potential probed by the atom. Atoms are sensitive to acceleration and rotation and due to the small de Broglie wavelengths, higher frequencies can be used as in optical interferometers, increasing the precision. Therefore, ultracold atoms in matter-wave interferometers are the ultimate test objects for a variety of forces and fields.

### 1.3.2 Quantum gases in microgravity: the QUANTUS project

This work is part of the German collaboration QUANTUS, *QUANTengase Unter Schwerelosigkeit - quantum gases in microgravity*<sup>2</sup>. This project paves the way for the application of matter-wave interferometers under microgravity and ultimately in space. Thereby, microgravity provides several benefits for the experiments with ultracold atoms. Due to longer free-fall times, the sensitivity of an atom interferometer can be improved, because it increases quadratically with the interrogation time  $T$  of the BECs in such devices [16]. Therefore, space platforms provide ultra-long interrogation and observation times, due to permanent microgravity. In addition, they are undisturbed by seismic noise, offering a ‘quiet’ environment.

As part of the QUANTUS-1 [57] project, the first BEC under microgravity was created in 2007, in the drop tower at the ZARM (*Zentrum für Angewandte Raumfahrttechnologie und Mikrogravitation - Center of Applied Space Technology and Microgravity*) in Bremen, which provides a free fall time of 4.7 s [58, 59]. Further, the realisation at the drop tower of an atom interferometer with a BEC under microgravity [40] demonstrates the high potential of matterwave interferometry using ultracold quantum gases. With QUANTUS-2 [57] the catapult operation doubles the microgravity duration to 9.4 s. In addition, a dual species interferometer of rubidium and supplementary potassium will be established. The miniaturisation,

<sup>2</sup> The QUANTUS project under the direction of the Leibniz University Hannover is supported from the DLR German Aerospace Center with funds provided by the Federal Ministry for Economic Affairs and Energy (BMWi), for the Technische Universität Darmstadt under Grant No. 50WM1137, 50WM1557, and 50WM1957 (<https://foerderportal.bund.de/foekat/jsp/SucheAction.do?actionMode=view&fkz=50WM1957>).



robustness and further restrictions on the cold atom experiments due to the environment at the drop tower, make the developed apparatus implementable in ballistic rockets or space missions. The first BEC in space was realised with the MAIUS (*MAteriewellenInterferometer Unter Schwerelosigkeit - matter-wave interferometers under microgravity*) rocket mission in 2017, with a several minutes lasting free fall [43]. Based on QUANTUS and MAIUS, the BECCAL (*Bose-Einstein Condensate and Cold Atom Laboratory*) project aims for the realisation of experiments with ultracold and condensed atoms on the International Space Station (ISS) [60].

A crucial requirement of these project is the fast, robust and miniaturised generation of BECs. On atom chips [61] the atoms can be decelerated and trapped in the smallest possible space. With this microfabricated device generated electric and magnetic fields confine, control and manipulate cold atoms. With the atom chips of the QUANTUS collaboration BECs of several hundred thousand atoms can be generated within a few seconds [62].

Overall, such challenging experiments with low repetition rates ask for realistic as possible simulations to provide precise predictions as well as simple analytical models to understand and describe the underlying physical concepts.

### 1.3.3 Quasi-Bragg diffraction

For ultra-sensitive atom interferometry a large and precise momentum transfer is essential [63–66]. Therefore, the quasi-Bragg regime of atomic diffraction with smooth temporal pulse shapes proves to be optimal [30, 41, 63–65, 67–71]. Bragg scattering [cf. Fig. 1.1 (b)] of atoms from a moving standing light wave [72–75], also in combination with further techniques like Bloch oscillations [30, 64, 66, 68, 76–80], provides an efficient transfer of photon momentum without changing the atomic internal state, while the diffracted populations can be controlled exactly to realise either a beamsplitter or a mirror.

The quasi-Bragg regime is preferred, because it provides a high diffraction efficiency with simultaneously low velocity dispersion for applicable pulse durations. In Fig. 1.4 the velocity selective population transfer is visualised for a mirror pulse.

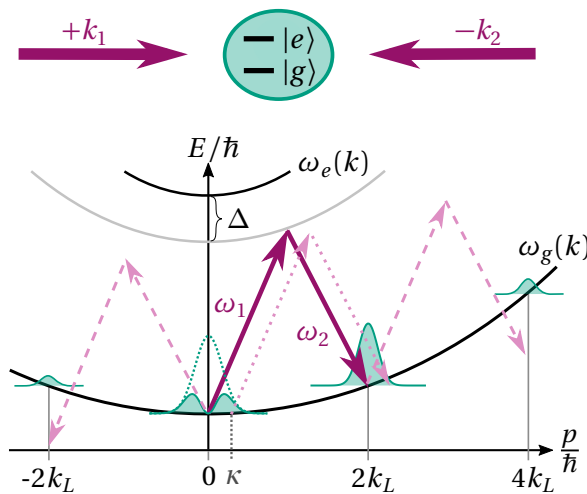


Figure 1.4: (Top) The interaction of two counter-propagating  $(+k_1, -k_2)$ , far detuned  $(\Delta)$  lasers (magenta) of wavenumbers  $k_1 + k_2 \equiv 2k_L$  with a two-level atom (green) is represented by the energy diagram for first order quasi-Bragg diffraction versus atomic wavenumber  $k = p/\hbar$  (bottom). The free ground and excited state's energies are  $\hbar\omega_g(k)$ ,  $\hbar\omega_e(k)$ . Mainly the momentum states  $|0\rangle$ ,  $|2\hbar k_L\rangle$  are coupled (magenta solid). The atomic population distributions are initially centred around 0 (green dotted) and after a mirror pulse around  $0, \pm 2\hbar k_L, \pm 4\hbar k_L, \dots$  (green shadowed). This is caused by losses into higher diffraction orders (magenta dashed) and the velocity selectivity of small momentum detunings  $\kappa$  (magenta dotted), due to off-resonant coupling.

In the limit of the deep-Bragg regime [72, 81, 82] with detrimentally long interaction times and shallow optical potentials a perfect on-resonance diffraction efficiency is accompanied by an adversely sharp velocity dispersion. However, they can be used as a velocity filter

[41, 64]. While the contrasting Raman-Nath limit [83–85] with short laser pulses provides a vanishing velocity dispersion, the diffraction efficiency is very low. However, these limits have the advantage that particularly for constant interaction strengths, viz. rectangular pulse shapes and no spatial variations of the laser beams, simple analytical solutions can be given.

### 1.3.4 Sources of aberrations

For precise predictions, both, losses into higher diffraction orders and the velocity dispersion [86] of the quasi-Bragg diffraction must be considered. Because atomic clouds do have a finite momentum width, the velocity selectivity of the Bragg diffraction results in an incomplete population transfer, as shown in Fig. 1.4. The population loss into higher diffraction orders signals the crossover from the deep-Bragg- towards the Raman-Nath regime, referred to as quasi-Bragg regime [67].

In general, smooth time-dependent laser pulses lead to equally smooth beamsplitter responses. In contrast, spatial envelopes lead to aberrations [30, 41, 87, 88], especially for large momentum transfer interferometers. Even very wide (collimated) Laguerre-Gaussian beams exhibit spatial inhomogeneity and wavefront curvature. This becomes relevant for large atomic clouds compared to the laser beamwaist or for significantly displaced clouds from the symmetry axis. Laser misalignment further degrades the diffraction efficiency and leads to rogue momentum components.

While for huge detunings and short interaction times ( $< 1$  ms) for most experiments spontaneous emission is not an issue, in general, it leads to incoherence and reasons aberrations.

In addition, there are sundry other technical sources of aberrations, such as mechanical vibrations (jiggling mirrors) and stochastic laser fields [89] (phase noise), but not considered in this framework.

## 1.4 VELOCITY FILTER FOR FAST AND HOT IONS

While in the context of matter-wave interferometers the diffraction processes are primarily used to transfer the entire velocity distribution of an ultracold atomic wavepacket, the use for fast and hot ions is the opposite as velocity filters. Here, the velocity selectivity of a stimulated Raman transition is exploited to filter out a velocity class that is as narrow as possible from an initially broad distribution. The transferred colder subensemble provides optimised initial conditions for subsequent precision collinear laser spectroscopy.

### 1.4.1 Collinear laser spectroscopy

In the context of fast ion and atom beams, collinear laser spectroscopy [46–48] enables the investigation of optical transitions with high resolution and sensitivity. The outstanding feature is the kinematical compression of the velocity width due to the electrostatic acceleration, with reducing the Doppler width of initially hot thermal samples to the typical natural linewidth of allowed optical dipole transitions [46]. This, together with the fast transport of the ions is the reason why collinear laser spectroscopy represents the ideal tool to study short-lived isotopes, produced at on-line facilities, with lifetimes in the millisecond range [90, 91]. Usually, these investigations are performed to determine nuclear ground state properties such as spins, charge radii and electromagnetic nuclear moments [91–94]. In addition, collinear laser spectroscopy has been used for the ultratrace analysis of long-lived isotopes at very low

abundance [95] and it was proposed as a technique to measure high voltages  $U$  with very high precision, using Doppler velocimetry [96–98].

The kinematical compression of collinear laser spectroscopy is able to produce spectra with resolution close to the limit of the natural linewidth. However, also a substantial residual broadening can remain, for example when the ions are generated in a plasma. Moreover, instead of the ground state of the ion, an excited metastable level might be a better initial level for the spectroscopy. The transition from this level can provide atomic hyperfine fields with better accuracy or a higher angular momentum provides the possibility of determining the nuclear spin. In such cases, population transfer has already been used for collinear laser spectroscopy, but only while the ions were stored in a linear Paul trap. In [99], pulsed lasers efficiently excite ions of all velocity classes into a higher-lying state that has a decay branch into the metastable state. After ejection from the trap, this state is addressed by collinear laser spectroscopy. However, such schemes often suffer from various decay paths into a multitude of levels after the resonant excitation. In contrast, with a Raman transition the population is transferred between two levels without occupying a third level with potential leakage into dark states. So far, one experiment reported on a Raman transition in collinear laser spectroscopy [100], where a transition between two hyperfine components of  $Y^+$  was induced using a single laser beam that was frequency modulated using an electro-optic modulator.

In the framework of this thesis, two counterpropagating laser beams are applied to theoretically investigate the possibility of using Raman transitions to selectively transfer ions from the ground state to a higher-lying metastable state. Afterwards, high-resolution collinear laser spectroscopy can be performed on this excited population. As a first potential application for such a scheme, high-voltage measurements using calcium ions  $^{40}\text{Ca}^+$ , are addressed by the group of Prof. Dr. W. Nörtershäuser at the Technische Universität Darmstadt.

### 1.4.2 Raman diffraction

The Raman scheme is used as a velocity filter to prepare ions in a very narrow velocity distribution in a meta-stable state. Therefore, beams from different lasers have to be used to bridge the large excitation energy, coupling the  $\Lambda$ -system depicted in Fig. 1.5.

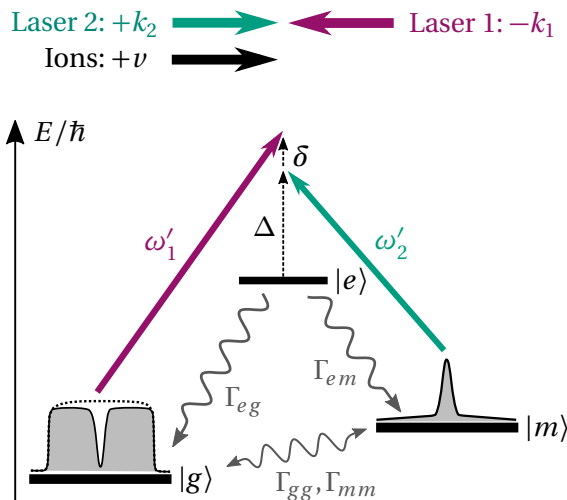


Figure 1.5: (Top) The interaction of two counterpropagating, far detuned lasers of wavenumbers  $k_1, k_2$  with moving ions is represented by the  $\Lambda$ -type energy diagram for Raman diffraction versus atomic wavenumber  $k = p/\hbar$  (bottom). In the rest frame of the ions, the one-photon detuning is  $\Delta$  and the two-photon detuning is  $\delta$  with respect to the Doppler-shifted frequencies  $\omega'_1, \omega'_2$ . The spontaneous decay rates  $\Gamma_{eg}, \Gamma_{em}$  and decoherence rates  $\Gamma_{gg}, \Gamma_{mm}$  induced by laser noise, diminish the efficiency of the Raman filter, transferring from the initial population (dotted) in the ground state  $|g\rangle$  with a broad velocity distribution a narrow cutout (shaded) into the metastable state  $|m\rangle$  without populating the excited state  $|e\rangle$ .

### 1.4.3 Sources of aberrations

The ideal filter is characterised by transferring one velocity class of initially hot ions with 100 % transfer efficiency into another internal ground state, in the limit of a delta function. Aberrations lead to a broadening of that resonance and a reduced transfer efficiency, especially for the resonant velocity, as indicated in Fig. 1.5. In particular, the filter efficiency is diminished by rogue resonances. The spontaneous emission from the two single-photon resonances in the  $\Lambda$ -system, each coupled by mainly one of the lasers, leads to broad velocity distributions, which can cover the narrow Raman resonance. In addition, laser noise with finite laser linewidths leads to ground-state decoherence, broadening the Raman resonance. Just as for atomic beamsplitters, spatial intensity variations of the laser beams lead to aberrations for the Raman velocity filter, while wavefront curvature is not an issue here. However, also the spatial distribution of the ion beam needs to be considered, because its size is in the same range as the laser beams and can be even larger.

## 1.5 STRUCTURE OF THE THESIS

This work is organised in four parts.

Part I starts with the concepts and methods of light-matter interaction in Chapter 2, covering the interaction of classical laser light with ultracold atoms as well as with hot ions. The essential methods to solve the time-evolution of the interacting system represent the special tools of the trade for this thesis, outlined in Chapter 3.

Part II covers the diffraction of ultracold atoms by classical laser light. It starts in Chapter 4 with the resonant diffraction with one laser beam. The analytical treatment provides physical insight into the basic mechanism of the diffraction of ultracold atoms. The focus of this thesis lies on the atomic quasi-Bragg diffraction with two counterpropagating laser beams. Therefore, Chapter 5 provides the fundamentals for the atomic diffraction by two counterpropagating pulsed Laguerre-Gaussian laser beams, covering the aberrations due to the velocity dispersion of the beamsplitter response as well as losses into higher diffraction orders. Here, plane laser waves with constant interaction strengths are considered. Different temporal envelopes are studied in Chapter 6, providing the opportunity to smooth the beamsplitter response. Spatial envelopes as well as laser misalignment reduce the diffraction efficiency and lead to rogue velocity components, considered in Chapter 7. The diminishing effects of spontaneous emission are included in Chapter 8. Derived analytical models as well as numerical simulations are verified by experimental data [1]. Finally, the effects of the multitude of aberrations are summarised in Chapter 9.

Part III deals with the diffraction of hot ions by classical laser light. The presented theoretical studies are motivated by the possible use of Raman velocity filters as a new tool to measure high voltages (Sec. 10.1). They are based on an experiment performed in the research group of Prof. Dr. W. Nörtershäuser at the Technische Universität Darmstadt, which is briefly introduced in Section 10.2. These experimental boundary conditions are covered by the derived theoretical model in Section 10.3. The results of numerical and analytical studies are presented in the frequency domain in Chapter 11 as well as in the time domain in Chapter 12. The former demonstrates the contributions of different resonances. The latter gives the ideal lower bound of the velocity width of the transferred ions as well as the broadening effects due to aberrations caused by rogue resonances, finite laser linewidths and spatial intensity variations of the ion and the laser beams. These results show promise for the realisation of optical high-voltage measurements with spectroscopic precision.

Finally, this thesis concludes with a summary of the findings and an outlook about further interesting research options in Part IV.

The elaborated, numerical and analytical concepts, methods and solutions has been implemented into the MATTERWAVESIM Python software package of the group of Prof. Dr. R. Walser at the Technische Universität Darmstadt. Central results of this thesis are or will be published in scientific journals:

**A. Neumann**, M. Gebbe, R. Walser [101]

*Aberrations in (3+1)-dimensional Bragg diffraction using pulsed Laguerre-Gaussian laser beams*

Phys. Rev. A **103**, 043306 (2021)

Based on Chapter 1 and Part II: Chapters 5, 6, and 7.

O. Marchukov, **A. Neumann**, J. Teske, R. Walser

*Collimation of Bose-Einstein condensates within Bragg-beam splitters applying pulsed Laguerre-Gaussian laser beams*

In preparation

Contribution by Part II: Chapter 7, especially Section 7.3.

**A. Neumann**, M. Gebbe, R. Walser

*Aberrations in (3+1)-dimensional Bragg diffraction due to misaligned, pulsed Laguerre-Gaussian laser beams*

In preparation

Based on Part II: Chapter 7, especially Section 7.5.

**A. Neumann**, W. Nörtershäuser, R. Walser [102]

*Raman velocity filter as a tool for collinear laser spectroscopy*

Phys. Rev. A **101**, 052512 (2020), Editors' Suggestion<sup>3</sup>

Based on Chapter 1 and Part III.

---

<sup>3</sup> 'A small number of Physical Review A papers that the editors and referees find of particular interest, importance, or clarity.'



# Part I

---

## FUNDAMENTAL CONCEPTS AND METHODS

---





---

## CONCEPTS OF LIGHT-MATTER INTERACTION

---

The interaction of electromagnetic radiation and matter leads to fascinating physical effects and numerous scientific advances [103–105]. Ultracold atoms interacting with laser light are of special interest to investigate elementary questions in quantum physics. For ultracold temperatures close to the absolute zero, typically in the regime of nano- to microkelvin, the quantum mechanical properties of the atoms become essential. Then, the atoms behave more like waves than classical particles. In addition, the main concept of the diffraction of alkali-like ions is similar to that of ultracold atomic diffraction.

In the next Sections 2.1- 2.3 the basic concepts for a dilute gas of ultracold, neutral atoms interacting with classical laser fields in the dipole approximation are given. In this framework semi-classical approaches are almost always adequate in practice. These lay the foundations and introduce the notations for the main topic of this thesis: the description of the diffraction process of matter waves engendered by laser light. Section 2.4 shows the different aspects, which must be taken into account for the treatment of hot alkali-like ions.

### 2.1 COLD ATOMS INTERACTING WITH LASER LIGHT

Within the semi-classical quantum theory, which is used to describe the interaction dynamic of coherent light fields with one ultracold, hydrogen-like atom, the atomic system is treated quantum mechanically, while the light fields are treated classically.

#### 2.1.1 Interaction Hamilton operator

**THE LIGHT FIELD** The electromagnetic field is generated by one or two monochromatic lasers providing coherent light in the visible (390 nm – 790 nm) to near-infrared (700 nm – 1000 nm) spectrum. Before different approaches describe explicitly the spatial properties of the laser fields in Section 2.2, firstly a general description considering both spatial and temporal variations is given. The transverse electric field of one single-mode laser  $L$  is

$$\mathbf{E}_L(t, \mathbf{r}) = \epsilon_L \mathcal{E}_{0,L}(t, \mathbf{r}) \cos[\omega_L t + \Phi_L(\mathbf{r})], \quad (2.1)$$

with polarisation vector  $\epsilon_L$ . The field is decomposed into a slowly varying amplitude  $\mathcal{E}_{0,L}(t, \mathbf{r}) \in \mathbb{R}$  as well as the spatial phase  $\Phi_L(\mathbf{r})$ , including the rapidly oscillating carrier phase  $\mathbf{k}_L \mathbf{r}$ . Here, the vacuum dispersion relation  $\omega_L = c k_L$  applies, with the speed of light  $c$  and the positive wavenumber  $k_L = |\mathbf{k}_L| > 0$ . The total electric field is consequently the sum over all  $N_L$  laser beams

$$\mathbf{E}(t, \mathbf{r}) = \sum_{L=1}^{N_L} \mathbf{E}_L(t, \mathbf{r}). \quad (2.2)$$

**THE ATOMIC MODEL** The considered atomic matter is a cold, dilute gas of neutral atoms with relative velocities much smaller than the speed of light. Although ensembles of many atoms should be considered, we start with the description of one single atom of mass  $M$ . Different approaches to define a quantum mechanical state for (an ensemble of) ultracold atoms are given in Section 2.3.

The simplest atomic model for the quantum mechanical description of atom-light interaction is the two-level system. Here, the internal structure of the atoms is modelled with two electronic levels  $\{|g\rangle, |e\rangle\}$ , referred to as the ground- and excited state, spanning the Hilbert space  $\mathcal{H}_{\text{int}}$ . The corresponding energies  $\hbar\omega_g$  and  $\hbar\omega_e$  define the transition frequency  $\omega_0 = \omega_e - \omega_g$ . Together with the external degrees of freedom, namely the non-relativistic centre-of-mass motion in three dimensions  $\mathcal{H}_{\text{com}}$ , the total single-particle Hilbert space for the atomic degrees of freedom results in the product  $\mathcal{H}_1 = \mathcal{H}_{\text{int}} \otimes \mathcal{H}_{\text{com}}$ . Considering an atomic medium, which is very dilute, atom-atom interactions can be safely ignored.

**THE QUANTUM MECHANICAL MODEL OF THE INTERACTION** Bringing both interaction parts together, the system Hamilton operator contains the kinetic centre-of-mass energy as well as the atomic internal energy and the atom-laser interaction potential

$$\hat{H}(t, \hat{\mathbf{r}}, \hat{\mathbf{p}}) = \frac{\hat{\mathbf{p}}^2}{2M} + \hbar\omega_g |g\rangle\langle g| + \hbar\omega_e |e\rangle\langle e| + \hat{V}(t, \hat{\mathbf{r}}). \quad (2.3)$$

When the lasers are far detuned from the atomic resonance frequencies  $|\omega_0 - \omega_L| \gg \Gamma$ , where  $\Gamma$  is the natural linewidth of the transition, the population loss into unobserved states is negligible and the two-level atom without spontaneous emission is a suitable approximation.

For the further theoretical description of atomic diffraction, different coordinate frames occur, giving rise for several frame transformations. Therefore, it is important to note that the system Hamilton operator (2.3) refers to the laboratory frame, the inertial rest frame of the atomic chip experiment. In this frame, denoted with  $S_0$ , the centre-of-mass motion of the particle with mass  $M$  is parametrised with phase-space coordinates  $(\mathbf{r}, \mathbf{p})$ .

Concentrating on interactions with optical fields, it is adequate to apply the long-wavelength or electric dipole approximation [103]. This utilises that the electric field with an optical wavelength in the range of hundreds of nano-meters to micro-meters does not change significantly over the size of the atom with angstroms scales. Therewith, the resulting interaction potential is restricted to the lowest-order term and purely defined through the dipole interaction energy

$$\hat{V}(t, \hat{\mathbf{r}}) = -\hat{\mathbf{d}} \cdot \mathbf{E}(t, \hat{\mathbf{r}}). \quad (2.4)$$

The dipole operator for the two-level system can be written in terms of the Pauli matrices for the two-level system  $\hat{\sigma} = |g\rangle\langle e|$ ,  $\hat{\sigma}^\dagger = |e\rangle\langle g|$  and the non-zero dipole matrix elements  $\mathbf{d}_{eg} \equiv \langle e|\hat{\mathbf{d}}|g\rangle = \mathbf{d}_{ge}$  [106]

$$\hat{\mathbf{d}} = \langle e|\hat{\mathbf{d}}|g\rangle (\hat{\sigma} + \hat{\sigma}^\dagger). \quad (2.5)$$

It is worth mentioning, that in the long-wavelength approximation the electric field is evaluated at the atomic centre-of-mass location  $\mathbf{r}$ .

Finally, the Hamilton operator defining the total energy of the quantised atom is

$$\hat{H}(t, \hat{\mathbf{r}}, \hat{\mathbf{p}}) = \frac{\hat{\mathbf{p}}^2}{2M} + \hbar\omega_g \hat{\sigma}_g + \hbar\omega_e \hat{\sigma}_e + \hat{V}(t, \hat{\mathbf{r}}), \quad \hat{V}(t, \hat{\mathbf{r}}) = -\mathbf{d}_{eg} \mathbf{E}(t, \hat{\mathbf{r}}) (\hat{\sigma} + \hat{\sigma}^\dagger), \quad (2.6)$$

with the Pauli spin operators  $\hat{\sigma}_\zeta \equiv \hat{\sigma}_{\zeta\zeta} = |\zeta\rangle\langle\zeta|$ .

### 2.1.2 Rotating-wave approximation

The electric field of any laser field (2.1) as well as the dipole operator (2.5) can be decomposed into positive- and negative-rotating parts

$$\mathbf{E} = \mathbf{E}^{(+)} + \mathbf{E}^{(-)}, \quad \mathbf{E}^{(\pm)}(t, \mathbf{r}) = \epsilon \mathcal{E}^{(\pm)}(t, \mathbf{r}) e^{\mp i\omega t}, \quad \mathcal{E}^{(\pm)}(t, \mathbf{r}) = \mathcal{E}_0(t, \mathbf{r}) e^{\mp i\Phi(\mathbf{r})}, \quad (2.7)$$

$$\mathbf{d} = \mathbf{d}^{(+)} + \mathbf{d}^{(-)}, \quad \mathbf{d}^{(+)} = \langle e | \hat{\mathbf{d}} | g \rangle \hat{\sigma} \sim e^{-i\omega_0 t}, \quad \mathbf{d}^{(-)} = \langle e | \hat{\mathbf{d}} | g \rangle \hat{\sigma}^\dagger \sim e^{+i\omega_0 t}. \quad (2.8)$$

The expectation value of  $\hat{\sigma}$  is the evolution of  $|e\rangle$  with the free atomic Hamilton operator with the unperturbed time dependence  $e^{-i\omega_0 t}$ . Within the rotating-wave approximation (RWA) [107], the antiresonant, rapidly oscillating terms  $\mathbf{d}^{(\pm)} \mathbf{E}^{(\pm)}$  are neglected in  $\hat{V}$ , because they have no contribution on average. Concentrating on the slow dynamics, the dipole potential simplifies to

$$\hat{V}_{\text{RWA}}(t, \hat{\mathbf{r}}) = -\frac{1}{2} \hat{\sigma}^\dagger \sum_{L=1}^{N_L} \langle e | \epsilon_L \cdot \hat{\mathbf{d}} | g \rangle \mathcal{E}_L(t, \hat{\mathbf{r}}) e^{-i\phi_L(t, \hat{\mathbf{r}})} + \text{h.c.}, \quad (2.9)$$

with introducing the slowly varying complex envelope  $\mathcal{E}_L(t, \mathbf{r})$  [the real amplitude is  $\mathcal{E}_{0,L}(t, \mathbf{r})$ ] and rapidly oscillating carrier phase  $\phi_L(t, \mathbf{r})$  of one certain laser  $L$ , defined with

$$\mathcal{E}_L(t, \mathbf{r}) = \mathcal{E}_{0,L}(t, \mathbf{r}) e^{i\varphi_L(\mathbf{r})}, \quad \varphi_L = -\mathbf{k}_L \mathbf{r} - \Phi_L, \quad \phi_L(t, \mathbf{r}) = \omega_L t - \mathbf{k}_L \mathbf{r}. \quad (2.10)$$

The RWA<sup>1</sup> (2.9) is valid for no overly strong coupling strengths  $\mathbf{d}_{eg} \epsilon_L \mathcal{E}_L(t, \mathbf{r}) / \hbar \ll \omega_L$  [108] and obviously, only for not extremely far detuned lasers  $|\omega_L - \omega_0| \ll \omega_0, \omega_L$ .

### 2.1.3 Rabi frequency

Introducing the Rabi frequency for each laser

$$\Omega_L(t, \mathbf{r}) \equiv \Omega_{0,L}(t, \mathbf{r}) e^{i\varphi_L(\mathbf{r})} \equiv -\frac{\langle e | \epsilon_L \cdot \hat{\mathbf{d}} | g \rangle \mathcal{E}_L(t, \mathbf{r})}{\hbar}, \quad (2.11)$$

the coupling potential between the light and the atomic transition finally reads

$$\hat{V}(t, \hat{\mathbf{r}}) = \frac{\hbar}{2} \hat{\sigma}^\dagger \Omega_{N_L}(t, \hat{\mathbf{r}}) + \text{h.c.}, \quad \Omega_{N_L}(t, \mathbf{r}) \equiv \sum_{L=1}^{N_L} \Omega_{0,L}(t, \mathbf{r}) e^{-i\Phi_L(t, \mathbf{r})}. \quad (2.12)$$

In the experiments, the Rabi frequency is defined by the total measured power  $P$ , the beam waist  $w_0$  and the effective coupling strength of the transition  $\mathcal{D}_{\text{eff}}$  [109]

$$\Omega_0 = \frac{|\mathcal{D}_{\text{eff}}|}{\hbar} \mathcal{E}_0 = \frac{|\mathcal{D}_{\text{eff}}|}{\hbar} \sqrt{\frac{4P}{\pi \epsilon_0 c w_0^2}}, \quad (2.13)$$

with the real electric field amplitude  $\mathcal{E}_0 = \mathcal{E}_0(\mathbf{r} = 0) \in \mathbb{R}$  and the vacuum permittivity  $\epsilon_0$ . In order of spatial intensity variations this represents the maximum Rabi frequency (in the centre) of the laser region. The effective coupling strength is proportional to the reduced matrix element  $\mathcal{D} = \langle J || e \mathbf{r} || J' \rangle$ , which can be calculated from the lifetime via [109]

$$\frac{1}{\tau} = \frac{\omega_0^3}{3\pi \epsilon_0 \hbar c^3} \frac{2J+1}{2J'+1} |\mathcal{D}|^2. \quad (2.14)$$

Assuming the lasers are far detuned from the atomic resonance of the rubidium-87  $D_2$ -line [110], they interact with the full  $J = 1/2 \rightarrow J' = 3/2$  transition. They are linearly polarised, interacting only with one (of three) component of the dipole operator. Therefore, the effective transition strength is given by the reduced dipole matrix element lowered to  $\mathcal{D}_{\text{eff}} = \mathcal{D} / \sqrt{3}$ . For the rubidium-87  $D_2$ -transition,  $\mathcal{D}$  is listed in Table A.1.

1 The specifying index 'RWA' of the interaction potential will be skipped in the further course of this thesis.

## 2.2 SPATIAL MODES OF THE ELECTROMAGNETIC FIELD

So far the classical laser light field was introduced most generally in (2.1) with spatio-temporal variations. Making for a certain laser  $L$  the ansatz of a monochromatic field

$$\mathbf{E}_L(t, \mathbf{r}) = \epsilon_L \mathcal{E}_L^{(+)}(\mathbf{r}) e^{-i\omega_L t} + c.c., \quad (2.15)$$

the spatial mode  $\mathcal{E}_L(\mathbf{r}) = \mathcal{E}_L^{(+)} + \mathcal{E}_L^{(-)}$  is a solution of the scalar Helmholtz equation [111]

$$\nabla^2 \mathcal{E}_L(\mathbf{r}) + k_L^2 \mathcal{E}_L(\mathbf{r}) = 0, \quad (2.16)$$

where the wavenumber satisfies the dispersion relation  $|\mathbf{k}_L| = \omega_L/c$ . Two types of spatial modes solve this equation: plane waves with  $\mathcal{E}^+ \sim \exp(i\mathbf{k}\mathbf{r})$  (cf. Sec. 2.2.1) and spherical waves with  $\mathcal{E}^+ \sim \exp(i\mathbf{k}\mathbf{r})/|\mathbf{r}|$  leading with an imaginary source point to realistic Laguerre-Gaussian laser beams (cf. 2.2.2).

### 2.2.1 Plane waves

Collimated laser beams are usually approximated with plane waves. Therefore, the complex amplitude of the positive frequency field reads

$$\mathcal{E}_L^{(+)}(\mathbf{r}) = \mathcal{E}_L(\mathbf{r}) e^{i\mathbf{k}_L \mathbf{r}} = \mathcal{E}_{L,0} e^{-i\Phi_L}, \quad \Phi_L = -\mathbf{k}_L \mathbf{r}, \quad (2.17)$$

representing a solution of the Helmholtz equation (2.16). These plane waves provide wavefront normals that coincide with the propagation direction but their intensity is constant  $I(\mathbf{r}) = |\mathcal{E}_L^{(+)}(\mathbf{r})|^2 = \mathcal{E}_{L,0}^2$  unlike the spatial confinement of real laser beams. However, this idealisation is amenable for analytical treatments and can be used as reference to quantify aberrations due to more realistic laser beams.

### 2.2.2 Laguerre-Gaussian beams

Laguerre-Gaussian (LG) beams [112] exhibit the characteristics of a realistic optical beam: the angular and spatial confinement. Even if lasers are collimated, they are still LG-beams, characterised by transversal as well as longitudinal intensity variations and wavefront curvature. For one LG-beam, propagating in its intrinsic reference frame  $S_L$  in  $x$ -direction, the ansatz

$$\mathcal{E}_L^{(+)}(\mathbf{r}) = \mathcal{E}_{L,0} u_L(\mathbf{r}) e^{ik_L x} \quad (2.18)$$

is appropriate. Here, the complex envelope  $u_L(\mathbf{r})$  is a slowly varying function in the propagation direction, with  $\partial_x u_L \ll u_L/\lambda_L$ . Therefore,  $\partial_x^2 u_L \ll k_L \partial_x u_L \ll k_L^2 u_L$ , which leads to the two-dimensional paraxial approximation of the Helmholtz equation [113]

$$i\partial_x u_L(x, \boldsymbol{\varrho}) = -\frac{\beta_L}{2} \nabla_{\boldsymbol{\varrho}}^2 u_L(x, \boldsymbol{\varrho}), \quad \beta_L = k_L^{-1}, \quad \boldsymbol{\varrho} = (y, z). \quad (2.19)$$

Hence, the scalar fundamental mode  $u_L(\mathbf{r})$  of a circularly symmetric LG-beam (visualised in Fig. 2.1) follows with

$$u_L(x, \boldsymbol{\varrho}) = \frac{x_R}{iq(x)} e^{i\frac{k_L \boldsymbol{\varrho}^2}{2q(x)}}, \quad q(x) = x - ix_R, \quad (2.20)$$

using the complex beam parameter  $q(x)$  and  $\boldsymbol{\varrho} = \sqrt{y^2 + z^2}$  is the radial distance to the symmetry axis. The solution (2.20) can be described with a real envelope  $u_L(x, \boldsymbol{\varrho})$  and the slowly varying phase  $\varphi_L(x, \boldsymbol{\varrho})$  as

$$u_L(x, \boldsymbol{\varrho}) = u_L e^{i\varphi_L}, \quad u_L(x, \boldsymbol{\varrho}) = \frac{w_0}{w(x)} e^{-\frac{\boldsymbol{\varrho}^2}{w(x)^2}}, \quad \varphi_L(x, \boldsymbol{\varrho}) = \frac{k_L \boldsymbol{\varrho}^2}{2R(x)} - \zeta(x). \quad (2.21)$$

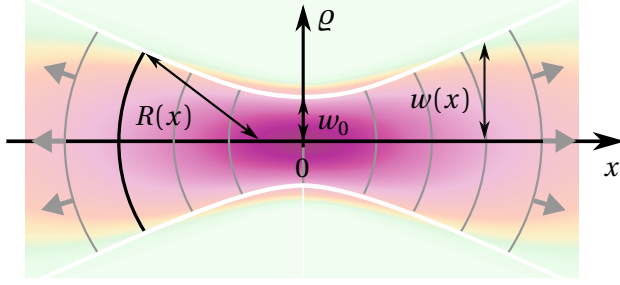


Figure 2.1: Laguerre-Gaussian beam propagating in  $x$ -direction, with colour coded spatial intensity, beamwaist  $w_0$ , minimum waist  $w_0$  and radius of curvature of the beam's wavefronts  $R(x)$ , where the local orientation of the wavevector is indicated with grey arrows.

The characterising beam parameters are: the beamwaist  $w(x)$ , the radius of curvature  $R(x)$ , the Gouy phase  $\zeta(x)$  and the Rayleigh range  $x_R$ , reading

$$w(x) = w_0 \sqrt{1 + \left(\frac{x}{x_R}\right)^2}, \quad R(x) = x \left[1 + \left(\frac{x_R}{x}\right)^2\right], \quad \zeta(x) = \arctan\left(\frac{x}{x_R}\right), \quad x_R = \frac{\pi w_0^2}{\lambda_L}, \quad (2.22)$$

with the minimum waist  $w_0 = 2\sigma_L$  and the wavelength  $\lambda_L = 2\pi/k_L$ . Finally, the complex amplitude of the positive-rotating part of the electric field (2.18) is parametrised with

$$\mathcal{E}_L^{(+)}(\mathbf{r}) = \mathcal{E}_{L,0} u_L(\mathbf{r}) e^{ik_L x} = \mathcal{E}_{L,0} u_L(x, \varrho) e^{-i\Phi_L(\mathbf{r})}, \quad \Phi_L(\mathbf{r}) = -k_L x - \varphi_L(x, \varrho). \quad (2.23)$$

Propagation directions unequal to  $x$  will be considered later on with geometric coordinate transformations  $S_L \mapsto S$ , including translations and rotations (cf. Sec. 3.4.2).

**COLLIMATED BEAMS** Collimated (c) laser beams are characterised by an almost constant beam radius for moderate propagation distances  $w(x) \approx w_0$ . For Laguerre-Gaussian laser beams this requires a long Rayleigh length in comparison to the envisaged propagation distance  $x_R \gg x$ . Therefore, large radii  $w_0 \gg \lambda_L$  are essential, because the Rayleigh length scales with the square of the beamwaist. Therefore, the spatially evolved mode  $u_L(x, \varrho)$  (2.21) simplifies to

$$u_L(x, \varrho) \stackrel{w_0 \gg \lambda_L}{\approx} u_L^c(\varrho) = e^{-\frac{\varrho^2}{w_0^2}}. \quad (2.24)$$

The slowly varying phase  $\varphi_L$  vanishes, because for relevant propagation distances  $x \ll x_R$  one can approximate  $R \rightarrow \infty$  and  $\zeta \approx 0$ .

## 2.3 SPATIAL MODES OF MATTER WAVES

In quantum theory wave-particle duality is a central aspect. To define proper spatial modes (cf. Sec. 2.3.3-2.3.7) it is necessary to take a closer look at the quantum mechanical model of the two-level atomic initial states (cf. Sec. 2.3.1, 2.3.2).

### 2.3.1 Single-particle systems

The single-particle ( $N = 1$ ) wavefunction includes three external degrees of freedom, i.e. its position. In addition, the internal degree of freedom is spanned by the atomic internal states  $|\zeta\rangle$ , with  $\zeta \in \{g, e\}$  for the two-level system. Working in the complete orthonormal basis  $\mathcal{B}$  of the single-particle Hilbert space  $\mathcal{H}_1$

$$\mathcal{B} = \{|\zeta\rangle, |\mathbf{r}\rangle : \zeta \in \{g, e\}, \mathbf{r} \in \mathbb{R}^3\}, \quad \langle \zeta, \mathbf{r} | \zeta', \mathbf{r}' \rangle = \delta_{\zeta\zeta'} \delta(\mathbf{r} - \mathbf{r}'), \quad (2.25)$$

the complete quantum states are denoted with  $|\zeta, \mathbf{r}\rangle$ . The non-relativistic, normalised single-

particle quantum system is represented by  $|\psi\rangle$  with

$$|\psi\rangle = \int d^3r \sum_{\varsigma} \psi_{\varsigma}(\mathbf{r}) |\varsigma, \mathbf{r}\rangle, \quad \psi_{\varsigma}(\mathbf{r}) = \langle \varsigma, \mathbf{r} | \psi \rangle, \quad \|\psi\|^2 \equiv \langle \psi | \psi \rangle = \int d^3r \sum_{\varsigma} |\psi_{\varsigma}(\mathbf{r})|^2 = 1, \quad (2.26)$$

where  $\psi_{\varsigma}(\mathbf{r})$  is the amplitude, viz. the spatial mode of the single-particle matter wave, and  $\|\psi\|$  is the continuum norm. The coherent time-evolution of  $|\psi\rangle$  is characterised by the Hamilton operator (2.6) and given by the single-particle Schrödinger equation

$$i\hbar \partial_t |\psi(t)\rangle = \hat{H} |\psi(t)\rangle. \quad (2.27)$$

In the position space, the time evolution of the two spatial modes  $\psi_{\varsigma=e,g}(\mathbf{r})$  reads

$$i\partial_t \begin{pmatrix} \psi_e(t, \mathbf{r}) \\ \psi_g(t, \mathbf{r}) \end{pmatrix} = \begin{pmatrix} -\frac{\hbar \nabla^2}{2M} + \omega_e & \Omega_{N_L}(t, \mathbf{r}) \\ \Omega_{N_L}^*(t, \mathbf{r}) & -\frac{\hbar \nabla^2}{2M} + \omega_g \end{pmatrix} \begin{pmatrix} \psi_e(t, \mathbf{r}) \\ \psi_g(t, \mathbf{r}) \end{pmatrix}, \quad (2.28)$$

using the definition of  $\Omega_{N_L}(t, \mathbf{r})$  from Eq. (2.12).

### 2.3.2 Many-particle systems

Atomic clouds are many-body system of indistinguishable particles that are either bosons or fermions. For their quantum mechanical representation the second quantisation [114] is appropriate. Therefore, the non-relativistic atomic field operator  $\hat{\Psi}_{\varsigma}(\mathbf{r})$  annihilates a particle at the position  $\mathbf{r}$ , in the internal state  $\varsigma$ . Regarding bosons<sup>2</sup>, they satisfy the following commutation rules

$$[\hat{\Psi}_{\varsigma}(\mathbf{r}), \hat{\Psi}_{\varsigma'}^{\dagger}(\mathbf{r}')] = \delta_{\varsigma\varsigma'} \delta(\mathbf{r} - \mathbf{r}'), \quad [\hat{\Psi}_{\varsigma}(\mathbf{r}), \hat{\Psi}_{\varsigma'}(\mathbf{r}')] = 0. \quad (2.29)$$

It is convenient to expand  $\hat{\Psi}_{\varsigma}(\mathbf{r})$  in a complete set of orthonormal single-particle functions, using here the Fourier sum with

$$\hat{\Psi}_{\varsigma}(\mathbf{r}) = \sum_{\mathbf{k}} \langle \mathbf{r} | \mathbf{k} \rangle \hat{a}_{\varsigma \mathbf{k}}. \quad (2.30)$$

In Eq. (2.30),  $\langle \mathbf{r} | \mathbf{k} \rangle$  is the position representation of the momentum<sup>3</sup> eigenstates, representing the wavefunctions  $\psi_{\varsigma \mathbf{k}}(\mathbf{r})$  in the single-particle basis  $|\varsigma, \mathbf{k}\rangle$ , i.e. plane wave amplitudes

$$\psi_{\mathbf{k}}(\mathbf{r}) = \langle \mathbf{r} | \mathbf{k} \rangle = \frac{e^{i\mathbf{k}\mathbf{r}}}{\sqrt{(2\pi)^3}}, \quad (2.31)$$

and  $\langle \varsigma', \mathbf{r} | \varsigma, \mathbf{k} \rangle = \delta_{\varsigma\varsigma'} \psi_{\varsigma \mathbf{k}}(\mathbf{r})$ . The bosonic creation and annihilation operators  $\hat{a}_{\varsigma \mathbf{k}}^{\dagger}, \hat{a}_{\varsigma \mathbf{k}}$  satisfy the bosonic commutation rules

$$[\hat{a}_{\varsigma \mathbf{k}}, \hat{a}_{\varsigma' \mathbf{k}'}^{\dagger}] = \delta_{\varsigma\varsigma'} \delta_{\mathbf{k}\mathbf{k}'}, \quad [\hat{a}_{\varsigma \mathbf{k}}, \hat{a}_{\varsigma' \mathbf{k}'}] = 0. \quad (2.32)$$

In the Fock space  $\mathcal{F} = \mathcal{H}_0 \oplus \mathcal{H}_1 \oplus \mathcal{H}_2 \oplus \dots$ , which is the direct sum of the  $N$ -particle Hilbert spaces  $\mathcal{H}_N$  for  $N = 0, 1, 2, \dots$ , they are defined through the relations

$$\begin{aligned} \hat{a}_{\alpha}^{\dagger} |n_0, n_1, \dots, n_{\alpha}, \dots\rangle &= \sqrt{n_{\alpha} + 1} |n_0, n_1, \dots, n_{\alpha} + 1, \dots\rangle, \\ \hat{a}_{\alpha} |n_0, n_1, \dots, n_{\alpha}, \dots\rangle &= \sqrt{n_{\alpha}} |n_0, n_1, \dots, n_{\alpha} - 1, \dots\rangle, \end{aligned} \quad (2.33)$$

<sup>2</sup> Rubidium-87 and rubidium-85 atoms are bosons, where rubidium-87 is considered in the experiments [1], but for example other isotopes such as rubidium-82 or potassium-40 are fermions.

<sup>3</sup> In the field of atomic diffraction naturally the momentum  $\mathbf{p} = \hbar \mathbf{k}$  occurs in units of the reduced Planck constant  $\hbar$ . For the sake of simplicity, the wavenumber  $\mathbf{k}$  is therefore equivalently referred to as the momentum. The reader is kindly asked to forgive this indistinctness.

where  $\alpha \equiv \zeta \mathbf{k}$  represents the complete set of quantum numbers. Here, the number  $n_\alpha \in \mathbb{N}_0$  of atoms in the single-particle state  $\alpha$  are the eigenvalues of the occupation-number operator

$$\hat{n}_\alpha = \hat{a}_\alpha^\dagger \hat{a}_\alpha, \quad \hat{n}_\alpha |\mathbf{n}\rangle = n_\alpha |\mathbf{n}\rangle, \quad |\mathbf{n}\rangle = |n_0, n_1, \dots, n_\alpha, \dots\rangle. \quad (2.34)$$

The generic state of the many-body system of the Fock space  $\mathcal{F}$  can be written in occupation number representation as linear combination of the many-body basis states  $|\mathbf{n}\rangle$  with

$$|\Psi\rangle = \sum_{\mathbf{n}} \psi_{\mathbf{n}} |\mathbf{n}\rangle, \quad |\mathbf{n}\rangle = \prod_{\alpha} \frac{(\hat{a}_\alpha^\dagger)^{n_\alpha}}{\sqrt{n_\alpha!}} |0\rangle. \quad (2.35)$$

In the Schrödinger representation, the state  $|\Psi\rangle$  can be expressed as  $N$ -particle amplitudes, reading

$$|\Psi\rangle = \sum_{N=0}^{\infty} |\Psi^{(N)}\rangle = \psi^{(0)} |0\rangle \quad (2.36)$$

$$+ \int d^3 r_1 \sum_{\zeta_1} \psi_{\zeta_1}^{(1)}(\mathbf{r}_1) \hat{\Psi}_{\zeta_1}^\dagger(\mathbf{r}_1) |0\rangle \quad (2.37)$$

$$+ \int d^3 r_2 d^3 r_1 \sum_{\zeta_1, \zeta_2} \psi_{\zeta_1, \zeta_2}^{(2)}(\mathbf{r}_1, \mathbf{r}_2) \hat{\Psi}_{\zeta_1}^\dagger(\mathbf{r}_1) \hat{\Psi}_{\zeta_2}^\dagger(\mathbf{r}_2) |0\rangle \quad (2.38)$$

$$+ \int d^3 r_3 d^3 r_2 d^3 r_1 \sum_{\zeta_1, \zeta_2, \zeta_3} \psi_{\zeta_1, \zeta_2, \zeta_3}^{(3)}(\mathbf{r}_1, \mathbf{r}_2, \mathbf{r}_3) \hat{\Psi}_{\zeta_1}^\dagger(\mathbf{r}_1) \hat{\Psi}_{\zeta_2}^\dagger(\mathbf{r}_2) \hat{\Psi}_{\zeta_3}^\dagger(\mathbf{r}_3) |0\rangle \quad (2.39)$$

$$+ \dots, \quad (2.40)$$

where  $\psi^{(0)}$  is the vacuum amplitude, Eq. (2.37) represents a single-particle state, Eq. (2.38) a two-particle state and Eq. (2.39) a three-particle state, where for the  $N$ -particle state  $|\Psi^{(N)}\rangle$ ,  $N$  particles are created with applying  $N$  field operators to the vacuum  $|0\rangle$ . In general,  $N$ -particle amplitudes  $\psi_{\zeta_1, \dots, \zeta_N}^{(N)}(\mathbf{r}_1, \dots, \mathbf{r}_N)$  do not factorise.

THE TIME EVOLUTION of the field operator  $\hat{\Psi}_\zeta(\mathbf{r})$  is defined by the Heisenberg equation

$$i \hbar \partial_t \hat{\Psi}_\zeta(t, \mathbf{r}) = [\hat{\Psi}_\zeta(t, \mathbf{r}), \hat{H}_H(t)], \quad (2.41)$$

where  $\hat{H}_H$  denotes the Hamilton operator in second quantisation, given by

$$\hat{H}_H(t) = \hat{H}_{\text{sp}}(t) + \hat{V}_d(t) + \hat{V}_2(t). \quad (2.42)$$

In the Fock space  $\mathcal{F}$ , the single-particle Hamiltonian  $\hat{H}_{\text{sp}}$ , including an external potential  $V_{\text{ext}}$  for example gravity or a trapping potential  $V_t$ , the dipole interaction  $\hat{V}_d$  and the two-body interatomic interactions  $\hat{V}_2$  read (cf. [114, 115])

$$\hat{H}_{\text{sp}}(t) = \int d^3 r \sum_{\zeta} \hat{\Psi}_\zeta^\dagger(\mathbf{r}) \left[ -\frac{\hbar^2}{2M} \nabla^2 + \hbar \omega_\zeta + V_{\text{ext}}(t, \mathbf{r}) \right] \hat{\Psi}_\zeta(\mathbf{r}), \quad (2.43)$$

$$\hat{V}_d(t) = \frac{\hbar}{2} \int d^3 r \Omega_{N_L}(t, \mathbf{r}) \hat{\Psi}_e^\dagger(\mathbf{r}) \hat{\Psi}_g(\mathbf{r}) + \text{h.c.}, \quad (2.44)$$

$$\hat{V}_2(t) = \frac{1}{2} \int d^3 r d^3 r' \sum_{\zeta, \zeta'} \hat{\Psi}_\zeta^\dagger(\mathbf{r}) \hat{\Psi}_{\zeta'}^\dagger(\mathbf{r}') V_2^{\zeta, \zeta'}(\mathbf{r} - \mathbf{r}') \hat{\Psi}_{\zeta'}(\mathbf{r}') \hat{\Psi}_\zeta(\mathbf{r}), \quad (2.45)$$

with  $\Omega_{N_L}$  from Eq. (2.12). For the considered dilute gases it is appropriate to restrict the particle-particle interactions to two-particle interactions  $\hat{V}_2$ . The pair potential, which is assumed to be local and exhibits translational invariance, depends on the particle distance  $V_2^{\zeta, \zeta'}(\mathbf{r} - \mathbf{r}')$  and in general different scattering properties for atoms in different states  $\zeta$  are considered.



**DILUTE GAS APPROXIMATION** Within the very dilute gas, during the short atomic diffraction pulses, two-particle interactions are assumed to be negligible  $\hat{V}_2 = 0$ . Therefore, the time evolution (2.41) simplifies to

$$i\partial_t \begin{pmatrix} \hat{\Psi}_e(t, \mathbf{r}) \\ \hat{\Psi}_g(t, \mathbf{r}) \end{pmatrix} = \begin{pmatrix} -\frac{\hbar\nabla^2}{2M} + \omega_e + \frac{V_{\text{ext}}(t, \mathbf{r})}{\hbar} & \Omega_{N_L}(t, \mathbf{r}) \\ \Omega_{N_L}^*(t, \mathbf{r}) & -\frac{\hbar\nabla^2}{2M} + \omega_g + \frac{V_{\text{ext}}(t, \mathbf{r})}{\hbar} \end{pmatrix} \begin{pmatrix} \hat{\Psi}_e(t, \mathbf{r}) \\ \hat{\Psi}_g(t, \mathbf{r}) \end{pmatrix}, \quad (2.46)$$

which is dynamically equivalent to the single-particle Schrödinger equation (2.28) for  $V_{\text{ext}} = 0$ , but has operator valued amplitudes.

**CLASSICAL FIELD APPROXIMATION** Optimal initial states for matter-wave interferometers are Bose-Einstein condensates (BECs). In these states a collection of bosonic atoms occupies macroscopically one quantum state. In the mean-field approximation for  $T \ll T^c$  the BEC has a macroscopic mean value of the field operator [116]

$$\hat{\Psi}_\zeta(t, \mathbf{r}) = \psi_\zeta^c(t, \mathbf{r}) + \delta\hat{\Psi}_\zeta(t, \mathbf{r}) \approx \psi_\zeta^c(t, \mathbf{r}). \quad (2.47)$$

The complex, condensate (c) wavefunction  $\psi_\zeta^c(t, \mathbf{r}) \equiv \langle \hat{\Psi}_\zeta(t, \mathbf{r}) \rangle$  is defined as the expectation value of the field operator and quantum fluctuations  $\delta\hat{\Psi}_\zeta(t, \mathbf{r})$  cause only small deviations around it, i.e.  $\langle \delta\hat{\Psi}_\zeta(t, \mathbf{r}) \rangle = 0$ . Applying the approximation (2.47) to the time evolution (2.46) yields equations of motions formally identical to the two component Schrödinger equation (2.28) for single particle quantum states. From the many-particle treatment only the normalisation to the particle number  $N$  is left over, as expected for non-interacting particles. This results from the expectation value  $N = \langle \hat{N} \rangle$  of the particle-number operator

$$\hat{N} = \int d^3r \sum_\zeta \hat{n}_\zeta(\mathbf{r}), \quad \langle \hat{N} \rangle = \int d^3r \sum_\zeta n_\zeta^c(\mathbf{r}) + \int d^3r \sum_\zeta \langle \hat{n}_\zeta^t(\mathbf{r}) \rangle = N^c + N^t, \quad (2.48)$$

Here,  $\hat{n} = \sum_\zeta \hat{n}_\zeta$  is the density operator and for one internal state  $\hat{n}_\zeta$  reads

$$\hat{n}_\zeta(\mathbf{r}) = \hat{\Psi}_\zeta^\dagger(\mathbf{r})\hat{\Psi}_\zeta(\mathbf{r}) = n_\zeta^c(\mathbf{r}) + \hat{n}_\zeta^t(\mathbf{r}) + \delta\hat{\Psi}_\zeta^\dagger\psi_\zeta^c(\mathbf{r}) + \delta\hat{\Psi}_\zeta\psi_\zeta^{c*}(\mathbf{r}), \quad (2.49)$$

$$n_\zeta^c(\mathbf{r}) = |\psi_\zeta^c(\mathbf{r})|^2, \quad \hat{n}_\zeta^t(\mathbf{r}) = \delta\hat{\Psi}_\zeta^\dagger(\mathbf{r})\delta\hat{\Psi}_\zeta(\mathbf{r}), \quad (2.50)$$

with the density of the condensate  $n_\zeta^c$  and the density operator of the quantum depletion  $\hat{n}^t$ . For very low temperatures  $T \ll T^c$  one gets  $N^t \ll N^c$ , limiting in  $N \approx N^c$  for  $T \ll T^c$ .

**ATOMIC INITIAL STATES** For the diffraction analysis, the initial population is in the internal ground state. Therefore, the following sections present different approaches for the spatial modes  $\psi_g(t=0, \mathbf{r})$ , skipping in the following the index  $g$ .

Bose-Einstein condensates provide a narrow velocity respectively momentum spread  $\Delta p$ . Therefore, in the ideal limit of a vanishing  $\Delta p \rightarrow 0$  the condensate wavefunction  $\psi^c(t=0, \mathbf{r})$  can be approximated with plane-wave modes (cf. Sec. 2.3.3). However, this as well as Gaussian wavepackets, which provide a finite momentum expansion (cf. Sec. 2.3.4), are more theoretical approaches to model reasonably the position and momentum expansion of an atomic initial state with a single-particle wavefunction. To approximate the condensate wavefunction more realistically, an external trapping potential and particle-particle interactions are taken into account in Section 2.3.5. In general, there are also thermal clouds (cf. Sec. 2.3.6 and Sec. 2.3.7). These incoherent mixed states have a wide velocity spread in comparison to BECs, even for small temperatures. In regard to temperatures, especially the momentum distribution of a state is relevant. Indeed, for the diffraction efficiency of atomic beamsplitters with large collimated laser beams, where a plane-wave approximation for the laser beams is appropriate, the required information about the atomic initial state is completely given by its momen-



tum density distribution. Heisenberg's uncertainty principle  $\Delta x \Delta p \geq \hbar/2$  defines (in one dimension) the minimum relation between the confinement of a state in the position and the momentum space, because it is impossible to measure the two canonically conjugate variables with arbitrary precision. Therefore, the initial distributions of the following approaches are sketched in the phase-space  $(x, p)$  to assign them to the temperature scale (cf. Fig. 1.2).

### 2.3.3 Plane waves

An idealised case are initial states with ultimate momentum confinement, thus with a precisely defined momentum  $\mathbf{p}_0 = \hbar \mathbf{k}_0$ , provided by plane wave modes

$$\psi(t, \mathbf{r}) = e^{i(\mathbf{k}_0 \mathbf{r} - \omega(\mathbf{k}_0)t)} \quad (2.51)$$

in the position representation. They are solutions of the free Schrödinger equation

$$i\partial_t \psi(t, \mathbf{r}) = -\frac{\alpha}{2} \nabla^2 \psi(t, \mathbf{r}), \quad \alpha = \frac{\hbar}{M}, \quad (2.52)$$

where for  $t > 0$  the phase velocity  $v_\phi(\mathbf{k}) = \omega/\mathbf{k}$  with  $\omega(\mathbf{k}) = \hbar \mathbf{k}^2/2M$  is considered. With a suitable normalisation they are the momentum eigenstates in position representation  $\langle \mathbf{r} | \mathbf{k} \rangle = \exp(i\mathbf{k} \mathbf{r})/\sqrt{(2\pi)^3}$  (2.31) called de Broglie waves with assigning to all particles with the momentum  $p = |\mathbf{p}| = \hbar |\mathbf{k}|$  the wavelength  $\lambda = h/p$  [55].

The density  $n(t, \mathbf{r}) = |\psi(t, \mathbf{r})|^2$  (2.51) gives the probability distribution of the particle. While plane waves carry only one linear momentum component, they are not spatially localized  $n(t, \mathbf{r}) = 1 \mu\text{m}^{-3}$ , as prescribed by Heisenberg's uncertainty principle. In Fig. 2.2 the canonically conjugated density and phase are depicted for  $t = 0$  and using a one-dimensional expansion. The density in the position space  $n(x) = 1 \mu\text{m}^{-1}$  [cf. Eq. (2.51)] is obviously constant, while the phase  $\varphi(x) = \arg[\psi(x)] = k_{x,0}x$  depends linearly on  $x$ . In the momentum space the population of only one momentum component is apparent  $n(k_x) = |\Psi(k_x)|^2 = \delta(k_x - k_{x,0})$ , while the phase vanishes  $\varphi(k_x) = 0$ . Free time-evolved plane waves receive an additional constant phase in the position space with  $0 \leq \omega(\mathbf{k}_0)t < 2\pi$ .

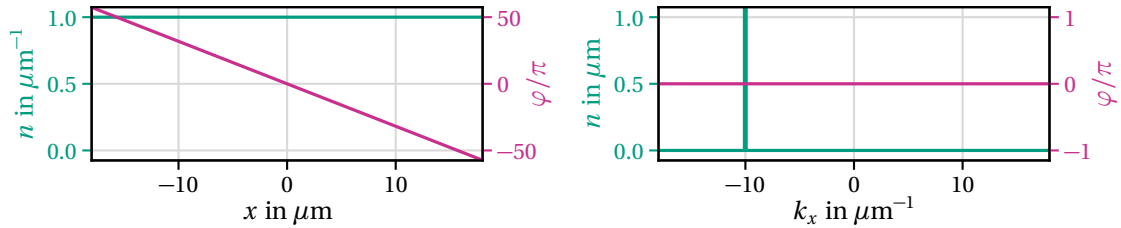


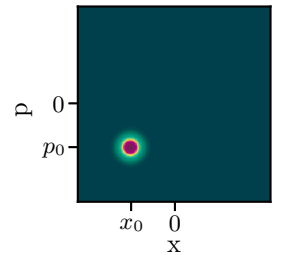
Figure 2.2: Density and phase of a one dimensional plane wave in position (left) and momentum  $p_x = \hbar k_x$  space (right), with  $k_{0,x} = -10 \mu\text{m}^{-1}$ .

### 2.3.4 Coherent states

Coherent states are the most *classical* single-particle quantum states, invented by E. Schrödinger [117]. They can be introduced differently. With the displacement operator  $\hat{T}$ , they are defined as displaced vacua

$$|\alpha\rangle = \hat{T}(\alpha)|0\rangle, \quad \hat{T}(\alpha) = e^{\alpha \hat{a}^\dagger - \alpha^* \hat{a}}, \quad \hat{a} = \frac{1}{\sqrt{2}} \left( \frac{\hat{x}}{a_0} + i a_0 \frac{\hat{p}}{\hbar} \right), \quad (2.53)$$

where  $\hat{a}$  is the dimensionless annihilation operator with  $[\hat{a}, \hat{a}^\dagger] = 1$  and  $a_0 = \sqrt{\hbar/(M\omega)}$  is the harmonic oscillator ground state size. In a position representation coherent states are GAUSSIAN WAVEPACKETS with minimum uncertainty. Therefore,

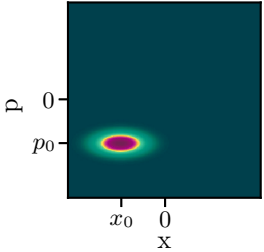


they provide a good localisation in the position as well as in the momentum space, connected by the Heisenberg principle  $\sigma_x \sigma_k = 1/2$ , with the spatial width  $\sigma_x$  and the momentum width  $\sigma_k$ . The free  $d$ -dimensional, not-normalised, stationary wavefunction of the Gaussian wavepacket is a linear combination of plane waves, defined as [118]

$$\psi_0(\mathbf{r}) = e^{i\mathbf{k}_0(\mathbf{r}-\mathbf{r}_0) - \frac{1}{2}(\mathbf{r}-\mathbf{r}_0)(2\Sigma_0)^{-1}(\mathbf{r}-\mathbf{r}_0)} = \int d^d k \frac{e^{i\mathbf{k}\mathbf{r}}}{(2\pi)^{d/2}} \Psi_0(\mathbf{k}), \quad (2.54)$$

$$\Psi_0(\mathbf{k}) = \sqrt{|2\Sigma_0|} e^{-i\mathbf{k}\mathbf{r}_0 - \frac{1}{2}(\mathbf{k}-\mathbf{k}_0)(2\Sigma_0)(\mathbf{k}-\mathbf{k}_0)} = \int d^d r \frac{e^{-i\mathbf{k}\mathbf{r}}}{(2\pi)^{d/2}} \psi_0(\mathbf{r}). \quad (2.55)$$

This wavepacket is initially centred at  $(\mathbf{r}_0, \mathbf{k}_0) = (\langle \mathbf{r} \rangle, \langle -i\nabla \rangle)$  and its norm is  $\int d^d r |\psi_0|^2 = \sqrt{|2\pi\Sigma_0|}$  with the covariance matrix  $\Sigma_0 = \langle (\mathbf{r}-\mathbf{r}_0) \otimes (\mathbf{r}-\mathbf{r}_0) \rangle$ .



Ballistically spreading Gaussian wavepackets represent SQUEEZED STATES, with  $\sigma_x \sigma_k > 1/2$ . They are useful input states to test a beamsplitter. Using different expansion times  $t$ , one can vary the position width  $\sigma_x$ , while keeping the momentum width  $\sigma_k$  constant. The three-dimensional  $d = 3$  free Schrödinger equation (2.52) [equivalent to the paraxial approximation of the Helmholtz equation (2.19)] describes the spreading of a matter wave

$$\psi(t, \mathbf{r}) = \int d^d k e^{-it \frac{\alpha}{2} k^2} \frac{e^{i\mathbf{k}\mathbf{r}}}{(2\pi)^{d/2}} \Psi_0(\mathbf{k}) = \mathcal{A}(t) e^{-i\theta(t)} e^{i\mathbf{k}_0[\mathbf{r}-\mathbf{r}_0] - \frac{1}{2}[\mathbf{r}-\mathbf{r}_0(t)][2\Sigma(t)]^{-1}[\mathbf{r}-\mathbf{r}_0(t)]}, \quad (2.56)$$

using the Fourier-transformed field  $\Psi_0(\mathbf{k})$  implicitly defined in (2.54). The evolving centre position  $\mathbf{r}_0(t)$ , spreading covariance  $\Sigma(t)$ , dynamical phase  $\theta(t)$  and scale-factor  $\mathcal{A}(t)$  read

$$\mathbf{r}_0(t) = \mathbf{r}_0 + t\alpha\mathbf{k}_0, \quad \Sigma(t) = \Sigma_0 + it \frac{\alpha}{2}, \quad \theta(t) = t \frac{\alpha k_0^2}{2}, \quad \mathcal{A}(t) = \sqrt{\frac{|\Sigma_0|}{|\Sigma(t)|}}. \quad (2.57)$$

For the simulations, isotropic initial states are used with an identical expansion in all dimension in the position space, with  $\Sigma_{ij} = \delta_{ij}\sigma_x^2$  and a time-dependent spatial spreading

$$\sigma_x(t) = \sigma_x \sqrt{1 + (t/t_H)^2}, \quad t_H = 2\sigma_x^2 M / \hbar, \quad (2.58)$$

with the Heisenberg time  $t_H$ . The momentum width follows from the Heisenberg uncertainty  $\sigma_k(t) = \sigma_x(t=0)/2$ . Therefore, the ballistically evolved wavepacket in position space simplifies to

$$\psi(\tilde{t}, \mathbf{r}) = \left( \frac{\sigma_x}{\sqrt{2\pi}(\sigma_x^2 + \frac{i\tilde{t}}{2})} \right)^{d/2} e^{i(\mathbf{k}_0(\mathbf{r}-\mathbf{r}_0) - \mathbf{k}_0^2 \frac{\tilde{t}}{2})} e^{-\frac{(\mathbf{r}-\mathbf{r}_0 - \mathbf{k}_0 \tilde{t})^2}{4(\sigma_x^2 + \frac{i\tilde{t}}{2})}}, \quad (2.59)$$

where it is useful to introduce the scaled time  $\tilde{t} = \hbar t / M$ . In the momentum representation

$$\Psi(\tilde{t}, \mathbf{k}) = \left( \frac{2\sigma_x}{\sqrt{2\pi}} \right)^{d/2} e^{-i(\mathbf{k}\mathbf{r}_0 + \mathbf{k}^2 \frac{\tilde{t}}{2})} e^{-(\mathbf{k}-\mathbf{k}_0)^2 \sigma_x^2}, \quad (2.60)$$

the constant momentum width becomes obvious, while the spreading in the position space with the scaled time is  $\sigma_x(\tilde{t}; \tilde{t}_H)$  (2.58) with  $\tilde{t}_H = 2\sigma_x^2$ . In addition, the centre of the wavepacket is moving with  $\mathbf{v}_0 = \hbar \mathbf{k}_0 / M$ . These properties are visualised in Fig. 2.3 in one dimension  $x$  ( $d = 1$ ), with the densities  $n(\tilde{t}, x) = |\psi(\tilde{t}, x)|^2$  and  $n(k_x) = |\Psi(k_x)|^2$ , i.e.

$$n(\tilde{t}, x) = \left( \frac{\sigma_x^2}{2\pi(\sigma_x^4 + \frac{\tilde{t}^2}{4})} \right)^{1/2} e^{-\frac{\sigma_x^2(x-x_0-k_{x,0}\tilde{t})^2}{2(\sigma_x^4 + \frac{\tilde{t}^2}{4})}}, \quad n(k_x) = \frac{2\sigma_x}{\sqrt{2\pi}} e^{-(k_x - k_{x,0})^2 \sigma_x^2} \quad (2.61)$$

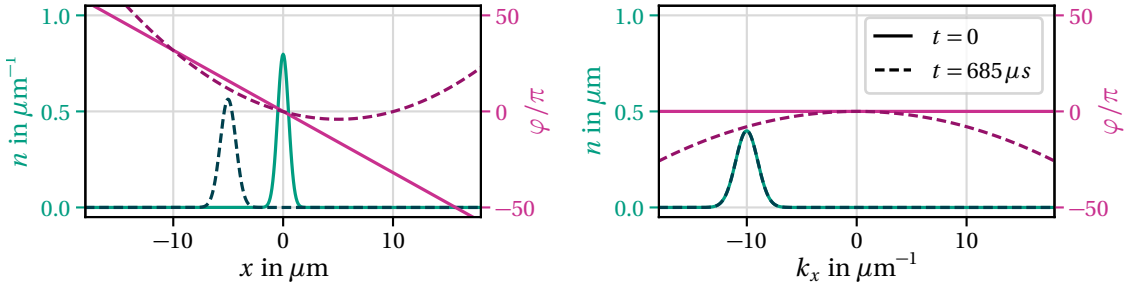


Figure 2.3: Density and phase of a one dimensional Gaussian wavepacket in position (left) and momentum space (right), without ballistical expansion (solid) and after  $t = 685 \mu\text{s}$  (dashed). The initial position is  $x_0 = 0$  and the initial momentum  $k_{0,x} = -10 \mu\text{m}^{-1}$ . The expansion size is  $\sigma_x = 0.5 \mu\text{m}$  leading to the momentum width  $\sigma_k = 1 \mu\text{m}^{-1}$ .

and the phases  $\varphi(\tilde{t}, x) = \arg[\psi(\tilde{t}, x)]$  and  $\varphi(\tilde{t}, k_x) = \arg[\Psi(\tilde{t}, k_x)]$ , i.e.

$$\varphi(\tilde{t}, x) = k_{x,0}(x - x_0) + \frac{\tilde{t}}{2} \left( \frac{(x - x_0 - k_{x,0}\tilde{t})^2}{4\sigma_x^4 + \tilde{t}^2} - k_{x,0}^2 \right) - \arctan \left( \frac{\tilde{t}}{2\sigma_x^2 + \sqrt{4\sigma_x^4 + \tilde{t}^2}} \right), \quad (2.62)$$

$$\varphi(\tilde{t}, k_x) = -x_0 k_x - \frac{\tilde{t}}{2} k_x^2. \quad (2.63)$$

The initial wavepacket centred at  $x = 0$  shows the characterising momentum and simultaneously spatial confinement, where the density in the position as well as in the momentum space is Gaussian distributed, also for  $t > 0$  [cf. Eq. (2.61)]. Similar to plane waves, for  $t = 0$  they have a linear phase in position space, which vanishes in momentum space for  $x_0 = 0$  [cf. Eq. (2.62)]. After free evolution, the atom is moving corresponding to its initial momentum and spreading in  $x$ , while the density distribution in  $k$  stays constant [cf. Eq. (2.61)]. In contrast, a quadratic phase is received for both, the position and the momentum representation but with a different sign of the curvature [cf. Eq. (2.62)].

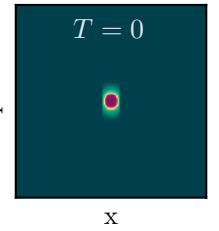
### 2.3.5 Bose-Einstein condensates

At ultracold temperatures  $T \ll T^c$ , a bosonic gas can become a Bose-Einstein condensate. In the framework of preparing an ultracold initial state for the atomic diffraction, the focus is on harmonically trapped gases of  $N$  bosonic atoms with temperatures well below this Bose-Einstein phase-transition  $T^c$ . For non-interacting bosons this temperature is given by [116]

$$k_B T^c = \hbar \bar{\omega} \left( \frac{N}{\zeta(3)} \right)^{1/3} \approx \hbar \bar{\omega} N^{1/3}, \quad (2.64)$$

where  $k_B$  is the Boltzmann constant,  $\zeta(n)$  the Rieman- $\zeta$  function. For experimentally<sup>4</sup> given values in Table A.1 the transition temperature is  $T^c = (34 \pm 1) \text{ nK}$ . For an anisotropic harmonic oscillator potential in  $d = 3$  dimensions

$$V_t(\mathbf{r}) = \frac{1}{2} M \left( \omega_x^2 x^2 + \omega_y^2 y^2 + \omega_z^2 z^2 \right), \quad (2.65)$$



<sup>4</sup> For experiments with ultracold atoms the  $D_2$ -line of rubidium-87 atoms serves optimal conditions, accessible for common optical devices. Table A.1 lists fundamental parameters as well as explicit parameters used in experiments, which are used to gauge the numerical simulation results.

the geometric average of the trap frequencies is  $\bar{\omega} = (\omega_x \omega_y \omega_z)^{1/3}$ . For non-interacting bosons one can use single-particle formulations and in such a harmonic trap the ground-state density has the form of a Gaussian wavepacket  $\psi_0(\mathbf{r})$  (2.54) normalised to the particle number  $N = \int d^3r |\psi_0(\mathbf{r})|^2$ . However, even for weak interactions the shape of the condensate can be significantly different [116]. Therefore, for temperatures well below  $T^c$ , the coherent mode of the condensate can be described using the Gross-Pitaevskii mean-field equation [116, 119]. Further, for strong interactions with mean-field energies much larger than the vacuum energy, one can use the Thomas-Fermi approximation [120], to obtain relevant physical observables, like the position and momentum width. Both approaches are derived in the following.

### **Gross-Pitaevskii classical field approximation**

The dilute gas of  $N$  interacting bosons in the internal ground state  $|g\rangle$  with the scalar field operator  $\hat{\Psi}(\mathbf{r}) \equiv \hat{\Psi}_g(\mathbf{r})$ , confined by an external potential  $V_t$  are described by the many-body Hamilton operator (2.42) for  $\varsigma = g$ , where the energy is shifted to be zero in the ground state and  $\hat{V}_d = 0$ , resulting in [116]

$$\hat{H}_{II} = \int d^3r \hat{\Psi}^\dagger(\mathbf{r}) \left[ -\frac{\hbar^2}{2M} \nabla^2 + V_t(\mathbf{r}) \right] \hat{\Psi}(\mathbf{r}) + \frac{1}{2} \int d^3r d^3r' \hat{\Psi}^\dagger(\mathbf{r}) \hat{\Psi}^\dagger(\mathbf{r}') V_2(\mathbf{r} - \mathbf{r}') \hat{\Psi}(\mathbf{r}') \hat{\Psi}(\mathbf{r}). \quad (2.66)$$

Therefore, the time evolution of the field operator, described by the Heisenberg equation (2.41) with the Hamilton operator (2.66), reads

$$i\hbar \partial_t \hat{\Psi}(t, \mathbf{r}) = \left[ -\frac{\hbar^2}{2M} \nabla^2 + V_t(\mathbf{r}) + \int d^3r' \hat{\Psi}^\dagger(t, \mathbf{r}') V_2(\mathbf{r} - \mathbf{r}') \hat{\Psi}(t, \mathbf{r}') \right] \hat{\Psi}(t, \mathbf{r}). \quad (2.67)$$

Using for the field operator the classical field approximation, neglecting the quantum depletion  $\hat{\Psi}(t, \mathbf{r}) \approx \psi^c(t, \mathbf{r})$  (2.47), the essential time evolution of the condensate wavefunction  $\psi^c(t, \mathbf{r})$  is given by the classical Gross-Pitaevskii mean-field equation

$$i\hbar \partial_t \psi^c(t, \mathbf{r}) = \left[ -\frac{\hbar^2}{2M} \nabla^2 + V_t(\mathbf{r}) + g n^c(t, \mathbf{r}) \right] \psi^c(t, \mathbf{r}), \quad N^c = \int d^3r n^c(t, \mathbf{r}), \quad (2.68)$$

where the atomic density is normalised to the particle number in the condensate  $N^c$  [cf. Eqs. (2.48)-(2.50)]. The Gross-Pitaevskii equation (2.67) has the form of a non-linear Schrödinger equation. The non-linearity is given by the internal mean-field energy  $g n^c(\mathbf{r})$ , which arises from the van der Waals interaction. At sufficiently low temperatures, with a thermal de Broglie wavelength  $\lambda_{dB} = \hbar \sqrt{2\pi/Mk_B T}$  much longer than the range of two-particle interactions, the interaction term in Eq. (2.66) can be approximated with an effective contact potential  $V_2(\mathbf{r}' - \mathbf{r}) = g \delta(\mathbf{r}' - \mathbf{r})$ , where the strength  $g = 4\pi \hbar^2 a_s / M$  is characterised by the  $s$ -wave scattering length  $a_s$ . This is compatible with replacing  $\hat{\Psi}(t, \mathbf{r})$  with  $\psi^c(t, \mathbf{r})$  in the time evolution.

For the stationary state of the condensate wavefunction one uses the ansatz  $\psi^c(t, \mathbf{r}) = \psi^c(\mathbf{r}) \exp(-i\mu t/\hbar)$ . This leads to the time-independent Gross-Pitaevskii equation

$$\left[ -\frac{\hbar^2}{2M} \nabla^2 + V_t(\mathbf{r}) + g n^c(\mathbf{r}) \right] \psi^c(\mathbf{r}) = \mu \psi^c(\mathbf{r}), \quad (2.69)$$

where  $\mu$  is the energy of the ground state and is identified as the chemical potential.

### Thomas-Fermi approximation

In the Thomas-Fermi (TF) limit [116] for mean-field energies much larger than the vacuum energy, the stationary condensate wavefunction  $\psi_{\text{TF}}^c(\mathbf{r})$  can be approximated by the solution of the Gross-Pitaevskii equation (2.69), neglecting the quantum pressure

$$[V_t(\mathbf{r}) + g n_{\text{TF}}^c(\mathbf{r}) - \mu] \psi_{\text{TF}}^c(\mathbf{r}) = 0. \quad (2.70)$$

The algebraic solution  $\psi_{\text{TF}}^c = \sqrt{n_{\text{TF}}^c}$  of Eq. (2.70) is given by

$$n_{\text{TF}}^c(\mathbf{r}) = \begin{cases} [\mu - V_t(\mathbf{r})]/g, & \mu > V_t(\mathbf{r}), \\ 0, & \mu \leq V_t(\mathbf{r}). \end{cases} \quad (2.71)$$

For a harmonic trap  $V_t$  (2.65), the Fourier transform of the TF-field is a Bessel function [120]

$$\Psi_{\text{TF}}^c(\mathbf{k}) = \int \frac{d^d r}{(2\pi)^{\frac{d}{2}}} e^{-i\mathbf{k}\mathbf{r}} \psi_{\text{TF}}^c(\mathbf{r}) = \sqrt{\frac{\pi\mu}{2g}} \frac{J_{\frac{d+1}{2}}(k' r')}{(k' r')^{\frac{d+1}{2}}}, \quad (2.72)$$

$$k' r' = \sqrt{(k_x x_{\text{TF}})^2 + (k_y y_{\text{TF}})^2 + (k_z z_{\text{TF}})^2}, \quad \text{for } d = 3. \quad (2.73)$$

The trap frequencies  $\omega_a$ ,  $a \in \{x, y, z\}$  define the TF-radii  $a_{\text{TF}} = \sqrt{2\mu/M\omega_a^2}$  and the geometrical average  $\bar{\omega} = (\omega_x \omega_y \omega_z)^{1/3}$  the averaged TF-radius  $r_{\text{TF}}$  as well as the chemical potential  $\mu$

$$r_{\text{TF}} = \sqrt{\frac{2\mu}{m\bar{\omega}^2}}, \quad \mu = \frac{\hbar\bar{\omega}}{2} \left( \frac{15N^c a_s}{\bar{a}} \right)^{2/5}, \quad \bar{a} = \sqrt{\frac{\hbar}{M\bar{\omega}}}, \quad (2.74)$$

with the harmonic oscillator length  $\bar{a}$ .

For the given atom and trap parameters (cf. Table A.1) the TF-approximation is suitable, because  $N^c a_s/\bar{a} \gg 1$ , thus the mean-field energies are much larger than the vacuum energy [116]. The position and momentum distributions are depicted in Fig. 2.4, where the phase vanishes. The typical parabolic shape in the position space is visible. This demonstrates the influence of the boson-boson interactions leading to a condensate shape differing to the non-interacting Gaussian wavepacket. Due to the wide wings of the Bessel function towards large momenta, the TF-wavefunction has no finite momentum width. However, for the diffraction analysis only the distribution around the maximum, especially the  $1/e$ -width, is important. Therefore, it can be approximated very well with an anisotropic Gaussian wavepacket (2.54) with momentum widths  $\sigma_{k_x} = 0.39 \mu\text{m}^{-1}$ ,  $\sigma_{k_y} = 0.15 \mu\text{m}^{-1}$  and  $\sigma_{k_z} = 0.26 \mu\text{m}^{-1}$ , also depicted in Fig. 2.4. The beamsplitter performance is much more sensitive to the momentum distribution than to the spatial distribution of the initial state. Therefore, even the TF-limit of strong interactions indicates that Gaussian wavepackets (cf. Sec. 2.3.4) are appropriate test states for the beamsplitter simulations.

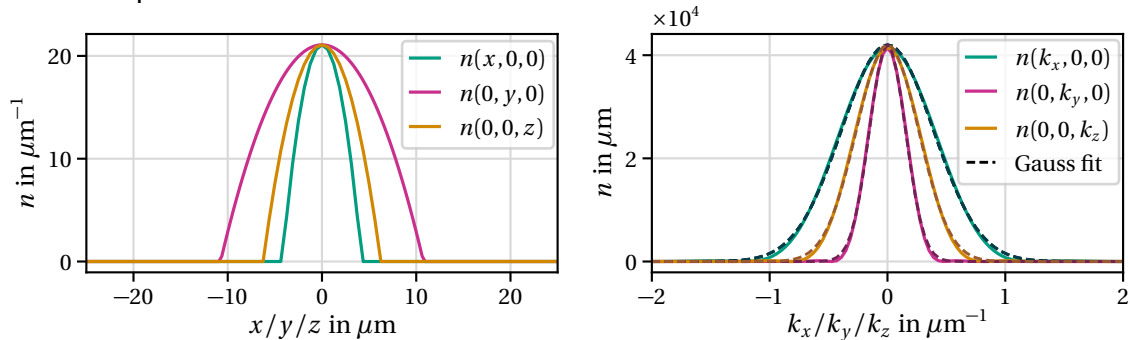
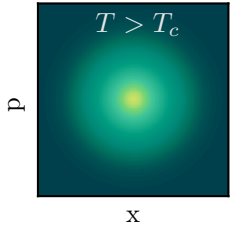


Figure 2.4: Density  $n = n_{\text{TF}}^c$  of the three-dimensional Thomas-Fermi wavefunction resulting from the atom and trap parameters of Table A.1, together with a Gaussian fit (2.54) as slices through the origin in position (left) and momentum space (right) with vanishing initial momentum.

### Free propagation of the BEC

In the experiment the diffraction pulses are applied to the atomic cloud, after release from the trap and some milliseconds time-of-flight (TOF). Therefore, the condensate expands in position space and also in momentum space due to atomic mean-field interaction, in contrast to a non-interacting Gaussian wavepacket [121]. To compare the diffraction simulations later with experimental data this needs to be considered within the initial state. The time-evolved condensate is simulated by Jan Teske from the TU Darmstadt by solving the (3+1)D Gross-Pitaevskii equation (2.68) for the given parameters of Table A.1 and the experimental time-of-flight. These results are confirmed by the scaling approach [122–125] to the numerical Gross-Pitaevskii ground state. Details will be published in Jan Teske's dissertation.

### 2.3.6 Thermal clouds



A thermal ensemble of  $N = \langle \hat{N} \rangle$  particles, above the BEC transition temperature  $T > T^c$ , is represented as statistical mixture of coherent states. These MIXED STATES are described with the density operator  $\hat{\rho}$  as weighted sum over all possible, normalised states  $|\Psi\rangle \in \mathcal{F}$  of the many-body Fock space

$$\hat{\rho} = \sum_{\Psi} p_{\Psi} |\Psi\rangle \langle \Psi|, \quad \text{Tr}\{\hat{\rho}\} = \sum_{\Psi} p_{\Psi} = 1, \quad \langle \Psi | \Psi \rangle = 1, \quad (2.75)$$

where  $p_{\Psi} \geq 0$  is a probability to find a quantum many-body system in the quantum state  $|\Psi\rangle$ .

For a system in equilibrium at finite temperature, the density operator of the grand canonical ensemble reads

$$\hat{\rho} = \frac{e^{-\beta(\hat{H} - \mu\hat{N})}}{Z}, \quad Z = \text{Tr}\{e^{-\beta(\hat{H} - \mu\hat{N})}\}, \quad \beta = \frac{1}{k_B T}, \quad (2.76)$$

with the partition function  $Z$  as normalisation factor, ensuring  $\text{Tr}\{\hat{\rho}\} = 1$ , and the inverse temperature  $\beta$ . Although a system with fixed particle number represents a canonical ensemble with  $\hat{\rho} = e^{-\beta\hat{H}}/Z$ , it is easier to move to the grand canonical ensemble (2.76), where the particle number  $N$  is variable and the partition function  $Z$  is determined in the Fock space  $\mathcal{F}$ . For the condition of a fixed  $N$  in the grand-canonical ensemble, the chemical potential  $\mu$  is determined as a function of the temperature  $T$  and the particle number  $N$  with choosing  $\mu(N)$  such that  $N = \sum_{\mathbf{k}} \langle \hat{n}_{\mathbf{k}} \rangle$ , where  $\hat{n}_{\mathbf{k}} = \hat{a}_{\mathbf{k}}^\dagger \hat{a}_{\mathbf{k}}$  measures the occupancy  $n_{\mathbf{k}} \in \mathbb{N}_0$  of the state  $|\mathbf{k}\rangle$  with energy  $\epsilon_{\mathbf{k}}$  [cf. Eq. (2.34)]. For a system of non-interacting bosons the Hamilton operator is diagonalizable and therefore additive, just like the particle number operator  $\hat{N}$  with

$$\hat{H} = \sum_{\mathbf{k}} \epsilon_{\mathbf{k}} \hat{n}_{\mathbf{k}}, \quad \hat{N} = \sum_{\mathbf{k}} \hat{n}_{\mathbf{k}}. \quad (2.77)$$

Therefore, the grand canonical density operator can be described as product of the single-mode density operators  $\hat{\rho}_{\mathbf{k}}$  with

$$\hat{\rho} = \frac{e^{-\beta(\hat{H} - \mu\hat{N})}}{Z} = \prod_{\mathbf{k}} \hat{\rho}_{\mathbf{k}}, \quad Z = \text{Tr}\{e^{-\beta(\hat{H} - \mu\hat{N})}\} = \prod_{\mathbf{k}} Z_{\mathbf{k}}, \quad (2.78)$$

$$\hat{\rho}_{\mathbf{k}} = \frac{e^{-\beta(\hat{H}_{\mathbf{k}} - \mu\hat{n}_{\mathbf{k}})}}{Z_{\mathbf{k}}}, \quad Z_{\mathbf{k}} = \text{Tr}\{e^{-\beta(\hat{H}_{\mathbf{k}} - \mu\hat{n}_{\mathbf{k}})}\} = \sum_{n_{\mathbf{k}}} e^{-\beta n_{\mathbf{k}}(\epsilon_{\mathbf{k}} - \mu)} = \frac{1}{1 - e^{-\beta(\epsilon_{\mathbf{k}} - \mu)}}. \quad (2.79)$$

Using the geometrical series  $\sum_{n=0}^{\infty} x^n = (1 - x)^{-1}$  in Eq. (2.79) implies  $\epsilon_{\mathbf{k}} > \mu$ . From the expectation value  $N = \langle \hat{N} \rangle = \partial_{\mu} k_B T \ln(Z) = \sum_{\mathbf{k}} \langle \hat{n}_{\mathbf{k}} \rangle$  one obtains the average occupation

number of the single-particle state  $|\mathbf{k}\rangle$ , which is given by the Bose distribution function [119]

$$f(\epsilon_{\mathbf{k}}) \equiv \langle \hat{n}_{\mathbf{k}} \rangle = \frac{1}{e^{\beta(\epsilon_{\mathbf{k}} - \mu)} - 1}. \quad (2.80)$$

**SEMI-CLASSICAL APPROXIMATION** Considering harmonically trapped bosons with  $T > T^c$ , in the semi-classical approximation the thermal energy is much larger than the quantum mechanical level spacing  $k_B T \gg \hbar \omega_{x,y,z}$  of the trapping potential  $V_t$  (2.65). Therefore, the lengthscale over which the trapping potential varies significantly is large in comparison to the thermal de Broglie wavelengths  $\lambda_{\text{dB}} = \hbar \sqrt{2\pi/M k_B T}$  of the particles. Thus, variations over the quantum mechanical uncertainty  $\Delta \mathbf{r}$ ,  $\Delta \mathbf{p}$  are negligible and the energy of the particle can be approximated with its classical single-particle energy at the location  $\mathbf{r}$ , thus  $\epsilon_{\mathbf{k}} = H_0(\mathbf{r}, \mathbf{p}) = \mathbf{p}^2/2M + V_t(\mathbf{r})$ , including the kinetic energy and the trapping potential  $V_t(\mathbf{r})$  (2.65). Therefore, the initial position and momentum of the bosons are distributed according to [119]

$$f(\mathbf{r}, \mathbf{p}) = \frac{1}{e^{\beta(H_0(\mathbf{r}, \mathbf{p}) - \mu)} - 1}. \quad (2.81)$$

For a known chemical potential the density of the thermal cloud can be calculated by [119]

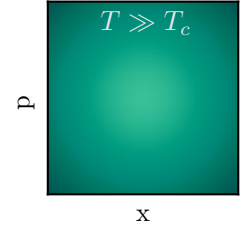
$$n^t(\mathbf{r}) = \int \frac{d^3 p}{(2\pi\hbar)^3} f(\mathbf{r}, \mathbf{p}) = \frac{1}{\lambda_{\text{dB}}^3} g_{3/2}[z(\mathbf{r})], \quad z(\mathbf{r}) = \exp\left(\frac{\mu - V_t(\mathbf{r})}{k_B T}\right) \quad (2.82)$$

and it is normalised to the number of thermal atoms  $N^t = \int d^3 r n^t(\mathbf{r})$ . Here, the effects of quantum statistics are taken into account with  $g_j(z) = \sum_i z^i / i^j$ . Due to the indistinguishability of bosons, the density is increased by  $g_{3/2}(z)/z$  in comparison to a distribution of distinguishable particles.

**CLASSICAL LIMIT** Well above the Bose-Einstein condensation temperature  $T \gg T^c$  (2.64), one finds the Maxwell-Boltzmann result of an anisotropic Gaussian distribution [119]

$$n^t(\mathbf{r}, T \gg T^c) = \frac{N^t}{\pi^{3/2} R_x R_y R_z} e^{-x^2/R_x^2} e^{-y^2/R_y^2} e^{-z^2/R_z^2}, \quad (2.83)$$

with the thermal size  $R_{a=\{x,y,z\}}^2 = 2k_B T / m \omega_a^2$ .

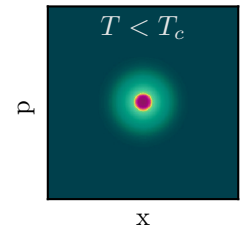


### 2.3.7 Partially condensed clouds

Partially condensed clouds arise for temperatures between the two limits of a fully condensed (c) Bose gas at  $T = 0$  K (cf. Sec. 2.3.5) and a thermal (t) cloud for  $T > T^c$  (cf. Sec. 2.3.6). Analogue to the separation in Eq. (2.47) the single-body coherence matrix of the atomic gas in position representation can be separated [126–128]

$$\rho^{(1)}(\mathbf{r}, \mathbf{r}') = \langle \mathbf{r} | \hat{\rho}^{(1)} | \mathbf{r}' \rangle = \langle \hat{\Psi}^\dagger(\mathbf{r}') \hat{\Psi}(\mathbf{r}) \rangle \quad (2.84)$$

$$= \rho^c(\mathbf{r}, \mathbf{r}') + \rho^t(\mathbf{r}, \mathbf{r}') = \psi^{c*}(\mathbf{r}') \psi^c(\mathbf{r}) + \rho^t(\mathbf{r}, \mathbf{r}') \quad (2.85)$$



into a mean-field contribution  $\rho^c(\mathbf{r}, \mathbf{r}')$ , describing the condensate, and a fluctuation  $\rho^t(\mathbf{r}, \mathbf{r}')$  around it as the thermal background, each contributing with the ratio  $p^{a=\{c,t\}} = N^a/N$  of the total atom number  $N$ . The weight  $p^c$  of the condensed part increases with decreasing the



temperature (cf. Sec. 2.2.1, page 24 in [119]). The density of the partially condensed cloud is also a bimodal distribution [129]

$$n(\mathbf{r}) \equiv \rho^{(1)}(\mathbf{r}, \mathbf{r}) = n^c(\mathbf{r}) + n^t(\mathbf{r}) = n_{\max}^c f^c(\mathbf{r}) + n_{\max}^t f^t(\mathbf{r}), \quad \int d^3r n(\mathbf{r}) = N^c + N^t = N. \quad (2.86)$$

For the condensate part  $n^c$  applying the TF-density, thus a parabolic distribution at zero temperature, with [129]

$$f^c(\mathbf{r}) \approx f_{\text{TF}}^c(\mathbf{r}) = \max\left(1 - \sum_{a=\{x,y,z\}} \frac{a^2}{a_{\text{TF}}^2}, 0\right), \quad f_{\text{TF}}^c(a) = \max\left(1 - \frac{a^2}{a_{\text{TF}}^2}, 0\right), \quad (2.87)$$

is appropriate. The thermal density  $n^t$  can be described as a broader, Bose-enhanced Gaussian distribution at the transition temperature with [129]

$$f^t(\mathbf{r}) = \frac{1}{g_{3/2}(1)} g_{3/2} \left( \prod_{a=\{x,y,z\}} e^{-a^2/2\sigma_a^2} \right), \quad g_j(z) = \sum_i z^i / i^j, \quad (2.88)$$

according to Eq. (2.82) for the anisotropic harmonic oscillator potential (2.65). This distribution is similar to a Maxwell distribution (2.83), but with different *temperatures*  $T_a$  for the three directions  $a \in \{x, y, z\}$ . Even in this case of Bose enhancement, the wings of the spatial distribution decays generally as  $e^{-a^2/2\sigma_a^2}$ . Therefore, the momentum widths  $\sigma_{k_a}^t$  of the thermal background can be estimated from time-of-flight measurements of  $\sigma_a(t)$  (2.58) of the freely expanding cloud. This results in

$$\sigma_{k_a}^t = M \sigma_{v_a} / \hbar = \sqrt{k_B T_a M / \hbar}, \quad a \in \{x, y, z\}, \quad (2.89)$$

with  $\sigma_{v_a} = \sigma_a(0)/t_H$ , and is in turn linked to the different *temperatures*  $T_a$  in the three directions. For these measurements the experimentally observed, also bimodal marginal one-dimensional density distributions are used as fit-functions with

$$n(a) = N^c \frac{3}{4a_{\text{TF}}} f_{\text{TF}}^c(a) + N^t \frac{1}{\sqrt{2\pi}\sigma_a} e^{-\frac{a^2}{2\sigma_a^2}}, \quad a \in \{x, y, z\}. \quad (2.90)$$

For example, a temperature of  $T = 20 \text{ nK}$  leads to a momentum width  $\sigma_k^t = 1.89 \mu\text{m}^{-1} = 0.23 k_L$  (in units of the wavenumber  $k_L$ , given in Table A.2) of the thermal cloud, much broader than those of the condensate (cf. TF-Approximation 2.3.5) [119, 130].

Partially condensed clouds with bimodal density distributions represent the most realistic ultracold atomic ensembles, considered within the framework of this thesis. It turns out, that this is necessary to reproduce real experimental results with the numerical atomic diffraction simulations. Therefore, the condensed part is not characterised with the approximated TF parabolic shape but even with a more realistic numerical simulation taking mean field expansion after release from the trapping potential into account.

## 2.4 HOT ALKALI-LIKE IONS INTERACTING WITH LASER LIGHT

The knowledge gained by the diffraction processes of ultracold, neutral atoms can be applied to other kinds of light-matter interactions, like the interaction of alkali-like ions with classical laser light. In Part III, the transfer and application of these findings to the topic of optical



high-voltage measurements with spectroscopic precision, using Raman transitions, is shown. Hence, this Section 2.4 provides the necessary theoretical fundamentals of the therefore used ion-light interaction. While the main concept of the diffraction of alkali-like ions is similar to that of atomic diffraction, the full theory is not repeated, but the differences are presented in detail.

Alkali-like ions possess only one outermost valence electron similar to alkali-atoms and therewith a hydrogen-like electronic structure. That is the reason why a single alkali-like ion experiences the same dipole-interaction, presented in Section 2.1 with

$$\hat{V} = -\hat{\mathbf{d}} \cdot \mathbf{E}(t, \hat{\mathbf{r}}). \quad (2.91)$$

Considering multiple ions, in general they interact with each other via the Coulomb interaction, due to their electric charge. However, in the framework of this thesis, the treatise is restricted to very dilute ion beams, where the ion-ion interactions are negligible. In contrast, for the velocity distribution of the ions their electric charge is relevant. They are accelerated with high voltages to large velocities in the range of one per mill of the speed of light, but a non-relativistic theory is still valid.

The velocity spread of the ions  $\Delta v_I = (10 - 100)\text{m/s}$  is connected to a temperature  $T = M\Delta v_I^2/3k_B \sim (10^8 - 10^{10})\text{nK}$ . It reasons a large momentum uncertainty  $M\Delta v_I \gg \hbar k$  compared to the photon momentum recoil  $\hbar k$  and momentum widths of ultracold atomic clouds  $\sigma_k < k$ , as depicted with the phase-space distributions for ensembles with different temperatures in Fig. 1.2. This represents the essential difference of the ion-light interaction to the interaction with ultracold atoms: the ions can be treated as classical particles in the sense of a vanishing wavelength in the range of  $\lambda = h/Mv \sim 10^{-14}\text{m}$ ,  $v \approx 0.001c$  and thermal de Broglie wavelength  $\lambda_{\text{dB}} \sim 10^{-10}\text{m}$ . While for ultracold atoms both, the internal and the external degrees of freedom need to be treated quantum mechanically [cf. Eq. (2.25)], for the diffraction of hot ions still the quantum mechanically internal states need to be considered but the external motion can be treated purely classically. That is the reason, why in the theoretical description of the ion-light interaction mechanical light effects are disregarded. The mixed state [cf. Eq. (2.75)] of the ion ensemble is described with the density operator  $\hat{\rho}(t) = \hat{\rho}_{\text{int}} \otimes \hat{\rho}_{\text{ext}}$ . In the classical limit, the position  $\mathbf{r}$  and the momentum of the particle  $\mathbf{p} = M\mathbf{v}$  can be treated as parameters, thus the single-body coherence matrix reads

$$\hat{\rho}^{(1)}(t; \mathbf{r}, \mathbf{p}) = \sum_{\zeta, \zeta'} \rho_{\zeta\zeta'}(t; \mathbf{r}, \mathbf{p}) |\zeta\rangle\langle\zeta'|, \quad \rho_{\zeta\zeta'} = \langle\zeta|\hat{\rho}^{(1)}|\zeta'\rangle, \quad (2.92)$$

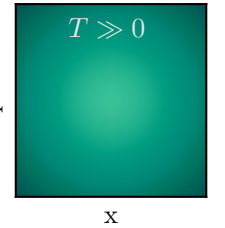
with  $\zeta, \zeta' \in \{g, e, m\}$  for the three-level system, depicted in Fig. 1.5. Consequently, observables  $\langle\hat{A}\rangle$  are obtained by static averaging over the initial phase-space distribution  $f(\mathbf{r}, \mathbf{p})$  of the ions with

$$\langle\hat{A}(t)\rangle = \int d^3r d^3p f(\mathbf{r}, \mathbf{p}) \text{Tr}\{\hat{A}(t, \mathbf{r}, \mathbf{p}) \hat{\rho}^{(1)}(t; \mathbf{r}, \mathbf{p})\}. \quad (2.93)$$

The interaction Hamilton operator is given by

$$\hat{H} = \hbar \sum_{\zeta} \omega_{\zeta} \hat{\sigma}_{\zeta\zeta} + \hat{V}(t, \mathbf{r}), \quad \hat{\sigma}_{\zeta\zeta} = |\zeta\rangle\langle\zeta|. \quad (2.94)$$

Due to the large velocity spread the ballistic evolution can be eliminated and no intrinsic kinetic energy distribution needs to be considered within the Hamilton operator (2.94). As a more detailed derivation, respectively description of this ionic diffraction is strongly connected with the experimental boundary conditions, it is detailed in Part III.





---

## TIME EVOLUTION OF LIGHT-MATTER INTERACTION

---

The performance of matter-wave diffraction is given by the time evolution of the interacting system. During the short diffraction pulses only the light-matter interaction is considered, matter-matter interactions are assumed to be negligible. Therefore, different approaches are given, which are adequate to consider the characteristic properties of a certain system. The Schrödinger equation (cf. Sec. 3.1) is used for single-particle quantum mechanics, respectively, if the initial state can be modelled with one collective mean wavefunction of a many-particle system, like the BEC ground state. The von-Neumann equation (cf. Sec. 3.2) handles statistically mixed states like the many-particle systems of thermal clouds. Finally, the master equation (cf. Sec. 3.3) also takes dissipation into account. In particular, methods are presented, which are efficient to solve the certain equations of motions numerically.

### 3.1 SCHRÖDINGER EQUATION

The Schrödinger equation

$$i\hbar\partial_t|\psi\rangle = \hat{H}|\psi\rangle, \quad (3.1)$$

describes the coherent time evolution of a non-relativistic quantum mechanical state with a Hamilton operator  $\hat{H}$ , possibly time- and/or position-dependent. The formal solution reads

$$|\psi(t)\rangle = \hat{U}(t, t_0)|\psi(t_0)\rangle, \quad \hat{U}(t, t_0) = \mathcal{T} \exp \left[ -\frac{i}{\hbar} \int_{t_0}^t dt' \hat{H}(t', \hat{\mathbf{r}}, \hat{\mathbf{p}}) \right] \quad (3.2)$$

with  $t > t_0$  and the time-evolution operator  $\hat{U}(t, t_0)$ . In case this equation cannot be solved analytically, numerical simulation methods on orthorhombic Fourier grids (cf. App. B.1) are applied. Important properties and methods for these simulations are given in Appendix B.

The Hamiltonian system, describing the light-matter interaction as a two-component (3+1)D problem, consists of the kinetic energy  $\hat{T}$  as well as the potential  $\hat{V}$

$$\hat{H}(t, \hat{\mathbf{r}}, \hat{\mathbf{p}}) = \hat{T}(\hat{\mathbf{p}}) + \hat{V}(t, \hat{\mathbf{r}}). \quad (3.3)$$

For time-independent potentials or approximating  $\hat{V}$  to be constant during one sufficiently small time step  $\tau = t - t_0$  (lower sum of the temporal envelope), the time-evolution reads

$$\hat{U}(\tau) = \exp \left[ -\frac{i}{\hbar} \hat{H}(\hat{\mathbf{r}}, \hat{\mathbf{p}}) \tau \right] = \exp \left[ -\frac{i}{\hbar} (\hat{T}(\hat{\mathbf{p}}) + \hat{V}(\hat{\mathbf{r}})) \tau \right]. \quad (3.4)$$

Evaluating an exponential function  $\exp[-i(\hat{T} + \hat{V})\tau/\hbar]$  with non-commutative operators  $\hat{T}$  and  $\hat{V}$ , where  $\tau$  is a small real number, is in general not possible. However, due to the separability of the Hamilton operator, symplectic integrators can be used to split the time evolution operator into parts depending on either the momentum  $\mathbf{p}$  or the position  $\mathbf{r}$ . Then, the kinetic part of the form  $\exp[-i\hat{T}(\hat{\mathbf{p}})\tau/\hbar]$  can be easily calculated, with Fourier transforming the wavefunction into momentum space. On the other hand, the impact of the potential part  $\exp[-i\hat{V}(\hat{\mathbf{r}})\tau/\hbar]$  can be calculated also exactly with the methods of disentangling an exponential of the  $SU(2)$  algebra, given in Section 3.1.2. The methods for constructing these symplectic algorithms are given in the next Section 3.1.1.

### 3.1.1 Symplectic integration

Symplectic integrators are numerical integration schemes for Hamiltonian systems. In comparison to other common integration schemes like Runge-Kutta-methods [131, 132], symplectic integrators provide great advantages. They preserve the geometry of phase space and conserved quantities such as the total system energy and angular momentum. Further, they are easy to implement. The integrator of order  $n$  uses the following expansion [133]

$$\hat{U}(\tau) = e^{\tau(\hat{T}+\hat{V})} = \prod_{i=1}^k e^{c_i \tau \hat{T}} e^{d_i \tau \hat{V}} + \mathcal{O}(\tau^{n+1}), \quad \hat{U}(0) = \mathbb{1}. \quad (3.5)$$

The difference of the exponential function  $\hat{U}$  and the product of exponential functions on the right side is of the order of  $\tau^{n+1}$ . Expanding both sides of Eq. (3.5) to the same order of  $\tau$  determines the coefficients  $c_i$  and  $d_i$ . Within the framework of this thesis, second, fourth or sixth order splitting is applied, depending on which one is more efficient for the used size of one time step and the required accuracy.

For SECOND ORDER SPLITTING the coefficients are  $c_1 = c_2 = 1/2$ ,  $d_1 = 1$ ,  $d_2 = 0$  and therefore the expansion reads

$$\hat{U}(\tau) = \hat{U}_2(\tau) + \mathcal{O}(\tau^3), \quad \hat{U}_2(\tau) = e^{\frac{1}{2}\tau\hat{T}} e^{\tau\hat{V}} e^{\frac{1}{2}\tau\hat{T}}. \quad (3.6)$$

The index of  $\hat{U}$  indicates the used splitting order. Combining several consecutive time steps reduces the arithmetic operations. This becomes obvious in the time-evolution of two consecutive time steps  $t_2 = t_0 + 2\tau$

$$\hat{U}_2(t_2, t_0) = \hat{U}_2(t_2, t_1) \hat{U}_2(t_1, t_0) = \hat{U}_2(\tau) \hat{U}_2(\tau) = e^{\frac{1}{2}\tau\hat{T}} e^{\tau\hat{V}} e^{\tau\hat{T}} e^{\tau\hat{V}} e^{\frac{1}{2}\tau\hat{T}}. \quad (3.7)$$

For FOURTH ORDER SPLITTING the expansion reads

$$\hat{U}(\tau) = \hat{U}_4(\tau) + \mathcal{O}(\tau^5), \quad \hat{U}_4(\tau) = e^{c_1 \tau \hat{T}} e^{d_1 \tau \hat{V}} e^{c_2 \tau \hat{T}} e^{d_2 \tau \hat{V}} e^{c_3 \tau \hat{T}} e^{d_3 \tau \hat{V}} e^{c_4 \tau \hat{T}}, \quad (3.8)$$

where some more coefficients are required

$$c_1 = c_4 = \frac{\alpha}{2}, \quad c_2 = c_3 = \frac{\alpha + \beta}{2}, \quad d_1 = d_3 = \alpha, \quad d_2 = \beta, \quad \alpha = \frac{1}{2 - 2^{1/3}}, \quad \beta = -\frac{2^{1/3}}{2 - 2^{1/3}}. \quad (3.9)$$

The fourth order splitting time evolution for two consecutive time steps follows with

$$\hat{U}_4(t_2, t_0) = e^{\frac{\alpha}{2}\tau\hat{T}} e^{\alpha\tau\hat{V}} e^{c_2\tau\hat{T}} e^{\beta\tau\hat{V}} e^{c_2\tau\hat{T}} e^{\alpha\tau\hat{V}} e^{\alpha\tau\hat{T}} e^{\alpha\tau\hat{V}} e^{c_2\tau\hat{T}} e^{\beta\tau\hat{V}} e^{c_2\tau\hat{T}} e^{\alpha\tau\hat{V}} e^{\frac{\alpha}{2}\tau\hat{T}}. \quad (3.10)$$

The SIXTH ORDER SPLITTING is the highest splitting order considered within this work, with

$$\begin{aligned} \hat{U}_6(\tau) = & e^{c_1 \tau \hat{T}} e^{d_1 \tau \hat{V}} e^{c_2 \tau \hat{T}} e^{d_2 \tau \hat{V}} e^{c_3 \tau \hat{T}} e^{d_3 \tau \hat{V}} e^{c_4 \tau \hat{T}} e^{d_4 \tau \hat{V}} e^{c_5 \tau \hat{T}} e^{d_5 \tau \hat{V}} \times \\ & e^{c_6 \tau \hat{T}} e^{d_6 \tau \hat{V}} e^{c_7 \tau \hat{T}} e^{d_7 \tau \hat{V}} e^{c_8 \tau \hat{T}} e^{d_8 \tau \hat{V}} e^{c_9 \tau \hat{T}} e^{d_9 \tau \hat{V}} e^{c_{10} \tau \hat{T}}, \end{aligned} \quad (3.11)$$

and the following coefficients, using  $\alpha$  and  $\beta$  from Eq. (3.9),

$$d_1 = d_3 = d_7 = d_9 = \alpha\alpha', \quad d_2 = d_8 = \beta\alpha', \quad d_4 = d_6 = \alpha\beta', \quad d_5 = \beta\beta', \quad (3.12)$$

$$c_i = (d_{i-1} + d_i)/2, \quad i = 2, 3, \dots, 9, \quad c_1 = c_{10} = d_1/2, \quad \alpha' = \frac{1}{2 - 2^{1/5}}, \quad \beta' = -\frac{2^{1/5}}{2 - 2^{1/5}}. \quad (3.13)$$

### Numerical verification

The achievable precision of the different splitting orders is demonstrated in Fig. 3.1 depending on the number of simulation time steps  $N_t$ , under monitoring the needed computational time  $t_c$ . Therefore, anticipating Part II about the diffraction of ultracold atoms, the numerical one-dimensional simulations of an atom interacting with one resonant laser [cf. Fig. 1.1 (a), Eq. (4.6) in Chap. 4] are used as test example. The interaction time is chosen to invert

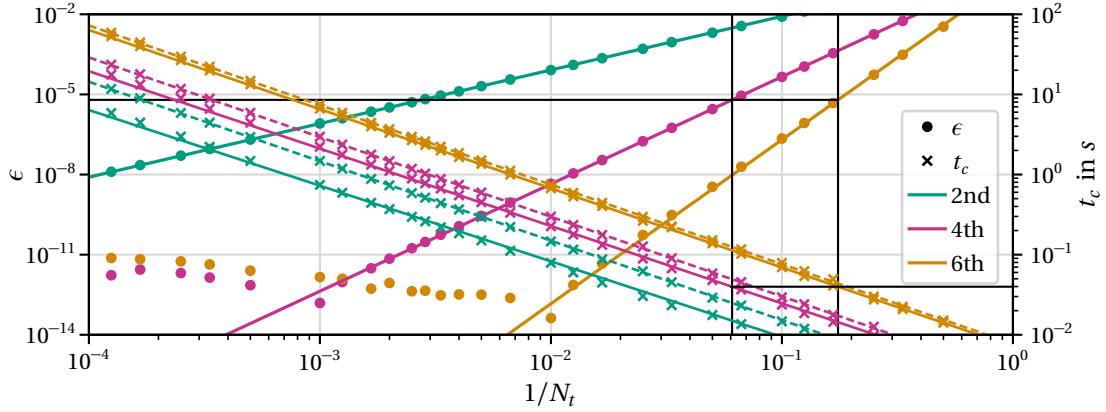


Figure 3.1: Relative energy conservation  $\epsilon = |H(t) - H(0)|/H(0)$  and required computational time  $t_c$  versus inverse number of simulation time steps  $N_t$ , for 2nd, 4th, 6th splitting order of the symplectic integrators. Combining consecutive time steps (solid) reduces the computational time compared to separating them (dashed). As highlighted, to achieve  $\epsilon = 5.5 \times 10^{-6}$ , the computational time is the same for using splitoperators of 4th or 6th order.

the population (initially in ground state, finally in excited state), realising an atomic mirror. Neglecting spontaneous emission, for constant laser powers the Hamilton operator in the rotating frame (4.6) is time-independent  $\hat{H}(t) = \text{const}$ . Therefore, additionally to the norm of the wavefunction also the expectation value  $H(t) \equiv \langle \hat{H}(t) \rangle = T(t) + V(t) = H(0)$  is conserved (cf. App. B.1.2). The latter is more sensitive and therefore the precision  $\epsilon = |H(t) - H(0)|/H(0)$  is depicted. Be aware that this conserved quantity is not equivalent to energy conservation, due to the absorption and emission of photons from the laser beam, which is only conserved, concerning both, the energy of the atom and of the laser.

By construction, one expects a power law for the precision  $\epsilon \propto \tau^m = (1/N_t)^m$ , where  $m$  identifies the splitting order. In the double-logarithmic scale this reveals the linear behaviour

$$\log(\epsilon) = m_\epsilon \log(1/N_t) + b. \quad (3.14)$$

Indeed, the results of the  $\epsilon$  conservation show different slopes  $m_\epsilon = \{2.0, 4.0, 6.1\}$  related to the splitting orders. The computational time shows also a linear dependence  $\log(t_c) = m_t \log(N_t) + b$  but with a slope  $m_t \approx 1$  approximately independent of the splitting order. The numerical double precision is reached for  $\epsilon \sim 10^{-13}$ , cancelling higher energy precisions for larger numbers of simulated time steps. Combining consecutive time steps reduces the arithmetic operations and consequently the computation time, as depicted. However, to monitor the temporal evolution of an observable, it is necessary to split the time evolution.

From this example, one can define optimal working regimes: For  $\epsilon \geq 2.9 \times 10^{-2}$  the 2nd splitting order provides the lowest computational times, while for  $6.2 \times 10^{-6} < \epsilon \leq 2.9 \times 10^{-2}$  the 4th order and for  $\epsilon < 6.2 \times 10^{-6}$  the 6th order are optimal. However, in general the better the requested precision of the energy conservation, also the higher splitting orders are beneficial, but usually the 4th splitting order is the appropriate choice.

### 3.1.2 Disentangling an exponential sum

Applying the potential part  $\exp[-iV(\hat{\mathbf{r}})\tau/\hbar]$  of the Hamilton operator to the wavefunction can be done exactly with the methods of disentangling an exponential of the  $SU(2)$  algebra described in [134]. Here, the main aspects are recaptured. For a finite-dimensional Lie algebra, like the  $SU(2)$ , the in general infinite expansion to disentangling an exponential

$$e^{\hat{A}+\hat{B}} = e^{\hat{A}} e^{\hat{B}} e^{\hat{C}_1} e^{\hat{C}_2} \dots \quad (3.15)$$

is finite, more precisely only three terms are necessary to disentangling the potential

$$e^{-\frac{i}{\hbar}\tau\hat{V}} = e^{i\tau(\alpha_+\hat{\sigma}^\dagger + \alpha_z\hat{\sigma}_z + \alpha_-\hat{\sigma})} = e^{f_+(\tau)\hat{\sigma}^\dagger} e^{f_z(\tau)\hat{\sigma}_z} e^{f_-(\tau)\hat{\sigma}} = \begin{pmatrix} F_z^{-1} + f_+f_-F_z & f_+F_z \\ f_-F_z & F_z \end{pmatrix}, \quad (3.16)$$

with the complex functions

$$f_\pm = \frac{i\alpha_\pm}{\Gamma_1} \frac{\sin(\Gamma_1\tau)}{F_z}, \quad f_z = -\ln(F_z), \quad F_z = \cos(\Gamma_1\tau) - \frac{i\alpha_z}{\Gamma_1} \sin(\Gamma_1\tau). \quad (3.17)$$

They depend on the laser interaction [cf. Eq. (2.12)] with

$$\Gamma_1^2 = \alpha_+\alpha_- + \alpha_z^2, \quad \alpha_+ = -\frac{1}{2}\Omega_{N_L}(t, \mathbf{r}), \quad \alpha_- = -\frac{1}{2}\Omega_{N_L}^*(t, \mathbf{r}), \quad \alpha_z = -\frac{1}{2}\Delta. \quad (3.18)$$

The non-trivial derivation of the matrix form of  $\exp[-i\hat{V}\tau/\hbar]$  as well as of the solutions of the functions  $f_\pm, f_z$  can be found in Appendix C.

### 3.2 VON-NEUMANN EQUATION

The time evolution of incoherent mixed states in the Schrödinger picture is given by the quantum analogue to the classical Liouville equation, the von-Neumann equation

$$\frac{d}{dt}\hat{\rho} = -\frac{i}{\hbar}[\hat{H}, \hat{\rho}]. \quad (3.19)$$

The mixed state is described with the density operator as weighted superposition of all possible, normalised states  $|\psi_i\rangle$  of the event set  $\Omega$  with probabilities  $p_i \geq 0$ , reading

$$\hat{\rho} = \sum_{i \in \Omega} p_i |\psi_i\rangle \langle \psi_i|, \quad \sum_{i \in \Omega} p_i = 1. \quad (3.20)$$

The trace of the density operator is  $\text{Tr}\{\hat{\rho}\} = 1$ . The formal solution of the von-Neumann equation reads

$$\hat{\rho}(t) = \hat{U}(t, t_0)\hat{\rho}(t_0)\hat{U}(t, t_0)^\dagger, \quad (3.21)$$

with  $t > t_0$  and the Schrödinger time-evolution operator  $\hat{U}(t, t_0)$  (3.2).

### 3.3 MASTER EQUATION

In case spontaneous emission cannot be neglected any longer, or rather dissipation in general should be considered, the incoherent dynamics of the system are treated by the master equation approach (cf. Chap. 1 in [135]), describing the dissipative coupling between a small system and a large reservoir. With tracing over the reservoir variables of the total density matrix  $\hat{\rho} = \text{Tr}_{\text{res}} \hat{\rho}_{\text{full}}$  the time evolution of the density operator of the small system  $\hat{\rho}$  (3.20) is defined by the master equation in Lindblad form [136]

$$\frac{d}{dt}\hat{\rho} = -\frac{i}{\hbar}[\hat{H}, \hat{\rho}] + \mathcal{L}(\hat{\rho}). \quad (3.22)$$

For small temperatures, the Lindblad superoperator  $\mathcal{L}$  acts on the density operator with [137]

$$\mathcal{L}(\hat{\rho}) = -\frac{1}{2} \sum_m (\hat{C}_m^\dagger \hat{C}_m \hat{\rho} + \hat{\rho} \hat{C}_m^\dagger \hat{C}_m) + \sum_m \hat{C}_m \hat{\rho} \hat{C}_m^\dagger. \quad (3.23)$$

It can be used to describe most of the dissipative quantum optics problems in vacuum of a zero temperature reservoir, where the contributions of stimulated absorption and emission vanish (cf. Chap. 2 in [135]). The relaxation operator contains at least one to an infinite number of Lindblad, also called jump operators  $\hat{C}_m$ , depending on the physical problem.

RELAXATION FOR A TWO-LEVEL SYSTEM Considering spontaneous emission in a two-level atom, there is only one operator  $\hat{C} = \sqrt{\Gamma}\hat{\sigma}$ , contributing to the relaxation operator (3.23)

$$\mathcal{L}_{2LS}(\hat{\rho}) = \Gamma\hat{\sigma}\hat{\rho}\hat{\sigma}^\dagger - \frac{\Gamma}{2}(\hat{\sigma}^\dagger\hat{\sigma}\hat{\rho} + \hat{\rho}\hat{\sigma}^\dagger\hat{\sigma}). \quad (3.24)$$

The excited state  $|e\rangle$  has a lifetime  $\Gamma^{-1}$ , decaying into the stable ground state  $|g\rangle$ , giving reasons for the lowering and raising operators  $\hat{\sigma} = |g\rangle\langle e|$ ,  $\hat{\sigma}^\dagger = |e\rangle\langle g|$ .

### 3.3.1 Quantum Monte Carlo wavefunction method

The Quantum Monte Carlo wavefunction (QMCWF) method was devolved by Dum, Zoller and Ritsch [138] and Dalibard, Castin and Mølmer [139] in 1992. Within this method a stochastic solution of the Schrödinger equation is used rather than the explicit resolution of the master equation. Therefore,  $M$  quantum trajectories are calculated, reducing the dimension of the problem from  $\dim(\hat{\rho}) = N^2$  to  $\dim(\hat{H}) = M \times N$ . Especially for large  $N$  the QMCWF-method becomes very efficient in comparison to solving the master equation. Therefore, for two- or three-level systems solving the master equation is the appropriate working tool, but considering thermal states, a statistical mixture of many coherent states with different initial positions and momenta (cf. Sec. 2.3.6), the QMCWF-method is favourable.

The evolution of one stochastic wavefunction is described with a non-Hermitian Hamiltonian and randomly decided quantum jumps, followed by wavefunction renormalisation. It can be easily shown, that in the statistical average of many simulated quantum-trajectories the QMCWF-method results are equivalent to that one of the master equation treatment [137]. Physically observable expectation values are given by averaging over single expectation values

$$\langle \hat{A}(t) \rangle = \frac{1}{M} \sum_{i=1}^M \langle \hat{A}^{(i)}(t) \rangle = \frac{1}{M} \sum_{i=1}^M \langle \psi^{(i)}(t) | \hat{A}(t) | \psi^{(i)}(t) \rangle, \quad (3.25)$$

where  $|\psi^{(i)}\rangle$  represents one of  $M$  quantum trajectories.

In the framework of this thesis, the QMCWF-method is used within the atomic beamsplitter description. Therefore, the general procedure is taken from [137], while the focus lies on the application to a two-level atom with the Liouville-relaxation operator  $\mathcal{L}_{2LS}(\hat{\rho})$  (3.24).

#### QMCWF-procedure

In the course of the QMCWF-method an initially normalised wavefunction  $|\psi(t)\rangle$  is evolved for discrete timesteps  $\delta t$ . For each timestep a uniform variate  $\varepsilon$ , namely a random number uniformly distributed in  $[0, 1]$  is used to decide whether a quantum jump occurs (with probability  $\delta p$ ) or the wavefunction is propagated with a non-hermitian effective Hamilton operator. Regarding the Lindblad equation (3.22) with the dissipation operator (3.23) the master equation can be rewritten as

$$\frac{d}{dt}\hat{\rho} = -\frac{i}{\hbar}(\hat{H}_{\text{eff}}\hat{\rho} - \hat{\rho}\hat{H}_{\text{eff}}^\dagger) + \sum_m \hat{C}_m\hat{\rho}\hat{C}_m^\dagger, \quad (3.26)$$

giving rise to the effective Hamiltonian

$$\hat{H}_{\text{eff}} = \hat{H} - \frac{i\hbar}{2} \sum_m \hat{C}_m^\dagger \hat{C}_m \quad (3.27)$$

and specifically for the two-level system

$$\hat{H}_{\text{eff}} = \hat{H} - \frac{i\hbar}{2} \Gamma \hat{\sigma}^\dagger \hat{\sigma}. \quad (3.28)$$

The probability of occurrence of a quantum jump is

$$\delta p = \delta t \frac{i}{\hbar} \langle \psi(t) | \hat{H}_{\text{eff}} - \hat{H}_{\text{eff}}^\dagger | \psi(t) \rangle = \sum_m \delta p_m, \quad \delta p_m = \delta t \langle \psi(t) | \hat{C}_m^\dagger \hat{C}_m | \psi(t) \rangle \geq 0, \quad (3.29)$$

with  $\delta p \ll 1$ , why  $\delta t$  must be sufficient small. For the two-level system the probability reads

$$\delta p = \delta t \Gamma \langle \psi(t) | \hat{\sigma}^\dagger \hat{\sigma} | \psi(t) \rangle = \delta t \Gamma |\langle \psi(t) | e \rangle|^2. \quad (3.30)$$

**QUANTUM JUMP** If  $\varepsilon < \delta p$  a quantum jump occurs and with choosing one realisation  $\hat{C}_m$  with a probability  $\prod_m = \delta p_m / \delta p$ , the new normalised wavefunction reads

$$|\psi(t + \delta t)\rangle = \frac{1}{\sqrt{\delta p / \delta t}} \hat{C}_m |\psi(t)\rangle. \quad (3.31)$$

For the two-level system one possibility remains

$$|\psi(t + \delta t)\rangle = \frac{1}{\sqrt{|\langle \psi(t) | e \rangle|^2}} \hat{\sigma} |\psi(t)\rangle. \quad (3.32)$$

**PROPAGATION** If  $\varepsilon \geq \delta p$ , the wavefunction is propagated with the non-hermitian effective Hamilton operator (3.27)

$$|\psi'(t + \delta t)\rangle = e^{-\frac{i}{\hbar} \hat{H}_{\text{eff}} \delta t} |\psi(t)\rangle. \quad (3.33)$$

This evolution can be solved with different approaches depending on the particular form of  $\hat{H}$ . However, because  $\hat{H}_{\text{eff}}$  is non-hermitian in all cases the propagated wavefunction needs to be normalised with

$$|\psi(t + \delta t)\rangle = \frac{|\psi'(t + \delta t)\rangle}{\| \psi'(t + \delta t) \|} = \frac{1}{\sqrt{|\langle \psi | \psi \rangle|}} |\psi'(t + \delta t)\rangle, \quad \| \psi \| = \sqrt{|\langle \psi | \psi \rangle|}. \quad (3.34)$$

**FULL SOLUTION** Calculating the time evolution for all time steps results in the time-dependent solution of one quantum trajectory. Finally, averaging over a sufficient large number of trajectories gives the solution of the master equation (3.22).

### QMCWF-method including center-of-mass motion

For the beamsplitter description considering the center-of-mass motion is essential. Therefore, the induced recoil due to spontaneous emission of photons needs to be taken into account with the relaxation operator [137]

$$\mathcal{L}(\hat{\rho}) = -\frac{\Gamma}{2} (\hat{\mathbf{S}}^\dagger \hat{\mathbf{S}} \hat{\rho} + \hat{\rho} \hat{\mathbf{S}}^\dagger \hat{\mathbf{S}}) + \frac{3\Gamma}{8\pi} \int d^2\Omega \sum_{\epsilon \perp \mathbf{k}_0} e^{-i\mathbf{k}_0 \mathbf{r}} (\epsilon^* \hat{\mathbf{S}}) \hat{\rho} (\epsilon \hat{\mathbf{S}}^\dagger) e^{i\mathbf{k}_0 \mathbf{r}}. \quad (3.35)$$

Here,  $\hat{\mathbf{S}}^\dagger$  and  $\hat{\mathbf{S}}$  are raising and lowering operators proportional to the atomic dipole operator. The relaxation operator contains the spontaneous decay of excited state populations and coherences as well as of optical coherences together with the corresponding growing of the ground state populations and coherences. Now, the direction as well as the polarisation of the emitted photon is taken into account. One photon is emitted spontaneously with wavevector  $\mathbf{k}_0 = k_0 \mathbf{n}$  ( $|\mathbf{k}_0| = k_0 = \omega_0 / c$ ) and one integrates over the direction of the photon defined by the solid angle  $\Omega$  with the differential  $d^2\Omega = \sin\beta d\beta d\alpha$ . The polarisation  $\epsilon$  must be orthogonal to  $\mathbf{k}_0$ , wherefore the sum includes a basis set of these two polarisations. This sum can be explicitly calculated, defining  $\mathbf{q}$  as direction of the atomic dipole operator and using (cf. page 36 in [140])

$$\sum_{\epsilon \perp \mathbf{k}_0} |\epsilon \cdot \mathbf{X}|^2 = \mathbf{X} \cdot \mathbf{X}^* - \frac{(\mathbf{k}_0 \cdot \mathbf{X})(\mathbf{k}_0 \cdot \mathbf{X}^*)}{|\mathbf{k}_0|^2}. \quad (3.36)$$



Therewith the relaxation operator can be written as

$$\mathcal{L}(\hat{\rho}) = -\frac{\Gamma}{2}(\hat{\sigma}^\dagger \hat{\sigma} \hat{\rho} + \hat{\rho} \hat{\sigma}^\dagger \hat{\sigma}) + \Gamma \int d^2\Omega W(\mathbf{q}, \mathbf{n}) e^{-ik_0 \mathbf{n} \mathbf{r}} \hat{\sigma} \hat{\rho} \hat{\sigma}^\dagger e^{ik_0 \mathbf{n} \mathbf{r}}, \quad (3.37)$$

$$W(\mathbf{n}, \mathbf{q}) = \frac{3}{8\pi} \left( 1 - \frac{(\mathbf{n} \cdot \mathbf{k}_0)^2}{|\mathbf{k}_0|^2} \right) = \frac{3}{8\pi} (1 - (\mathbf{n} \cdot \mathbf{q})^2) = \frac{3}{8\pi} \sin^2 \beta, \quad \int d^2\Omega W(\mathbf{n}, \mathbf{q}) = 1. \quad (3.38)$$

Defining the lowering operator as

$$\hat{C}_n = \sqrt{\Gamma} \hat{\sigma} e^{-ik_0 \mathbf{n} \mathbf{r}} \quad (3.39)$$

the relaxation operator can be written in the form of Eq. (3.23). Therefore, the effective Hamiltonian stays the same as in Eq. (3.28), but the quantum jump process needs to be adjusted. The probability is still determined by the total population of the excited state with Eq. (3.30).

**QUANTUM JUMP** When a quantum jump occurs, random angles  $\alpha, \beta$  specify the direction of the spontaneously emitted photon. Therefore,  $\alpha \in [0, 2\pi)$  is uniformly distributed, implemented by  $\alpha = \varepsilon 2\pi$  with a uniform variate  $\varepsilon$ . Under the terms of Eq. (3.38), for  $\beta$  random numbers distributed according to  $\sin^2 \beta$  must be generated. This can be done with the help of the inverse transform sampling method [141] for pseudo-random number sampling. Here, a uniform random variate  $\gamma$  is transformed into one distributed as an arbitrary desired, normalised distribution  $p_\beta(\beta)$

$$p_\beta(\beta) = \frac{2}{\pi} \sin^2 \beta, \quad \int_0^\pi d\beta p_\beta(\beta) = 1. \quad (3.40)$$

The inverse transform sampling method is based on matching the differential probabilities

$$p_\gamma(\gamma) d\gamma = p_\beta(\beta) d\beta. \quad (3.41)$$

Thus,  $\gamma$  is the indefinite integral  $P_\beta(\beta)$  of  $p_\beta(\beta)$  with

$$\gamma = P_\beta(\beta) = \int_0^\beta d\beta p_\beta(\beta) = \frac{\beta}{\pi} - \frac{\sin 2\beta}{2\pi}, \quad (3.42)$$

because  $p_\gamma(\gamma) = 1$  for the uniform random variate  $\gamma$ . Finally, numerically solving  $P_\beta(\beta) - \gamma = 0$  for uniform variates  $\gamma$ , results in the sought random numbers with  $\sin^2$ -distribution. The unit vector  $\mathbf{n} = (n_x, n_y, n_z)$  is then defined with spherical coordinates

$$\mathbf{n} = (\sin \beta \cos \alpha, \sin \beta \sin \alpha, \cos \beta). \quad (3.43)$$

In this way, the jump operator with the emission of a photon in the  $\mathbf{n}$ -direction can be applied

$$|\psi(t + \delta t, \mathbf{r})\rangle = (\sqrt{|\langle \psi(t) | e \rangle|^2})^{-1} \hat{\sigma} e^{-ik_0 \mathbf{n} \mathbf{r}} |\psi(t, \mathbf{r})\rangle. \quad (3.44)$$

**PROPAGATION** The propagation (3.33), taking into account the center-of-mass motion, can be estimated with the help of symplectic integrators as presented in Section 3.1.1, splitting the time evolution into the kinetic and the potential part with  $\hat{H}_{\text{eff}}(t, \hat{\mathbf{r}}, \hat{\mathbf{p}}) = \hat{T}(\hat{\mathbf{p}}) + \hat{V}_{\text{eff}}(t, \hat{\mathbf{r}})$ . The additional spontaneous emission term of  $\hat{H}_{\text{eff}}$  (3.28) is considered within the effective potential

$$\hat{V}_{\text{eff}}(t, \mathbf{r}) = \frac{\hbar}{2} \left[ \left( \Delta - i \frac{\Gamma}{2} \right) \hat{\sigma}_z + \Omega_{N_L}(t, \mathbf{r}) \hat{\sigma}^\dagger + \Omega_{N_L}^*(t, \mathbf{r}) \hat{\sigma} - i \frac{\Gamma}{2} \right]. \quad (3.45)$$

Therefore, the disentangling of  $\exp[-i \hat{V}_{\text{eff}} \delta t / \hbar]$  (cf. 3.1.2) reads

$$e^{-\frac{i}{\hbar} \delta t \hat{V}_{\text{eff}}} = e^{i \delta t (a_+ \hat{\sigma}^\dagger + a_z \hat{\sigma}_z + a_- \hat{\sigma})} e^{-\delta t \frac{\Gamma}{4}} = e^{-\delta t \frac{\Gamma}{4}} \begin{pmatrix} F_z^{-1} + f_+ f_- F_z & f_+ F_z \\ f_- F_z & F_z \end{pmatrix}, \quad (3.46)$$

with  $f_\pm, F_z$  and  $\Gamma_1$  built as in Eqs. (3.17) and (3.18), but with coefficients

$$a_+ = -\frac{1}{2} \Omega_{N_L}(t, \mathbf{r}), \quad a_- = -\frac{1}{2} \Omega_{N_L}^*(t, \mathbf{r}), \quad a_z = -\frac{1}{2} \left( \Delta - i \frac{\Gamma}{2} \right). \quad (3.47)$$

**FULL SOLUTION** Again going through the QMCWF-procedure for every time step and averaging over many trajectories gives the final solution of the master equation including now recoils of spontaneous emission.

### 3.4 COORDINATE TRANSFORMATIONS

Inertial frames are a central concept of physics. Coordinate transformations are used to describe a physical problem in reasonable coordinates. Therefore, the mathematical treatment of the time evolution of the light-matter interaction, discussed in the last Sections 3.1-3.3, simplifies enormously.

#### 3.4.1 Moving frames: Galilean transformation

In quantum mechanics the Galilean transformation is represented by the displacement operator

$$\hat{G}(t) = e^{\frac{i}{\hbar}(\mathbf{p}\hat{\mathbf{r}} - \mathbf{r}(t)\hat{\mathbf{p}})} = e^{-\frac{i}{2\hbar}\mathbf{p}\mathbf{r}(t)} e^{\frac{i}{\hbar}\mathbf{p}\hat{\mathbf{r}}} e^{-\frac{i}{\hbar}\mathbf{r}(t)\hat{\mathbf{p}}}, \quad (3.48)$$

with a time-dependent coordinate  $\mathbf{r}(t) = \mathbf{r}_0 + \mathbf{v}t$  and a momentum  $\mathbf{p} = m\mathbf{v}$ . It transforms the corresponding Heisenberg operators as

$$\begin{pmatrix} \hat{\mathbf{r}}' \\ \hat{\mathbf{p}}' \end{pmatrix} = \hat{G} \begin{pmatrix} \hat{\mathbf{r}} \\ \hat{\mathbf{p}} \end{pmatrix} \hat{G}^\dagger = \begin{pmatrix} \hat{\mathbf{r}} - \mathbf{r}(t) \\ \hat{\mathbf{p}} - \mathbf{p} \end{pmatrix}. \quad (3.49)$$

This transformation enables the relation of a measurement in one inertial reference frame to another moving with a constant velocity  $|\mathbf{v}| \ll c$  for classical motion, as non-relativistic limit of a Lorentz transformation. As our experience of nature, the laws of physics are the same in all inertial reference frames. Galileo himself illustrated for experiments observed from a standing ship as well as from a ship moving with constant velocity: ‘*When you have observed all these things carefully (though there is no doubt that when the ship is standing still everything must happen in this way), have the ship proceed with any speed you like, so long as the motion is uniform and not fluctuating this way and that. You will discover not the least change in all the effects named, nor could you tell from any of them whether the ship was moving or standing still.*’ [142]

The change of coordinates with the transformation (3.49) is referred as *passive picture*, where the state of the system remains unchanged. By contrast, in the Schrödinger picture,  $\hat{G}(t)$  transforms the laboratory frame state  $|\psi(t)\rangle = \hat{G}(t)|\psi'(t)\rangle$  into the state  $|\psi'(t)\rangle$  of the moving frame, while conserving the original coordinates. This corresponds to the *active picture* and is applied in the further course of this thesis. Evaluating the comoving-frame Hamilton operator  $\hat{H}'(t, \hat{\mathbf{r}}, \hat{\mathbf{p}}) = \hat{G}^\dagger(\hat{H} - i\hbar\partial_t)\hat{G}$ , the Schrödinger equation reads

$$i\hbar\partial_t|\psi'\rangle = \hat{H}'|\psi'\rangle = \hat{G}^\dagger(\hat{H} - i\hbar\partial_t)\hat{G}|\psi'\rangle. \quad (3.50)$$

For an ultracold atom interacting with classical laser light, most generally introduced in Chapter 2, this affects only the interaction potential

$$\hat{H}' = \frac{\hat{\mathbf{p}}^2}{2M} + \hbar\omega_g\hat{\sigma}_g + \hbar\omega_e\hat{\sigma}_e + \hat{V}(t, \hat{\mathbf{r}} + \mathbf{r}(t)). \quad (3.51)$$

In this frame, the velocity shift has to be considered in the boosted state with

$$\Psi'(\mathbf{p}) = \langle \mathbf{p} | \psi' \rangle = \langle \mathbf{p} | \hat{G}^\dagger | \psi \rangle = e^{\frac{i}{\hbar}(\mathbf{r}(t)\mathbf{p} + \frac{\mathbf{p}\mathbf{r}(t)}{2})} \Psi(\mathbf{p} + \mathbf{p}), \quad |\Psi'(t, \mathbf{p} - \mathbf{p})|^2 = |\Psi(\mathbf{p})|^2, \quad (3.52)$$

leading to an additional momentum  $\mathbf{p} = m\mathbf{v}$  of the state in frame  $S'$  in relation to  $S$ , apparent in the probability density in the momentum space  $|\Psi'(\mathbf{p})|^2$ .

### 3.4.2 Static frame transformations

Within the interaction of several laser fields and a cloud of ultracold atoms there are some salient directions that need to be considered: The in general unequal propagation directions of the laser fields, the orientation of the atom cloud, as soon as it is asymmetric and the orientation of the chip, resulting possibly in corresponding velocity components of the atoms. Therefore, it is important, firstly, to define precisely the used reference frame and secondly, to calculate carefully all needed transformations from other coordinate frames into this frame.

In Chapter 2, the reference frame  $S_0$  of the laboratory, i.e. the inertial rest frame of the atomic chip experiment, was introduced. Its coordinates are denoted with  $(x_0, y_0, z_0)$ . Assuming that in the reference frame used within this work and denoted with  $S$  and coordinates  $(x, y, z)$  laser 1 propagates exactly in positive  $x$ -direction, the misalignment of both lasers can be expressed as displacement and tilt of laser 2 with respect to the orientation of laser 1. The origin  $O$  of the reference frame  $S$  is chosen to be the initial<sup>1</sup> centre-of-mass position of the atoms, lying in between of both laser origins  $O_1$  and  $O_2$  as depicted in Fig. 3.2. The orientation of  $S$  is chosen to be identical to the propagation direction of laser 1. Therefore, ideally without a laser misalignment the diffraction direction coincides with the  $x$ -direction of frame  $S$ .

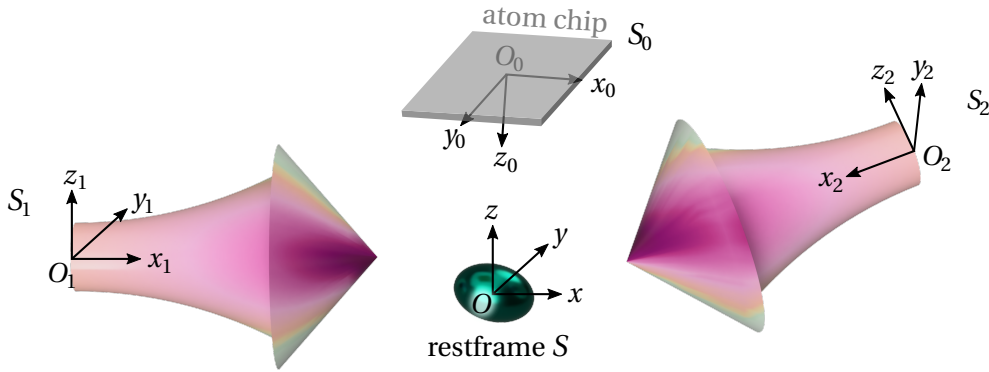


Figure 3.2: Two counterpropagating, bichromatic Laguerre-Gaussian laser beams, with their intrinsic reference frames  $S_{L=\{1,2\}}$ , with coordinates  $(x_L, y_L, z_L)$ , interact with an atomic cloud. While the laboratory frame of reference  $S_0$  is centred on the laboratory of the atomic chip experiment, the reference frame  $S$  with coordinates  $(x, y, z)$ , used for the theoretical description of the atomic diffraction, is centred at the initial centre-of-mass position of the atomic cloud and orientated as laser 1. The distance between the origins  $O$  and  $O_1$  is  $|\mathbf{d}|$  and the distance between  $O_1$  and  $O_2$  is  $|\ell|$ .

Based on the assumption that the atoms initially stay at rest and possess (in the majority of simulated cases) a symmetric expansion size, this frame  $S$  is an appropriate choice. Asymmetric expansions or small initial velocities of the atoms in arbitrary directions can be handled either explicitly expressed in the  $S$ -coordinates or by using an additional transformation. That would be a rotation of  $S$  according to a certain orientation characterised by the atoms.

The Laguerre-Gaussian (LG) laser beams are defined with (2.23) in their intrinsic reference frames  $S_L$ ,  $L \in \{1, 2\}$  with coordinates  $x_L, y_L, z_L$ , also depicted in Fig. 3.2. While here, the necessary transformations to express  $\mathcal{E}_L^{(+)}(\mathbf{r}_L)$  of laser  $L = 1$  and  $L = 2$  in coordinates  $x, y, z$  of frame  $S$  are presented, a detailed description of generally three-dimensional coordinate transformations is given for example in [143]. Using homogeneous coordinates, the translation and a linear map of an affine transformation, both can be represented using a single matrix

<sup>1</sup> The initial time is defined as the time, when the diffraction pulses are switched on.

multiplication. Therefore, all vectors are augmented to  $\mathbf{r} = (x, y, z, 1)$  and the matrices are also four dimensional. The augmented matrix is called an *affine transformation matrix*.

The origin of laser 1 is shifted in relation to the origin  $O$  of the coordinate system  $S$ , defined by the transformation

$$\mathbf{r}_1 = M_1^{-1} \mathbf{r}, \quad M_1 = T(-\mathbf{d}), \quad \mathbf{d} = (d_x, d_y, d_z), \quad d_{a=x,y,z} \geq 0, \quad (3.53)$$

with the translation matrix

$$T(\mathbf{d}) = \begin{pmatrix} 1 & 0 & 0 & d_x \\ 0 & 1 & 0 & d_y \\ 0 & 0 & 1 & d_z \\ 0 & 0 & 0 & 1 \end{pmatrix}, \quad T^{-1}(\mathbf{d}) = \begin{pmatrix} 1 & 0 & 0 & -d_x \\ 0 & 1 & 0 & -d_y \\ 0 & 0 & 1 & -d_z \\ 0 & 0 & 0 & 1 \end{pmatrix}. \quad (3.54)$$

For active transformations, used within this thesis, the inverse of the transformation matrix needs to be applied, resulting in

$$x_1 = x + d_x, \quad y_1 = y + d_y, \quad z_1 = z + d_z. \quad (3.55)$$

The transformation for laser 2 is

$$\mathbf{r}_2 = M_2^{-1} \mathbf{r}, \quad M_2 = T(-\mathbf{d} + \boldsymbol{\ell}). R(\alpha, \beta, 0). S_{yz}. \quad (3.56)$$

Here, the translation matrix takes into account not only the shift  $\mathbf{d}$ , but also the distance  $\boldsymbol{\ell} = (\ell_x, \ell_y, \ell_z)$ ,  $\ell_{a=x,y,z} \geq 0$ , between both laser origins  $O_1$  and  $O_2$ . Within the Tait-Bryan convention, the rotation matrix

$$R(\alpha, \beta, \psi) = \begin{pmatrix} c_\alpha c_\beta & c_\alpha s_\beta s_\gamma - c_\gamma s_\alpha & s_\alpha s_\gamma + c_\alpha c_\gamma s_\beta & 0 \\ c_\beta s_\alpha & c_\alpha c_\gamma + s_\alpha s_\beta s_\gamma & c_\gamma s_\alpha s_\beta - c_\alpha s_\gamma & 0 \\ -s_\beta & c_\beta s_\gamma & c_\beta c_\gamma & 0 \\ 0 & 0 & 0 & 1 \end{pmatrix}, \quad \begin{aligned} c_\theta &\equiv \cos(\theta), \\ s_\theta &\equiv \sin(\theta), \end{aligned} \quad (3.57)$$

describes intrinsic rotations around the  $z$ -,  $y'$ -,  $x''$ -axis. The so called Yaw-Pitch-Roll angles  $\alpha, \beta, \gamma$  play an important role in the vehicle and aircraft technology. However, this choice is also advantageous here, as the  $\gamma$ -rotation around  $x''$  can be skipped, since the LG-beams are rotationally symmetric for rotations around the propagation axis. For the counter-propagation of laser 2 in relation to laser 1, first of all a reflection  $(S_{yz})_{ij} = (-1)^{ij} \delta_{ij}$  on the  $yz$ -plane is added in equation (3.56). Applying the transformation  $M_2$  ends up with

$$\begin{aligned} x_2 &= -c_\beta(c_\alpha \tilde{x} + s_\alpha \tilde{y}) + s_\beta \tilde{z} \approx -\tilde{x} - \alpha \tilde{y} + \beta \tilde{z}, \\ y_2 &= c_\alpha \tilde{y} - s_\alpha \tilde{x} \approx \tilde{y} - \alpha \tilde{x}, \\ z_2 &= c_\beta \tilde{z} + s_\beta(c_\alpha \tilde{x} + s_\alpha \tilde{y}) \approx \tilde{z} + \beta \tilde{x} + \alpha \beta \tilde{y}, \end{aligned} \quad (3.58)$$

using the abbreviations  $\tilde{a} = a + d_a - \ell_a$  and on the right-hand side assuming only small misalignments where the small-angle-approximation can be applied with

$$\begin{aligned} \cos(\theta) &= 1 - \frac{\theta^2}{2!} + \frac{\theta^4}{4!} - \frac{\theta^6}{6!} + \mathcal{O}(\theta^8) \Rightarrow \cos(\theta) \approx 1, \\ \sin(\theta) &= \theta - \frac{\theta^3}{3!} + \frac{\theta^5}{5!} - \frac{\theta^7}{7!} + \mathcal{O}(\theta^9) \Rightarrow \sin(\theta) \approx \theta. \end{aligned} \quad (3.59)$$

Now, the positions and orientations of laser 1 and 2 are well-defined in the chosen frame of reference  $S$ .

# Part II

---

DIFFRACTION OF ULTRACOLD ATOMS

---



## DIFFRACTION WITH RESONANT LIGHT

While the focus of this thesis lies on the interaction with two counterpropagating laser beams, this Chapter 4 starts with a short overview of the simpler scenario: The interaction with only one laser demonstrates the basic mechanism of the diffraction of ultracold atoms. The analytical treatment gives deep physical insights into the interaction mechanisms of ultracold atoms with laser light. While some aberrations of atomic diffraction appear here unavoidably, an extensive aberration analysis is given for the interaction with two laser beams, in the next Chapters 5-8.

### 4.1 INTERACTION ENERGY

The diffraction of ultracold atoms is based on the stimulated absorption (and emission) of laser photons. In this Chapter 4, the two-level system, with ground state  $|g\rangle$  and excited state  $|e\rangle$ , is coupled resonantly with one laser, as depicted in Fig. 4.1. It is assumed that the spontaneous decay of the excited state proceeds mainly to an internal state which is not detected. Thus, the two-level system without spontaneous emission is an appropriate approximation and the time evolution can be described with the Schrödinger equation

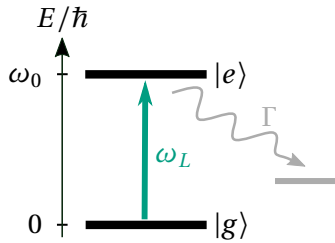


Figure 4.1: Two-level atom with ground state  $|g\rangle$  and excited state  $|e\rangle$  with transition frequency  $\omega_0$  coupled by laser light of frequency  $\omega_L$ . The spontaneous emission with rate  $\Gamma$  decays into an unobserved state.

equation

$$i\hbar\partial_t|\psi\rangle = \hat{H}|\psi\rangle. \quad (4.1)$$

The Hamilton operator  $\hat{H}$  of the interacting system consists of the kinetic energy  $\hat{T}$  of the atoms and the potential energy  $\hat{V}$ , including the potential energy of the internal atomic levels and the interaction potential (cf. Sec. 2.1)

$$\hat{H} = \hat{T} + \hat{V} = \frac{\hat{\mathbf{p}}^2}{2M} + \hbar\omega_g\hat{\sigma}_g + \hbar\omega_e\hat{\sigma}_e + \frac{\hbar}{2}\Omega_0(\hat{\sigma}^\dagger e^{i(\mathbf{k}_L\hat{\mathbf{r}}-\omega_L t)} + \hat{\sigma} e^{-i(\mathbf{k}_L\hat{\mathbf{r}}-\omega_L t)}). \quad (4.2)$$

Here, the laser is assumed to be a monochromatic plane wave (2.17) of angular frequency  $\omega_L = c|\mathbf{k}_L|$  and a temporal constant amplitude during the interaction time, viz. a rectangular pulse is applied. Transforming into a rotating frame  $|\psi\rangle = \hat{F}|\psi'\rangle$  with

$$\hat{F}(t) = \exp[-i\omega_g t - i\omega_L t \hat{\sigma}_e], \quad (4.3)$$

eliminates the rapid temporal oscillations and the transformed Hamilton operator results in

$$\hat{H}' = \hat{F}^\dagger \hat{H} \hat{F} + i\hbar(\partial_t \hat{F}^\dagger) \hat{F} = \frac{\hat{\mathbf{p}}^2}{2M} - \hbar\Delta\hat{\sigma}_e + \frac{\hbar}{2}\Omega_0(\hat{\sigma}^\dagger e^{i\mathbf{k}_L\hat{\mathbf{r}}} + \hat{\sigma} e^{-i\mathbf{k}_L\hat{\mathbf{r}}}). \quad (4.4)$$

Here, the detuning of the laser frequency  $\omega_L$

$$\Delta \equiv \omega_L - \omega_0 \quad (4.5)$$

in relation to the resonance frequency of the atom  $\omega_0 = \omega_e - \omega_g$  is introduced.

## 4.2 LOCAL RABI OSCILLATIONS

Neglecting the kinetic energy term  $\hat{T} = \hat{\mathbf{p}}^2/(2M)$ , local Rabi oscillations between the atomic internal states can be observed. Therefore, the Schrödinger equation  $i\hbar\partial_t|\psi\rangle = \hat{V}|\psi\rangle$  with  $|\psi(t)\rangle = \psi_e(t)|e\rangle + \psi_g(t)|g\rangle$  in matrix representation reads

$$i\partial_t \begin{pmatrix} \psi_e \\ \psi_g \end{pmatrix} = \begin{pmatrix} -\Delta & \Omega(\mathbf{r})/2 \\ \Omega^*(\mathbf{r})/2 & 0 \end{pmatrix} \begin{pmatrix} \psi_e \\ \psi_g \end{pmatrix} \equiv V \begin{pmatrix} \psi_e \\ \psi_g \end{pmatrix}, \quad \Omega(\mathbf{r}) = \Omega_0 e^{i\mathbf{k}_L \cdot \mathbf{r}}. \quad (4.6)$$

The solution is given by the exponential

$$|\psi(t)\rangle = \hat{U}(t)|\psi(0)\rangle = e^{-\frac{i}{\hbar}t\hat{V}}|\psi(0)\rangle, \quad (4.7)$$

which can be carried over into a transfer matrix  $U$ , using the methods of disentangling an exponential (cf. Sec. 3.1.2)

$$U(t) = e^{it\frac{\Delta}{2}} \begin{pmatrix} F_z^{-1} + f_+ f_- F_z & f_+ F_z \\ f_- F_z & F_z \end{pmatrix}, \quad f_{\pm} = \frac{i\alpha_{\pm}}{\Gamma_1} \frac{\sin(\Gamma_1 t)}{F_z}, \quad F_z = \cos(\Gamma_1 t) - \frac{i\alpha_z}{\Gamma_1} \sin(\Gamma_1 t). \quad (4.8)$$

The complex functions  $f_i, F_z$  are defined by the laser properties with

$$\alpha_{\pm} = -\frac{\Omega_0}{2} e^{\pm i\mathbf{k}_L \cdot \mathbf{r}}, \quad \alpha_z = \frac{\Delta}{2}, \quad \Gamma_1^2 = \alpha_+ \alpha_- + \alpha_z^2 = \frac{\Omega_0^2}{4} + \frac{\Delta^2}{4}. \quad (4.9)$$

Starting with the whole population initially in the ground state, the ground and excited state populations are

$$p_e(t) = |\psi_e(t)|^2 = |\langle e|\hat{U}(t)|\psi(0)\rangle|^2 = \frac{|\alpha_+|^2}{\Gamma_1^2} \sin^2(\Gamma_1 t) = \frac{\Omega_0^2}{\tilde{\Omega}_0^2} \sin^2\left(\frac{\tilde{\Omega}_0 t}{2}\right), \quad (4.10)$$

$$p_g(t) = |\psi_g(t)|^2 = |\langle g|\hat{U}(t)|\psi(0)\rangle|^2 = \cos^2(\Gamma_1 t) + \frac{\alpha_z^2}{\Gamma_1^2} \sin^2(\Gamma_1 t) = \cos^2\left(\frac{\tilde{\Omega}_0 t}{2}\right) + \frac{\Delta^2}{\tilde{\Omega}_0^2} \sin^2\left(\frac{\tilde{\Omega}_0 t}{2}\right), \quad (4.11)$$

with the generalised Rabi frequency

$$\tilde{\Omega}_0 = \sqrt{\Omega_0^2 + \Delta^2}. \quad (4.12)$$

This effective coupling strength results also from the difference of the eigenvalues of  $V$  (4.6). The resulting local Rabi oscillations are depicted in Fig. 4.2, with the oscillation frequency  $\tilde{\Omega}_0 t/2$ . The relation  $\Omega_0^2/\tilde{\Omega}_0^2$  defines the maximum population of the excited state. Therefore, only for  $\Delta = 0$  a full population inversion can be achieved. It is worth mentioning, that the solution can also be derived in the dressed state picture as a common initial value problem with evaluating the eigenvalues and eigenvectors of the coupling matrix  $V$  (this procedure is explained in quantum mechanic textbooks, like [144]). However, here the usability of the methods of disentangling an exponential is demonstrated.



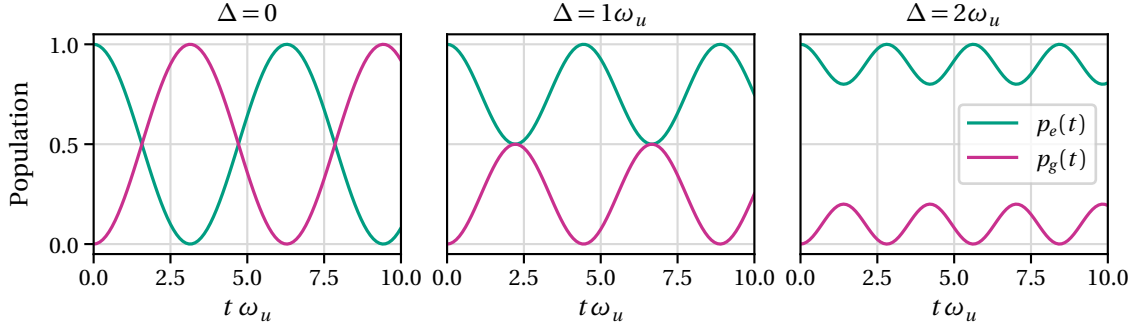


Figure 4.2: Local Rabi oscillations for different detunings  $\Delta$  and constant Rabi frequency  $\Omega_0 = 1\omega_u$ . An arbitrary frequency unit  $\omega_u$  is chosen.

### 4.3 ATOM MOVING IN A PLANE LASER WAVE

Taking into account the kinetic energy, the atom's external degrees of freedom also need to be considered, due to momentum conservation. Therefore, the wavefunction includes the internal state's coordinate and the position vector  $\mathbf{r}$  with

$$|\psi(t, \mathbf{r})\rangle = \psi_e(t, \mathbf{r})|e\rangle + \psi_g(t, \mathbf{r})|g\rangle. \quad (4.13)$$

Now the solution of the Schrödinger equation (4.1)

$$|\psi(t, \mathbf{r})\rangle = \hat{U}(t, \mathbf{r})|\psi(0, \mathbf{r})\rangle = e^{-\frac{i}{\hbar}t(\hat{T} + \hat{V})}|\psi(0, \mathbf{r})\rangle, \quad (4.14)$$

is not as simple as before, because  $\hat{T}$  and  $\hat{V}$  do not commute in general. A numerical solution is possible, using the methods of symplectic integrators to split the exponential in components, depending either on  $\hat{T}$  or on  $\hat{V}$ , as presented in Section 3.1.1. In addition, an analytical solution is derived in the following, using the dressed state picture.

To excite an atom from the ground to the excited state, one laser photon is absorbed. Therefore, the photon momentum  $\mathbf{p}_L$ , defined by the vacuum dispersion relation  $\omega_L = c p_L / \hbar = c k_L$  is transferred to the atom, with the absolute values  $p_L = |\mathbf{p}_L|$  and  $k_L = |\mathbf{k}_L|$ . The wavevector  $\mathbf{k} = \mathbf{p} / \hbar$  equates to the momentum in units of the reduced Planck constant. Therefore, in the field of atomic diffraction naturally the wavevector occurs instead of the momentum. In terms of the simplification to use natural units it is common, and used in the further course, to call the wavenumber equivalently momentum. The reader is kindly asked to forgive this indistinctness.

Absorption leads to a kick in the propagation direction of the laser. This momentum kick of the excited state can be taken into account with introducing

$$\psi_e(\mathbf{r}) = e^{i\mathbf{k}_L \mathbf{r}} \psi'_e(\mathbf{r}), \quad \psi_g(\mathbf{r}) = \psi'_g(\mathbf{r}), \quad (4.15)$$

because  $\exp(\pm i\mathbf{k}_L \hat{\mathbf{r}})$  is the translation operator of the momentum eigenstates  $|\mathbf{p}\rangle$

$$e^{\pm i\mathbf{k}_L \hat{\mathbf{r}}} = \int d^3p |\mathbf{p} \pm \hbar \mathbf{k}_L\rangle \langle \mathbf{p}|. \quad (4.16)$$

In addition, using the position representation of the momentum operator  $\hat{\mathbf{p}} = -i\hbar \nabla$ , the stationary Schrödinger equation

$$E|\psi(\mathbf{r})\rangle = (\hat{T} + \hat{V})|\psi(\mathbf{r})\rangle \quad (4.17)$$

leads in the position representation to two equations with coefficients not depending on  $\mathbf{r}$

$$E\psi'_e(\mathbf{r}) = \left( -\frac{\hbar^2}{2M}(\nabla^2 + 2i\mathbf{k}_L \nabla - \mathbf{k}_L^2) - \hbar\Delta \right) \psi'_e(\mathbf{r}) + \frac{\hbar}{2}\Omega_0\psi'_g(\mathbf{r}), \quad (4.18)$$

$$E\psi'_g(\mathbf{r}) = -\frac{\hbar^2}{2M}\nabla^2\psi'_g(\mathbf{r}) + \frac{\hbar}{2}\Omega_0\psi'_e(\mathbf{r}). \quad (4.19)$$

Such a system of partial differential equations with constant coefficients always possesses plane-wave solutions. Therefore, the following ansatz using plane waves is reasonable

$$\psi'_e(\mathbf{r}) = e^{i\mathbf{k}\mathbf{r}} a_e(\mathbf{k}), \quad \psi'_g(\mathbf{r}) = e^{i\mathbf{k}\mathbf{r}} a_g(\mathbf{k}). \quad (4.20)$$

Inserting this ansatz into Eqs. (4.18) and (4.19), the problem is studied in the momentum space, leading to

$$E \begin{pmatrix} a_e(\mathbf{k}) \\ a_g(\mathbf{k}) \end{pmatrix} = \hbar \begin{pmatrix} \frac{\hbar}{2M}(\mathbf{k}_L + \mathbf{k})^2 - \Delta & \Omega_0/2 \\ \Omega_0/2 & \frac{\hbar}{2M}\mathbf{k}^2 \end{pmatrix} \begin{pmatrix} a_e(\mathbf{k}) \\ a_g(\mathbf{k}) \end{pmatrix} \equiv \mathcal{H} \begin{pmatrix} a_e(\mathbf{k}) \\ a_g(\mathbf{k}) \end{pmatrix}. \quad (4.21)$$

Therewith, the solutions will depend on the atomic velocity  $\mathbf{v} = \hbar\mathbf{k}/M$ , which was neglected within the scope of local Rabi oscillations in Section 4.2. The direction of interest is the propagation direction of the laser. Assuming a propagation exactly in  $x$ -direction with  $\mathbf{k}_L = k_L \mathbf{e}_x$ , reduces the Hamilton matrix to one dimension

$$\mathcal{H} = \frac{\mathcal{H}}{\hbar\omega_r} = \begin{pmatrix} (1+k)^2 - \Delta & \Omega_0/2 \\ \Omega_0/2 & k^2 \end{pmatrix}. \quad (4.22)$$

Here, the recoil frequency

$$\boxed{\omega_r = \frac{\hbar k_L^2}{2M}} \quad (4.23)$$

emerges as frequency scale and the dimensionless quantities<sup>1</sup>

$$k = \frac{k_x}{k_L}, \quad \Delta = \frac{\Delta}{\omega_r}, \quad \Omega_0 = \frac{\Omega_0}{\omega_r} \quad (4.24)$$

are applied. The eigenfrequencies of the Hamilton matrix  $\mathcal{H}$  are given by

$$\omega_{\pm} = \frac{1}{2\hbar\omega_r} \left( \mathcal{H}_{11} + \mathcal{H}_{22} \pm \sqrt{(\mathcal{H}_{11} - \mathcal{H}_{22})^2 + 4|\mathcal{H}_{12}|^2} \right) = \frac{1}{2} \left( \Delta_k + 2k^2 \pm \sqrt{\Delta_k^2 + \Omega_0^2} \right), \quad (4.25)$$

with  $\Delta_k = 1 + 2k - \Delta$ . The frequency functions depending on the momentum in this direction are shown in Fig. 4.3, together with the unperturbed eigenfrequencies  $\omega'_g = k^2$  and  $\omega'_e = (1+k)^2 - \Delta$ . Obviously, the minima of  $\omega'_{e,g}$  are separated horizontally by the photon momentum  $k_L$ , because they are related to the ground and excited state energy which are distinguished kinetically by simply the photon momentum, as exploited in Eq. (4.15). The frequency difference of the minima is  $\Delta$ . In the weak interaction limit the two minima of  $\omega_{\pm}$  coincide approximately with the minima of  $\omega'_e$  and  $\omega'_g$ . The generalised Rabi frequency defines the spacing between the curves  $\omega_{\pm}$ , i.e. the frequency gap

$$\Omega_k = \Omega_k/\omega_r = \omega_+ - \omega_- = \sqrt{\Omega_0^2 + \Delta_k^2}. \quad (4.26)$$

<sup>1</sup> The usage of dimensionless variables provides a tremendous improvement of the readability of formulas. However, for a physical interpretation of quantities their dimension is indispensable. For this reason, always when explicit quantities appear, they are given in their physical units.

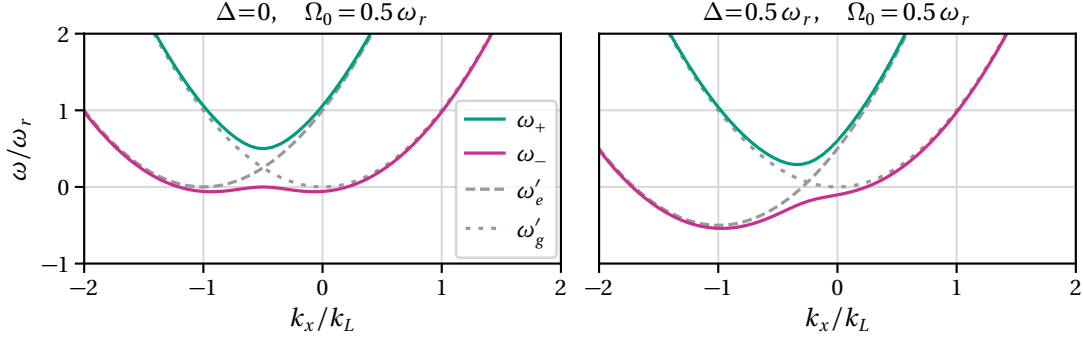


Figure 4.3: Eigenfrequencies  $\omega_+$  and  $\omega_-$  depending on the atomic momentum  $k_x$  in propagation direction of the laser for the Rabi frequency  $\Omega_0 = 0.5 \omega_r$  and different detunings  $\Delta$  in comparison to the eigenfrequencies for a vanishing laser beam  $\omega'_{e,g}$ .

In the limit  $k_x = -k_L/2$  it is  $k = -1/2$  and the generalised Rabi frequency is independent of the atomic velocity, recovering the expression in the framework of local Rabi oscillations (4.12). To estimate the velocity dependent population distributions, apart from the eigenenergies also the eigenstates need to be evaluated. In the dressed-state picture, the two eigensolutions are defined with an orthogonal eigenvector matrix

$$\begin{pmatrix} |+\rangle \\ |-\rangle \end{pmatrix} = R(\theta)M(\phi) \begin{pmatrix} |e\rangle \\ |g\rangle \end{pmatrix}, \quad R(\theta) = \begin{pmatrix} \cos \frac{\theta}{2} & \sin \frac{\theta}{2} \\ -\sin \frac{\theta}{2} & \cos \frac{\theta}{2} \end{pmatrix}, \quad M(\phi) = \begin{pmatrix} e^{-i\phi/2} & 0 \\ 0 & e^{i\phi/2} \end{pmatrix}, \quad (4.27)$$

that is parametrised through the angles  $\theta$  and  $\phi$ , namely

$$\sin \theta = \frac{2|\mathcal{H}_{12}|}{\sqrt{(\mathcal{H}_{11} - \mathcal{H}_{22})^2 + 4\mathcal{H}_{12}\mathcal{H}_{21}}} = \frac{\Omega_0}{\Omega_k}, \quad \phi = \arg(\mathcal{H}_{21}) = 0. \quad (4.28)$$

The time-dependent solution follows with

$$|a(\tau, k)\rangle = \lambda e^{-i\omega_+\tau} |+\rangle + \mu e^{-i\omega_-\tau} |-\rangle, \quad (4.29)$$

with the dimensionless time  $\tau = t\omega_r$ , scaled in accordance to the frequency scale  $\omega_r$  (4.23). The initial condition  $|a(\tau = 0, k)\rangle = a_g(0, k)|g, k\rangle + a_e(0, k)|e, k\rangle$  defines the coefficients  $\lambda = a_g(0, k)\sin(\theta/2) + a_e(0, k)\cos(\theta/2)$  and  $\mu = a_g(0, k)\cos(\theta/2) - a_e(0, k)\sin(\theta/2)$ . Therefore, the amplitudes of the excited and of the ground state are given by the matrix product

$$\begin{pmatrix} a_e(\tau, k) \\ a_g(\tau, k) \end{pmatrix} = e^{-i(\Delta_k + 2k^2)\frac{\tau}{2}} R(-\theta)M(\Omega_k\tau)R(\theta) \begin{pmatrix} a_e(0, k) \\ a_g(0, k) \end{pmatrix}. \quad (4.30)$$

To study the efficiency of the atomic diffraction the velocity dependent population of the excited state is of special interest

$$p_e(\tau, k) = |\langle e, k | \psi(\tau) \rangle|^2 = |a_e(\tau, k+1)|^2, \quad (4.31)$$

where the momentum shift  $k_L$  of  $\psi_e$  (4.15) must be considered. For the atom initially prepared in the ground state, one obtains

$$p_e(\tau, k-1) = |a_g(0, k)|^2 \frac{\Omega_0^2}{\Omega_k^2} \sin^2\left(\frac{\Omega_k\tau}{2}\right) = |a_g(0, k)|^2 \frac{\Omega_0^2}{\Omega_k^2} \sin^2\left(\frac{\Omega_k t}{2}\right), \quad (4.32)$$

$$p_g(\tau, k) = 1 - p_e(\tau, k-1). \quad (4.33)$$

In the closed system, the ground state population is given via the population conservation. Postulating that the Schrödinger equation is linear, with the superposition principle also the sum of plane waves should solve it. Therefore, the initial state is generated by a sum of plane waves with momentums  $k_x \in [-3k_L, 3k_L]$  respectively  $k_x/k_L = k \in [-3, 3]$ . Regarding Eq. (4.32), on resonance  $\Delta = 0$ , the maximum excited state population is reached for  $k = -1/2$  and the mirror time  $t_{\pi,0} = \pi/\Omega_0$ . In Fig. 4.4 the population of the ground and excited state after  $t_{\pi,0}$  is depicted in the momentum space.

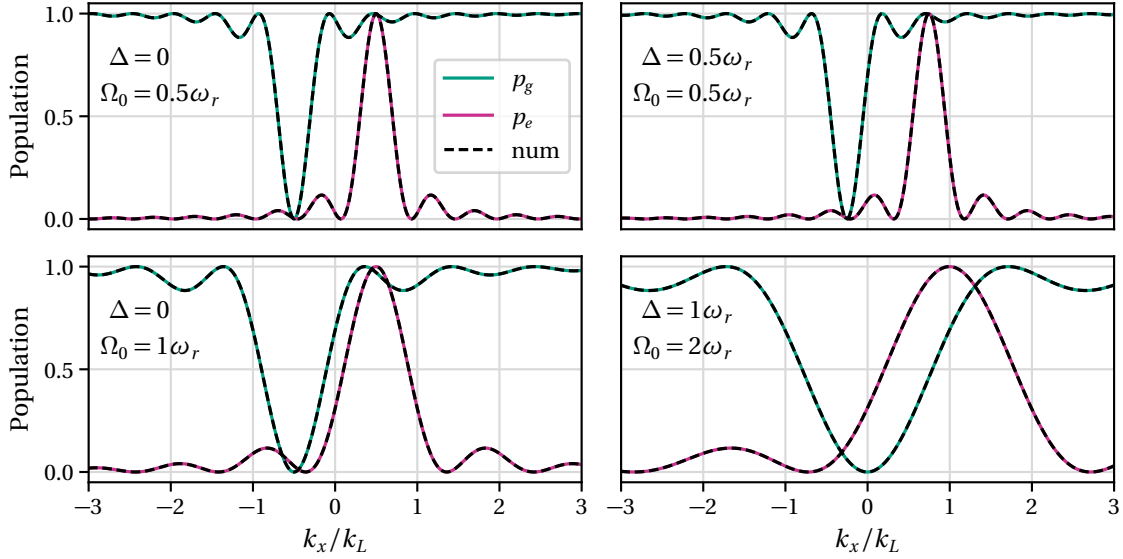


Figure 4.4: Velocity dispersion of the ground and excited state population  $p_{g,e}(k_x)$ . The analytical solutions (4.32), (4.33) (solid) are confirmed by the numerical integration (4.14) using symplectic integrators (dashed). Different detunings  $\Delta$  and Rabi frequencies  $\Omega_0$  are applied.

For vanishing detuning, the perfect transfer from  $|g, -k_L/2\rangle$  to  $|e, k_L/2\rangle$  is clearly visible. However, for  $\Delta \neq 0$  there is always one plane-wave momentum  $k_x = (\Delta - 1)/2$ , defined with equal unperturbed eigenfrequencies  $\omega'_g = \omega'_e$ , wherefore  $\Omega_k = \Omega_0$  and thus perfect transfer can be achieved for  $t_{\pi,0}$ . For  $\Delta = 0.5\omega_r$  this is the case for  $k_x = -k_L/4$ , respectively  $k_x = 0$  for  $\Delta = 1\omega_r$ . The sinc<sup>2</sup>-behaviour<sup>2</sup> is the typical response to rectangular pulses. The finite width of the transferred population shows that the velocity dispersion diminishes the total diffraction efficiency for wavepackets with finite momentum widths. Power broadening with larger Rabi frequencies reduces the velocity selectivity. The population distributions can become as broad as they overlap for the ground and the excited state. The numerical (1+1)D simulation (4.14) confirms the analytical results. Therefore, symplectic integrators are applied with 500 integration time steps  $\delta t = t_{\pi,0}/500$ , where for  $t_{\pi,0} = \pi/\Omega_0$  it is ensured  $\delta t \Omega_0 \ll 1$ .

**ABSORPTION LINE SHAPE** The absorption line shape  $\mathcal{A}$  of the diffraction is given by the envelope

$$\mathcal{A} = |a_g(0, k)|^2 \frac{\Omega_0^2}{\Omega_k^2} = |a_g(0, k)|^2 \frac{\Omega_0^2}{\Omega_0^2 + \Delta_k^2} = |a_g(0, k)|^2 \frac{\Omega_0^2}{\Omega_0^2 + (1 + 2k - \Delta)^2}, \quad (4.34)$$

depicted in Fig. 4.5. The excited state population for different interaction times is always enclosed by  $\mathcal{A}$ .

<sup>2</sup>  $\text{sinc}(x) = \sin(x)/x$

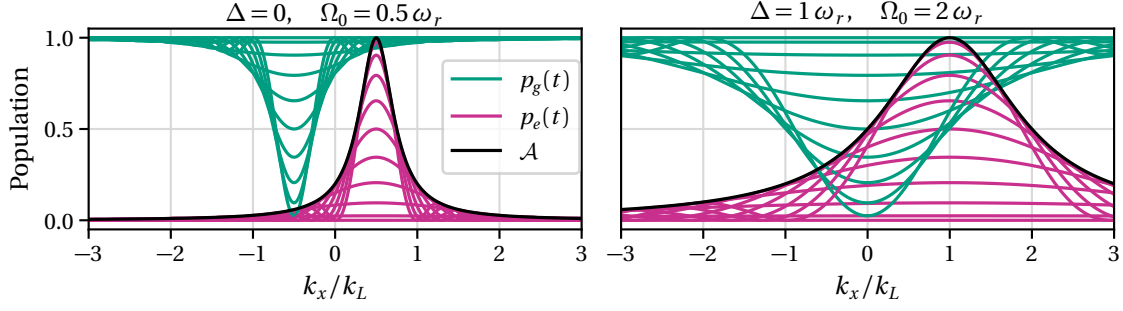


Figure 4.5: Velocity dispersion of the ground and excited state population  $p_i(k_x)$ ,  $i \in \{g, e\}$  for different times between  $0 \leq t \leq t_{\pi,0}$ . The absorption line shape  $\mathcal{A}$  (4.34) envelopes the excited state population. Different detunings  $\Delta$  and Rabi frequencies  $\Omega_0$  are applied.

**MOMENTUM KICK** The time-dependent velocity dispersion of the transfer efficiency defines the amount of the transferred momentum. Therefore, it is possible to realise an atomic beamsplitter, mirror and filter. To demonstrate their realisation the momentum expectation value in the propagation direction of the laser

$$\langle \hat{k}_x \rangle = \frac{\int d^3 k k_x |\Psi_g(\tau, \mathbf{k})|^2 + \int d^3 k k_x |\Psi_e(\tau, \mathbf{k})|^2}{\int d^3 k |\Psi(0, \mathbf{k})|^2} = \frac{\int d^3 k k_x |\Psi'_g(\tau, \mathbf{k})|^2 + \int d^3 k (k_x + 1) |\Psi'_e(\tau, \mathbf{k})|^2}{\int d^3 k |\Psi(0, \mathbf{k})|^2} \quad (4.35)$$

$$= \frac{\int d^3 k \hat{k}_x |\Psi_g(0, \mathbf{k})|^2 + \int d^3 k |\Psi_g(0, \mathbf{k})|^2 \frac{\Omega_0^2}{\Omega_k^2} \sin^2\left(\frac{\Omega_k^2 \tau}{2}\right)}{\int d^3 k |\Psi_g(0, \mathbf{k})|^2} \quad (4.36)$$

is studied. Assuming the whole population is initially in the ground state, Eq. (4.36) depends only on the initial ground state momentum density distribution  $|\Psi_g(0, \mathbf{k})|^2$ . As initial state  $\Psi_g(0, \mathbf{k})$  a not-normalised Gaussian wavepacket with  $\Psi_g(0, \mathbf{k}_0) = 1$  is considered by

$$\Psi_g(0, \mathbf{k}) = e^{-\frac{(\mathbf{k}-\mathbf{k}_0)^2}{(2\sigma_k)^2}}, \quad (4.37)$$

with momentum width  $\sigma_k = \sigma_k/k_L$ , initial momentum  $\mathbf{k}_0 = \mathbf{k}_0/k_L = -1/2 \mathbf{e}_x$  and located at  $\mathbf{r}_0 = (0, 0, 0)$ . On resonance  $\Delta = 0$  with  $\Omega_0 = 0.5 \omega_r$ , the final population distributions are shown in Fig. 4.6, restricting to one dimension  $x$ , the expansion direction of the laser.

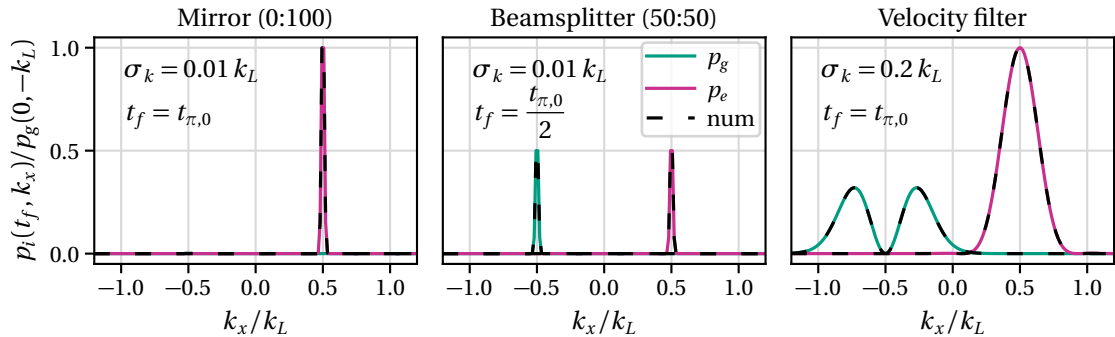


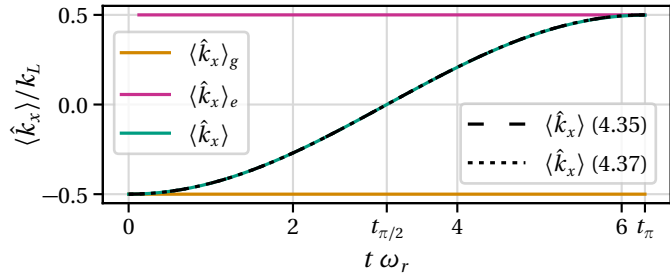
Figure 4.6: Velocity dispersion of the normalised ground and excited state population  $p_i(t_f, k_x)/p_g(0, -k_L)$ ,  $i \in \{g, e\}$  at time  $t_f$ . The analytical solutions (4.32), (4.33) (solid) are confirmed by the numerical integration (4.14). For a narrow initial wavepacket (4.37) with  $\sigma_k = 0.01 k_L$  a mirror [beamsplitter] is realised for  $t_f = t_{\pi,0} = \pi/\Omega_0$  [ $t_f = t_{\pi,0}/2$ ]. For a broad wavepacket with  $\sigma_k = 0.2 k_L$  a narrower packet with  $\sigma_{k,e} = 0.125 k_L$  is transferred into the excited state, realising a filter. The detuning is  $\Delta = 0$  and the Rabi frequency  $\Omega_0 = 0.5 \omega_r$ .

For a narrow initial wavepacket with  $\sigma_k = 0.01 k_L$  a mirror can be realised for  $t_f = t_{\pi,0}$ . Then the whole population is transferred into the excited state carrying a momentum  $\langle \hat{k}_x(t_f) \rangle = -\langle \hat{k}_x(0) \rangle = k_L/2$ . Therefore, the propagation direction of the wavepacket is reversed. After  $t_f = t_{\pi,0}/2$  only the half of the population is transferred into the excited state. Thus, a 50:50 beamsplitter is realised. The wavepacket is split into two equal parts, moving in opposite directions.

Regarding broad initial wavepackets with  $\sigma_k = 0.2 k_L$ , due to the velocity selectivity of the atomic diffraction, a narrower wavepacket  $\sigma_{k,e}(t_f) = \sqrt{\langle \hat{k}_x(t_f)^2 \rangle_e - \langle \hat{k}_x(t_f) \rangle_e^2} = 0.125 k_L$  is transferred to the excited state, working as a velocity filter, realising a cooling mechanism. In addition, as demonstrated in Fig. 4.3, the central momentum of the filtered wavepacket can be tuned, depending on the detuning  $\Delta$ .

Depicting the time-dependent momentum expectation value (4.35) of the two-level system in Fig. 4.7 also visualises the realisation of an atomic beamsplitter and mirror.

Figure 4.7: Time-dependent momentum expectation value  $\langle \hat{k}_x(t) \rangle$ , numerically (4.35) (coloured) and analytically (4.36), (4.38) (black) for a Gaussian initial wavepacket of momentum width  $\sigma_k = 0.01 k_L$ , a vanishing laser detuning  $\Delta = 0$  and a Rabi frequency  $\Omega_0 = 1 \omega_r$ .



While the part of the wavepacket in the ground-state carries the momentum  $\langle \hat{k}_x \rangle_g = -k_L/2$ , the excited-state population carries  $\langle \hat{k}_x \rangle_e = k_L/2$ , but the total momentum of the two-level system changes smoothly from initially  $\langle \hat{k}_x(t=0) \rangle = -k_L/2$  over realising a beamsplitter with  $\langle \hat{k}_x(t=t_{\pi/2}) \rangle = 0 k_L$  ending in a mirror with  $\langle \hat{k}_x(t=t_{\pi}) \rangle = k_L/2$ . Using the analytical solution for  $\Psi'_e$  (4.36) coincides exactly with the full numerical solution (4.35). In addition, approximating the atomic initial state with a plane wave  $\Psi_g(0, k) = \delta(k - k_0)$ , one obtains an analytical expression for the momentum expectation value

$$\langle \hat{k}_x \rangle = k_{x,0} + \frac{\Omega_0^2}{\Omega_{k_0}^2} \sin^2 \left( \frac{\Omega_{k_0} \tau}{2} \right). \quad (4.38)$$

For  $k_{x,0} = -k_L/2$  and  $\Delta = 0$  this simplifies further to  $\langle \hat{k}_x \rangle = -1/2 + \sin^2(\Omega_0^2 \tau/2)^2$ . This approximation matches also the numerical results, because  $\sigma_k \ll k_L$ . For larger momentum widths, population contributions with  $k \neq -k_L/2$  remain in the ground state. In this case,  $\langle \hat{k}_x \rangle$  would not reach exactly  $k_L/2$  after the mirror pulse.

## 4.4 CONCLUSION

The on-resonant diffraction of a two-level atom by a plane-wave laser beam can form a beamsplitter, mirror and velocity filter. Therefore, the coherent splitting of atomic wavepackets is realised due to momentum transfer between the ground and the excited state during the interaction. In general, if there is spontaneous emission from the excited state to the ground state, this incoherent process diminishes the diffraction efficiency. However, the considered analytically solvable interaction scenario provides deep physical insights in the diffraction process of ultracold atoms by laser light.

---

## CONCEPTS OF BRAGG DIFFRACTION

---

Bragg diffraction of ultracold atoms by moving standing light fields provides the opportunity for high precision acceleration and rotation measurements, using matter-wave interferometry. Like optical systems, matter-wave devices require exact specifications and ubiquitous imperfections need to be quantified. Therefore, the performance of atomic Bragg diffraction and its aberrations are studied with full (3+1)D simulations. In addition, simple analytical models are derived, providing deep physical insight into the underlying processes. The content of this Chapter 5 as well as of the next two Chapters 6 and 7 follows mainly [101]. However, it is described in more detail, here.

This Chapter 5 starts with the theoretical concepts of atomic Bragg diffraction with two counterpropagating, bichromatic laser beams. Therefore, momentum and energy conservation represent the fundamental cornerstones (cf. Sec. 5.1). The diffraction is revisited in the rest frame of the moving standing wave, using a Galilean transformation, which simplifies the mathematical treatment (cf. Sec. 5.2, 5.3). Defining the properties of ideal Bragg diffraction (cf. Sec. 5.4) enables to quantify the effect of different aberrations, introduced in Sec. 1.3.4. In addition, the plane-wave approximation (cf. Sec. 5.5) represents an origin to gauge more realistic calculations. Therefore, two common methods are compared to solve the Schrödinger equation with plane-wave laser beams. This is the Bloch-wave ansatz and an ad-hoc ansatz, leading to a more convenient extended zone scheme. Both include the velocity selectivity of the Bragg diffraction and losses into off-resonantly coupled diffraction orders in the quasi-Bragg regime.

Four non-adiabatic temporal pulse envelopes are studied in Chapter 6, where some are amenable for analytical models. Thereafter, in Chapter 7 also spatial variations are taken into account, considering more realistic Laguerre-Gaussian laser beams and misalignment. To complete, in Chapter 8 the effect of spontaneous emission is studied. In Chapter 9 several linear susceptibilities quantify and compare the influence of different aberrations, pointing the way to optimise the beamsplitter performance.

The corresponding comprehensive theoretical studies are applied to experiments on ground performed by Dr. Martina Gebbe at the ZARM in Bremen.

### 5.1 CONSERVATION LAWS

The basic mechanism of an atomic beamsplitter and mirror is the stimulated absorption and emission of two photons from counterpropagating laser beams [14, 145] respecting energy and momentum conservation

$$\hbar\omega_1 + \frac{\mathbf{p}_i^2}{2M} = \hbar\omega_2 + \frac{\mathbf{p}_f^2}{2M}, \quad \mathbf{p}_i + \hbar\mathbf{k}_1 = \mathbf{p}_f + \hbar\mathbf{k}_2. \quad (5.1)$$



Here  $\mathbf{p}_i$  and  $\mathbf{p}_f$  are the initial and final momenta of the particle with mass  $M$ , the photon momenta are  $\hbar \mathbf{k}_{1,2}$  and the laser frequencies  $\omega_{1,2}$ . The wavenumbers are positive  $k_i = |\mathbf{k}_i| > 0$  and the propagation directions are emphasised with explicit signs. Frequency and wavenumber are coupled by the vacuum dispersion relation  $\omega = ck$ , with the speed of light  $c$ . Energy and momentum conservation holds also for the resonant transfer of  $2\mathcal{N}$  photons, characterising  $\mathcal{N}$ th-order Bragg diffraction. This thesis focusses on the fundamental mechanism covered by first order Bragg diffraction with  $\mathcal{N} = 1$ . The overall resonant momentum transfer  $\hbar \mathbf{k}_{\text{eff}} = \mathbf{p}_f - \mathbf{p}_i$  is maximised for counterpropagating fields to  $\mathbf{k}_{\text{eff}} = 2k_L \mathbf{e}_x$  for  $\mathcal{N} = 1$  and lasers propagating in  $x$ -direction. Therefore, the average wavenumber and frequency

$$k_L \equiv \frac{k_1 + k_2}{2}, \quad \omega_L \equiv ck_L \quad (5.2)$$

are used. However, off-resonant  $2N$ -photon transfers with  $N > 1$  need to be considered because they lead to population loss into higher diffraction orders (dashed arrows in Fig. 5.1). In general, wavemechanics require the consideration of superpositions of initial  $|g, \mathbf{p}_i\rangle$  and final momentum states  $|g, \mathbf{p}_f\rangle$ , where  $g$  denotes the internal ground state of the atom. This is depicted in the energy diagram in Fig. 5.1, reduced to the beamsplitter direction, where both laser propagates exactly in  $x$ -direction with  $\mathbf{k}_1 = k_1 \mathbf{e}_x$  and  $\mathbf{k}_2 = -k_2 \mathbf{e}_x$ . Only a few transitions are permitted by energy conservation.

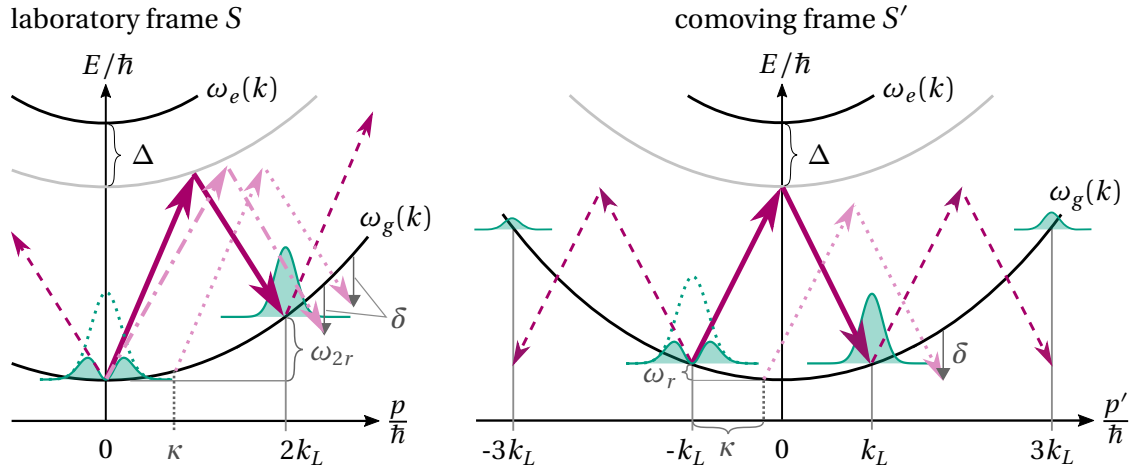


Figure 5.1: Energy diagram for first order quasi-Bragg diffraction versus atomic wavenumber  $k = p/\hbar$ . A Galilean transformation (cf. Sec. 3.4.1), transforms the laboratory frame  $S$  (left), with a moving grating and the atoms at rest to the frame  $S'$  (right) of symmetric diffraction with the grating at rest and a non-vanishing initial momentum of the atoms (green dotted). The ground and excited state's energies of a free particle are denoted with  $\hbar\omega_g(k)$  and  $\hbar\omega_e(k)$ , the recoil frequencies of the two-photon and the single photon transfer are  $\omega_{2r}$  and  $\omega_r$ . In the studied frame  $S'$  two counterpropagating lasers (magenta arrows) with wavenumbers  $k'_{1,2} = \pm k_L$  (5.2) couple mainly the initial  $|p'_i = -\hbar k_L\rangle$  and final atomic momentum states  $|p'_f = \hbar k_L\rangle$ . The momentum dependent population distributions (magenta) are initially centred around  $-k_L$  (green dotted) and after the diffraction around  $\pm k_L, \pm 3k_L$  (green shaded). This is caused by losses into higher diffraction orders (magenta dashed arrows) and the velocity selectivity of momentum detunings  $\kappa$  (magenta dotted arrows) due to off-resonant coupling. A frequency mismatch  $\delta\omega \approx \delta$  (5.7), (5.8) can lead to the same off-resonance (dashed-dotted arrows) and is therefore connected to the momentum detuning via relation (5.9).



### 5.1.1 On-resonance response

In the laboratory frame  $S$ , for atoms initially at rest  $p_i = 0$ , energy and momentum conservation (5.1) for the transfer of two photons (solid arrows in Fig. 5.1) is satisfied for bichromatic laser fields with frequencies

$$\omega_1 = \omega_2 + \omega_{2r} = \frac{1}{a} \left( 1 - a\omega_2 - \sqrt{1 - 4a\omega_2} \right) = \omega_2 + 2a\omega_2^2 + \frac{1}{a} \mathcal{O}((4a\omega_2)^3) \approx \omega_2 + \frac{\hbar(2k_2)^2}{2M}, \quad (5.3)$$

with  $a = \hbar/Mc^2$ . In Eq. (5.3) the two-photon recoil frequency

$$\boxed{\omega_{2r} \equiv 4\omega_r, \quad \omega_r = \frac{\hbar k_L^2}{2M}} \quad (5.4)$$

in terms of the single photon frequency  $\omega_r$  (4.23) is introduced, due to the two-photon recoil. The approximation in Eq. (5.3) holds for non-relativistic energies, just as the kinetic energy in (5.1). For these resonant laser frequencies (5.3), the most population (green) can be transferred from initially  $p_i = 0$  (green, dotted) to finally  $p_f = 2\hbar k_L$  (green shadowed).

### 5.1.2 Off-resonance response

Releasing ultracold atomic ensembles from traps provides localised wavepackets with a finite momentum dispersion. Therefore, one needs to study the response of the Bragg beamsplitter with finite initial momenta  $\tilde{p}_i = \kappa\hbar k_L$  and therefore  $\tilde{p}_f = (2 + \kappa)\hbar k_L$ , introducing a dimensionless momentum

$$\boxed{\kappa = \frac{\tilde{p}_i}{\hbar k_L}}. \quad (5.5)$$

This opens a frequency gap

$$\delta \equiv \frac{\tilde{p}_f^2}{2M\hbar} + \omega_2 - \frac{\tilde{p}_i^2}{2M\hbar} - \omega_1 = \omega_{2r} \left[ \left( 1 + \frac{\kappa}{2} \right)^2 - \frac{\kappa^2}{4} \right] - \omega_{2r} = \omega_{2r} \kappa, \quad (5.6)$$

leading to an off-resonant coupling as shown in Fig. 5.1 (a) (dotted magenta arrows), where the population transfer (green shadowed) is less efficient.

Alternatively, one can also probe the momentum response by a detuning of the laser frequencies  $\tilde{\omega}_{1,2}$  from the resonant values  $\omega_{1,2}$  (5.3). Conveniently, this detuning is measured by

$$\delta\omega \equiv (\omega_1 - \tilde{\omega}_1) - (\omega_2 - \tilde{\omega}_2). \quad (5.7)$$

Dash-dotted arrows mark the deviant frequencies in Fig. 5.1 (a). For a particle, which is initially at rest  $\tilde{p}_i = 0$  and acquires a momentum  $\tilde{p}_f = \hbar(\tilde{k}_1 + \tilde{k}_2) = (2 - \delta\omega/\omega_L)\hbar k_L$  after the momentum transfer, a frequency gap  $\delta$  is implied with

$$\delta = \frac{\tilde{p}_f^2}{2M\hbar} + \tilde{\omega}_2 - \tilde{\omega}_1 = \omega_{2r} \left( 1 - \frac{\delta\omega}{2\omega_L} \right)^2 - \omega_{2r} + \delta\omega \approx \delta\omega. \quad (5.8)$$

The approximation holds for  $|\tilde{\omega}_{1,2} - \omega_{1,2}| \ll \omega_L$ , which is satisfied very well in the present context of optical transitions, equivalently to  $\delta\omega/2\omega_L \ll 1$ , here  $\delta\omega/2\omega_L \sim 10^{-11}$ .

Comparing Eqs. (5.6) and (5.8), reasons the linear relation

$$\delta\omega = \omega_{2r}\kappa, \quad (5.9)$$

between laser-frequency mismatch  $\delta\omega$  and the dimensionless initial particle momentum  $\kappa$ . Therefore, both realisations are suitable to probe the momentum response of Bragg diffraction and their results are related by Eq. (5.9).

Experimentally, it is advantageous for examining the resonance shape of the Bragg diffraction to modify the laser-frequencies (cf. Sec. 5.1.2) and to prepare atomic wavepackets initially at rest in the lab-frame  $S$ . Theoretically, it is beneficial to emphasise the symmetries of the system, adopting a moving inertial frame  $S'$  (cf. Sec. 3.4.1, 5.3.1). In this frame, depicted in Fig. 5.1 (b) the Doppler-shifted laser-frequencies coincide  $\omega'_1 = \omega_1 - k_L v_g = \omega_L$ ,  $\omega'_2 = \omega_2 + k_L v_g = \omega_L$  and the momentum coupled states  $p'_i = -\hbar k_L$ ,  $p'_f = +\hbar k_L$  are distributed symmetrically. Therefore, in  $S'$  the grating is at rest, but the atoms get a non-vanishing initial momentum. To keep this symmetric diffraction scheme, the velocity dispersion can be scanned with detuning the atomic initial momentum.

## 5.2 COUNTERPROPAGATING BICHROMATIC FIELDS

The electric field of the superposition of two counterpropagating laser beams  $\mathbf{E} = \mathbf{E}_1 + \mathbf{E}_2$  is defined by the constituent fields  $\mathbf{E}_{l=\{1,2\}} = \mathbf{E}_l^{(+)} + \mathbf{E}_l^{(-)}$  with the positive frequency components

$$\mathbf{E}_l^{(+)}(t, \mathbf{r}) = \epsilon_l \mathcal{E}_l(t, \mathbf{r}) e^{-i\Phi_l(t, x)}. \quad (5.10)$$

Here,  $\epsilon_l$  denote the polarisation vectors,  $\mathcal{E}_l(t, \mathbf{r})$  the slowly varying complex Laguerre-Gaussian envelopes and  $\Phi_1(t, x) = \omega_1 t - k_1 x$ ,  $\Phi_2(t, x) = \omega_2 t + k_2 x$  are the rapidly oscillating carrier phases for fields propagating along the  $x$ -direction (cf. Sec. 2.1.2 and 2.2.2). From the superposition of these two scalar counterpropagating bichromatic fields

$$\mathcal{E} = \mathcal{E}_1 e^{-i\phi_1(t, x)} + \mathcal{E}_2 e^{-i\phi_2(t, x)}, \quad (5.11)$$

one obtains a steady motion of the intensity pattern

$$|\mathcal{E}|^2 = |\mathcal{E}_1|^2 + |\mathcal{E}_2|^2 + 2 \operatorname{Re}[\mathcal{E}_2^* \mathcal{E}_1 e^{i(k_1 + k_2)(x - v_g t)}], \quad (5.12)$$

where nodes move with the group velocity  $v_g$

$$v_g = \frac{\omega_1 - \omega_2}{\omega_1 + \omega_2} c, \quad |v_g| = \frac{\omega_{2r}}{2k_L} \ll c. \quad (5.13)$$

The frequency difference determines the direction of the motion, here  $v_g > 0$  for the assumption  $\omega_1 > \omega_2$ . If in the laboratory frame  $S$  the lasers are bichromatic, then the moving interference pattern defines another inertial frame  $S'$ , where the grating is at rest and the coordinates

$$x' = x - v_g t, \quad (5.14)$$

are related to the laboratory frame coordinates  $x$  by a passive Galilean transformation (cf. Sec. 3.4.1). This symmetrises the Bragg diffraction as depicted in Fig. 5.1. Therefore, it is useful to describe the atom-light interaction in this frame. However, for the theoretical description, the equivalent active Galilean transformation is advantageous and applied in the next Section.

### 5.3 INTERACTION ENERGY

The atom is represented by a ground  $|g\rangle$  and an excited state  $|e\rangle$ . These levels are separated by the transition frequency  $\omega_0 = \omega_e - \omega_g$  and coupled by the electric dipole matrix element  $\mathbf{d}_{eg} = \langle e|\hat{\mathbf{d}}|g\rangle$ . This two-level model does not describe the coupling of the excited state to unobserved states, leading to population losses. A sufficiently far detuning from the atomic resonance  $|\omega_0 - \omega_i| \gg \Gamma$ , where  $\Gamma$  is the natural linewidth of the transition, makes these losses negligible. Therefore, also spontaneous emission back to the ground state, diminishing the diffraction efficiency, is minimised.

In the laboratory frame  $S$  the Hamilton operator of an atom with mass  $M$  is given by

$$\hat{H}(t) = \frac{\hat{\mathbf{p}}^2}{2M} + \hbar\omega_g\hat{\sigma}_g + \hbar\omega_e\hat{\sigma}_e + \frac{\hbar}{2}\left(\hat{\sigma}^\dagger \sum_{l=1}^2 \Omega_l(t, \hat{\mathbf{r}}) e^{-i\phi_l(t, \hat{\mathbf{x}})} + \text{h.c.}\right), \quad (5.15)$$

using the Pauli spin operators  $\hat{\sigma}_{\zeta=e,g} = |\zeta\rangle\langle\zeta|$  and  $\hat{\sigma} = |g\rangle\langle e|$  [cf. Sec. 2.1, Eqs. (2.6) and (2.12)]. In the Bragg regime the effects of energy-momentum conservation are so severe that the kinetic energy distribution of the internal levels needs to be taken into account. The electric dipole interaction energy is evaluated in the rotating-wave approximation and denotes the Rabi frequencies as  $\Omega_l(t, \mathbf{r}) = -\epsilon_l \cdot \mathbf{d}_{ge} \mathcal{E}_l(t, \mathbf{r})/\hbar$  (2.11).

#### 5.3.1 Comoving, rotating frame

Making use of a transformation to the frame  $S'$  comoving with the nodes of the interference pattern and applying a suitable corotating internal frame  $S''$ , then the Hamilton operator simplifies to

$$\hat{H}''(t) = \frac{\hat{\mathbf{p}}^2}{2M} - \hbar\Delta\hat{\sigma}_e + \frac{\hbar}{2}\hat{\sigma}^\dagger (\Omega_1(t, \hat{\mathbf{r}}) e^{ik_L\hat{x}} + \Omega_2(t, \hat{\mathbf{r}}) e^{-ik_L\hat{x}}) + \text{h.c.} \quad (5.16)$$

Both transformations are derived in the following.

**GALILEAN TRANSFORMATION** The active Galilean transformation (cf. Sec. 3.4.1), comoving with the group velocity  $\mathbf{v} = v_g \mathbf{e}_x$  (5.13), transforms the interaction potential to [cf. Eq. (3.51)]

$$\hat{V}' = V(t, \hat{\mathbf{r}} + \mathbf{r}(t)), \quad \mathbf{r}(t) = (v_g t) \mathbf{e}_x. \quad (5.17)$$

Therefore, the Doppler shifted laser phases in  $x$ -direction

$$\phi'_1 = \omega_1 t - k_1(\hat{x} + v_g t) = \omega_L t - k_1(\hat{x} + v_g t), \quad (5.18)$$

$$\phi'_2 = \omega_2 t + k_2(\hat{x} + v_g t) = \omega_L t + k_2(\hat{x} + v_g t) \quad (5.19)$$

oscillate synchronously with

$$\omega_L = \frac{\omega_1 + \omega_2}{2} (1 - \beta^2) \approx \frac{\omega_1 + \omega_2}{2}. \quad (5.20)$$

The second order correction in  $\beta = v_g/c$  can be neglected safely in the nonrelativistic scenario. In this frame, the state  $|\psi\rangle = \hat{G}|\psi'\rangle$  is boosted with the displacement operator  $\hat{G}$  (3.48) in the Schrödinger picture, while the coordinate operators  $\hat{\mathbf{x}}, \hat{\mathbf{p}}$  remain unchanged.

COROTATING FRAME An additional local frame transformation  $|\psi'\rangle = \hat{F}|\psi''\rangle$ , with

$$\hat{F}(t) = \exp\left[-i\omega_g t - i\omega_L t \hat{\sigma}_e + \frac{i}{2}[k_{12}(\hat{x} - \chi_{12})]\hat{\sigma}_z\right] \quad (5.21)$$

eliminates the rapid temporal oscillations and establishes a single spatial period  $\lambda_L = 2\pi/k_L$  of the optical potential. Now, the transformed Schrödinger equation reads

$$i\hbar\partial_t|\psi''\rangle = \hat{H}''|\psi''\rangle, \quad (5.22)$$

$$\begin{aligned} \hat{H}'' = & \frac{(\hat{p}_x + \frac{1}{2}\hbar k_{12}\hat{\sigma}_z)^2}{2M} + \frac{\hat{p}_y^2 + \hat{p}_z^2}{2M} - \hbar\Delta\hat{\sigma}_e \\ & + \frac{\hbar}{2}[\hat{\sigma}^\dagger(\Omega_1(t, \hat{\mathbf{r}} + \mathbf{r}(t))e^{ik_L\hat{x}} + \Omega_2(t, \hat{\mathbf{r}} + \mathbf{r}(t))e^{-ik_L\hat{x}}) + \text{h.c.}], \end{aligned} \quad (5.23)$$

with the already defined common wavenumber  $k_L = (k_1 + k_2)/2$  (5.2) and a relative wavenumber mismatch  $k_{12} = \Delta k/2$  with

$$\Delta k \equiv k_1 - k_2. \quad (5.24)$$

The laser detuning  $\Delta \equiv \omega_L - \omega_0$  is measured with respect to the common Doppler-shifted frequency  $\omega_L$  (5.20). Global phases of the Rabi frequencies  $\tilde{\Omega}_l(t, \mathbf{r}) = \Omega_l(t, \mathbf{r})e^{-i\chi_l}$  do vanish with the proper gauge  $\chi_{12} = (\chi_1 + \chi_2)/2$  and the shifted coordinate origin  $\mathbf{r}_0 = (\chi_1 - \chi_2)/2k_L$ .

Please note,  $k_{12}$  is infinitesimal with  $\Delta k \sim 1 \times 10^{-10} \mu\text{m}^{-1} \sim 1 \times 10^{-11} k_L$  in comparison to other relevant momenta. Compared to reasonable momentum widths, in the range between the minimal width of trapped BECs  $\sigma_k \geq 10^{-2} k_L$  (cf. Sec. 2.3.5) and the width of thermal clouds  $\sigma_k \sim 10^{-1} k_L$  (cf. Sec. 2.3.7), the wavenumber mismatch  $k_{12}$  can be neglected safely. In addition, beamsplitter pulses are typical short ( $< 1$  ms), why the ballistic displacement  $v_g t \sim \mu\text{m} < \sigma_x$  is also negligible  $\Omega_l(t, \mathbf{r} + \mathbf{r}(t)) \approx \Omega_l(t, \mathbf{r})$ , leading to the Hamilton operator (5.16).

Therefore, considering two counterpropagating Laguerre-Gaussian laser beams (cf. Sec. 2.2.2), which are symmetrically displaced with respect to their waists by a distance  $\ell_x$  in  $x$ -direction, the dipole interaction energy in the comoving, rotating frame (5.23) reads

$$\hat{V}'' = \frac{\hbar}{2}\hat{\sigma}^\dagger[\Omega_1(t, \hat{x}_1, \hat{y}, \hat{z})e^{ik_L\hat{x}} + \Omega_2(t, \hat{x}_2, \hat{y}, \hat{z})e^{-ik_L\hat{x}}] + \text{h.c.}, \quad (5.25)$$

using  $\chi_{12} = (\chi_1 + \chi_2)/2 - k_L\ell_x/2$  and  $\mathbf{r}_0 = (\chi_1 - \chi_2)/2k_L - \Delta k\ell_x/4k_L \approx (\chi_1 - \chi_2)/2k_L$ <sup>1</sup>. The Rabi frequencies  $\Omega_l(t, \mathbf{r}_l)$  include the real pulse amplitudes  $\Omega_{0,l}(t)$  and complex spatial envelopes of Laguerre-Gaussian beams  $u(x_l, y, z)$  (2.23). For the displaced beams the shifted coordinates  $x_{1/2} = \pm(x + v_g t) + \ell_x/2$  are used (cf. Sec. 3.4.2). These define the beam parameters  $w_l = w(x_l)$ ,  $R_l = R(x_l)$  and  $\zeta_l = \zeta(x_l)$ , slowly varying for  $x \ll x_R$ . This demonstrate that the ballistic displacement  $v_g t \sim \mu\text{m} < \sigma_x \ll \ell_x, x_R$  is indeed negligible. In addition, for not too large atomic clouds  $\sigma_x < w_0/3$ , one can even approximate  $x_1 \approx x_2 \approx \ell_x/2$ .

Finally, it is essential that in the comoving, rotating frame  $S''$  with the Hamilton operator (5.16) the atom responds only to a single laser frequency  $\omega_L = (\omega_1 + \omega_2)/2$  and one carrier wavenumber  $k_L = (k_1 + k_2)/2$ .

1 The detailed transformations for arbitrarily misaligned laser beams are given in Section 7.5.1.

### 5.3.2 Time evolution

For large detunings  $\Delta$ , dissipative processes are not an issue. Therefore, the time evolution within the diffraction is given by the solution of the Schrödinger equation (cf. Sec. 3.1) for  $t > t_i$  and  $|\psi\rangle \equiv |\psi''\rangle$

$$|\psi(t)\rangle = G(t, t_i)|\psi(t_i)\rangle, \quad (5.26)$$

$$G(t, t_i) = \mathcal{T} e^{-i \int_{t_i}^t dt' H(t')} \theta(t - t_i), \quad i \partial_t G(t, t_i) = H(t)G + i\delta(t - t_i), \quad (5.27)$$

with the time-ordered propagator  $G(t, t_i)$ , as a retarded Green's function [146].

As introduced in Section 3.1, this two-component, (3+1)D problem is solved numerically, using Fourier methods with symplectic integrators (cf. Sec. 3.1.1) and operator disentangling (cf. Sec. 3.1.2). Analytical solutions are examined later for rectangular pulses (Sec. 6.2) and hyperbolic secant pulses (Sec. 6.3).

## 5.4 IDEAL BRAGG BEAMSPLITTER AND MIRROR

**PULSE AREA** The interaction of a two-state system with laser pulses can be understood qualitatively by the pulse area [147] which is rather an angle by dimension

$$\theta(t) = \int_{-\infty}^t dt' \Omega(t'), \quad \Omega(t) = \frac{|\Omega_0(t)|^2}{2\Delta}. \quad (5.28)$$

Here, the time-dependent two-photon Rabi frequency  $\Omega(t)$  is introduced, assuming equal amplitudes  $\Omega_{0,1}(t) = \Omega_{0,2}(t) = \Omega_0(t)$ . In the context of ideal first order Bragg scattering, the two states are the momentum states  $\{|-k_L\rangle_x, |k_L\rangle_x\}$ . One can visualise the evolution during the action of the Bragg pulse as a motion on the Bloch sphere [148]. An ideal, symmetrical 50:50 Bragg beamsplitter is a  $\theta = \pi/2$  rotation from the south pole to the equator at some longitude. This gives equal probability to the outputs channels  $|\pm k_L\rangle$ . A  $\theta = \pi$  rotation from the south pole to the north pole reverses the momenta  $|-k_L\rangle \rightarrow |k_L\rangle$  and thus acts like a mirror. The following discussion, is focussed on the mirror configuration as it is most susceptible to aberrations, due to the longer interaction time corresponding to the larger pulse area.

**DIFFRACTION EFFICIENCY** The polar decomposition of the transition amplitude

$$\langle \mathbf{k}' | G(t, t_i) | \mathbf{k} \rangle = \sqrt{\eta_{\mathbf{k}'\mathbf{k}}} e^{i\phi_{\mathbf{k}'\mathbf{k}}} \quad (5.29)$$

between initial  $|\mathbf{k}\rangle$  and final  $|\mathbf{k}'\rangle$  momentum state characterises the diffraction efficiency  $0 \leq \eta_{\mathbf{k}'\mathbf{k}} \leq 1$ . Anticipating the following results, it shows resonances at  $\mathbf{k}' = \mathbf{k} + 2N\mathbf{k}_L$ ,  $N \in \mathbb{Z}$ . This was visualised in Fig. 5.1 with the off-resonant coupling to higher diffraction orders. For atomic wavepackets the diffraction efficiency  $\eta_{\mathcal{N}}$  for  $\mathcal{N}$ -th order Bragg diffraction, i.e. resonant coupling of  $\mathbf{k}$  with  $\mathbf{k}' = \mathbf{k}'_{\mathcal{N}} \equiv \mathbf{k} + 2\mathcal{N}\mathbf{k}_L$ , is defined by the total population proportion that can be transferred into  $\mathbf{k}'_{\mathcal{N}}$ . For lasers propagating in  $x$ -direction and normalised wavepacktes  $\int d^3k n(\mathbf{k}) = 1$  with the density in the momentum space  $n(\mathbf{k}) = |\Psi(\mathbf{k})|^2$  the diffraction efficiency  $\eta_{\mathcal{N}}$  is given by the expectation value of  $\hat{R}_{\mathcal{N}}(k) = \Theta[(\mathcal{N} + 1)k_L - k]\Theta[k - (\mathcal{N} - 1)k_L]$  ( $\Theta$  is the Heaviside step function), reading

$$\eta_{\mathcal{N}} = \langle \hat{R}_{\mathcal{N}}(k'_x) \rangle = \int d^3k' R_{\mathcal{N}}(k'_x) |\Psi(\mathbf{k}', t)|^2, \quad \Psi(\mathbf{k}', t) = \int d^3k \langle \mathbf{k}' | G(t, t_i) | \mathbf{k} \rangle \Psi(\mathbf{k}, t_i). \quad (5.30)$$

For in general  $\int d^3k n(\mathbf{k}) \neq 1$ , the normalised diffraction efficiency  $\bar{\eta}_{\mathcal{N}}$  reads

$$\bar{\eta}_{\mathcal{N}} = \frac{\eta_{\mathcal{N}}}{\sum_N \eta_N}. \quad (5.31)$$

An important experimental observable represents the normalised diffraction efficiency of the resonantly coupled states for first-order diffraction  $\mathcal{N} = 1$

$$\bar{\eta} \equiv \bar{\eta}_1 = \frac{\eta_1}{\sum_N \eta_N}. \quad (5.32)$$

In the deep-Bragg regime, one obtains

$$\bar{\eta}_{+-} = \frac{N_+}{N_- + N_+} = \frac{\eta_{+1}}{\eta_{-1} + \eta_{+1}} \approx \bar{\eta} \quad (5.33)$$

from the number of diffracted atoms  $N_+$  into the first diffraction order with  $\mathbf{k}' = \mathbf{k} + 2\mathbf{k}_L$ ,  $-2\mathbf{k}_L \leq \mathbf{k} < 0$  and the undiffracted atoms  $N_-$  remaining in the initial momentum state  $\mathbf{k}' = \mathbf{k}$ . The approximation is exact in the deep-Bragg limit, where no population at all is lost into off-resonant diffraction orders.

**FIDELITY** The introduced diffraction efficiencies are independent of the phase of the final wavefunction. Therefore, to quantify the quality of the diffraction, additionally the phase sensitive fidelity  $F$  is used with

$$F \equiv F_1, \quad F_{\mathcal{N}} = |\langle \psi_{\text{ideal}} | \psi(t) \rangle|^2, \quad |\psi_{\text{ideal}}\rangle = e^{2i\mathcal{N}\mathbf{k}_L\hat{x}} |\psi_i\rangle, \quad (5.34)$$

characterising the overlap of the final state  $|\psi(t)\rangle$  of (5.26) and the ideal final mirror state  $|\psi_{\text{ideal}}\rangle$ , for first-order diffraction i.e.  $\mathcal{N} = 1$ . In the limit of a plane wave as atomic initial state (cf. Sec. 2.3.3), the fidelity corresponds to the diffraction efficiency  $F_{\mathcal{N}} = \bar{\eta}_{\mathcal{N}}$  with  $\mathbf{k}' = \mathbf{k} + 2\mathcal{N}\mathbf{k}_L$ .

## 5.5 PLANE-WAVE APPROXIMATION

Clearly, the basic mechanism of Bragg beamsplitters arises from the momentum transfer of plane waves with a real, constant Rabi frequency  $\Omega_1(t, \mathbf{r}) = \Omega_2(t, \mathbf{r}) = \Omega_0$  within the duration of a rectangular pulse. Due to the *long* interaction times in the Bragg regime, the details of switching on and off can be ignored, assuming the Rabi frequency to be constant. This model is the reference to gauge more realistic calculations. Consequently, the two components  $\{\psi_e(t, \mathbf{r}), \psi_g(t, \mathbf{r})\}$  of the Schrödinger field  $|\psi(t, \mathbf{r})\rangle = \psi_g(t, \mathbf{r})|g, \mathbf{r}\rangle + \psi_e(t, \mathbf{r})|e, \mathbf{r}\rangle$  evolve according to

$$i\partial_t \psi_e = \left( -\frac{\hbar}{2M} \nabla^2 - \Delta \right) \psi_e + \Omega_0 \cos(k_L x) \psi_g, \quad (5.35a)$$

$$i\partial_t \psi_g = -\frac{\hbar}{2M} \nabla^2 \psi_g + \Omega_0^* \cos(k_L x) \psi_e, \quad (5.35b)$$

using the Hamilton operator (5.16), together with plane-wave laser beams (2.17).

### 5.5.1 Adiabatic elimination of the excited state

Assuming the excited state is initially empty, the atom's kinetic energy is small and the lasers are far detuned from the excited state leads to the separation of frequency scales <sup>2</sup>

<sup>2</sup> The frequency scales are provided by the experimental parameters (cf. Tables A.1 and A.2). However, in general for Bragg diffraction a large detuning  $\Delta \gg \Gamma$  is required to keep the coherent photon transfer not impaired by spontaneous emission processes. This requires Rabi frequencies  $\Omega_0 > \Gamma$  or depending on the detuning  $\Omega_0 \gg \Gamma$  to achieve  $\pi$ -pulses for accessible pulse durations (cf. Sec. 6.1). Finally, the recoil frequency is approximately defined by the optical transition frequency, with  $\omega_r \ll \Gamma$  for rubidium-87 atoms.

$$\boxed{\omega_r \ll \Gamma \ll \Omega_0 \ll \Delta}. \quad (5.36)$$

Therefore, the excited state can be adiabatically eliminated [67, 149] using standard methods [150], resulting in

$$\psi_e \approx \frac{\Omega_0}{\Delta} \cos(k_L x) \psi_g. \quad (5.37)$$

Then, the ground state Schrödinger equation reads

$$i \partial_t \psi_g = \left( -\frac{\hbar}{2M} \nabla^2 + \mathcal{V}(x) \right) \psi_g, \quad \mathcal{V}(x) = \frac{|\Omega_0|^2}{\Delta} \cos^2(k_L x), \quad (5.38)$$

with the dipole potential  $\mathcal{V}(x)$ . Stationary solutions of this one-dimensional problem are Mathieu functions [151], but in general it is not possible to give a full analytical solution of such a Mathieu equation [67, 149]. Here, the primary interest is not the idealised case of determining stationary eigenmodes but to formulate a suitable ansatz for the (3+1) dimensional non-separable equation with time-dependent pulses.

### 5.5.2 Bloch-wave ansatz

The Bloch band picture is suitable to describe the velocity selective atomic diffraction by a standing laser wave [14, 152, 153]. The characteristic translation invariance of the Hamilton operator (5.38) by a displacement of  $a_x = \lambda_L/2$  defines a natural length scale. Its reciprocal is the lattice vector  $q_x = 2\pi/a_x = 2k_L$ , which is twice the laser wavenumber. It is convenient to embed the total three-dimensional wavefunction in an orthorhombic volume with lengths  $(N_x a_x, a_y, a_z)$ ,  $N_x \in \mathbb{N}$  and to impose periodic boundary conditions  $\psi_g(x + N_x a_x, y + a_y, z + a_z) = \psi_g(x, y, z)$ . Bragg scattering involves at least two photons, one photon from each of the counterpropagating lasers. Therefore, the two-photon recoil frequency  $\omega_{2r}$  (5.4) emerges as the frequency scale. In terms of the dimensionless length  $\xi = q_x x$  and dimensionless time<sup>3</sup>

$$\boxed{\tau = \omega_{2r} t}, \quad (5.39)$$

the Schrödinger field

$$\psi_g(t, \mathbf{r}) = \sum_{r=-\lfloor \frac{N_y}{2} \rfloor}^{\lfloor \frac{N_y}{2} \rfloor - 1} \sum_{s=-\lfloor \frac{N_z}{2} \rfloor}^{\lfloor \frac{N_z}{2} \rfloor - 1} e^{i(r q_y y + s q_z z - \bar{\omega}_{r,s} \tau)} h^{(r,s)}(\tau, \xi), \quad (5.40)$$

factorises into one-dimensional fields  $h^{(r,s)}(\tau, \xi)$  and two-dimensional plane waves with multiples of the transversal lattice vectors  $q_{y,z} = 2\pi/a_{y,z}$ . The integers  $N_{y,z} \in \mathbb{N}$  define the maximal momentum resolution  $q_i^{\max} = q_i \lfloor N_i/2 \rfloor$ . Please note the use of the Gauss brackets rounding towards the nearest integer at the ‘floor’  $\lfloor \cdot \rfloor$  or the ‘ceiling’  $\lceil \cdot \rceil$ . With a detuning dependent shift of the frequency

$$\bar{\omega}_{r,s} = \hbar \frac{r^2 q_y^2 + s^2 q_z^2}{2M \omega_{2r}} + \Omega, \quad (5.41)$$

the Schrödinger equation for each amplitude simplifies to

$$i \partial_\tau h(\tau, \xi) = \left( -\partial_\xi^2 + \Omega \cos \xi \right) h(\tau, \xi). \quad (5.42)$$

<sup>3</sup> The usage of dimensionless variables provides a tremendous improvement of the readability of formulas. However, for a physical interpretation of quantities their dimension is indispensable. For this reason, always when explicit quantities appear, they are given in their physical units.



Here, the two-photon Rabi frequency  $\Omega$  (dimensionless  $\Omega$ ) for equally strong laser beams

$$\boxed{\Omega = \frac{|\Omega_0|^2}{2\Delta}, \quad \Omega = \frac{\Omega}{\omega_{2r}}} \quad (5.43)$$

appears. By construction, the potential is  $2\pi$ -periodic and the eigenfunctions  $h(\tau, \xi) = e^{-i\tau\omega^{(b)}(q)} h^{(b)}(\xi, q)$  are given by Bloch-waves  $h^{(b)}(\xi, q)$  [154–157] with the lattice periodic function  $g^{(b)}(\xi, q)$  for momentum  $q$  and band index  $b$

$$h^{(b)}(\xi, q) = e^{iq\xi} g^{(b)}(\xi, q), \quad g^{(b)}(\xi + 2\pi, q) = g^{(b)}(\xi, q). \quad (5.44)$$

From the periodic boundary conditions for the wavefunction  $h^{(b)}(\xi + 2\pi N_x, q) = h^{(b)}(\xi, q)$ , one obtains a quantisation of the wavenumber  $q_n = n/N_x$  with  $n \in \mathbb{Z}$ . The interval  $-1/2 \leq q_n < 1/2$  defines the first Brillouin zone in the reduced zone scheme, whose extent equals the *crystal momentum*  $Q = 1$ .

Bloch wavefunctions are also periodic in momentum space  $h^{(b)}(\xi, q + Q) = h^{(b)}(\xi, q)$ , provided one defines

$$g^{(b)}(\xi, q) = \sum_{m=-\mathcal{N}}^{\mathcal{N}-1} e^{im\xi} g^{(b)}(m + q), \quad (5.45)$$

by a Fourier series for a maximal diffraction order  $\mathcal{N} \in \mathbb{N}$  with boundary condition  $g^{(b)}(q + \mathcal{N}) = g^{(b)}(q - \mathcal{N}) = 0$ . From a superposition of these Bloch waves, one obtains the ansatz

$$h(\tau, \xi) = \sum_{n=-\lfloor \frac{N_x}{2} \rfloor}^{\lfloor \frac{N_x}{2} \rfloor - 1} \sum_{m=-\mathcal{N}}^{\mathcal{N}-1} e^{i(m+q_n)\xi} g(\tau, m + q_n), \quad (5.46)$$

for the time-dependent solution of Eq. (5.42), compatible with the Bloch theorem and suitable for numerical computation. This ansatz transforms the partial differential equation into the parametric difference equation

$$i\partial_\tau g_m(\tau, q) = (m + q)^2 g_m + \frac{\Omega}{2} (g_{m+1} + g_{m-1}). \quad (5.47)$$

The  $q$ -dependence of the  $m$ -th order scattering amplitude  $g_m(\tau, q) \equiv g(\tau, m + q)$  leads to the velocity dispersion of Bragg diffraction. Assuming Dirichlet boundary conditions, one can use a  $(2\mathcal{N} - 1)$ -dimensional representation  $\mathbf{g}^e = (g_{1-\mathcal{N}}, \dots, g_{\mathcal{N}-1})$ , to study the initial value problem

$$i\dot{\mathbf{g}}^e = H^e(q) \mathbf{g}^e, \quad H^e = D^e + L + L^\dagger. \quad (5.48)$$

For the indices  $1 - \mathcal{N} \leq m \leq \mathcal{N} - 1$ , the Hamilton matrix  $H^e$  is formed by a diagonal matrix  $D^e$  and a lower triangular matrix  $L$

$$D_{m,n}^e = (m + q)^2 \delta_{m,n}, \quad L_{m,n} = \frac{\Omega}{2} \delta_{m,n+1}. \quad (5.49)$$

In order to study the discrete Bloch energy bands  $\omega^{(b)}(q)$ , one has to solve the eigenvalue problem

$$\mathbf{g}^e(\tau, q) = e^{-i\tau\omega(q)} \mathbf{g}^e(q), \quad \omega(q) \mathbf{g}^e = H^e(q) \mathbf{g}^e. \quad (5.50)$$

In Fig. 5.2, the lowest few energy bands  $\omega^{(b)}(q)$  are depicted versus the lattice momentum  $q$  in an extended momentum zone scheme. For reference, the quadratic dispersion relation



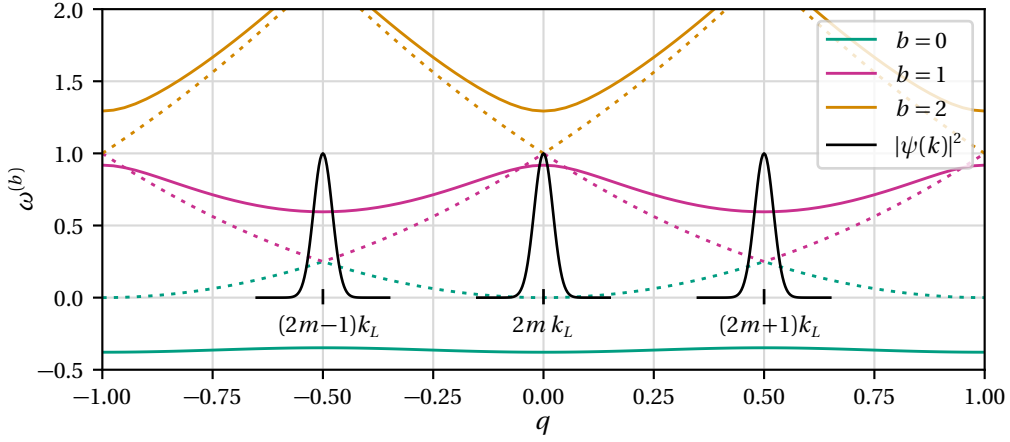


Figure 5.2: Energy bands  $\omega^{(0,1,2)}(q)$  of a periodic lattice in the extended zone scheme depending on the quasimomentum  $q$  for the empty lattice  $\Omega = 0$  (dotted) and a finite depth  $\Omega = 1$  (solid). The frequency unit is  $\omega_{2r} = 4\omega_r$ . Wavepackets with odd momenta  $(2m+1)k_L$  are located at the edges  $q = \pm \frac{1}{2}$  of the first Brillouin zone, even momenta  $2mk_L$  are located at the center  $q = 0$ .

of an *empty* lattice  $\Omega = 0$  and the dispersion relation for a moderately deep lattice with  $\Omega = 1$  is shown. In dimensional units, this lattice is  $\Omega = \Omega \omega_{2r} = 1\omega_{2r} = 4\omega_r = 4(\hbar k_L^2/2M)$  deep. The ideal situation for a Bragg beamsplitter are narrow momentum wavepackets  $\psi(k)$  with  $\sigma_k \ll k_L$ . If they are located at the band edges  $k = q q_x = (m \pm 1/2)2k_L$ , the two-photon process covers at least three Brillouin zones. For wavepackets at the center of the band  $k = q q_x = 2mk_L$ , only two Brillouin zones are coupled by a Bragg pulse.

### 5.5.3 Ad-hoc ansatz

There are alternative formulations [67, 86] to the Bloch-wave ansatz. Therefore, a Fourier series on the periodic lattice  $h(\tau, x + N_x a_x) = h(\tau, x)$  is defined as

$$h(\tau, x) = \sum_{l=-\infty}^{\infty} e^{i \frac{2\pi l}{N_x a_x} x} g_l(\tau), \quad \frac{2\pi l}{N_x a_x} = \frac{2l}{N_x} k_L. \quad (5.51)$$

By decomposing the index  $l = N_x m + r$  into a quotient  $m = \lfloor l/N_x \rfloor$  and a remainder  $0 \leq r < N_x$ , one obtains with  $n = r - \lfloor N_x/2 \rfloor$

$$h(\tau, x) = \sum_{n=-\lfloor \frac{N_x}{2} \rfloor}^{\lfloor \frac{N_x}{2} \rfloor - 1} \sum_{\mu=2m+1}^{N-1} g_\mu(\tau, \kappa_n) e^{i k_\mu^n x} \quad (5.52)$$

$$= \sum_{n=-\lfloor \frac{N_x}{2} \rfloor}^{\lfloor \frac{N_x}{2} \rfloor - 1} \sum_{\mu=2m+1}^{N-1} g_\mu^+(\tau, \kappa_n) \cos(k_\mu^n x) + g_\mu^-(\tau, \kappa_n) \sin(k_\mu^n x). \quad (5.53)$$

In this series expansion a momentum as multiples of the laser wavenumber  $k_L$

$$k_\mu^n = (\mu + \kappa_n) k_L, \quad \kappa_n = \frac{\kappa_n}{k_L}, \quad (5.54)$$

is used with the dimensionless quasimomentum  $\kappa_n$

$$-1 \leq \kappa_n = \frac{2n}{N_x} - \frac{\lfloor \frac{N_x}{2} \rfloor - \lfloor \frac{N_x}{2} \rfloor}{N_x} < 1, \quad (5.55)$$

in an extended Brillouin zone. The first form (5.52) uses complex plane waves with well defined momentum, while the second form (5.53) uses real plane waves with well defined parity  $\pm$ . As the Schrödinger equation (5.42) has even parity, parity is a conserved quantity.

However, the decomposition of the index  $l = N_x m + n$  is not unique, admitting signed integral remainders within the limits  $-[N_x/2] \leq n < [N_x/2]$ . This implies a quotient  $m = [(l + [N_x/2])/N_x]$ . Now, the Fourier series reads

$$h(\tau, x) = \sum_{n=-[N_x/2]}^{[N_x/2]-1} \sum_{m=-N}^{N-1} g_\mu(\tau, \kappa_n) e^{ik_\mu^n x} = \sum_{n=-[N_x/2]}^{[N_x/2]-1} \sum_{m=-N}^{N-1} g_\mu^+(\tau, \kappa_n) \cos(k_\mu^n x) + g_\mu^-(\tau, \kappa_n) \sin(k_\mu^n x), \quad (5.56)$$

with the quasimomentum  $\kappa_n$

$$-1 \leq \kappa_n = \frac{2n}{N_x} \leq 1 - \frac{1}{N_x}. \quad (5.57)$$

The definition of the quasimomenta in Eqs. (5.55) and (5.57) agree exactly for even numbers  $N_x = 2n$  of lattice sites or coincide asymptotically for  $N_x \rightarrow \infty$ . The even/odd ambiguity of number of lattice sites cannot be of physical significance as the periodic boundary condition are mere mathematical convenience. They have no physical counterparts in reality. Therefore, assuming an even number of lattice sites is no limitation. Consequently, it is advantageous to use Eq. (5.52) for wavepackets located around odd multiples of  $k_L$  or Eq. (5.56) for wavepackets located around even multiples of  $k_L$  (cf. Fig. 5.2).

Using time-dependent amplitudes  $g_\mu(\tau, \kappa_n)$  in the even/odd series Eqs. (5.52) and (5.56), transforms the Schrödinger equation (5.42) into a single difference equation, valid for all  $\mu \in \mathbb{Z}$

$$i \partial_\tau g_\mu(\tau, \kappa) = \frac{1}{4}(\mu + \kappa)^2 g_\mu + \frac{\Omega}{2}(g_{\mu+2} + g_{\mu-2}). \quad (5.58)$$

Due to the two-photon transfer, there is a selection rule, which avoids coupling between the even (e) and odd (o) solution manifolds. As the focus of this thesis lies on symmetric Bragg diffraction in the comoving frame  $S'$ , coupling mainly  $|-k_L\rangle$  with  $|+k_L\rangle$ , the odd solution manifold with  $\mu = 2m + 1$  is of special interest. Therefore, Eq. (5.58) can be cast into a tridiagonal system of linear differential equations

$$i \dot{\mathbf{g}}^o = H^o(\kappa) \mathbf{g}^o, \quad H^o = D^o + L + L^\dagger, \quad (5.59)$$

for  $\mathbf{g}^o = (g_{-2N+1}, g_{-2N+3}, \dots, g_{2N-1})$  with  $L$  from Eq. (5.49) and a diagonal matrix

$$D_{\mu,\nu}^o = \frac{1}{4}(\mu + \kappa)^2 \delta_{\mu,\nu} \equiv D_{\mu,\nu} + \varpi \delta_{\mu,\nu}, \quad (5.60)$$

with the frequency offset  $\varpi = (\kappa - 1)^2/4$ . In the following, it will be reasonable to adopt a rotating frame with this offset, using the transformation

$$\mathbf{g}^o(\tau, \kappa) = e^{-i\varpi\tau} \mathbf{g}(\tau, \kappa), \quad (5.61)$$

to obtain the frequency shifted tridiagonal system of linear differential equations

$$i \dot{\mathbf{g}} = \mathcal{H}(\kappa) \mathbf{g}, \quad \mathcal{H} = D + L + L^\dagger, \quad (5.62a)$$

$$D_{\mu,\nu} = \omega_\mu \delta_{\mu,\nu}, \quad \omega_\mu = \frac{1}{4}(\mu + \kappa)^2 - \varpi, \quad (5.62b)$$

with the lower triangular matrix  $L$  (5.49). This transformation grounds the energy  $\hbar\omega_{-1}$  of the amplitude  $g_{-1}$  to zero.

## (1+1)D BRAGG DIFFRACTION: TEMPORAL PULSES

Commencing with the basic model of Bragg scattering, using the ad-hoc ansatz, successively more realistic processes are considered to assess their contribution to aberrations. This Chapter 6 focuses on temporal envelopes. Therefore, the plane-wave approximation is used, considering four different temporal Bragg-pulse shapes  $f_j(\tau)$  with simulations in (1+1)D. Their influence on the velocity dispersion as well as losses into higher diffraction orders are analysed.

### 6.1 PULSE SHAPES

The examined temporal envelopes are Gaussian (G), rectangular (R), hyperbolic secant (S) and Blackman (B) Rabi pulses, with

$$\Omega(\tau) = \Omega f_j(\tau), \quad j \in \{G, R, S, B\}. \quad (6.1)$$

The shape functions  $f_j$ , defining the temporal envelope and depicted in Fig. 6.1, are all normalised to unity at maximum and characterised by a window width  $\tau_j$ . Different Rabi pulses (6.1) can be compared physically, if they cover the same pulse area (5.28)

$$\theta \equiv \theta(\tau = \infty) = \Omega T, \quad T \equiv T_j(-\infty, \infty), \quad T_j(\tau_i, \tau_f) = \int_{\tau_i}^{\tau_f} d\tau f_j(\tau), \quad (6.2)$$

for equal nominal time  $T = T_G = T_R = T_B = T_S$ .

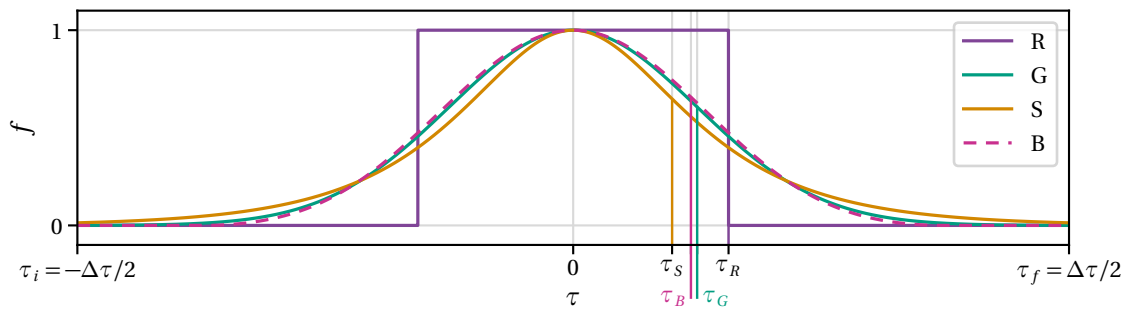


Figure 6.1: Temporal envelopes  $f(\tau)$  of a **R**ectangular-, **G**aussian-, hyperbolic **S**ecant- and **B**lackman-pulse, for equal nominal time  $T = T_j$ , with  $j \in \{R, G, S, B\}$ , and total pulse length  $\Delta\tau = 8\tau_G$ . The vertical lines indicate the pulse widths  $\tau_j$ .

**RECTANGULAR PULSES** are popular in theory, as they are constant during the interaction time and lead to simple analytical approximations. They read

$$f_R(|\tau| \leq \tau_R) = 1, \quad T_R = 2\tau_R \quad (6.3)$$

and  $f_R(|\tau| > \tau_R) = 0$ , elsewhere. In experiments, where interaction time is precious, they provide short pulse widths.

GAUSSIAN PULSES of width  $\tau_G$  provide a smooth temporal envelope

$$f_G(\tau) = \exp\left(-\frac{\tau^2}{2\tau_G^2}\right), \quad T_G = \sqrt{2\pi} \tau_G. \quad (6.4)$$

However, for finite pulse durations they have to be truncated, which introduces higher spectral components.

BLACKMAN PULSES rectify this, providing minimal spectral sidebands at finite pulse durations. They are characterised by a window function [158–161]

$$f_B(\tau) = w_B\left(\frac{\tau}{\tau_B}\right), \quad w_B(|\phi| \leq \pi) = \frac{1}{50} [21 + 25 \cos(\phi) + 4 \cos(2\phi)], \quad T_B = \frac{21\pi}{25} \tau_B, \quad (6.5)$$

and  $w_B(|\phi| > \pi) = 0$  elsewhere. Due to this cut-off, like rectangular pulses, they provide shorter total pulse lengths in comparison to Gaussian pulses, but nevertheless a smooth envelope.

HYPERBOLIC SECANT PULSES provide also a smooth temporal envelope and are defined with

$$f_S(\tau) = \operatorname{sech}\left(\frac{\tau}{\tau_S}\right), \quad T_S = \pi \tau_S. \quad (6.6)$$

They are amenable for closed analytical solutions [162–164].

### **Definition of $\pi$ - and $\frac{\pi}{2}$ -pulses**

The symmetrical 50:50 beamsplitter pulse and the 0:100 mirror pulse are the two most relevant applications of atomic Bragg diffraction (cf. Sec. 5.4). Irrespective of the pulse shape, a symmetrical beamsplitter pulse is defined by a pulse area of  $\theta_{\pi/2} = \pi/2$ , while a complete specular reflection in momentum space is achieved for  $\theta_{\pi} = \pi$ . This defines the nominal mirror and beamsplitter time

$$T_{\pi} = \frac{\pi}{|\Omega|}, \quad T_{\pi/2} = \frac{T_{\pi}}{2}. \quad (6.7)$$

In particular, the four pulse shapes yields mirror widths

$$\tau_{R\pi} = \frac{\pi}{2|\Omega|}, \quad \tau_{G\pi} = \frac{\sqrt{\pi}}{\sqrt{2}|\Omega|}, \quad \tau_{B\pi} = \frac{25}{21|\Omega|}, \quad \tau_{S\pi} = \frac{1}{|\Omega|}. \quad (6.8)$$

These are related to each other with the equal nominal mirror time  $T_{\pi} = T_{R\pi} = T_{G\pi} = T_{B\pi} = T_{S\pi} = \pi$ . Due to linearity, the beamsplitter width is just a half of the mirror width  $\tau_{\pi/2} = \tau_{\pi}/2$ .

## **6.2 DIFFRACTION WITH RECTANGULAR PULSES**

Constant interaction strengths within rectangular pulse shapes provide the advantage that with no spatial variations of the laser beams, simple analytical solutions can be given at least for some limits of interaction times and strengths.

### **6.2.1 Velocity selective Pendellösung**

In the deep-Bragg regime ( $\mathcal{N} = 1$ ) off-resonantly coupled diffraction orders are negligible. Thus, for first-order diffraction ( $N = 1$ ), the state vector in the beamsplitter manifold  $\{k_{\pm}\}$

$$k_{\pm} \equiv (\pm 1 + \kappa)k_L, \quad (6.9)$$

simplifies to the amplitude tuple  $\mathbf{g}_{\mp}(\tau) = (g_{-1}, g_{+1})$  and their equations of motion within the rectangular pulse window (6.3) follow from (5.62a)

$$i \dot{\mathbf{g}}_{\mp} = \mathcal{H}_{\mp} \mathbf{g}_{\mp}, \quad \mathcal{H}_{\mp} = \begin{pmatrix} 0 & \frac{\Omega}{2} \\ \frac{\Omega}{2} & \kappa \end{pmatrix}. \quad (6.10)$$

With the initial datum  $\mathbf{g}_{\mp}(\tau_i) = (1, 0)$  their well-known Pendellösung [165, 166]

$$g_{-1}(\tau) = e^{-i\varphi} \left( \cos \vartheta - \frac{\kappa}{i\Omega_{\kappa}} \sin \vartheta \right), \quad g_{+1}(\tau) = e^{-i\varphi} \frac{\Omega}{i\Omega_{\kappa}} \sin \vartheta, \quad (6.11)$$

depends on the angles  $\varphi = \kappa(\tau - \tau_i)/2$  and  $\vartheta = \Omega_{\kappa}(\tau - \tau_i)/2$  as well as the generalised two-photon Rabi-frequency  $\Omega_{\kappa} = \sqrt{\kappa^2 + \Omega^2}$ . With this solution the mirror pulse width (6.8) can be generalised for arbitrary  $\kappa \neq 0$ . The condition of utmost population transfer  $|g_{+1}(\tau_{\pi})|^2 = 1$  is obviously  $\vartheta = \pi/2$  and determines the mirror pulse width

$$\tau_{R\pi}(\kappa) = \frac{\pi}{2\Omega_{\kappa}}. \quad (6.12)$$

Thereby,  $\kappa = \kappa_L$  should be chosen as the central momentum component of the initial wavepacket. Choosing appropriate laser frequencies, this is optimally  $\kappa = 0$ . However, in general, on resonance ( $\kappa = 0$ ), the definition (6.8) is recaptured, leading to the diffraction efficiency  $\eta_{k',k}$  (5.29) after a mirror pulse with total pulse duration  $\Delta\tau_{R\pi} = 2\tau_{R\pi} = \pi/|\Omega|$

$$\eta_{+-}(\tau_{R\pi}) = |g_{+1}(\tau_{R\pi})|^2 = \frac{\Omega^2}{\Omega_{\kappa}^2} \sin^2 \vartheta_{\pi}, \quad \vartheta_{\pi} = \frac{\pi}{2} \frac{\Omega_{\kappa}}{\Omega}. \quad (6.13)$$

The index  $+-$  indicates abbreviatory the momentums  $k' = k_+$  and  $k = k_-$  (6.9). The relative phase of the transfer function (5.29) between the final  $k' = k_-$  and  $k' = k_+$  components is

$$\Delta\phi \equiv \phi_{--} - \phi_{+-} = \arctan\left(\frac{\kappa}{\Omega_{\kappa}} \tan \vartheta\right) - \frac{\pi}{2}. \quad (6.14)$$

For  $\vartheta = \vartheta_{\pi}$ , one obtains the phase shift after a mirror pulse  $\Delta\phi(\tau_{R\pi})$ .

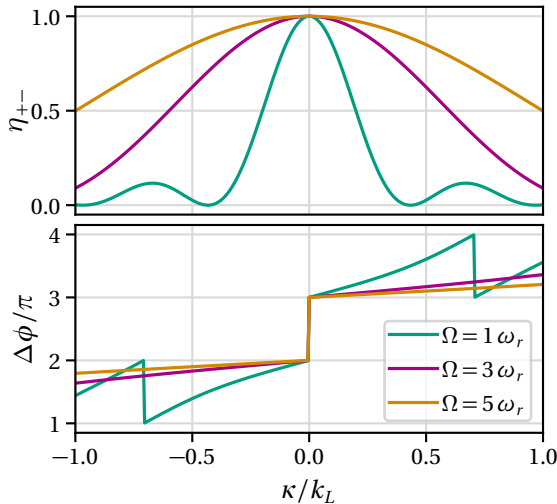


Figure 6.2: Velocity dispersion of the diffraction efficiency  $\eta_{+-}(\kappa)$  (top) and of the phase shift  $\Delta\phi(\kappa)$  (bottom) after a rectangular mirror pulse with total interaction time  $\Delta\tau_{R\pi} = 2\tau_{R\pi}(\Omega)$  (6.8), calculated for the deep-Bragg limit, for three Rabi frequencies  $\Omega = \Omega\omega_{2r}$ .

In Fig. 6.2 the diffraction efficiency  $\eta_{+-}$  (6.13) and the phase shift  $\Delta\phi$  (6.14) after a mirror pulse  $\tau = \tau_{R\pi}(\Omega)$  (6.8) is depicted depending on the detuning  $\kappa$  (5.5), demonstrating the velocity dispersion of the Bragg diffraction. As for the Pendellösung losses into higher diffraction orders are neglected, a perfect efficiency is reached on resonance ( $\kappa = 0$ ), while the phase shift shows a  $\pi$ -jump here, as well as on the side maxima of  $\eta_{+-}$ . The sinc-behaviour of the efficiency is the typical Fourier-response to rectangular pulse shapes. With increasing the two-photon Rabi frequency  $\Omega$  (5.43) the resonance is power broadened.

### 6.2.2 Losses into higher diffraction orders: Kato solution

In general, the transfer function  $\langle \mathbf{k}' | G(t, t_i) | \mathbf{k} \rangle$  (5.29) exhibits resonances at  $\mathbf{k}' = \mathbf{k} + 2N\mathbf{k}_L$ ,  $|N| \leq \mathcal{N}$ , which needs to be considered in the quasi-Bragg regime. Therefore, Eq. (5.59) is truncated at a sufficiently large  $\mathcal{N}$ . This initial value problem (5.62) is solved by diagonalisation.

On the one hand, resonances with  $N \neq 1$  lead to a population loss from the  $N = 1$  beam-splitter manifold  $\{k_{\pm}\}$  and reduce the diffraction efficiency. On the other hand, they diminish the coupling strength within the beamsplitter manifold. Consequently, this increases the optimal  $\pi$ -pulse time  $\tilde{\tau}_{\pi} > \tau_{\pi}$  of a Bragg mirror compared to the prediction of the Pendellösung (6.8). Gochnauer *et al.* [167] have demonstrated this effect experimentally for Gaussian pulses, proving that the effective coupling strength is given by the energy bandgap in the quasimomentum space. Hartmann *et al.* [168] also find an effective pulse area, considering double Raman diffraction.

#### *Effective $\pi$ -pulse time and degenerate perturbation theory*

The population loss into higher diffraction orders leads to an effectively reduced Rabi frequency. Therefore, to achieve furthermore a  $\pi$ -pulse longer interaction times are necessary.

#### KATO'S THEORY

To rectify the Pendellösung (6.11) with contributions from higher order diffraction, Kato's method is employed for the stationary eigenvalue problem in the presence of degeneracy [169–171]. On resonance, all eigenvalues of the diagonal part  $D_0 = D(\kappa = 0)$  of the Bragg-Hamilton operator (5.62a) are doubly degenerated  $1 \leq \alpha \leq 2$ . Therefore, the flow of the eigensystem  $\mathcal{H}(\lambda)\mathbf{v}_{i,\alpha}(\lambda) = \omega_{i,\alpha}(\lambda)\mathbf{v}_{i,\alpha}(\lambda)$  is considered in the degenerate subspace  $\mathcal{E}_i$  with splitting the frequency shifted Hamiltonian  $\mathcal{H}$  (5.62a) in

$$\mathcal{H} = D_0 + \lambda\mathcal{V}, \quad \mathcal{V} = D(\kappa) - D_0 + L + L^\dagger, \quad 0 \leq \lambda \leq 1. \quad (6.15)$$

Denoting the orthonormal eigenvectors of  $D_0$  with  $\mathbf{v}_{i,\alpha}^{(0)}$  and their eigenvalues with  $\omega_{i,\alpha}^{(0)}$ , then the eigenvectors of the interacting Hamilton operator  $\mathcal{H}_i(\lambda)$  restricted to the subspace  $\mathcal{E}_i$ , are  $\mathbf{v}_{i,\alpha}(\lambda) = P_i(\lambda)\mathbf{v}_{i,\alpha}^{(0)}$ . Now, all efforts are put in the perturbative evaluation of the projection operator  $P_i(\lambda)$ , which evolves from the unperturbed projection  $P_i^{(0)}$ . This results in the generalised eigenvalue problem

$$\mathcal{H}_i\mathbf{v}_{i,\alpha}^{(0)} = \omega_{i,\alpha}K_i\mathbf{v}_{i,\alpha}^{(0)}, \quad (6.16)$$

$$\mathcal{H}_i = P_i^{(0)}\mathcal{H}P_i^{(0)}, \quad K_i = P_i^{(0)}P_iP_i^{(0)}, \quad (6.17)$$

with power series expressions for the projection operators

$$P_i(\lambda) = P_i^{(0)} + \sum_{n=1}^{\infty} \lambda^n A_i^{(n)}, \quad A_i^{(n)} = - \sum_{(n)} S_i^{(k_1)} \mathcal{V} S_i^{(k_2)} \mathcal{V} \dots \mathcal{V} S_i^{(k_{n+1})}. \quad (6.18)$$

Here,  $\sum_{(n)}$  is a sum over all combinations of  $k_i \in \mathbb{N}_0$  satisfying  $k_1 + k_2 + \dots + k_{n+1} = n$  and

$$S_i^{(0)} = -P_i^{(0)}, \quad S_i^{(k>0)} = (S_i)^k, \quad S_i = \frac{\mathbb{1} - P_i^{(0)}}{\omega_i^{(0)}\mathbb{1} - D_0}. \quad (6.19)$$

The eigenvalues and eigenvectors of  $\mathcal{H}$  are the eigenvalues and -vectors of

$$\mathcal{H}P_i(\lambda) = \omega_i^{(0)}P_i(\lambda) + \sum_{n=1}^{\infty} \lambda^n B_i^{(n)}, \quad B_i^{(n)} = \sum_{(n-1)} S_i^{(k_1)} \mathcal{V} S_i^{(k_2)} \mathcal{V} \dots \mathcal{V} S_i^{(k_{n+1})}, \quad (6.20)$$

in the subspace  $i$  with projection  $P_i$ . Equally, the eigenvalues are given by the roots of  $\det[\mathcal{H}_i - \omega_i K_i] = 0$ , respectively by the eigenvalues of  $\tilde{\mathcal{H}}_i = K_i^{-1} \mathcal{H}_i$ .

It is straight forward to evaluate  $\mathcal{H}_i$  and  $K_i$  from (6.17) for the ground-state manifold  $i = 1$  to order  $\mathcal{O}(\lambda^n)$ . A third order truncation of the series

$$\begin{aligned} \mathcal{H}_1 &= \begin{pmatrix} 0 & \frac{\Omega}{2} \\ \frac{\Omega}{2} & \kappa \end{pmatrix} - 2\mathcal{I} \begin{pmatrix} 1 & 0 \\ 0 & 1 \end{pmatrix} - \mathcal{I} \begin{pmatrix} \kappa & \Omega \\ \Omega & 0 \end{pmatrix} + \mathcal{O}(\lambda^4), \\ K_1 &= (1 - \mathcal{I}) \begin{pmatrix} 1 & 0 \\ 0 & 1 \end{pmatrix} - \mathcal{I} \begin{pmatrix} \kappa & \frac{\Omega}{2} \\ \frac{\Omega}{2} & -\kappa \end{pmatrix} + \mathcal{O}(\lambda^4), \end{aligned} \quad \mathcal{I} = \frac{\Omega^2}{16}, \quad (6.21)$$

agrees very well with the numerical results. The roots of the characteristic equation  $|\mathcal{H}_1 - (\omega_1 - \omega_1^{(0)})K_1| = 0$ , determine the corrected eigenfrequencies of the Pendelösung. As the frequency shifts  $\omega_1(\lambda) - \omega_1^{(0)}$ , are already  $\mathcal{O}(\lambda)$ , it is consistent to use a lower approximation for  $K_1$ , which leads to better results at the specified order. In particular, here  $\tilde{\mathcal{H}}_1 = K_1^{-1} \mathcal{H}_1$  are evaluated and Taylor expanded to the specified order

$$\tilde{\mathcal{H}}_1 = \lim_{\lambda \rightarrow 1} \begin{pmatrix} -\mathcal{I}\lambda^2(2 + \kappa\lambda) & \frac{\Omega}{2}\lambda(1 - \mathcal{I}\lambda^2) \\ \frac{\Omega}{2}\lambda(1 - \mathcal{I}\lambda^2) & \kappa\lambda - \mathcal{I}\lambda^2(2 - \kappa\lambda) \end{pmatrix} + \mathcal{O}(\lambda^4) = \begin{pmatrix} -\mathcal{I}(2 + \kappa) & \frac{\Omega}{2}(1 - \mathcal{I}) \\ \frac{\Omega}{2}(1 - \mathcal{I}) & \kappa - \mathcal{I}(2 - \kappa) \end{pmatrix} + \mathcal{O}(\lambda^4). \quad (6.22)$$

This leads to the succinct expression for the eigenvalues and -vectors

$$\omega_{1,\pm} = \frac{\kappa}{2} - 2\mathcal{I} \pm \frac{\tilde{\Omega}}{2}, \quad \mathbf{v}_{1,\pm}^{(0)} = \begin{pmatrix} 2(\mathcal{I} - 1)\sqrt{\mathcal{I}} \\ -\frac{1}{2}\kappa(1 + 2\mathcal{I}) \pm \tilde{\Omega} \end{pmatrix}, \quad (6.23)$$

in terms of a corrected Rabi frequency  $\tilde{\Omega} = \sqrt{\kappa^2(1 + 2\mathcal{I})^2 + \Omega^2(1 - \mathcal{I})^2}$ . For this correction an expansion at least up to the order  $\lambda^3$  in this  $i = 1$  subspace is necessary, for lower expansion orders  $\tilde{\Omega} = \Omega_\kappa$  is recovered. Remarkably, Kato's first order perturbation theory coincides with the Pendellösung (6.11).

Analogous to the subspace  $i = 1$ , the eigenvalues of the next subspace, coupling  $\mu = \pm 3$  can be calculated. This subspace represents the most important loss channel, because higher diffraction orders are even less populated. Therefore, to handle the quasi-Bragg regime perturbatively, it is sufficient to consider only the two subspaces  $\mu = \pm 1$  and  $\mu = \pm 3$ . In this way, the eigenvalues of  $\mathcal{H}$  are given by  $\{\omega_{1,\pm}, \omega_{3,\pm}\}$ . The latter can be calculated from  $\tilde{\mathcal{H}}_3 = K_3^{-1} \mathcal{H}_3$

$$\tilde{\mathcal{H}}_3 = \begin{pmatrix} 2(1 + \mathcal{I}) - \kappa & 0 \\ 0 & 2(1 + \mathcal{I}) + 2\kappa \end{pmatrix} + \mathcal{O}(\lambda^3), \quad (6.24)$$

skipping the  $\lambda^3$  terms, which overestimate the losses into  $\mu = \pm 3$ . Including higher expansion orders would correct this, but the lower expansion, with its simple result (6.24), is already sufficient. The eigenvalues and -vectors of  $\tilde{\mathcal{H}}_3$  are

$$\omega_{3,\pm} = 2(1 + \mathcal{I}) + \frac{\kappa}{2} \pm \frac{3\kappa}{2}, \quad (\mathbf{v}_{3,+}^{(0)}, \mathbf{v}_{3,-}^{(0)}) = \mathbb{1}_2. \quad (6.25)$$

The eigenvectors  $\mathbf{v}_{i,j} = P_i \mathbf{v}_{i,j}^{(0)}$  are defined by the projections (6.18), which are also expanded up to  $\lambda^3$  for  $\mu = \pm 1$  and  $\lambda^2$  for  $\mu = \pm 3$ ,

$$P_1 = \begin{pmatrix} (1+\kappa)\mathcal{I} & p_{1+} & -(1+\frac{3}{2}\kappa)\mathcal{I} & 2\mathcal{I}^{3/2} \\ p_{1+} & 1-(1+\kappa)\mathcal{I} & -2\mathcal{I}^{3/2} & -(1-\frac{3}{2}\kappa)\mathcal{I} \\ -(1+\frac{3}{2}\kappa)\mathcal{I} & -2\mathcal{I}^{3/2} & 1-(1-\kappa)\mathcal{I} & p_{1-} \\ 2\mathcal{I}^{3/2} & -(1-\frac{3}{2}\kappa)\mathcal{I} & p_{1-} & (1-\kappa)\mathcal{I} \end{pmatrix}, \quad P_3 = \begin{pmatrix} 1-\mathcal{I} & p_{3+} & \mathcal{I} & 0 \\ p_{3+} & \mathcal{I} & 0 & \mathcal{I} \\ \mathcal{I} & 0 & \mathcal{I} & p_{3-} \\ 0 & \mathcal{I} & p_{3-} & 1-\mathcal{I} \end{pmatrix}, \quad (6.26)$$

with  $p_{1\pm} = (\mathcal{I} - 1 - \frac{\kappa(2\pm\kappa)}{4})\sqrt{\mathcal{I}}$  and  $p_{3\pm} = \frac{1}{2}(2\pm\kappa)\sqrt{\mathcal{I}}$ . Then the solution of the Schrödinger equation with the Kato Hamiltonian (6.15) results in

$$\mathbf{g}^K(\tau) = \frac{\tilde{\mathbf{g}}^K(\tau)}{|\tilde{\mathbf{g}}^K(\tau)|}, \quad \tilde{\mathbf{g}}^K(\tau) = \sum_{i=\{1,3\}} \sum_{j=\{+,-\}} c_{i,j} e^{-i\omega_{i,j}(\tau-\tau_i)} \mathbf{v}_{i,j}, \quad (6.27)$$

where the eigenvectors  $\mathbf{v}_{i,j}$  are normalised and the integration constants  $c_{i,j}$  are defined by the initial condition  $\tilde{\mathbf{g}}^K(\tau_i) = (0, 1, 0, 0)$ , with  $\tilde{\mathbf{g}}^K(\tau_i) = (\tilde{g}_{-3}^K, \tilde{g}_{-1}^K, \tilde{g}_{+1}^K, \tilde{g}_{+3}^K)$ . The exact expressions are uninspiring, but their calculation is given in Appendix D.1.

The population of the  $\mu = 1$  state is of special interest, because it defines the diffraction efficiency  $\eta_{+-}$ . On resonance ( $\kappa = 0$ ), already  $\tilde{\mathbf{g}}^K(\tau)$  is approximately normalised. Therefore, the on-resonance diffraction efficiency  $\eta_r$  can be approximated to

$$\eta_r^K(\tau) \approx |\tilde{g}_{+1}^K(\tau)|^2 = a \left( 1 + \ell \cos[4\tau'(\mathcal{I}-1)\sqrt{\mathcal{I}}] + c \cos[2\tau'(1+\sqrt{\mathcal{I}}+2\mathcal{I}-\mathcal{I}^{3/2})] \right. \\ \left. + d \cos[2\tau'(1-\sqrt{\mathcal{I}}+2\mathcal{I}-\mathcal{I}^{3/2})] \right), \quad (6.28)$$

with  $\tau' = \tau - \tau_i$  and coefficients, expanded up to the suited order  $\mathcal{O}(\mathcal{I}^2)$

$$a = \frac{1}{2} - \mathcal{I} - \frac{\mathcal{I}^2}{2} + \mathcal{O}(\mathcal{I}^3), \quad \ell = -1 + \mathcal{O}(\mathcal{I}^3), \quad c = -d = -4\mathcal{I}^{3/2} + \mathcal{O}(\mathcal{I}^{5/2}). \quad (6.29)$$

#### EFFECTIVE $\pi$ -PULSE TIME

From the third order perturbation calculation  $\mathcal{O}(\Omega_\kappa^4)$  the renormalised Rabi frequency

$$\tilde{\Omega} = \sqrt{\kappa^2(1+2\mathcal{I})^2 + \Omega^2(1-\mathcal{I})^2} \xrightarrow{\mathcal{I} \ll 1} \Omega_\kappa, \quad (6.30)$$

within the beamsplitter manifold, is derived in Eq. (6.23), using the abbreviation  $\mathcal{I} = \Omega^2/16$ . For weak dressing  $\mathcal{I} \ll 1$ , it reduces to the generalised Rabi frequency of the Pendellösung. With the effective Rabi frequency  $\tilde{\Omega}$  and Eq. (6.8), one can evaluate the  $\pi$ -pulse time stretching factor

$$\zeta_\pi^\kappa = \frac{\tilde{\tau}_{R\pi}}{\tau_{R\pi}} = \frac{\Omega_\kappa}{\tilde{\Omega}}, \quad \zeta_\pi \equiv \zeta_\pi^{\kappa=0} = \frac{1}{1-\mathcal{I}} (\approx 1 + \mathcal{I}). \quad (6.31)$$

Figure 6.3 depicts a contour plot of the fidelity  $F(\mathcal{I}, \zeta)$  (5.34) as well as of the normalised diffraction efficiency  $\bar{\eta}(\mathcal{I}, \zeta)$  (5.32) for a Bragg-mirror pulse versus the bare two-photon intensity  $\mathcal{I}$  and the inverse pulse stretching factor  $\zeta^{-1} = \tau_{j\pi}/\tau_j$ ,  $j \in \{G, B, S, R\}$ . This representation uncovers the linear relation (6.31). The numerical calculation considers four off-resonant diffraction orders ( $\mathcal{N} = 5$ ). As initial condition 1D Gaussian wavepackets (2.54) are considered, which are centred at  $k_0 = -k_L$  with momentum width  $\sigma_k$  and localised in the centre of the laser beams  $x_0 = 0$ . Here, in the plane-wave approximation, the results are independent of the expansion size. This size  $\sigma_x = (2\sigma_k)^{-1}$  follows from the Heisenberg uncertainty. Clearly, the  $\pi$ -pulse stretching factor  $\zeta_\pi$  (6.31) traverses the optimal fidelity and efficiency regions for



all pulse shapes and momentum widths, as a universal rule, motivating the effective  $\pi$ -pulse widths

$$\tilde{\tau}_{j\pi} = \zeta_\pi \tau_{j\pi}, \quad j \in \{G, B, S, R\}, \quad (6.32)$$

with  $\tau_{j\pi}$  from Eq. (6.8).

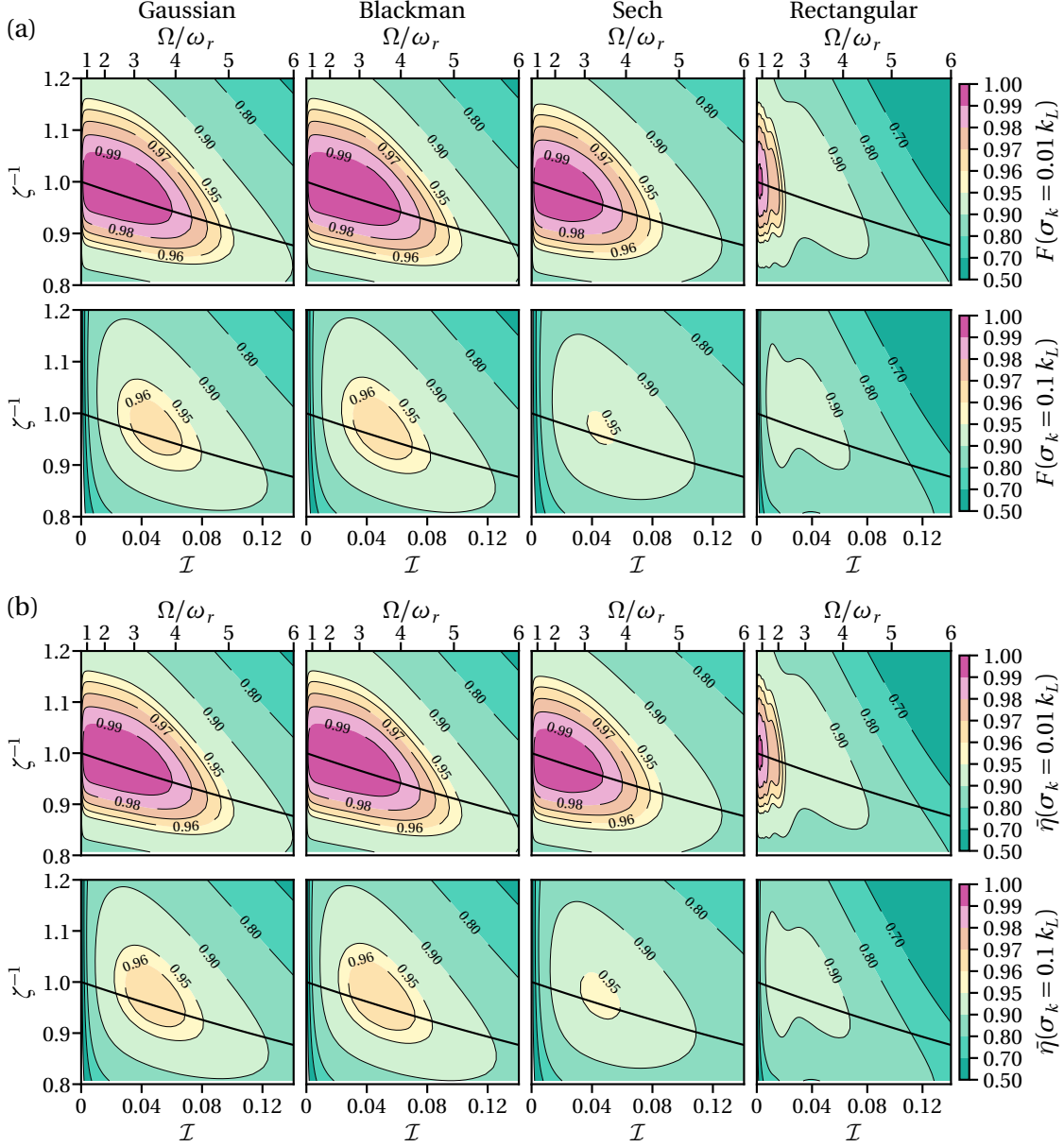


Figure 6.3: (a) Fidelity  $F$  (5.34) and (b) diffraction efficiency  $\tilde{\eta}$  (5.32) versus two-photon intensity  $\mathcal{I} = \Omega^2/16$ , respectively two-photon Rabi frequency  $\Omega = \Omega\omega_{2r}$ , and inverse  $\pi$ -pulse stretching factor  $\zeta_\pi^{-1} = \tau_{j\pi}/\tau_j$ ,  $j \in \{G, B, S, R\}$ , in columns for Gaussian, Blackman, sech and rectangular pulses. The initial state is a 1D Gaussian wavepacket (2.54), initially centered at  $(x, k_x) = (0, -k_L)$  with momentum width  $\sigma_k = 0.01 k_L$  (top rows),  $\sigma_k = 0.1 k_L$  (bottom rows). The optimal stretching factor  $\zeta_\pi$  (6.31) (solid line) traverses the regions of maximal fidelity and efficiency. For the numerical (1+1)D integration (5.26) with pulse widths  $\zeta\tau_{j\pi}$ , and total pulse length  $\Delta\tau_j = 8\zeta\tau_G$ , typical laser and atom parameters, used in experiments of Tables A.1 and A.2, are applied.

As expected, for the extremely small momentum width  $\sigma_k = 0.01 k_L$  the atomic initial state is approximately a plane wave, why the fidelity and the diffraction efficiency show no significant difference (cf. Sec. 5.4). In contrast, for finite  $\sigma_k = 0.1 k_L$  the areas of maximum diffraction efficiency are slightly larger than the areas of maximum fidelity.

#### EFFECTIVE $\pi$ -PULSE EFFICIENCY

In Fig. 6.4 the velocity dispersion of the response of an atomic mirror is visualised for typical parameters used in experiments (cf. Tables A.1, A.2). The results of the numerical solution (5.26), considering losses into four off-resonant diffraction orders ( $\mathcal{N}=5$ ), are compared to the perturbative Kato solution (6.27), considering the losses into the most important loss channels ( $\mathcal{N}=2$ ) and the Pendellösung (6.11), neglecting all losses ( $\mathcal{N}=1$ ). Please note that the numerical results are identical to the solution of the initial value problem (5.62a). A mirror pulse is applied of width  $\tilde{\tau}_{R\pi}(\Omega)$  (6.32) for the numerical as well as the Kato solution and  $\tau_{R\pi}(\Omega)$  (6.8) for the Pendellösung for different two-photon Rabi frequencies  $\Omega = \Omega \omega_{2r}$ .

The diffraction efficiency  $\eta_{k'k}$  reveals the velocity selectivity of the Bragg condition [cf. Fig. 6.4 (a)] and the population loss into higher diffraction orders [cf. Fig. 6.4 (c) and (d)]. For a weak coupling  $\Omega = 1 \omega_r$ , the diffraction efficiency exhibits still the sinc-behaviour of the Pendellösung. Equally, increasing  $\Omega$ , the response is power broadened, but now in conjunction with a reduced efficiency. Therefore, in the quasi-Bragg regime the Pendellösung is not suitable. In contrast, the Kato solution provides reliable predictions. For large Rabi frequencies, only at the

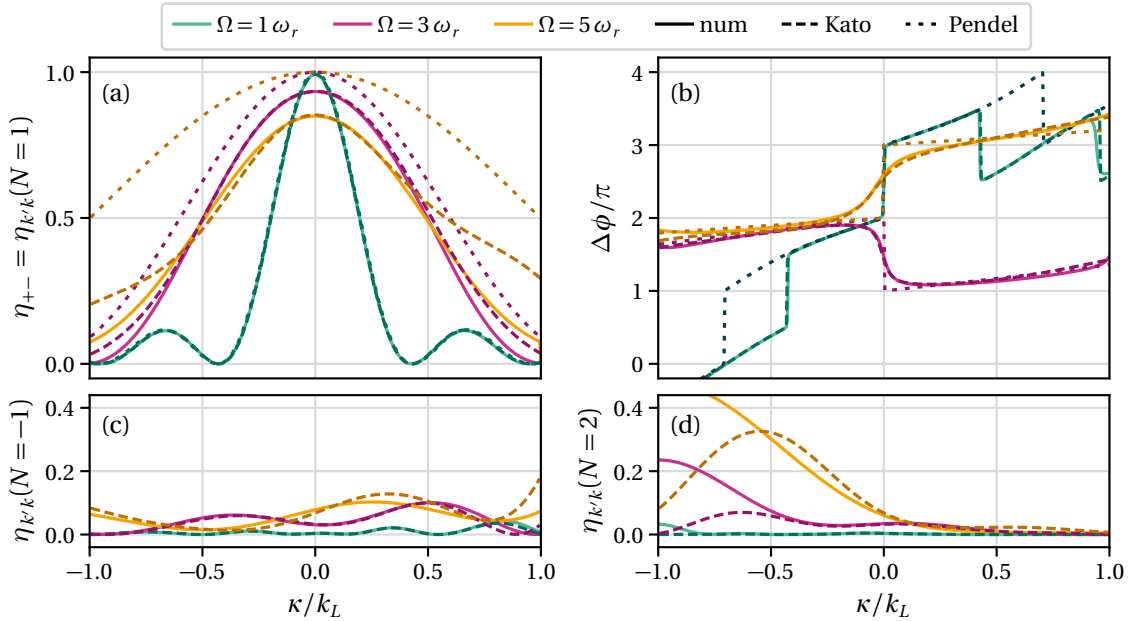


Figure 6.4: Velocity dispersion after a rectangular mirror pulse of (a) the diffraction efficiency  $\eta_{+-}(\kappa)$  in the beamsplitter manifold  $N=1$ , (b) the relative phase shift  $\Delta\phi(\kappa)$  (6.14) and losses into higher diffraction orders for (c)  $N=-1$  and (d)  $N=2$ , with  $k = (-1 + \kappa)k_L$  and  $k' = k + 2Nk_L$ . The numerical solution (solid) considers four off-resonant diffraction orders ( $\mathcal{N}=5$ ), the Kato approximation (6.27) (dashed) the next off-resonant diffraction order ( $\mathcal{N}=2$ ) and the Pendellösung (6.13), (6.14) the closed system of the resonant order ( $\mathcal{N}=1$ ). For the numerical as well as for the Kato solution the applied pulse width is  $\tilde{\tau}_{\pi R}(\Omega)$  (6.32) and for the Pendellösung (dotted)  $\tau_{\pi R}(\Omega)$  (6.8). Different two-photon Rabi frequencies  $\Omega = \Omega \omega_{2r}$  are compared, defining these  $\pi$ -pulse widths.

band edges  $\kappa \rightarrow \pm 1$  the Kato solution shows deviations, especially for  $N=2$ , but the efficiency around the resonance  $\kappa = 0$  can be approximated further.

The phase difference  $\Delta\phi$  (6.14) [cf. Fig. 6.4 (b)] shows a smoothed  $\pi$ -jump at the resonance and in contrast to the Pendellösung at the minima. Again, the Kato solution (6.27) describes the beamsplitter response very well. Even at the band edges the deviations to the numerical results are extremely small for the phase shift.

In addition, the accuracy of the Kato solution especially at resonance is demonstrated in Fig. 6.5. Here, the diffraction efficiency on resonance  $\eta_r = \eta_{+-}(\kappa = 0)$  and the full width half maximum of the diffraction efficiency in the beamsplitter manifold  $\Delta\eta_{+-}$  depending on the two photon Rabi frequency is depicted. The Kato approximation (6.27) is gauged by the numerical solution (5.26). For an ideal mirror  $\eta_r = 1$  and  $\Delta\eta_{+-} \rightarrow \infty$  are desirable, but impossible. Different pulse widths are compared to study the optimal interaction time. In particular, the approximation  $\tau_{R\pi}$  (6.8) for strict first-order diffraction of the Pendellösung in the deep-Bragg regime

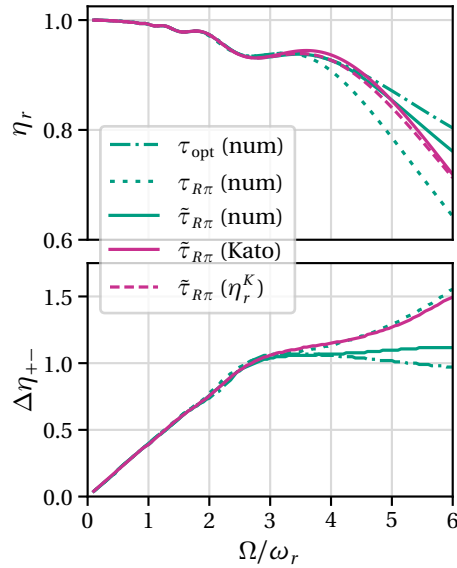


Figure 6.5: (Top) Resonant transfer efficiency  $\eta_r$  and (bottom) efficiency width  $\Delta\eta_{+-}$  versus two-photon Rabi frequency  $\Omega = \Omega\omega_{2r}$  after a  $\pi$ -pulse. Different pulse widths  $\tau(\Omega)$  are compared.

and  $\tilde{\tau}_{R\pi}$  (6.32) for the quasi-Bragg regime, considering higher diffraction orders, are compared to the optimal interaction time. This time is defined by the maximum numerical transfer efficiency at resonance  $\kappa = 0$ <sup>1</sup>. With increasing  $\Omega$ , in a regime where the losses into higher diffraction orders are important, the approximation  $\tau_{R\pi}$  is less accurate, while  $\tilde{\tau}_{R\pi}$  can be used further. Please note that for the maximised transfer efficiency the velocity acceptance  $\Delta\eta_{+-}$  is reduced, while for  $\tilde{\tau}_{R\pi}$  it remains larger, for increasing  $\Omega$ . The results of the Kato solution (6.27) show the applicability of the on-resonance diffraction efficiency. Due to the deviations for large detunings  $\kappa$ , the width is overestimated for large Rabi frequencies. In addition, from the full Kato solution a simple analytic form for the diffraction efficiency on resonance (6.28), for the effective  $\pi$ -pulse time  $\tilde{\tau}_{R\pi} = \pi/[2|\Omega|(1-\mathcal{I})]$  (6.32) can be derived to

$$\eta_r^K(\tilde{\tau}_{R\pi}) = (1 - 2\mathcal{I}) \left[ 1 + |\Omega|\mathcal{I} \sin\left(\frac{2\pi}{|\Omega|} \frac{1 + 2\mathcal{I}}{1 - \mathcal{I}}\right) \right], \quad (6.33)$$

which is also depicted in Fig. 6.5. It predicts losses into higher diffraction orders within the convergence radius  $\Omega = \Omega\omega_{2r} < 4\omega_r$  ( $\mathcal{I} < 0.0625$ ), very well. Beyond this point, it remains positive up to  $\Omega = 8\sqrt{2}\omega_r$  ( $\mathcal{I} = 0.5$ ).

### 6.3 DIFFRACTION WITH HYPERBOLIC SECANT PULSES

The shape of hyperbolic secant pulses is very similar to that of the smooth pulse shapes of Gaussian envelopes, but in contrast to these, they are amenable for closed analytical solutions of second order differential equations, using the Demkov-Kunike (DK) model [162–164].

<sup>1</sup> It is calculated with a basin-hopping algorithm [172–175].

### 6.3.1 Velocity selective Demkov-Kunike Pendellösung

For hyperbolic secant envelopes  $\Omega(\tau) = \Omega f_S(\tau)$  (6.6), an analytical solution for first order Bragg diffraction ( $\mu = \pm 1$ ) can be obtained. The system of two first-order differential equations

$$i \dot{\mathbf{g}}(\tau) = \begin{pmatrix} 0 & \frac{\Omega(\tau)}{2} \\ \frac{\Omega(\tau)}{2} & \kappa \end{pmatrix} \mathbf{g}(\tau), \quad \mathbf{g} = (g_{-1}, g_{+1}) \quad (6.34)$$

can be decoupled due to the adopted corotating frame (5.61). Using

$$g_{+1} = \frac{2i}{\Omega(\tau)} \dot{g}_{-1}, \quad (6.35)$$

leads to Hill's second order differential equation [151]

$$0 = \ddot{g}_{-1} - \left( \frac{\dot{\Omega}(\tau)}{\Omega(\tau)} - i\kappa \right) \dot{g}_{-1} + \frac{\Omega(\tau)^2}{4} g_{-1}. \quad (6.36)$$

With the nonlinear map

$$z(\tau) = \frac{1}{2} \left( 1 + \tanh \frac{\tau}{\tau_S} \right), \quad (6.37)$$

the differential equation for  $\gamma(z) \equiv g_{-1}(\tau)$  emerges as

$$0 = z(1-z)\gamma'' + [c - z(1+a+b)]\gamma' - ab\gamma, \quad (6.38)$$

with the coefficients  $a = \Omega\tau_S/2$ ,  $b = -a$  and  $c = (1 + i\kappa\tau_S)/2$ . This represents the hypergeometric differential equation with hypergeometrical Gauss solutions  $f_1 = {}_2F_1(a, b; c; z)$ ,  $f_2 = z^{1-c} {}_2F_1(1+a-c, 1+b-c; 2-c; z)$  and Wronski determinant  $w = (1-z)^{c-1} z^{-c}$  [151]. Straightforward analysis leads to the Demkov-Kunike (DK) solution with the unitary propagator  $G_{\mp}(\tau, \tau_i)$

$$\mathbf{g}_{\mp}(\tau) = G_{\mp}(\tau, \tau_i) \mathbf{g}_{\mp}(\tau_i), \quad G_{\mp}(\tau_i, \tau_i) = \mathbb{1}. \quad (6.39)$$

The two-dimensional Green's function  $G_{\mp}$  (5.27) of the DK-model can be expressed completely for  $\Omega$ ,  $\kappa \neq 0$  with the hypergeometric basis functions  $f_1$  and  $f_2$

$$G_{\mp}(\tau, \tau_i) = M(z)S(z)S^{-1}(z_i)M^{-1}(z_i), \quad M = \begin{pmatrix} 1 & 0 \\ 0 & \frac{i}{a} \sqrt{z(1-z)} \end{pmatrix}, \quad S = \begin{pmatrix} f_1 & f_2 \\ f_1' & f_2' \end{pmatrix}. \quad (6.40)$$

For the initial datum  $\mathbf{g}_{\mp}(\tau_i) = (1, 0)$ , one obtains

$$g_{-1}(\tau) = \frac{f_1(\tau)f_2'(\tau_i) - f_2(\tau)f_1'(\tau_i)}{w(\tau_i)}. \quad (6.41)$$

The total pulse duration  $\Delta\tau$  in the experiment is sufficiently large  $\Delta\tau \gg \tau_S$ . Therefore, one can expand to a pulse beginning in the remote past  $\tau_i \rightarrow -\infty$ , leading to

$$g_{-1}(\tau) = {}_2F_1(a, -a; c; z), \quad (6.42a)$$

$$g_{+1}(\tau) = \frac{a}{i\kappa} \sqrt{z(1-z)} {}_2F_1(1-a, 1+a; 1+c; z). \quad (6.42b)$$

The diffraction efficiency reads

$$\eta_{+-}^{DK}(\tau, \kappa) = |g_{+1}(\tau)|^2 = 1 - |g_{-1}(\tau)|^2. \quad (6.43)$$

Further, for very long pulse durations  $\tau_S \ll \tau_f, |\tau_i|$ , the diffraction efficiency simplifies to

$$\eta_{+-}^{DK}(\kappa, \Omega, T) = \text{sech}^2\left(\frac{\kappa T}{2}\right) \sin^2\left(\frac{\Omega T}{2}\right), \quad (6.44)$$

with the nominal time  $T = \pi\tau_S$  (6.2).

In the important case of exact resonance  $\kappa = 0$ , the unitary propagator simplifies to

$$G_{\mp}(\tau, \tau_i) = \begin{pmatrix} \cos \Delta\varphi & -i \sin \Delta\varphi \\ -i \sin \Delta\varphi & \cos \Delta\varphi \end{pmatrix}, \quad \begin{aligned} \Delta\varphi &= \varphi(z) - \varphi(z_i), \\ \varphi(z) &= \Omega\tau_S \arcsin \sqrt{z}. \end{aligned} \quad (6.45)$$

In order to achieve full diffraction efficiency on resonance  $\eta_r^{DK} = \eta_{+-}^{DK}(\kappa = 0) = 1$ , regarding the efficiency for unlimited pulse duration (6.44) one should choose the  $\pi$ -pulse width as  $\tau_{S\pi} = |\Omega|^{-1}$ . This is in agreement with the pulse area (6.8). Waiting indefinitely long is hardly ever an option [176]. Therefore, the finite time approximation for the  $\pi$ -pulse width

$$\eta_r^{DK}(\tau; \tau_S = \tau_{S\pi}) \approx z = \frac{1 + \tanh \Omega\tau}{2} \quad (6.46)$$

reveals the exponential convergence past several  $\pi$ -pulse times  $\tau \gg \tau_S$ . Please note that the approximation (6.46) requires additionally  $\Omega = \Omega\omega_{2r} < 3\omega_r$ .

Obviously, for the  $\pi$ -pulse width, the diffraction efficiency on resonance reaches always its maximum, independent of the Rabi frequency, as shown in Fig. 6.6. Here, the diffraction efficiency  $\eta_{+-}^{DK}$  (6.43) and the phase shift  $\Delta\phi$  between  $g_{-1}$  and  $g_{+1}$  are depicted, depending on the detuning  $\kappa$ , after a mirror pulse of width  $\tau = \tau_{S\pi}$  (6.8). The limit of an infinite pulse duration  $\eta_{+-}^{DK}(T)$  (6.44) describes the sech-behaviour of the efficiency perfectly. Therefore, in contrast to rectangular pulses, the diffraction efficiency is smoothed, showing no side maxima. The  $\pi$ -jump of the phase shift on resonance is also a bit smoothed in comparison to the rectangular Pendellösung (cf. Fig. 6.2).

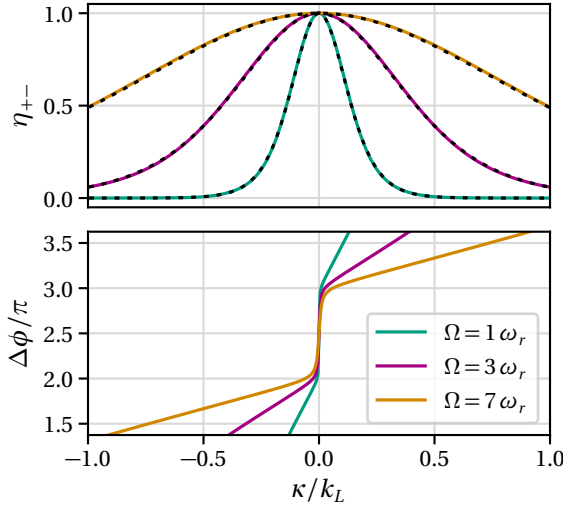


Figure 6.6: (Top) Velocity dispersion of the diffraction efficiency  $\eta_{+-}(\kappa)$  and (bottom) of the phase shift  $\Delta\phi(\kappa)$  after a sech-mirror pulse, calculated for the deep-Bragg limit, for three Rabi frequencies  $\Omega = \Omega\omega_{2r}$ . The efficiency for an infinite pulse  $\eta_{+-}^{DK}(T)$  (6.44) (dotted) fits the results with finite interaction time (6.43)  $\Delta\tau_{S\pi} = 8\tau_{G\pi}$  (solid).

### 6.3.2 Losses into higher diffraction orders: extended DK-model

Losses into higher diffraction orders can be taken into account with a time-dependent perturbation theory. Therefore, the Hamilton operator (5.62a) is split into

$$i\dot{\mathbf{g}} = \mathcal{H}(\tau)\mathbf{g}, \quad \mathcal{H}(\tau) = \mathcal{H}_0(\tau) + \mathcal{H}_1(\tau). \quad (6.47)$$

The free evolution  $\mathcal{H}_0(\tau)$  consists of a direct sum

$$\mathcal{H}_0(\tau) = \bigoplus_{\substack{\mu=-\mathcal{N}+1 \\ \mu \neq 0,1}}^{\mathcal{N}} \omega_{2\mu-1} \bigoplus \mathcal{H}_{\mp}(\tau) \quad (6.48)$$

of the DK-generator  $\mathcal{H}_\mp(\tau)$  (6.34) in the beamsplitter manifold and the unperturbed energies  $\omega_\mu = \frac{1}{4}(\mu + \kappa)^2 - \frac{1}{4}(1 - \kappa)^2$  (5.62b) in the higher momentum states. The perturbation  $\mathcal{H}_1(\tau)$  is simply the complement of the complete Hamilton operator.

Regarding the time-evolution, the definitions of the retarded Green's functions (5.27) hold equally for the free evolution  $G_0(\tau, \tau_i)$  by substituting  $\mathcal{H} \rightarrow \mathcal{H}_0$ . This leads to the Dyson-Schwinger integral equation

$$G(\tau, \tau_i) = G_0 - i \int_{-\infty}^{\infty} d\tau' G_0(\tau, \tau') \mathcal{H}_1(\tau') G(\tau', \tau_i), \quad (6.49)$$

which is central to time-dependent perturbation theory. Here, the free retarded propagator is defined for  $\tau \geq \tau_i$  as

$$G_0(\tau, \tau_i) = \bigoplus_{\substack{\mu = -\mathcal{N}+1 \\ \mu \neq 0,1}}^{\mathcal{N}} e^{-i\omega_{2\mu-1}(\tau-\tau_i)} \bigoplus G_\mp(\tau, \tau_i) \quad (6.50)$$

and vanishes elsewhere. It involves the DK-Pendellösung  $G_\mp$  (6.40) and the free time evolution of off-resonant momentum states. The complete solution

$$\mathbf{g}(\tau) = G(\tau, \tau_i) \mathbf{g}(\tau_i) \quad (6.51)$$

follows from the solution  $G(\tau, \tau_i)$  of the integral equation (6.49). A second order approximation couples to the  $\pm 3k_L, \pm 5k_L$  momentum states and shifts the frequencies of the beamsplitter manifold

$$\begin{aligned} G(\tau, \tau_i) = G_0 - i \int_{-\infty}^{\infty} d\tau' G_0(\tau, \tau') \mathcal{H}_1(\tau') G_0(\tau', \tau_i) \\ - \int_{-\infty}^{\infty} d\tau' d\tau'' G_0(\tau, \tau') \mathcal{H}_1(\tau') G_0(\tau', \tau'') \mathcal{H}_1(\tau'') G_0(\tau'', \tau_i). \end{aligned} \quad (6.52)$$

The second term of  $G$  leads to population of the off-resonantly coupled orders  $g_{\pm 3}$ . This is required to observe the stretching of the  $\pi$ -pulse time. The third term adjusts  $g_{\pm 1}$  such that mainly population remains in  $g_{-1}$  especially for off-resonant detunings  $\kappa \neq 0$ , what is essential to approximate the velocity dispersion. In addition, the third term leads to very little populations of the  $\mu = \pm 5$  diffraction order. An explicit analytical approximation for the propagator (6.52) can be obtained. It is derived in Appendix D.2, considering the most important loss channels  $\mu = \pm 3$  as for the perturbative Kato solution for rectangular pulses. It is numerically efficient and useful for the interpretation, but remains unwieldy for display.

In Fig. 6.7, the simple DK-Pendellösung (6.42) and the extended DK-model (6.51) after a  $\pi$ -pulse are compared with the corresponding numerical (1+1)D simulations (5.26). The diffraction efficiency is depicted in Fig. 6.7 (a) and the phase shift  $\Delta\phi$  between the coupled states in Fig. 6.7 (b). The simple DK-Pendellösung (6.42) is valid for  $\Omega = \Omega \omega_{2r} < 3 \omega_r$ . For  $\Omega > 3 \omega_r$ , losses into higher diffraction orders are significant, but the extended solution (6.52) still matches the numerical solution.

**ADIABATICITY** The crossover from the deep- to the quasi-Bragg regime at  $\Omega \approx 3 \omega_r$  for atomic mirrors using  $\tilde{\tau}_{j\pi}$  (6.32) is related to the adiabaticity criterium [177]

$$\max_{\tau \in [\tau_i, \tau_i + \Delta\tau]} \left| \frac{d}{d\tau} \left( \frac{\mathbf{g}_n^o(\tau)^* \dot{\mathbf{g}}_m^o(\tau)}{\omega_n(\tau) - \omega_m(\tau)} \right) \right| \Delta\tau \ll 1, \quad \forall m \neq n, \quad (6.53)$$



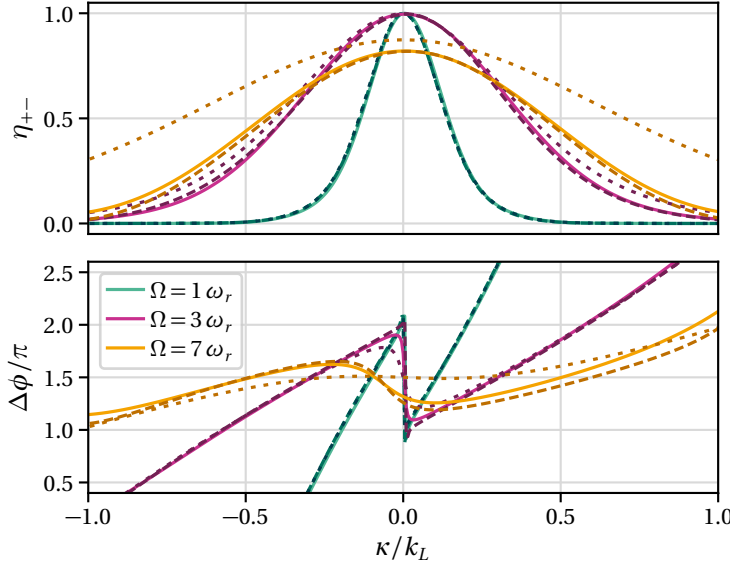


Figure 6.7: Velocity dispersion of (top) the diffraction efficiency  $\eta_{+-}(\kappa)$  and (bottom) of the phase shift  $\Delta\phi(\kappa)$  for sech-pulses with pulse width  $\tau_S = \tilde{\tau}_{S\pi}(\Omega)$  (6.32), total interaction time  $\Delta\tau = 8\tilde{\tau}_{G\pi}$  and different Rabi frequencies  $\Omega = \Omega \omega_{2r}$ . The DK-Pendellösung (6.42) (dotted) is suitable for  $\Omega < 3\omega_r$  while the extended model (6.52) (dashed) matches the numerical results (5.26) (solid) very well also for larger  $\Omega$ .

with the eigenvalues  $\omega_m(\tau)$  and eigenvectors  $\mathbf{g}_m^o(\tau)$  of  $H^o$  (5.59). Equation (6.53) results in  $\Omega = \Omega \omega_{2r} \ll 4\omega_r$  for  $\tilde{\tau}_{S\pi}$  at  $\kappa = 0$ . This is confirmed by the results of Gochnauer et al. [167] and visible in Figs. 6.7, 6.10, 6.11. Adiabaticity is given in the deep-Bragg regime, where losses into higher diffraction orders are negligible and therefore  $\eta_{+-} \approx 1$ , here for  $\Omega \lesssim 3\omega_r$ . Thus, while the DK-Pendellösung (6.42) is valid in the adiabatic regime, the extended model (6.52) can be used even for non-adiabatic pulses.

## 6.4 DIFFRACTION WITH GAUSSIAN PULSES

In the compared beamsplitter experiments, Gaussian laser pulses are used. There is a good reason for it, as they are self-Fourier-transform functions. Unfortunately, they are not amenable to closed analytical models. However, due to the similarity of the Gaussian- (6.4) to the sech-pulses (6.6) (cf. Fig. 6.1), one can estimate the velocity selective diffraction efficiency for infinitely long Gaussian pulses in the deep-Bragg regime. The different pulses have equal nominal times (6.2). Therefore, approximating  $\text{sech}^2(a)$  from Eq. (6.44), with a similar exponential form, providing the same integration area as  $\int_{-\infty}^{\infty} da \text{sech}^2(a) = \int_{-\infty}^{\infty} da \exp(-\pi a^2/4) = 2$ , leads to

$$\eta_{+-}^G(\kappa, \Omega, T) = \exp\left(-\pi \left(\frac{\kappa T}{4}\right)^2\right) \sin^2\left(\frac{T\Omega}{2}\right), \quad (6.54)$$

with the nominal time  $T = \sqrt{2\pi}\tau_G$  (6.2). The results are depicted in Fig. 6.8. The efficiency becomes power-broadened for increasing the Rabi frequency. As long as losses into higher diffraction orders are negligible  $\Omega < 3\omega_r$ , the approximation (6.54) for infinite pulses matches the numerical results (5.26) with finite integration time  $\Delta\tau_G = 8\tilde{\tau}_{G\pi}(\Omega)$ . However, due to the similarity to sech-pulses the extended DK-model (6.52) can estimate the results also in the quasi-Bragg regime, as shown in Fig. 6.9. The results depicted in Fig. 6.8 and 6.9, as well as the explicit formula  $\eta_{+-}^G$  (6.54) demonstrates, that the Gaussian pulses are self-Fourier-transform functions. The velocity dispersion of the diffraction efficiency is free of the side lobes of rectangular pulses, seen in Fig. 6.4 (a).

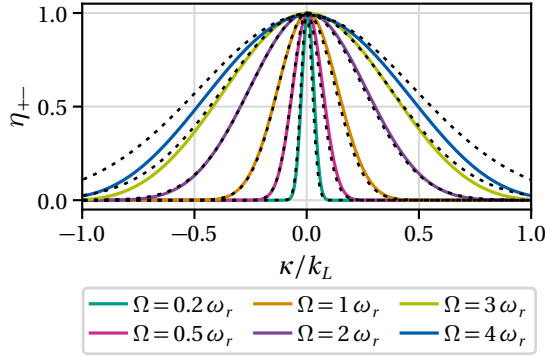


Figure 6.8: Velocity selective diffraction efficiency  $\eta_{+-}(\kappa)$  of a Gaussian mirror pulse for Rabi frequencies  $\Omega = \Omega\omega_r$ . The approximation  $\eta_{+-}^G$  (6.54) (dotted) fits the numerical results with  $\Delta\tau_G = 8\tau_{G\pi}(\Omega)$  (solid) for  $\Omega \leq 3\omega_r$ .

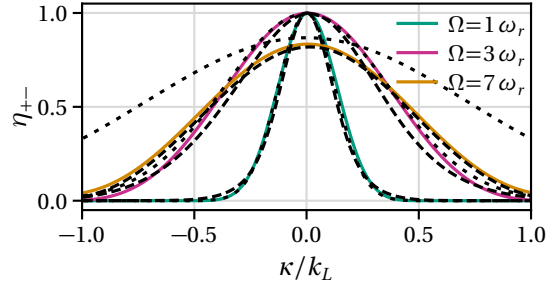


Figure 6.9: Velocity dependent diffraction efficiency  $\eta_{+-}(\kappa)$  for a Gaussian pulse [ $j = G$ , solid: numerical, dotted: deep-Bragg limit (6.54)] and a sech pulse [ $j = S$ , dashed: extended DK-model (6.52)]. A mirror pulse of width  $\tilde{\tau}_{j\pi}(\Omega)$  (6.32) with total pulse duration  $\Delta\tau = 8\tilde{\tau}_{G\pi}$  is applied for three two-photon Rabi frequencies  $\Omega = \Omega\omega_r$ .

## 6.5 COMPARISON OF THE DIFFRACTION FOR ALL PULSE SHAPES

Because, all smooth pulse shapes ( $j = G, B, S$ ) with pulse widths  $\tilde{\tau}_{j\pi}(\Omega)$  (6.32) are very similar (cf. Fig. 6.1) they exhibit quasi identical results for the diffraction efficiency, phase shift and fidelity, as depicted in Fig. 6.10 and Fig. 6.11. The advantages in comparison to rectangular pulses are clearly visible. The diffraction efficiency and the fidelity are improved for smooth temporal envelopes. Beyond  $\Omega > 3\omega_r$ , scattering into higher diffraction order depletes the population in the beamsplitter manifold, but less than for rectangular pulses [cf. Fig. 6.10 (b), Fig. 6.11]. However, it is worth mentioning that rectangular pulses provide a wider velocity acceptance [cf. Fig. 6.10 (d)].

In Fig. 6.11, the phase-sensitive fidelity  $F$  (5.34) is compared for different momentum widths  $\sigma_k$  of an initial Gaussian wavepacket in 1D (2.54). In addition, the normalised diffraction efficiency  $\bar{\eta}$  (5.32) of the wavepackets is depicted. Increasing  $\sigma_k$  reduces the range of admissible Rabi frequencies  $\Omega = \Omega\omega_r$ , which shifts the optimum to higher values.

In Fig. 6.10 and Fig. 6.11, the explicit Kato solution (6.27) matches the results for rectangular pulses very well, demonstrating also its applicability for wavepackets with finite momentum width. The Pendellösung for Gaussian pulses (6.54) as well as the DK-Pendellösung (6.42) matches the numerical simulations for  $\Omega < 3\omega_r$ , while the extended DK-model (6.52), taking off-resonantly coupled diffraction orders into account, remains further valid. The explicit solution for sech-pulses deviates slightly from the results for Gaussian- and Blackman-pulses, but provides very detailed forecasts. The Blackman-pulse shape differs only marginally from the Gaussian pulse, resulting in a nearly identical beamsplitter response, but indeed marginal improvements can be achieved, like slightly larger diffraction efficiencies in Fig. 6.10 (b), Fig. 6.11, a wider velocity acceptance in Fig. 6.10 (d) and larger fidelities in Fig. 6.11. In particular, for  $\Omega = 3\omega_r$  Blackman pulses achieve slightly better results for the on-resonance diffraction efficiency  $\eta_r^B = 0.9992$ , efficiency width  $\Delta\eta^B = 0.864$ , fidelity  $F^B = \{0.9989, 0.9901, 0.9620, 0.8474\}$  and total efficiency  $\bar{\eta}^B = \{0.9989, 0.9903, 0.9647, 0.8775\}$  for  $\sigma_k = \{0.01, 0.05, 0.1, 0.2\}k_L$  in comparison to Gaussian pulses with  $\eta_r^G = 0.9989$ ,  $\Delta\eta^G = 0.854k_L$ ,  $F^G = \{0.9987, 0.9896, 0.9607, 0.8440\}$  and  $\bar{\eta}^G = \{0.9987, 0.9898, 0.9634, 0.8743\}$ . The additional benefit of Blackman pulses is that while they achieve the same or even better diffraction results than the other smooth pulses, they provide a shorter total interaction time, due to their cut-off (6.5). In experiments this reduces diminishing effects like the expansion of the atomic cloud, or detrimental movements



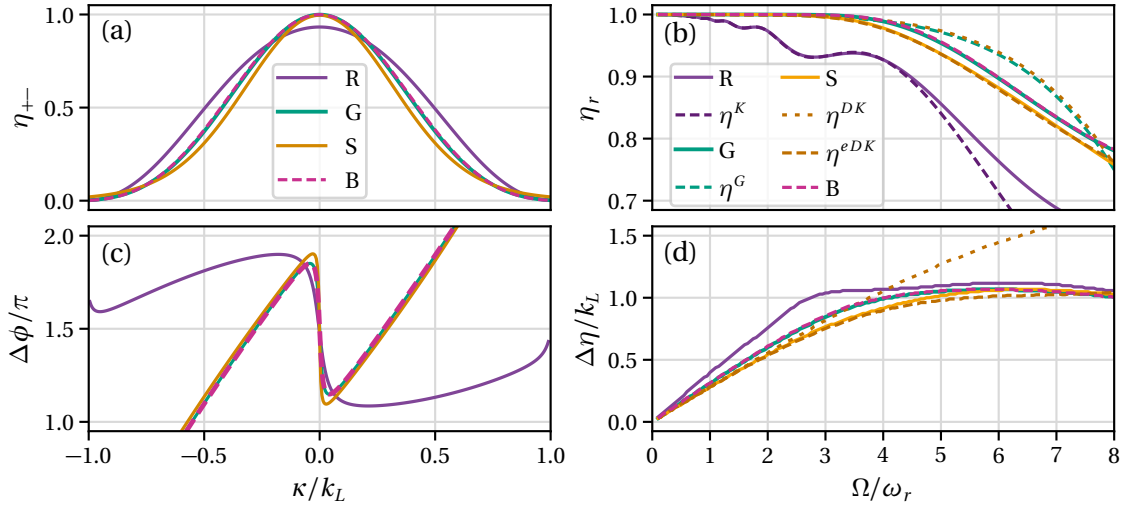


Figure 6.10: Comparison of the Bragg diffraction for a mirror pulse of width  $\tilde{\tau}_{j\pi}(\Omega)$  (6.32), for rectangular (R, violet, solid: numerical, dashed: Kato solution (6.33)), Gaussian (G, green, solid: numerical, dashed: G-Pendellösung (6.54)), sech (S, yellow, solid: numerical, dotted: DK-Pendellösung (6.42), dashed: extended DK (6.52)) and Blackman (B, magenta, dashed) pulses. The total interaction time is  $\Delta\tau = 8\tilde{\tau}_{G\pi}$  for the smooth pulses and  $\Delta\tau = 2\tilde{\tau}_{R\pi}$  for the rectangular pulse. (a) Velocity dispersion of the numerical diffraction efficiency  $\eta_{+-}(\kappa)$  and (c) phase shift  $\Delta\phi(\kappa)$  for  $\Omega = \Omega\omega_{2r} = 3\omega_r$ . (b) On-resonance diffraction efficiency  $\eta_r(\Omega)$  and (d) width of the diffraction efficiency  $\Delta\eta(\Omega)$  depending on the two-photon Rabi frequency  $\Omega = \Omega\omega_{2r}$ .

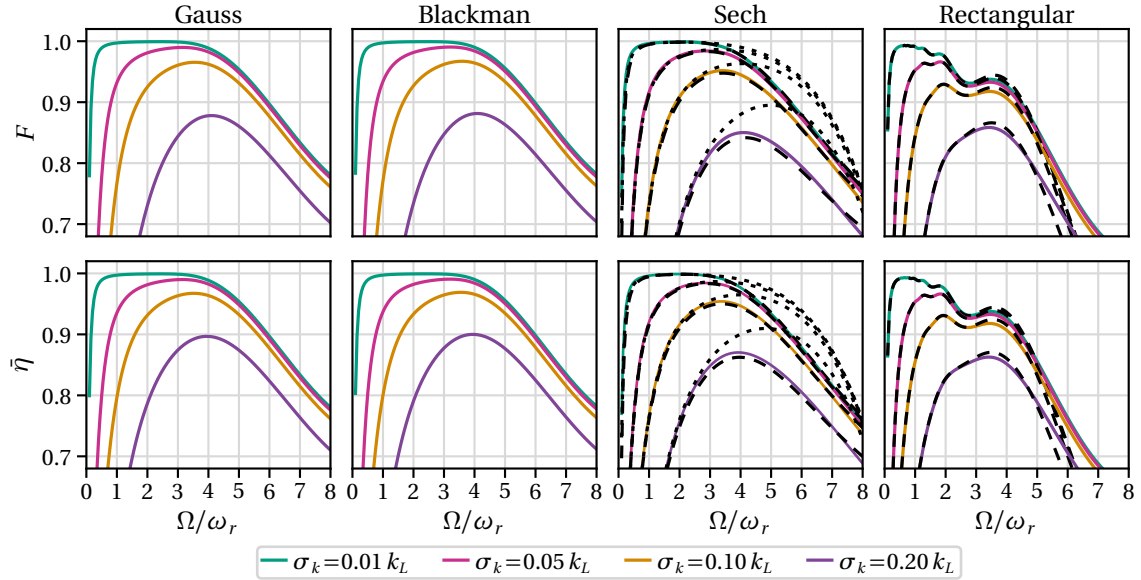


Figure 6.11: (Top) Fidelity  $F(\Omega; \sigma_k)$  (5.34) and (bottom) diffraction efficiency  $\tilde{\eta}(\Omega; \sigma_k)$  (5.32) after a mirror pulse of width  $\tilde{\tau}_{j\pi}$  versus two-photon Rabi frequency  $\Omega = \Omega\omega_{2r}$  for different initial atomic momentum widths  $\sigma_k$  for Gaussian, Blackman, sech and rectangular pulses. Via Eq. (2.89) the momentum width  $\sigma_k = \{0.01, 0.05, 0.1, 0.2\} k_L$  is connected to a temperature  $T(\sigma_k) = \{0.04, 1, 4, 15\}$  nK. The total interaction time is  $\Delta\tau = 8\tilde{\tau}_{G\pi}$ . The 1D initial Gaussian wavepacket (2.54) is centered at  $(x, k_x) = (0, -k_L)$ . The DK-Pendellösung (6.42) (dotted) matches the results of the numerical integration (5.26) (solid) for sech pulses very well for  $\Omega < 3\omega_r$  and considering population loss to higher diffraction orders with the extended model (6.52) (dashed) also for larger  $\Omega$ . For rectangular pulses, the Kato solution (6.27) (dashed) matches also the numerical results.

during the interaction time. For the simulations this means a reduction of the necessary number of calculated timesteps, shortening the simulation time. Therefore, the Blackman pulse represents the optimal temporal envelope (of the here considered pulse shapes).

It is worth mentioning that for finite total interaction times  $\Delta\tau$ , with pulse areas [cf. Eq. (6.2)]

$$\theta_j = \Omega T_j(-\Delta\tau/2, \Delta\tau/2) = \Omega \int_{-\Delta\tau/2}^{\Delta\tau/2} d\tau f_j(\tau), \quad (6.55)$$

the  $\pi$ -pulse conditions are not met exactly  $\theta_j \approx \pi$ . One could adjust the pulse width  $\tilde{\tau}_{j\pi}$  (6.32) for each pulse shape  $j$  to obtain a  $\pi$ -pulse individually  $\theta_j = \pi$ , but this leads to unequal nominal times  $T_j \neq T$  (6.2) causing significant phase differences. Thus, the same total interaction time  $\Delta\tau = 8\tilde{\tau}_{G\pi}$  of a  $\pi$ -pulse is considered for all pulse shapes and the widths  $\tau_j = \tilde{\tau}_{j\pi}$  are connected via  $T_j = T$ . The resulting differences in the pulse areas  $\theta_j$  (6.55) are negligible.

## 6.6 PROVING THE DEMKOV-KUNIKE MODEL EXPERIMENTALLY

To verify the predictions of the Demkov-Kunike model and thereof derived formulas, they are gauged to experimental diffraction efficiencies [1].

### 6.6.1 Experimental scenario

Experimentally, an atom chip apparatus [59, 66] is employed to prepare Bose-condensed  $^{87}\text{Rb}$  atoms, with a condensate (c) fraction of  $N^c = (10 \pm 1) \times 10^3$  and a quantum depletion (thermal cloud, t) of  $N^t = (7 \pm 1) \times 10^3$  atoms. After release from the trap (laboratory chip frame  $S_0$ ), with trap frequencies  $[\omega_x, \omega_y, \omega_z] = 2\pi \times [46(2), 18(1), 31(1)] \text{ Hz}$ , they expand ballistically and fall vertically towards nadir. The Bragg-laser beams are aligned horizontally. It is sufficient to consider inertial motion during the short Bragg pulses ( $< \text{ms}$ ). At the beginning of the diffraction pulses, after 10 ms time-of-flight (TOF), the temperature of the thermal cloud is obtained from a bimodal fit (2.90) of TOF-measurements as  $T \leq (20 \pm 3) \text{ nK}$  (cf. App. E.1). At this time, the size of the cloud  $\sigma_x \approx 20 \mu\text{m} \ll w_0 = 1386 \mu\text{m}$  is extremely small in comparison to the beam waist  $w_0$ , wherefore the plane-wave approximation is suitable. This will be demonstrated in the next Chapter 7.

### 6.6.2 Measured observable: normalised diffraction efficiency

Experimentally, the first-order diffraction efficiency in the deep-Bragg regime (5.33)

$$\bar{\eta}_{+-} = \frac{N_+}{N_- + N_+} = \frac{p_+}{p_- + p_+} \quad (6.56)$$

is obtained from the number of diffracted atoms  $N_+$  into the first diffraction order  $k' = k_+$  and the undiffracted atoms  $N_-$  remaining in the initial momentum state  $k' = k_-$ . It is identical to the ratio of the proportions  $p_{\pm} = N_{\pm}/N^A$  with the total atom number<sup>2</sup>  $N^A = N^c + N^t$ . In the experiment, the diffraction efficiency (6.56) is a function of the detuning  $\delta\omega$  (5.7) of the laser from the two-photon resonance with a fixed atomic preparation, where ideally the atoms are

<sup>2</sup> Now the total atom number is called  $N^A$  to avoid confusions with the Bragg resonances  $\mathbf{k}' = \mathbf{k} + 2N\mathbf{k}_L$  (Sec. 5.4).

initially at rest  $\langle \hat{p}_x(\tau_i) \rangle = 0$ . However, this efficiency can also be the response for resonant lasers and an initial wavepacket centred at

$$\langle \hat{p}_x(\tau_i) \rangle = (-1 + \bar{\kappa}) \hbar k_L, \quad \bar{\kappa} = \frac{\delta\omega}{\omega_{2r}}, \quad (6.57)$$

directly connected to the laser detuning via Eq. (5.9) (cf. Sec. 5.1.2). In theory, the velocity dispersion of the diffraction efficiency is probed in this way, by a variation of the center-of-mass momentum  $\langle \hat{p}_x(\tau_i) \rangle$  (6.57) of the atomic cloud in the rest frame  $S'$  of the nodes of the bichromatic Bragg beamsplitter (cf. Sec. 5.3.1).

Therefore, theoretically, the diffraction efficiency (6.56) is computed in the laser plane-wave approximation from the number of diffracted atoms

$$N_{\pm}(\bar{\kappa}) = \int_{-1}^1 d\kappa \eta_{\pm}(\kappa) n(\kappa, \bar{\kappa}), \quad (6.58)$$

resulting from a reaction equation derived in the following, which completely encloses the wavepacket with the effectively one-dimensional momentum density  $n(\kappa, \bar{\kappa})$  and the average initial momentum  $\bar{\kappa}$  (6.57). In the limit of ideal plane matter waves with wavenumber  $\bar{\kappa}$  the diffraction efficiency (6.56) reduces to  $\eta = \eta_{+-}(\bar{\kappa})$ .

### *Diffraction efficiency for partially coherent bosonic fields*

In the experiment, both, the coherent BEC and the incoherent thermal cloud have a finite momentum width and contribute to the population parts  $N_+$  and  $N_-$ . The bosonic amplitude  $\hat{a}_g(\mathbf{k})$  describes the ground state atoms in momentum space and obeys the commutation relation  $[\hat{a}_g(\mathbf{k}), \hat{a}_g^\dagger(\mathbf{k}')] = \delta(\mathbf{k} - \mathbf{k}')$ . For a Bose-condensed sample, the single-particle density matrix

$$\rho(\mathbf{k}, \mathbf{k}') \equiv \langle \hat{a}_g^\dagger(\mathbf{k}') \hat{a}_g(\mathbf{k}) \rangle = \rho^c(\mathbf{k}, \mathbf{k}') + \rho^t(\mathbf{k}, \mathbf{k}'), \quad (6.59)$$

separates into a condensate  $\rho^c(\mathbf{k}, \mathbf{k}') = \alpha^*(\mathbf{k}')\alpha(\mathbf{k})$  and a quantum depletion  $\rho^t(\mathbf{k}, \mathbf{k}')$  [cf. Sec. 2.3.7, skipping the index (1)]. The equally bimodal momentum density

$$n(\mathbf{k}) \equiv \rho(\mathbf{k}, \mathbf{k}) = n^c(\mathbf{k}) + n^t(\mathbf{k}) = N^A [p^c n^c(\mathbf{k}) + p^t n^t(\mathbf{k})], \quad (6.60)$$

is the observable in a beamsplitter<sup>3</sup>. It is normalised to the total number of atoms  $N^A = \int_{-\infty}^{\infty} d^3k n(\mathbf{k}) = N^c + N^t$ . The densities  $n^c, n^t$  are probability normalised, thus defining a condensate fraction  $p^c = N^c / N^A = 0.59 \pm 0.07$  and a thermal fraction  $p^t = N^t / N^A = 0.41 \pm 0.06$ . Dynamically, the classical field  $\alpha(t)$  obeys the Gross-Pitaevskii equation and extensions thereof for  $\rho^t(t)$  [178–180].

For the diffraction efficiency (6.56), the number of diffracted atoms  $N_{\pm}$  are given by

$$N_{\pm} = \int_{-k_L \pm k_L}^{k_L \pm k_L} dk'_x \int_{-\infty}^{\infty} dk'_y \int_{-\infty}^{\infty} dk'_z \langle \mathbf{k}' | \hat{\rho}(\tau) | \mathbf{k}' \rangle. \quad (6.61)$$

During the short beamsplitter pulse ( $< 1$  ms), only single particle dynamics (5.26) are relevant, given by the von-Neumann equation (cf. Sec. 3.2) with the Schrödinger time evolution operator, described as Green's functions  $G(\tau, \tau_i)$  (5.26)

$$\rho(\tau) = G(\tau, \tau_i) \rho(\tau_i) G^\dagger(\tau, \tau_i), \quad (6.62)$$

<sup>3</sup> Experimentally, the spatial density is the observable. After some time of free evolution the wavepackets with different momenta are separated in space. In the momentum space, this separation is visible directly after the diffraction pulses.

for the condensate as well as the thermal cloud. In the plane-wave approximation (with lasers propagating in  $x$ -direction), the three-dimensional Fourier propagator  $\mathcal{G}(\mathbf{k}, \mathbf{k}') = \mathcal{G}_{\parallel} \mathcal{G}_{\perp}$  (5.29) factorises into the transverse propagator of free time evolution

$$\mathcal{G}_{\perp}(\tau, \tau_i, \mathbf{k}_{\perp}, \mathbf{k}'_{\perp}) = \exp\left(-i \frac{\hbar(k_y^2 + k_z^2)}{2M}(\tau - \tau_i)\right) \delta^{(2)}(\mathbf{k}_{\perp} - \mathbf{k}'_{\perp}), \quad \mathbf{k}_{\perp} = (k_y, k_z) \quad (6.63)$$

and the longitudinal Greens function in  $x$ -direction, describing the diffraction process

$$G_{\parallel}(\tau, \tau_i, x, x') = \sum_{\mu, \mu', n} \frac{\mathcal{G}_{\mu', \mu}(\tau, \kappa'_n)}{N_x a_x} \exp[i(k_{\mu}^n x - k_{\mu'}^n x')]. \quad (6.64)$$

The latter follows from the diffraction solution of the Schrödinger equation (5.52), using the definitions  $k_{\mu}^n = (\mu + \kappa'_n)k_L$  (5.54) and (5.55). The discrete Green's matrix  $\mathcal{G}_{\mu', \mu}(\tau, \tau_i, \kappa'_n)$  satisfies the system of differential equations (5.59) with initial condition  $\mathcal{G}_{\mu', \mu}(\tau_i, \tau_i, \kappa'_n) = \delta_{\mu, \mu'}$ . In the continuum limit, one uncovers the momentum conservation on a lattice with  $k_x = (\mu + \kappa)k_L$  and  $k'_x = (\mu' + \kappa')k_L = k_x + 2N k_L$ , from the Fourier transformation of Eq. (6.64)

$$\mathcal{G}_{\parallel}(\tau, \tau_i, k_x, k'_x) = \delta(\kappa - \kappa') \mathcal{G}_{\mu', \mu}(\tau, \tau_i, \kappa'). \quad (6.65)$$

From the propagation equation (6.62), one obtains the final momentum density

$$\begin{aligned} n_f(\mathbf{k}') &= \langle \mathbf{k}' | \hat{\rho}(\tau_f) | \mathbf{k}' \rangle = \int_{\mathbb{R}^3} d^3k \int_{\mathbb{R}^3} d^3q \langle \mathbf{k}' | G(\tau_f, \tau_i) | \mathbf{k} \rangle \langle \mathbf{k} | \hat{\rho}(\tau_i) | \mathbf{q} \rangle \langle \mathbf{q} | G^{\dagger}(\tau_f, \tau_i) | \mathbf{k}' \rangle \\ &= \int_{-\infty}^{\infty} dk_x \int_{-\infty}^{\infty} dq_x \mathcal{G}_{\parallel}(\tau_f, \tau_i, k_x, k'_x) \rho(\tau_i, k_x, k'_y, k'_z, q_x, k'_y, k'_z) \mathcal{G}_{\parallel}^{\dagger}(\tau_f, \tau_i, q_x, k'_x), \end{aligned} \quad (6.66)$$

which is needed to calculate the atom numbers  $N_{\pm}$  (6.61) for the diffraction efficiency  $\eta$  (6.56). All observables are along the  $x$ -direction. Thus, averaging over the transversal directions introduces the marginal momentum densities at time  $\tau$

$$n(\tau, k_x) = \int_{-\infty}^{\infty} dk_y dk_z n(\tau, \mathbf{k}). \quad (6.67)$$

Assuming that the initial ensemble is well localised around  $k_x = (\mu + \kappa)k_L$  with  $\mu = -1$ , its density is denoted by  $n_i(\kappa) = n(\tau_i, k_x)$ . From the final density (6.66) with  $\mathcal{G}_{\parallel}$  from Eq. (6.65) one obtains  $n_f(\kappa) = n(\tau_f, k'_x)$ , with  $k'_x = (\mu' + \kappa')k_L$  at the diffraction order  $\mu'$

$$n_f(\mu', \kappa') = |\mathcal{G}_{\mu', -1}(\tau_f, \tau_i, \kappa')|^2 n_i(\kappa'). \quad (6.68)$$

Now, one can identify the diffraction efficiencies with  $\mu' = \{+1, -1\}$  as  $\eta_{+-}(\kappa) = |\mathcal{G}_{1, -1}(\kappa, \tau_f)|^2$  and  $\eta_{-+}(\kappa) = |\mathcal{G}_{-1, -1}(\kappa, \tau_f)|^2$ . Thus, for atomic clouds with initial momentum  $\langle \hat{p}_x(\tau_i) \rangle = (-1 + \bar{\kappa})\hbar k_L$  (6.57), the observables in first-order diffraction theory, which are the number of diffracted atoms  $N_{\pm}$ , read

$$N_{\pm}(\bar{\kappa}) = \int_{-1}^1 d\kappa \eta_{\pm-}(\kappa) n_i(\kappa, \bar{\kappa}) = N^A p_{\pm}(\bar{\kappa}), \quad p_{\pm}(\bar{\kappa}) = \int_{-1}^1 d\kappa \eta_{\pm-}(\kappa) [p^c n^c(\kappa_n, \bar{\kappa}) + p^t n^t(\kappa_n, \bar{\kappa})]. \quad (6.69)$$

For the proportions  $p_{\pm} = N_{\pm}/N^A$  the definitions of the densities  $n^{a=\{c, t\}} = N^A p^a n^a$  (6.60) are used. In the deep-Bragg regime losses into higher diffraction orders are negligible, wherefore theoretically  $N_+ + N_- = N^A$  and the diffraction efficiency (6.56) simplifies to

$$\bar{\eta}_{+-} = \frac{N_+(\bar{\kappa})}{N^A} = p^c n_+^c(\bar{\kappa}) + p^t n_+^t(\bar{\kappa}), \quad n_+^{a=\{c, t\}}(\bar{\kappa}) = \int_{-1}^1 d\kappa \eta_{+-}(\kappa) n^a(\kappa, \bar{\kappa}), \quad (6.70)$$

splitting into a condensate and a thermal cloud fraction.

Approximating the normalised initial momentum distributions  $n_i^c(\kappa, \bar{\kappa}) \approx \tilde{n}^c(\kappa, \bar{\kappa})$  and  $n_i^t(\kappa, \bar{\kappa}) \approx \tilde{n}^t(\kappa, \bar{\kappa})$  (6.60) by Gaussian functions

$$\tilde{n}(\kappa, \bar{\kappa}) = \frac{1}{\sqrt{2\pi}\tilde{\sigma}_k} \exp\left(-\frac{(\kappa - \bar{\kappa})^2}{2(\tilde{\sigma}_k)^2}\right), \quad \tilde{\sigma}_k = \frac{\sigma_k}{k_L}, \quad \int_{-\infty}^{\infty} d\kappa \tilde{n}(\kappa, \bar{\kappa}) = 1, \quad (6.71)$$

of widths  $\sigma_k^c = 0.087 k_L$ ,  $\sigma_k^t = (0.237 \pm 0.015) k_L$  (cf. Sec. 6.6.2) and using the Gaussian approximation (6.54) for the diffraction efficiency  $\eta_{\pm-}(\kappa)$ , one obtains the analytical model for the first-order diffraction efficiency (6.56)

$$\bar{\eta}_{+-} = \sin^2\left(\frac{\Omega T}{2}\right) \sum_{a=\{c,t\}} \frac{p^a}{\tilde{\sigma}_k^a(\tilde{T})} \exp\left(-\frac{1}{2}\left(\frac{\bar{\kappa}\tilde{T}}{\tilde{\sigma}_k^a(\tilde{T})}\right)^2\right), \quad (6.72)$$

with  $\tilde{\sigma}_k^a(\tilde{T}) = \sqrt{1 + (\tilde{T}\tilde{\sigma}_k^a)^2}$ ,  $\tilde{T} = T\sqrt{\pi/8}$  and  $\tilde{\sigma}_k^a = \sigma_k^a/k_L$ . For this diffraction efficiency the required information about the atomic initial state is fully characterised with the condensate ratio and the momentum widths of the condensate and the thermal background.

### Initial momentum distributions

**MOMENTUM DISTRIBUTION OF THE CONDENSATE** After release from the trap, the width of the BEC in momentum space increases due to atomic mean-field interaction [121]. Jan Teske determines the momentum distribution by solving the (3+1)D Gross-Pitaevskii equation (2.68) for the given parameters of Table A.1 and 10 ms time-of-flight before the diffraction pulses (cf. Sec. 2.3.5). The result is confirmed by the scaling approach [122–125] applied to the numerical Gross-Pitaevskii ground state. Finally, the doubly-integrated momentum density distribution of the BEC at the beginning of the diffraction pulses  $n_i^c(\kappa, \bar{\kappa}) \approx \tilde{n}^c(\kappa, \bar{\kappa})$  (6.67), can be approximated with a Gaussian distribution (6.71) of width  $\sigma_k^c = (0.087 \pm 0.001)k_L$ <sup>4</sup>, as depicted in Fig. 6.12.

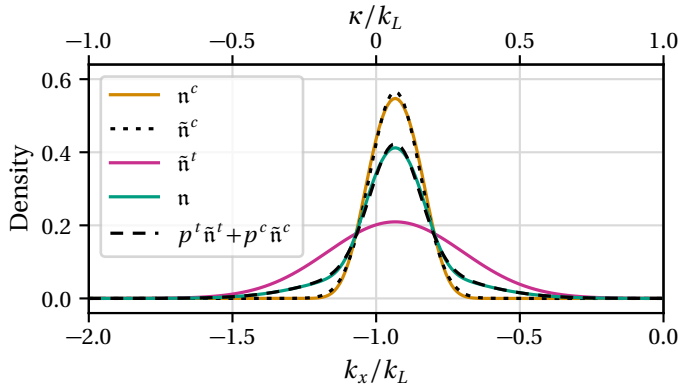


Figure 6.12: One-dimensional density  $n = p^c n^c + p^t n^t$  (6.60), with condensate ratio  $p^c = 0.49$  and  $p^t = 0.51$ , versus momentum  $k_x$ , respectively momentum detuning  $\kappa$ . The thermal cloud  $n^t$  as well as the condensate  $n^c$ , obtained from a (3+1)D GP simulation, can be approximated with a Gaussian distribution  $n^{a=\{c,t\}} \approx \tilde{n}^a$  (6.71).

**MOMENTUM DISTRIBUTION OF THE THERMAL CLOUD** The thermal cloud is also approximately a Gaussian distribution, where the marginal, one-dimensional momentum width  $\sigma_k^t = \sqrt{M k_B T / \hbar}$  introduces a temperature  $T$  (cf. Sec. 2.3.6). Experimentally, time-of-flight measurements (cf. App. E.1.1) of the spatial expansion  $\sigma_x(t)$  (2.58) lead to the momentum width  $\sigma_k^t = (0.237 \pm 0.015) k_L$  of the density  $n^t$  (6.71). The horizontal trap direction  $x' = x \cos \phi$ ,  $\phi = 5.5^\circ \pm 1^\circ$  differs slightly from the beamsplitter direction  $x$ . However, the resulting difference in the momentum width  $|\sigma_{k_x} - \sigma_{k'_x}| = 0.001 k_L$  is negligible within the uncertainty.

<sup>4</sup> For the fit of the numerical (3+1)D GP result with the Gaussian distribution (6.71) the flanks are stronger weighted to match the  $1/e$  width of the simulation results.

### 6.6.3 Results

In Fig. 6.13 the diffraction efficiency (6.56) is depicted for different laser powers  $P$ . In Fig. 6.13 (A) Gaussian pulses of width  $\tau_G$  (6.4) and total interaction time  $\Delta\tau = 8\tau_G$  are applied for the laser powers  $P_\bullet = 20$  mW and  $P_\blacktriangledown = 30$  mW. In addition, in (B) rectangular pulses of width  $\tau_R = \Delta\tau_G/2$  are applied for  $P_\blacksquare = 5$  mW and  $P_\blacktriangle = 10$  mW. Therefore, the diffraction efficiency for the atomic cloud with finite momentum width cannot be calculated analytically, however numerical simulations can be compared to the experimental data.

The laser power defines with Eq. (2.13) the Rabi frequency  $\Omega_0$  and with Eq. (5.43) the two-photon Rabi frequency  $\Omega$ , which characterises the interaction strength. In the experiment, the atoms are significantly displaced with respect to the axis of the beamsplitter beams to  $z_0 = (1165 \pm 50)\mu\text{m} = (0.84 \pm 0.04)w_0$ , while  $x_0 \approx y_0 \approx 0\mu\text{m}$  (cf. App. E.1.2). This reduces the effective Rabi frequency at the location of the atoms  $\Omega(\mathbf{r}_0)$ , according to the intensity of collimated ( $w_0 \gg \lambda_L$ ) Laguerre-Gaussian laser beams [cf. Sec. 2.2.2, Eq. (2.24)] to  $\Omega(\mathbf{r}_0) \approx \Omega \exp(-2\rho_0^2/w_0^2)$ , with the transversal displacement  $\rho_0^2 = y_0^2 + z_0^2$ .

Fits using the model (6.72) describe the experimental data for Gaussian pulses very well and provide appropriate starting parameters [ $p^c$ ,  $\Omega(\mathbf{r}_0)$ ] for the effective (1+1)D numerical simulations with Gaussian pulses [using Eqs. (6.56), (6.58), (5.26), (5.27), (5.29)], fully matching the experimental data. The experimental, numerical and fit parameters are listed in Table 6.1.

In Fig. 6.13 (a), the velocity dispersion of the diffraction efficiency uncovers a residual initial motion  $k_x^S = \bar{\kappa}^S k_L = 0.12 k_L$  (A) respectively  $k_x^S = 0.105 k_L$  (B) of the atomic cloud in the laboratory frame S. Considering this in an atomic initial momentum  $\langle \hat{p}_x(\tau_i) \rangle = (-1 + \bar{\kappa}^S + \bar{\kappa})\hbar k_L$  with  $\bar{\kappa} = \delta\omega/\omega_{2r}$  leads to a very good match of the fit model (6.72), the numerical simulations and the experimental data.

In Fig. 6.13 (b), the diffraction efficiencies display damped Rabi oscillations versus the total pulse length  $\Delta\tau = 8\tau_G$ . This is a typical inhomogeneous line-broadening caused by the momentum widths  $\sigma_k^c$ ,  $\sigma_k^t$ , the two-photon detuning  $\delta\omega = \bar{\kappa}\omega_{2r} \neq 0$  and a residual velocity  $\bar{\kappa}^S \neq 0$ , as also revealed by the Gaussian approximation (6.72). Here, the fit results for Gaussian pulses (A) for the two-photon Rabi frequency are also the optimal values for the numerical simulations, matching the experiment within the error level. For rectangular pulses (B) additionally to the decay of the efficiency, it is not possible to reach a full transfer back into the initial state after  $2n\pi$ -pulses,  $n \in \mathbb{Z}_+$ .

It is worth mentioning, that the velocity dispersion of the efficiency [Fig. 6.13 (a)] is less sensitive to the condensate ratio  $p^c$  than the Rabi oscillations [Fig. 6.13 (b)]. The Gaussian approximation (6.72) underestimates the second maxima, but the fit of  $p^c$  matches the experimental value within its uncertainty. The numerical simulations (for Gaussian and rectangular pulses) predict a condensate ratio at the lower bound of the experimental ratio, but still within the uncertainty. Please note, that reducing the condensate fraction  $p^c$  for the simulations and the Gaussian approximation is equivalent to increasing the momentum width of the condensate or of the thermal cloud. However, for the theoretical results the momentum widths are kept constant with  $\sigma_k^c = 0.087 k_L$  and  $\sigma_k^t = 0.237 k_L$ , although they contain uncertainties, while the ratio  $p^c$  is used as a free parameter.

Thus, the Gaussian approximation (6.72) of the DK-model gives a very good prediction of the experimental data for Gaussian pulses. It assumes weak local two-photon Rabi frequencies  $\Omega(\mathbf{r}_0) < 3\omega_r$ , justifying the Pendellösung (6.44), with  $\eta_{+-} + \eta_{--} = 1$  and small atomic clouds  $\sigma_x \ll w_0$  to approximate Laguerre-Gaussian beams by plane waves. The numerical results for both, the Gaussian and the rectangular pulses, agree with the experimental data systematically without any bias.



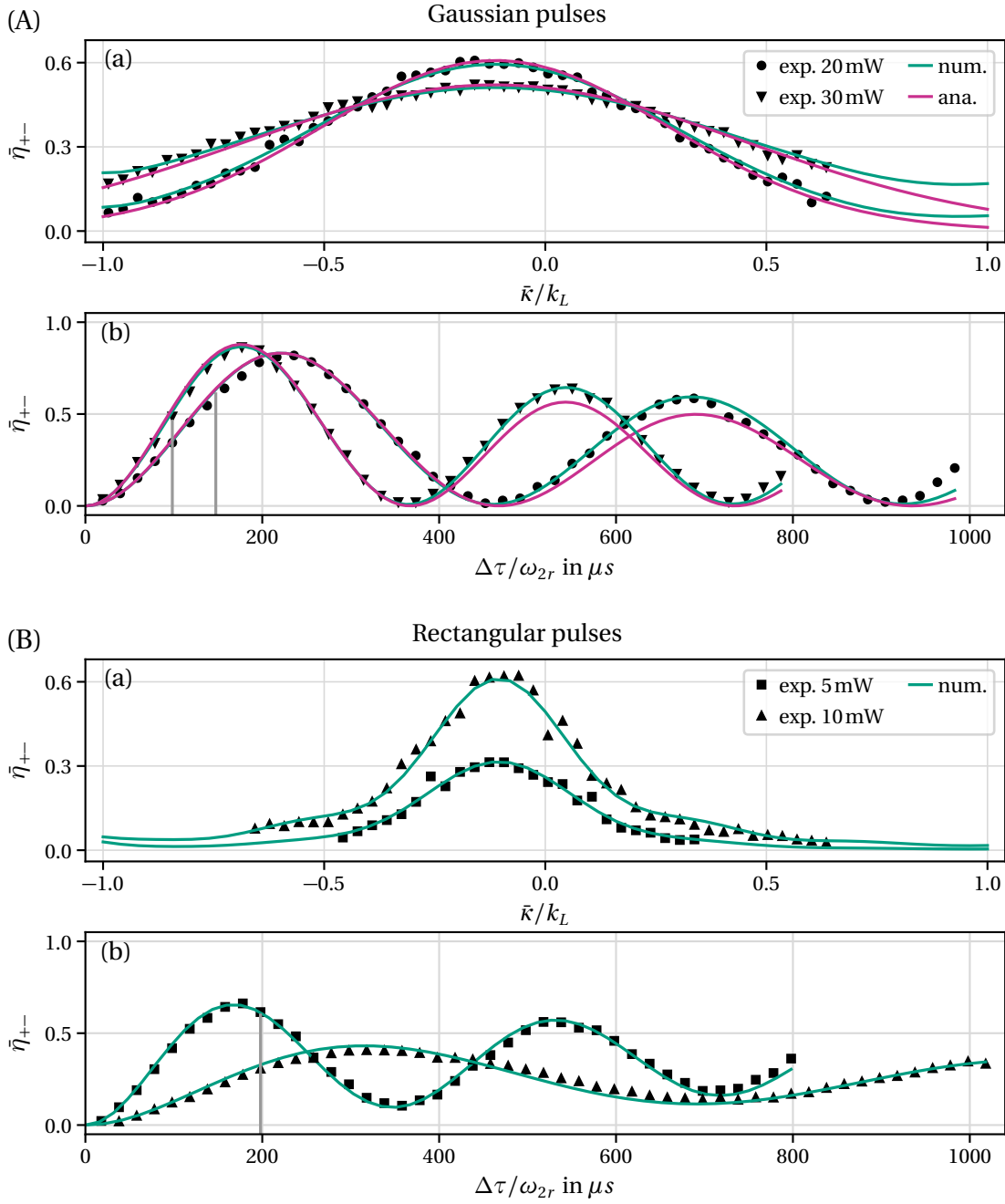


Figure 6.13: Experimental diffraction efficiency  $\bar{\eta}_{+-}$  (6.56) (black) for different laser powers with numerical simulations (green) and fits (6.72) (magenta) based on the DK-model. In (A) temporal Gaussian pulses of width  $\tau_G = \Delta\tau/8$  are applied for  $P_\bullet = 20$  mW and  $P_\blacktriangledown = 30$  mW. In (B) temporal rectangular pulses of width  $\tau_B = \Delta\tau/2$  are applied for  $P_\blacksquare = 5$  mW and  $P_\blacktriangle = 10$  mW. (a) Velocity dispersion of the diffraction efficiency  $\bar{\eta}_{+-}$  versus detuning  $\bar{\kappa}$  of the initial central momentum  $\langle \hat{p}_x(\tau_i) \rangle = (-1 + \bar{\kappa}^S + \bar{\kappa})\hbar k_L$ , where  $\bar{\kappa}^S = \bar{\kappa}^S k_L = 0.12 k_L$  is a small initial velocity of the atoms in the laboratory frame  $S$  and  $\bar{\kappa} = \delta\omega/\omega_{2r}$ . (b) Rabi oscillations of the diffraction efficiency versus total interaction time  $\Delta\tau$  and highlighted pulse widths of (a). Other parameters cf. Tables 6.1, A.1 and A.2.

(A)		Gaussian pulses	
		$P_{\bullet}=(20 \pm 2) \text{ mW}$	$P_{\blacktriangledown}=(30 \pm 3) \text{ mW}$
	exp.	$p^c$ $\Omega$ (2.13), (5.43) $\Omega(\mathbf{r}_0)$ $\bar{\kappa}^S$	$0.59 \pm 0.08$ $(6.60 \pm 0.66) \omega_r$ $(9.89 \pm 0.99) \omega_r$ $(1.61 \pm 0.27) \omega_r$ $(2.41 \pm 0.40) \omega_r$ $(0.12 \pm 0.01) k_L$
	(a) exp.	$\Delta t = 8\tau_G/\omega_{2r}$ $\theta_G$ (6.55)	$147.45 \mu\text{s}$ $98.3 \mu\text{s}$ $(0.56 \pm 0.09) \pi$
	ana.	$p^c$ $\Omega(\mathbf{r}_0)$	$0.59 \pm 0.06$ $0.59 \pm 0.14$ $(1.74 \pm 0.01) \omega_r$ $(2.27 \pm 0.01) \omega_r$
	num.	$p^c$ $\Omega(\mathbf{r}_0)$	$0.59$ $0.59$ $1.71 \omega_r$ $2.28 \omega_r$
	(b) exp.	$\delta\omega/2\pi$ (5.7)	$-2 \text{ kHz}$ $-2.5 \text{ kHz}$
	ana.	$p^c$ $\Omega(\mathbf{r}_0)$	$0.55 \pm 0.03$ $0.59 \pm 0.04$ $(1.81 \pm 0.01) \omega_r$ $(2.30 \pm 0.01) \omega_r$
	num.	$p^c$ $\Omega(\mathbf{r}_0)$	$0.52$ $0.52$ $1.81 \omega_r$ $2.30 \omega_r$

(B)		Rectangular pulses	
		$P_{\blacksquare}=(5.0 \pm 0.5) \text{ mW}$	$P_{\blacktriangle}=(10 \pm 1) \text{ mW}$
	exp.	$p^c$ $\Omega$ (2.13), (5.43) $\Omega(\mathbf{r}_0)$ $\bar{\kappa}^S$	$0.59 \pm 0.08$ $(1.65 \pm 0.16) \omega_r$ $(3.30 \pm 0.33) \omega_r$ $(0.40 \pm 0.07) \omega_r$ $(0.80 \pm 0.13) \omega_r$ $(0.105 \pm 0.005) k_L$
	(a) exp.	$\Delta t = 2\tau_R/\omega_{2r}$ $\theta_R$ (6.55)	$198 \mu\text{s}$ $(0.60 \pm 0.10) \pi$ $(1.10 \pm 0.19) \pi$
	num.	$p^c$ $\Omega(\mathbf{r}_0)$	$0.52$ $0.52$ $0.33 \omega_r$ $0.7 \omega_r$
	(b) exp.	$\delta\omega/2\pi$ (5.7)	$-2 \text{ kHz}$ $-1.5 \text{ kHz}$
	num.	$p^c$ $\Omega(\mathbf{r}_0)$	$0.52$ $0.52$ $0.34 \omega_r$ $0.7 \omega_r$

Table 6.1: Parameters of the results in Fig. 6.13 for the experiment (exp.), the numerical simulation (num.) and the analytical approximation (6.72) (ana.): laser power  $P$ , condensate fraction  $p^c$ , maximum two-photon Rabi frequency  $\Omega$ , local two-photon Rabi frequency  $\Omega(\mathbf{r}_0)$  at the initial atomic position  $\mathbf{r}_0$ , initial atomic momentum in  $x$ -direction  $\hbar\bar{\kappa}^S$ , total interaction time  $\Delta\tau$ , pulse width  $\tau_j$ , pulse area  $\theta_j$ , laser frequency detuning  $\delta\omega$ .



## (3+1)D BRAGG DIFFRACTION: SPATIAL ENVELOPES

Spatial envelopes in addition to temporal envelopes can affect the beamsplitter performance. Eventually, the spatial envelopes of Laguerre-Gaussian (LG) laser beams are added in this Chapter 7 to consider the cumulative effect. Therefore, full (3+1)D simulations are used. For LG-laser beams both, the intensity and the phase show spatial variations, adversely affecting the fidelity as well as the diffraction efficiency of the beamsplitter and leading to an additional transfer of transverse momentum components.

To illustrate these effects and motivate the need of as realistic as possible (3+1)D simulations, the final column integrated density of the wavepacket in the momentum space is depicted in Fig. 7.1. An ideal and an adverse mirror pulse are compared, where the latter is generated with LG-laser beams. For completion, the results using the plane-wave (PW) approximation are also shown. Obviously the effect of realistic LG-laser beams can be crucial. Quantifying this, here, the fidelity is reduced drastically from ideal  $F_i = 1$  to  $F_{\text{PW}} = 0.61$ ,  $F_{\text{LG}} = 0.08$ . The diffraction efficiency is also reduced from  $\bar{\eta}_i = 1$  to  $\bar{\eta}_{\text{PW}} = 0.69$ ,  $\bar{\eta}_{\text{LG}} = 0.41$ . The

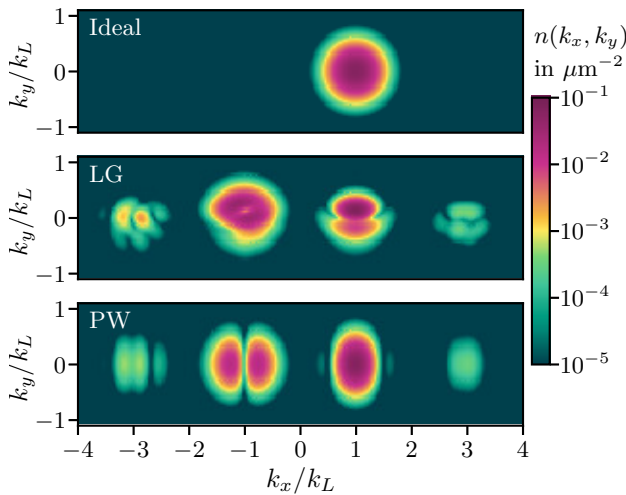


Figure 7.1: Column integrated, atom density in momentum space  $n(k_x, k_y) = \int dk_z |\Psi_g(\mathbf{k})|^2$  after a  $\pi$ -pulse, normalised with  $\int d^3k |\Psi(\mathbf{k})|^2 = 1$ . The initial state is a temporally evolved, symmetric Gaussian wavepacket (2.59) transversally displaced to  $\mathbf{r}_0 = (0, 0.9w_0, 0)$  with momentum width  $\sigma_k = 0.2 k_L$  and expansion size  $\sigma_x = w_0/5 = 2\mu\text{m}$ . Rectangular pulses with  $\Omega = 6\omega_r$ ,  $\tau_R = \tilde{\tau}_{R\pi}(\Omega(\mathbf{r}_0))$  (6.32) and beamwaist  $w_0 = 10\mu\text{m}$  are applied. The ideal situation is compared to the results with Laguerre-Gaussian laser beams (LG) and the plane-wave approximation (PW).

spatial profile of the LG-laser beams is characterised in Section 7.1. In addition to the extreme disadvantages depicted in Fig. 7.1, also weak deviations from the plane-wave idealisation lead to aberrations, which are apparent in the spatially resolved beamsplitter results presented in Section 7.2. Thereby, the influence of the wavefront curvature and the intensity variations to the beamsplitter performance can be differentiated with the radiative force exerted by the laser light field, acting on the atoms. This force is studied in Section 7.3, where it is further used to quantify the transferred transverse momentum components. The influence on the fidelity and diffraction efficiency in details is presented in Section 7.4. Finally, Section 7.5 concludes with analysing misalignment of the laser beams and comparing the results to experiments [1].

## 7.1 SPATIAL PROFILE OF TWO COUNTERPROPAGATING GAUSS-LAGUERRE LASER BEAMS

The fields of experimental beamsplitters are pulsed, bichromatic  $k_{l=\{1,2\}}$ , counterpropagating Laguerre-Gaussian modes (cf. Sec. 2.2.2). In the specific frame  $S'$  (cf. Fig. 5.1), comoving with the nodes of the interference pattern, establishing one single wavenumber  $k_L$  (cf. Sec. 5.3.1). The slowly varying amplitude of the electric field  $\mathcal{E}_l = \mathcal{E}_{0,l} u_l(\mathbf{r})$  (2.21) leads to Rabi frequencies (2.11)

$$\Omega_l(t, \mathbf{r}) = \Omega_{0,l}(t, x_l, \varrho_l) e^{i\varphi(x_l, \varrho_l)}, \quad \Omega_{0,l}(t, x_l, \varrho_l) = \Omega_{0,l}(t) \frac{w_0}{w_l} e^{-\frac{\varrho_l^2}{w_l^2}}, \quad \varphi_l(x_l, \varrho_l) = \frac{k_L \varrho_l^2}{2R_l} - \zeta_l, \quad (7.1)$$

with beam parameters  $p_l = p(x_l)$  (2.22) and the transverse direction  $\varrho_l = \sqrt{y_l^2 + z_l^2}$ . The laser coordinates  $l = \{1, 2\}$  are most generally defined in Section 3.4.2. However, for symmetrically displaced but otherwise perfectly aligned beams, as depicted in Fig. 7.2, the coordinates simplify to  $\varrho_1 = \varrho_2 = \varrho$  and  $x_{1/2} = \ell_x/2 \pm x$  for a distance  $\ell_x$  between both laser beamwaists. This is used in the following, before in Section 7.5 misaligned lasers are taken into account.

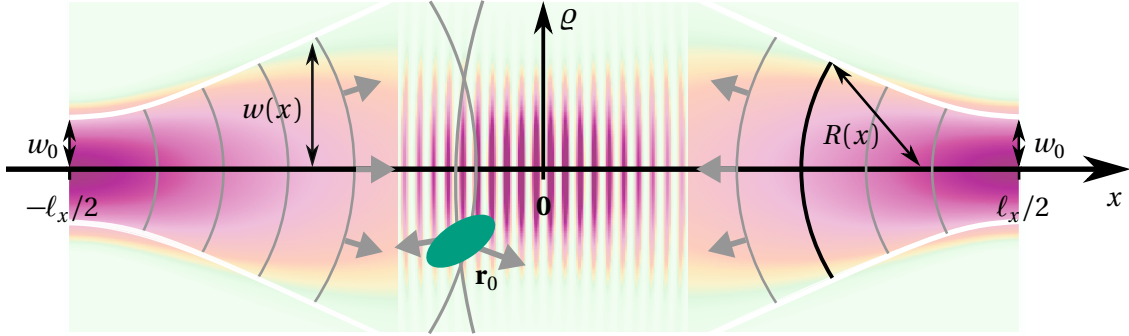


Figure 7.2: Two counterpropagating, bichromatic Laguerre-Gaussian laser beams build a standing wave (5.13) in the frame  $S'$ , with an intensity pattern in cylindrical coordinates  $(x, \varrho)$ . The grey arrows are the local wavevectors,  $w(x)$  is the local waist and the radius of curvature  $R(x)$  are indicated by a black arrow. The distance between the two beamwaists is  $\ell_x$ . The atomic cloud, generally localised at  $\mathbf{r}_0$  is indicated as green ellipse.

Furthermore, for initial states with  $\sigma_x < w_0/3$  one can approximate  $x_{1/2} = \ell_x/2$  for the beam parameters (2.22)  $w_{1,2} = w(\ell_x/2)$ ,  $R_{1,2} = R(\ell_x/2)$ ,  $\zeta_{1,2} = \zeta(\ell_x/2)$ . In case of collimated beams, where  $x_R \gg w(x) \approx w_0 \gg \lambda$ , the phase  $\varphi(x, \varrho) \approx 0$  vanishes according to Eq. (2.24).

### 7.1.1 Local plane-wave approximation

To isolate the momentum transfer of the beamsplitter from the momentum imparted by the dipole force, a local plane-wave (PW) approximation of the LG-beam at the initial centre-of-mass position  $\mathbf{r}_0 = (x_0, \varrho_0)$ ,  $\varrho_0 = (y_0, z_0)$  of the atomic cloud is considered with

$$\Omega_l(t, \mathbf{r}) \approx \Omega_l(t, \mathbf{r}_0) = \Omega_{0,l}(t, x_0, \varrho_0) e^{i\varphi_l(x_0, \varrho_0)} \frac{w_0 \gg \lambda_L}{w_0} \Omega_{0,l}(t) e^{-\varrho_0^2/w_0^2}. \quad (7.2)$$

Thus, the atomic cloud feels only a reduced Rabi frequency but experiences no spatial inhomogeneity. Therefore, simulations with plane waves are independent of the size of the initial state and thus of the ratio  $\sigma_x/w_0$  as long as  $\sigma_x > \lambda$ . For  $\sigma_x \leq \lambda$ , there is still no variation in transversal direction but for these size ratios the interference pattern in propagation direction becomes relevant.

## 7.2 3D BEAMSPLITTER IN POSITION AND MOMENTUM SPACE

Aberrations due to realistic LG-laser beams are apparent already in the density distributions<sup>1</sup>

$$n(t, \mathbf{r}) = |\psi(t, \mathbf{r})|^2, \quad n(t, x, y) = \int dz n(t, \mathbf{r}), \quad N^A = \int d^3r n(t, \mathbf{r}), \quad (7.3a)$$

$$n(t, \mathbf{k}) = |\Psi(t, \mathbf{k})|^2, \quad n(t, k_x, k_y) = \int dk_z n(t, \mathbf{k}), \quad N^A = \int d^3k n(t, \mathbf{k}), \quad (7.3b)$$

as it was visualised for an extreme example in Fig. 7.1. However, there are also recognisable impacts for more moderate scenarios. These can even improve the diffraction efficiency.

Therefore, the column integrated position and momentum density  $n(x, y)$ ,  $n(k_x, k_y)$  together with the phases  $\phi(x, y) = \arg[\psi(x, y, 0)]$ ,  $\phi(k_x, k_y) = \arg[\Psi(k_x, k_y, 0)]$  are shown for the (3+1)D simulations of a mirror [beamsplitter] pulse in Fig. 7.3 [Fig. 7.4]. In the momentum space, the splitting is visible directly after the diffraction pulse, in contrast to the experimental observable, the density distribution in position space is separated only after some time of free evolution. The results for *realistic* LG-laser beams (c), (d) are gauged to the idealised local PW-approximation (b). For the latter, no spatial confinement at all is taken into account, corresponding to  $w_0 \rightarrow \infty$ . Ballistically expanded Gaussian wavepackets (2.59) are considered as atomic initial states (a) with momentum width  $\sigma_k = 0.1 k_L$  and spatial expansion  $\sigma_x = w_0/20 = 2.5 \mu\text{m}$ , located at  $\mathbf{r}_0 = (0, 0, 0)$  for (a-c) and at  $\mathbf{r}_0 = (0, w_0/2, 0)$  in (d), respectively. In Section 6.5 Blackman pulses were found to be optimal. Therefore, they are applied with pulse widths  $\tilde{\tau}_{B\pi}(\Omega(\mathbf{r}_0))$  and  $\tilde{\tau}_{B\pi}/2$  (6.32). The Rabi frequencies  $\Omega(\mathbf{r}_0) = \Omega(\mathbf{r}_0)\omega_{2r} = 4\omega_r$  consider the atomic centre-of-mass position, according to the local PW-approximation (7.2). The longitudinal laser displacement  $\ell_x = 0.1 x_R$  is considered.

The logarithmic scale highlights the imperfections of the Bragg diffraction. The spatial density is modulated, because more than one momentum order is populated. This is elementary for the 50:50 (BS) configuration (Fig. 7.4), showing the oscillation period of  $\lambda_L/2 = 0.39 \mu\text{m}$  due the  $2k_L$  momentum transfer. For the 0:100 mirror (M) (Fig. 7.3) the initially concave spatial phase changes to a convex shape due to flipping the momentum expectation value from  $-k_L$  to  $k_L$ . The circular shape of the phase in the momentum space represents its quadratic form  $(k_x - k_L)^2 + k_y^2 + k_z^2$  (2.60). Using LG-laser beams a different momentum density distribution is observable compared to the PW-idealisation especially for the population remaining undiffracted in the initial state, more clearly for displaced atoms (d). For centred atoms (c) the LG-modes suppress the transfer into higher diffraction orders more strongly. Therefore, the fidelity (5.34)  $F_{\text{LG}} = 0.9653$  as well as the diffraction efficiency (5.33)  $\bar{\eta}_{\text{LG}} = 0.9667$  are insignificantly larger than for the PW-approximation with  $F_{\text{PW}} = 0.9636$  and  $\bar{\eta}_{\text{PW}} = 0.9660$ . However, for displaced atoms, even with the same local effective Rabi frequency, the LG-modes cause an adverse impact, leading to  $F_{\text{LG}}(\mathbf{r}_0 = (0, w_0/2, 0)) = 0.8839$  and  $\bar{\eta}_{\text{LG}}(\mathbf{r}_0 = (0, w_0/2, 0)) = 0.9466$ . The fidelity is reduced significantly, mainly because the dipole force leads to a rogue, transverse momentum component  $\langle k_y^{\text{M}} \rangle = 0.013 k_L$ , primary of the wavepacket in the *mirror-momentum* order  $k_+$  (6.9) with  $\langle k_{y,+}^{\text{M}} \rangle = 0.014 k_L$ , where

$$\langle k_{a=\{x,y,z\}} \rangle = \frac{1}{N^A} \int d^3k k_a n(t, \mathbf{k}), \quad \langle k_{y,+} \rangle = \frac{1}{N^A} \int_0^{2k_L} dk_x \int_{-\infty}^{\infty} dk_y \int_{-\infty}^{\infty} dk_z k_y n(t, \mathbf{k}). \quad (7.4)$$

However, the transfer efficiency is also affected, in particular for transverse momentum components  $k_y \neq 0$ , causing the reduced diffraction efficiency. For the beamsplitter the transverse mirror-momentum  $\langle k_{y,+}^{\text{BS}} \rangle = -0.048 k_L$  is in the opposite direction to  $\langle k_y^{\text{BS}} \rangle = 0.0064 k_L \approx \langle k_y^{\text{M}} \rangle/2$ .

Please note, while the diffraction efficiency and the fidelity depend only on the ratio  $\sigma_x/w_0$  as long as  $w_0 > \sigma_x > \lambda_L$  (cf. App. B.3), the transferred transverse momentum component is characterised by the actual value of the beamwaist as studied in the next Section 7.3.2.

<sup>1</sup> Due to the huge detuning  $\Delta \gg \Omega_0, \Gamma$  the excited state's population is negligible ( $< 10^{-6}$ ), why  $|\psi\rangle \approx \psi_g |g\rangle$ ,  $\psi_g \equiv \psi$ .

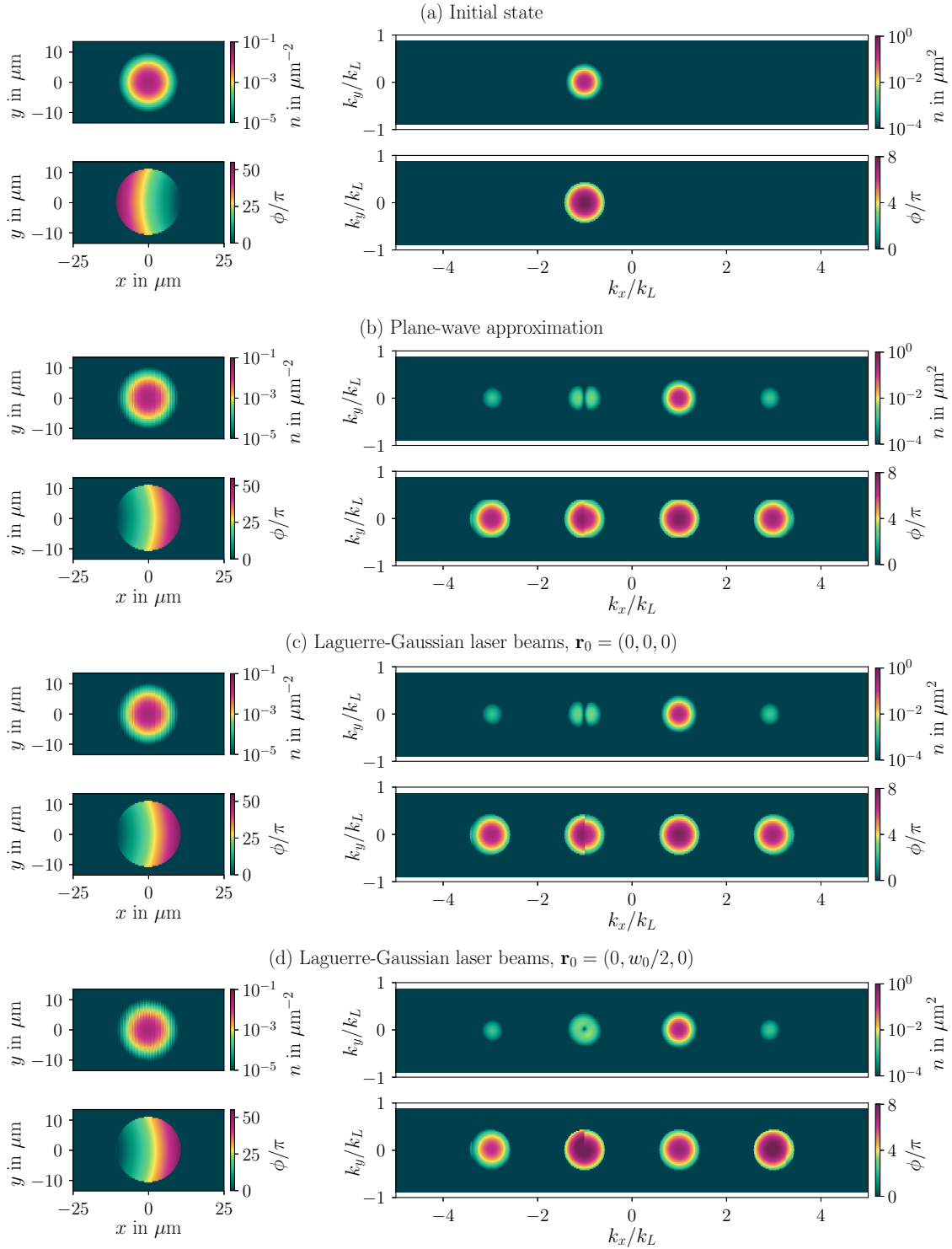


Figure 7.3: Mirror (0:100). Column integrated atomic density  $n$  (7.3) (here normalised to  $N^A = 1$ ) and phase  $\phi = \arg(\psi)$  at  $z = 0$  or  $k_z = 0$  in position (left) and momentum space (right). The phase is set to zero for vanishing densities. The initial state (a) is a temporally evolved Gaussian wavepacket (2.56) of size  $\sigma_x = w_0/20 = 2.5 \mu\text{m}$ , momentum width  $\sigma_k = 0.1 k_L$  and initial position  $\mathbf{r}_0$ . Blackman pulses of width  $\tilde{\tau}_{B\pi}(\Omega(\mathbf{r}_0))$  (6.32) with  $\Omega(\mathbf{r}_0) = \Omega(\mathbf{r}_0) \omega_{2r} = 4 \omega_r$ ,  $\Delta\tau = 2\pi\tilde{\tau}_{B\pi}$  and beamwaist  $w_0 = 50 \mu\text{m}$  are applied, considering idealised plane waves (b) and Laguerre-Gaussian laser beams (c), (d). Further parameters are given in Tables A.1 and A.2.

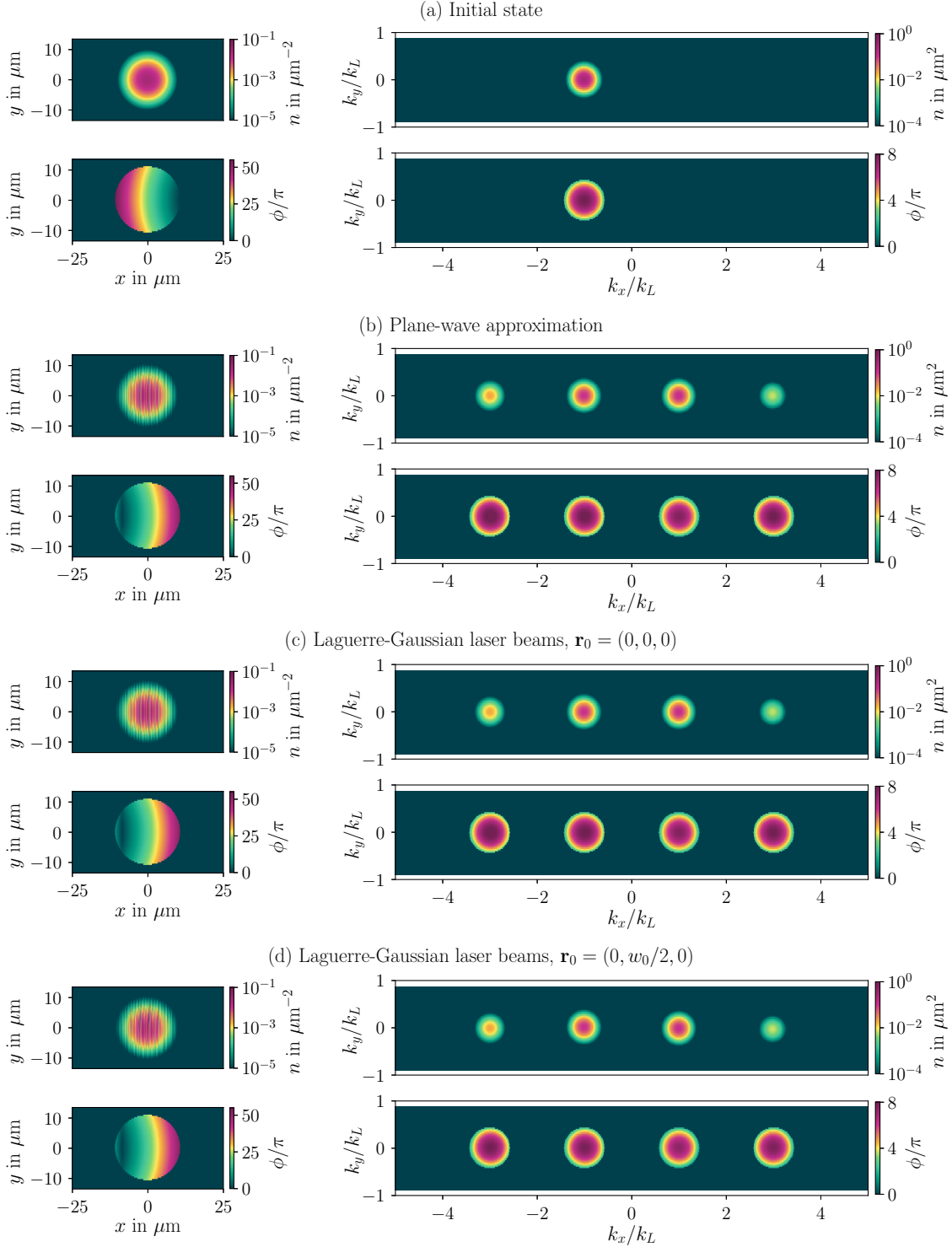


Figure 7.4: Beamsplitter (50:50). Column integrated atomic density  $n$  (7.3) (here normalised to  $N^A = 1$ ) and phase  $\phi = \arg(\psi)$  at  $z = 0$  or  $k_z = 0$  in position (left) and momentum space (right). The phase is set to zero for vanishing densities. The initial state (a) is a temporally evolved Gaussian wavepacket (2.56) of size  $\sigma_x = w_0/20 = 2.5 \mu\text{m}$ , momentum width  $\sigma_k = 0.1 k_L$  and initial position  $\mathbf{r}_0$ . Blackman pulses of width  $\tilde{\tau}_{B\pi}(\Omega(\mathbf{r}_0))/2$  (6.32) with  $\Omega(\mathbf{r}_0) = \Omega(\mathbf{r}_0)\omega_{2r} = 4\omega_r$ ,  $\Delta\tau = \pi\tilde{\tau}_{B\pi}$  and beamwaist  $w_0 = 50 \mu\text{m}$  are applied, considering idealised plane waves (b) and Laguerre-Gaussian laser beams (c), (d). Further parameters are given in Tables A.1 and A.2.

### 7.3 RADIATIVE FORCE

Even for perfectly aligned laser beams, the transverse intensity variations and the wavefront curvature can cause a momentum transfer in the transverse direction. The radiative force exerted during the light-matter interaction provides insights to which of them is dominant. The force operator  $\hat{\mathbf{F}}$  is given by the Heisenberg equation for the atomic momentum operator [181]

$$\hat{\mathbf{F}} = \partial_t \hat{\mathbf{p}} = \frac{i}{\hbar} [\hat{H}, \hat{\mathbf{p}}] = -\frac{\partial \hat{H}}{\partial \mathbf{r}} = -\nabla \hat{V}(\mathbf{r}), \quad \langle \hat{\mathbf{F}} \rangle = \text{Tr}\{\hat{\mathbf{F}} \hat{\rho}\}, \quad (7.5)$$

with the force expectation value  $\langle \mathbf{F} \rangle$  and the resulting momentum expectation value

$$\langle \hat{\mathbf{k}} \rangle = \frac{1}{\hbar} \int dt \text{Tr}\{\hat{\mathbf{F}}(t, \mathbf{r}) \hat{\rho}(t, \mathbf{r})\}. \quad (7.6)$$

Therefore, the reduced density operator  $\hat{\rho}$  of the atomic system needs to be considered.

In the classical approximation of the Ehrenfest theorem [182, 183] the force expectation value is Taylor expanded

$$\langle \hat{\mathbf{F}} \rangle = \mathbf{F}(\langle \hat{\mathbf{r}} \rangle) + \frac{1}{2} \mathbf{F}''(\langle \hat{\mathbf{r}} \rangle) (\Delta \mathbf{r})^2 + \dots \approx \mathbf{F}(\langle \hat{\mathbf{r}} \rangle). \quad (7.7)$$

Considering only the first, classical contribution is valid exactly if  $\hat{\mathbf{F}}$  is a linear function of the position  $\mathbf{r}$ , or approximately if the width of the probability density is small in comparison to the typical length scale of the force variations, here, for atomic initial states much smaller than the beamwaist  $\sigma_x \ll w_0$ .

Provided an interaction with one classical laser beam with a potential of the form (2.12)

$$\hat{V}(\mathbf{r}) = \frac{\hbar}{2} \Omega_0(\mathbf{r}) e^{-i\Phi(\mathbf{r})} \hat{\sigma}^\dagger + \text{h.c.}, \quad (7.8)$$

the force operator reads

$$\hat{\mathbf{F}} = -\frac{\hbar}{2} \hat{\sigma}^\dagger \Omega_0(\mathbf{r}) e^{-i\Phi(\mathbf{r})} [\alpha(\mathbf{r}) - i\beta(\mathbf{r})] + \text{h.c.} \quad (7.9)$$

The two contributions

$$\alpha(\mathbf{r}) = \frac{\nabla \Omega(\mathbf{r})}{\Omega(\mathbf{r})}, \quad \beta(\mathbf{r}) = \nabla \Phi(\mathbf{r}), \quad (7.10)$$

characterise the spatial intensity variations with  $\alpha$ , leading to the so-called *reactive* or *dipole force* and the variation of the phase with  $\beta$ , defining the *dissipative force* also called *radiation pressure*. Regarding one LG-laser beam in its intrinsic reference frame (2.23) the contributions to the different force components for cylindrical coordinates  $\hat{\mathbf{F}} = (\hat{F}_x, \hat{F}_\varrho, \hat{F}_\phi)$  in propagation  $x$ , transversal direction  $\varrho = \sqrt{y^2 + z^2}$  and vanishing  $\phi$ -component  $\hat{F}_\phi = \alpha_\phi = \beta_\phi = 0$ , can be easily evaluated and simplified for the limit of collimation

$$\alpha_x = \frac{x w_0^2}{x_R^2 w(x)^2} \left( \frac{2\varrho^2}{w(x)^2} - 1 \right) \stackrel{w(x) \approx w_0}{\approx} \frac{x}{x_R^2} \left( \frac{2\varrho^2}{w_0^2} - 1 \right) \stackrel{x \ll x_R}{\approx} 0, \quad (7.11)$$

$$\alpha_\varrho = \frac{2\varrho}{w(x)^2} \stackrel{w(x) \approx w_0}{\approx} \frac{2\varrho}{w_0^2} \stackrel{x \ll x_R}{\approx} -\frac{2\varrho}{w_0^2},$$

$$\beta_x = -k_L + \frac{w_0^2}{w(x)^2 x_R} - k_L \frac{\varrho^2}{x^2} \left( \frac{x_R^2}{R(x)^2} - \frac{x}{2R(x)} \right) \stackrel{w(x) \approx w_0}{\approx} -k_L \left( 1 + \frac{\varrho^2(x_R^2 - x^2)}{2(x_R^2 + x^2)^2} \right) + \frac{1}{x_R} \stackrel{w_0 \gg \lambda_L}{\approx} -k_L,$$

$$\beta_\varrho = \frac{k_L \varrho}{R(x)} \stackrel{w(x) \approx w_0}{\approx} -\frac{k_L \varrho}{R(x)} \stackrel{w_0 \gg \lambda_L}{\approx} 0. \quad (7.12)$$

2 This is a requirement, that can be true even for *small* laser beams, but it is automatically fulfilled for  $w_0 \gg \lambda_L$ .



The approximation demonstrates the expected momentum transfer  $k_L$  in longitudinal  $x$ -direction due to the radiation pressure ( $\beta$ ) as well as a rogue transverse momentum kick, for large lasers mainly due to the dipole force ( $\alpha$ ).

For optical wavelengths  $\lambda \lesssim \mu\text{m}$  and beamwaists of collimated beams in the range of  $w_0 \sim \text{mm}$ , the Rayleigh lengths  $x_R$  are several meters, thus

$$x_R \gg w_0 > \sigma_x > \lambda, \quad (7.13)$$

for sizes of the initial state in the range  $\sigma_x \sim 1$  to  $1000 \mu\text{m}$ . Therefore, as applied in Eq. (7.11), the transversal dipole forces are stronger than the dipole forces along the propagation direction  $x$ . Latter are actually negligible for  $x \ll x_R$ .

### 7.3.1 Radiation pressure due to wavefront curvature

While the essential beamsplitting process is based on the momentum translation operator (4.16) included in the radiation pressure, the transferred momentum in transverse direction originates in particular for collimated laser beams from the dipole force. However, the additional transverse momentum component transferred with the radiation pressure can be easily estimated, even without evaluating the dissipative force. Therefore, it can be decided quantitatively justified when the wavefront curvature needs to be taken into account. The effectively transferred momentum from the counterpropagating laser beams is given by

$$\mathbf{k}_{\text{eff}} = \mathbf{k}_1 - \mathbf{k}_2. \quad (7.14)$$

Therefore, knowing the spatial-dependent orientation of the laser wavevectors, the transferred transverse momentum component is directly determined. Regarding the total spatial dependent phase of the LG-field (2.23) propagating in  $x$ -direction

$$\Phi(\mathbf{r}) = -\varphi(x, \varrho) - k_L x = -k_L x - k \frac{\varrho^2}{2R(x)} + \zeta(x), \quad (7.15)$$

the wavefront curvature is given by the reciprocal of the radius of curvature  $R$ . This defines the orientation of the wavevector at a certain position  $(x_0, \varrho_0, 0)$  inside the laser region. Regarding the sketch in Fig. 7.5, its components are given by

$$k_{L,x}(x_0, \varrho_0)/k_L = \cos \theta = 1 - \mathcal{O}(\theta^2), \quad k_{L,\varrho}(x_0, \varrho_0)/k_L = \sin \theta = \theta - \mathcal{O}(\theta^3). \quad (7.16)$$

Within the small angle approximation (SAA) it simplifies to

$$k_{L,\varrho}^{\text{SAA}}(x_0, \varrho_0) \approx \theta k_L \approx \frac{\varrho_0 k_L}{R(x_0)} = -\beta_{\varrho}, \quad \theta = \arctan\left(\frac{\varrho_0}{R(x_0)}\right) = \frac{\varrho_0}{R(x_0)} - \mathcal{O}\left(\left(\frac{\varrho_0}{R(x_0)}\right)^3\right), \quad (7.17)$$

recovering the transversal contribution of the radiation pressure  $\beta$  (7.10). The maximum is reached for a minimal radius of curvature  $R_{\min} = R(x_R) = 2x_R$ . Therefore, together with a maximum transverse displacement of  $\varrho_0 = w_0$  the limit is  $k_{L,\varrho}^{\text{SAA}}(x_0, \varrho_0) \leq w_0 k_L / 2x_R = 1/w_0$  inversely proportional to the beamwaist  $w_0$ , which is why  $k_{L,\varrho}(x_0, \varrho_0)$  vanishes for large lasers  $w_0 \gg \lambda_L$ .

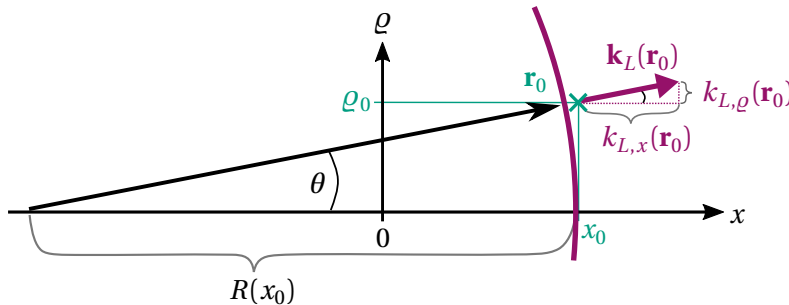


Figure 7.5: Orientation of the laser wavevector  $\mathbf{k}_L$ , normal to the wavefront (magenta), depending on the position  $\mathbf{r}_0 = (x_0, \varrho_0)$  inside the laser region and defined by the radius of curvature  $R(x_0)$  and the angle  $\theta$ .

Leaving tilted laser beams out of consideration, three different *limits* of geometric arrangements of the lasers are conceivable, depicted in Fig. 7.6.

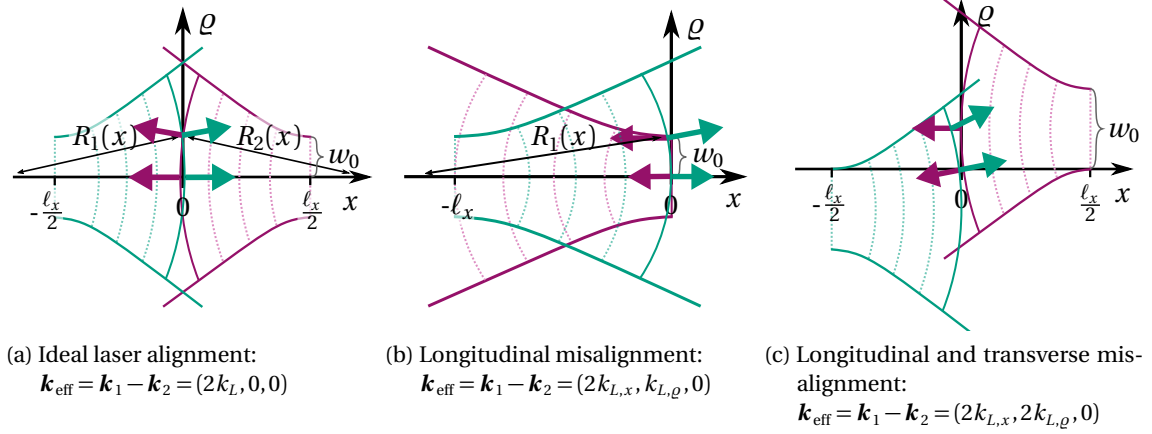


Figure 7.6: Different laser geometries lead to different momentum transfers to the atomic wavepacket  $\mathbf{k}_{\text{eff}} = \mathbf{k}_1 - \mathbf{k}_2$ . The amount is defined by the radius of curvature of laser 1 and 2, the distance between the laser origins  $\ell = (\ell_x, \ell_\rho, 0)$  and the position of the wavepacket inside the laser region, in units of the Rayleigh length  $x_R$  in longitudinal direction and in units of the minimal beamwaist  $w_0$  in transverse direction.

In scenario (a), the atoms are positioned exactly in the centre between both laser origins. In the ideal limit, the origin of both lasers coincides with the atomic initial position, but also for a finite distance  $\ell_x$  between both lasers the transferred transverse momentum components due to the wavefront curvature cancel each other. For a *maximal* longitudinal misalignment in (b), one laser origin coincides with the initial atomic position, corresponding here to a plane wave, while the other is displaced, providing a wavefront curvature at the atom's position. Therefore, the total transverse momentum component due to the wavefront curvature of the displaced laser is transferred to the atom without compensation. Adding an opposite transverse displacement to both lasers in (c), leads contrary to scenario (a) not to the compensation but rather to an enhancement of the transferred transverse momentum. For a symmetric displacement this limits in the sum  $k_{\text{eff},\rho} = k_{1,\rho} + k_{2,\rho}$ . Because setup (c) promises the largest rogue momentum components, it is studied for different beamwaists and transverse atomic initial positions. The analytical result for the  $\rho$ -component of the transferred momentum kick with an atomic initial location  $\mathbf{r}_0 = (0, \rho_0)$  with a transverse displacement of  $\rho_0 = \xi_0 w_0$  and a distance between both lasers  $\ell_x = 2\chi x_R$ ,  $\ell_\rho = 2\gamma w_0$ , with  $0 < \chi, \gamma \leq 1$ , yields the simple relation in the small-angle approximation

$$k_{\text{eff},\rho}^{\text{SAA}} = \left( \frac{\rho_1}{R(x_1)} - \frac{\rho_2}{R(x_2)} \right) k_L = \left( \frac{\xi_0 w_0}{R(\chi x_R)} - \frac{(\xi_0 - 2\gamma)w_0}{R(\chi x_R)} \right) k_L = \frac{4\gamma}{w_0 \chi (1 + \chi^{-2})} \leq \frac{2}{w_0}. \quad (7.18)$$

This is independent of the transverse displacement  $\xi_0$  and the maximum for  $\chi = \gamma = 1$  is purely defined by the beamwaist  $w_0$ . In an experiment, for  $\gamma > 1$  the laser misalignment is clearly observable, therefore one can restrict  $\gamma \leq 1$ . In Fig. 7.7, the result (7.18) for  $\chi = \gamma = 1$  is compared to the according numerical expectation value of the *mirror-momentum*<sup>3</sup> (7.4)  $\langle k_{y,+} \rangle$  with choosing for the Cartesian simulation grid  $z_0 = 0$  and thus  $\rho_0 = y_0$ . To observe only the transferred transverse momentum due to the radiation pressure the spatial intensity

3 The effective momentum  $k_{\text{eff}}$  gives the momentum transferred due to deep-Bragg diffraction. Therefore, the numerical analogue is the momentum expectation value of this part of the wavepacket, which is diffracted into the *mirror-diffraction order*, here for first-order diffraction in  $x$ -direction  $k'_x = k_+$  (6.9) with  $0 \leq k_+ < 2k_L$ .



variation of the laser fields is turned-off, using  $\Omega_l(t, \mathbf{r}) = \Omega_l(t) \exp(i k_L \rho_l^2 / 2R_l)$  (7.1). To address a suitable Bragg regime (cf. Fig. 6.11), a two-photon Rabi frequency of  $\Omega = 2\omega_r$  is applied for rectangular<sup>4</sup> (6.3)  $\pi$ -pulses of width  $\tilde{\tau}_{R\pi}(\Omega)$  (6.32). The initial atomic state is prepared as a time-evolved Gaussian wavepacket (2.59) with a symmetric expansion  $\sigma_x = 1.25 \mu\text{m}$  and momentum width  $\sigma_k = 0.1 k_L$ . The numerical results confirm the simple approximation (7.18). Only for highly focused laser beams an extremely weak linear dependence of the transverse displacement is visible but these deviations are negligible. Therefore, the transferred transverse momentum kick due to the wavefront curvature is practically independent of the size ratio between atomic cloud and laser  $\sigma_x / w_0$ . In addition, even the maximum transferred transverse momentum, as considered here in scenario (c) of Fig. 7.6, is insignificant for collimated beams with beamwaists in the range of millimetres resulting in  $\langle k_{y,+} \rangle \leq 2/w_0 \sim 0.002 \mu\text{m}^{-1} \approx 2 \times 10^{-4} k_L$ . Furthermore, the experimental scenario corresponds more to scenario (a), where  $\langle k_{y,+} \rangle$  vanishes due to symmetry with  $\lim_{\alpha, \gamma \rightarrow 0} k_{\text{eff},y}^{\text{SAA}} = 0$  (7.18).

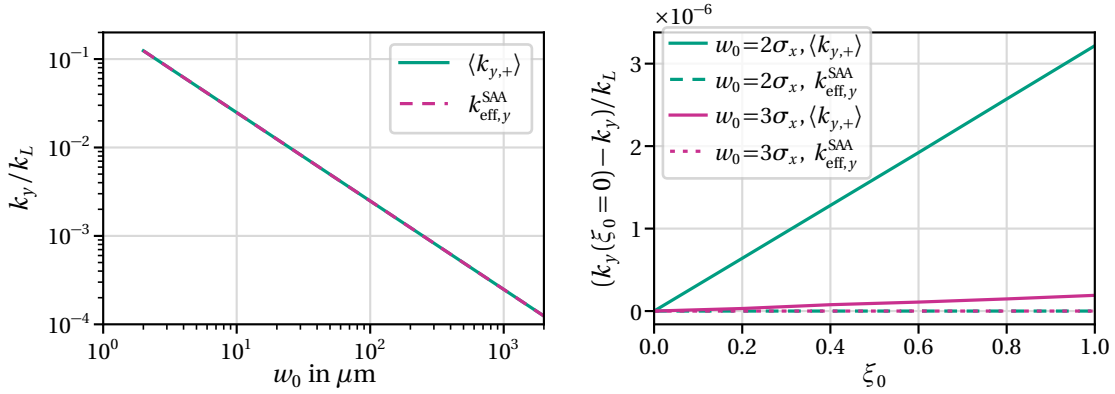


Figure 7.7: Transversal momentum kick  $k_y$  due to the radiation pressure, for a maximum atomic transversal displacement  $\xi_0 = y_0/w_0 = 1$  depending on the beamwaist  $w_0$  (left), respectively the difference  $k_y(\xi_0 = 0) - k_y(\xi_0)$  versus  $\xi_0$  for different  $w_0$  (right), where  $k_y(\xi_0 = 0) = 0.10[0.07]k_L$  for  $w_0 = 2.5[3.75]\mu\text{m}$ . The numerical results confirm the relation  $k_y = 2/w_0$  of Eq. (7.18) for  $\alpha = \gamma = 1$ .

### 7.3.2 Dipole force due to intensity variations

The intensity variations of the laser field, especially in transverse direction, cannot be neglected, if the atoms are not located at the centre of the beam line or if their expansion is not much smaller than the laser-beam size. In these cases, the atoms adopt a spatial dependent transverse momentum component and/or their transverse velocity spread becomes, depending on the sign of the laser detuning, squeezed or stretched.

To quantify this, the expectation value of the reactive force operator or rather the resulting momentum expectation value  $\langle \hat{k}_Q \rangle$  (7.6) in radial direction needs to be evaluated. Therefore, the full time-dependent solution  $\hat{\rho}(t, \mathbf{r})$  is required. But knowing the time-dependent solution and transforming it into the momentum space, one finds the ground-state momentum expectation value components directly from Eq. (7.4). However, a simple approximation without the requirement of the full beamsplitter solution is desirable and can be derived as follows.

<sup>4</sup> The effective momentum kick is independent of the pulse shape. Therefore, rectangular pulses are used, because they provide the shortest computational times for the simulations.

### Simple steady-state approximation

For collimated laser beams  $w_0 \gg \lambda_L$  the wavefront curvature and intensity variations in propagation direction are negligible as pointed out in Section 2.2.2, Eq. (2.24). Therefore, the transverse component of the reactive force operator for one (1) collimated (c) laser reads

$$\hat{F}_{1,\varrho}^c = \hbar \frac{\xi}{w_0} \Omega_0^c(\xi) e^{ik_L x} \hat{\sigma}^\dagger + \text{h.c.}, \quad \Omega_0^c(\xi) = \Omega_0 e^{-\xi^2}, \quad \xi \equiv \frac{\varrho}{w_0}, \quad (7.19)$$

because  $\alpha_\varrho = \partial_\varrho \Omega_0^c(\varrho)/\Omega_0^c(\varrho) = -2\varrho/w_0^2$ . Using a local density approach the force expectation value can be approximated, using the common semiclassical limit [103, 181] for atomic wavepackets sufficiently well localised in position as well as in momentum space. Their position is given by  $\mathbf{r} = \mathbf{r}_0 + \mathbf{v}_0 t = \mathbf{r}_0 + v_0 \mathbf{e}_x t$ , because in the chosen reference frame the atoms move in  $x$ -direction but initially without a velocity component in  $\varrho$ -direction. The Rabi frequency  $\Omega_0^c$  depends only on  $\varrho$  not on  $x$ . Therefore, at the atomic position it is time independent  $\Omega_0^c(\mathbf{r} = \mathbf{r}_0 + \mathbf{v}_0 t) = \Omega_0^c(\varrho_0)$ . On the other hand, the phase is now time dependent  $\varphi^c(t, \mathbf{r}) = -\mathbf{k}_L \mathbf{v}_0 t$ . This can be considered by taking into account the resulting Doppler shift within the detuning  $\Delta_D = \Delta - \mathbf{k}_L \mathbf{v}_0$ . Using the fact that the mean value of  $\hat{\sigma}^\dagger$  is  $\rho_{ge}(t)$  the optical Bloch equations<sup>5</sup>

$$\partial_t \rho_{ee} = -\Gamma \rho_{ee} - \frac{i}{2} \Omega_1^c(\mathbf{r}_0) \rho_{ge} + \frac{i}{2} \Omega_1^c(\mathbf{r}_0)^* \rho_{eg}, \quad (7.20)$$

$$\partial_t \rho_{gg} = +\Gamma \rho_{ee} - \frac{i}{2} \Omega_1^c(\mathbf{r}_0)^* \rho_{eg} + \frac{i}{2} \Omega_1^c(\mathbf{r}_0) \rho_{ge}, \quad (7.21)$$

$$\partial_t \rho_{eg} = (i\Delta_D - \frac{\Gamma}{2}) \rho_{eg} + \frac{i}{2} \Omega_1^c(\mathbf{r}_0) (\rho_{ee} - \rho_{gg}) \quad (7.22)$$

must be solved to evaluate the force expectation value. They depend on the local Rabi frequency for one collimated laser beam

$$\Omega_1^c(\mathbf{r}_0) \equiv \Omega_0^c(\xi_0) \exp(ik_L x_0), \quad \xi_0 \equiv \frac{\varrho_0}{w_0}. \quad (7.23)$$

Using further the local steady-state solutions  $\partial_t \rho = 0$  results in

$$\rho_{ge}^{c,st}(\mathbf{r}_0) = \frac{1}{2} \Omega_0 e^{-\xi_0^2} e^{-ik_L x_0} \frac{\Delta_D + i\frac{\Gamma}{2}}{\Delta_D^2 + \frac{\Gamma^2}{4} + \frac{|\Omega_1^c(\mathbf{r}_0)|^2}{2}}. \quad (7.24)$$

Therefore, the transverse local force expectation value at the position  $\varrho_0$  [cf. Eq. (7.7)] reads

$$\langle \hat{F}_{1,\varrho}^{c,st} \rangle|_{\varrho_0} = \hbar \Omega_0^2 \frac{\xi_0}{2w_0} e^{-2\xi_0^2} \left( \frac{\Delta_D + i\frac{\Gamma}{2}}{\Delta_D^2 + \frac{\Gamma^2}{4} + \frac{|\Omega_1^c(\mathbf{r}_0)|^2}{2}} + \text{h.c.} \right) = \hbar \Omega_0^2 \frac{\xi_0}{w_0} e^{-2\xi_0^2} \frac{\Delta_D}{\Delta_D^2 + \frac{\Gamma^2}{4} + \frac{|\Omega_1^c(\mathbf{r}_0)|^2}{2}} \quad (7.25)$$

and depends only on the transversal direction  $\varrho_0$ . However, the aim is to estimate the exerted force of the two counterpropagating lasers (given the same intensity). For low intensities with saturation parameters  $s = \Omega_0^2/2(\Delta^2 + \Gamma^2/4)^{-1} \ll 1$  the interference effects of the two beams can be neglected and the full local force is simply the sum

$$\langle \hat{F}_\varrho^{c,st} \rangle|_{\varrho_0} = \langle \hat{F}_{1,\varrho}^{c,st}(\mathbf{k}_L = k_L \mathbf{e}_x) \rangle|_{\varrho_0} + \langle \hat{F}_{1,\varrho}^{c,st}(\mathbf{k}_L = -k_L \mathbf{e}_x) \rangle|_{\varrho_0} \quad (7.26)$$

$$= \hbar \Omega_0^2 \frac{\xi_0}{w_0^2} e^{-2\xi_0^2} \left( \frac{\Delta + 2\mu_0 \omega_r}{(\Delta + 2\mu_0 \omega_r)^2 + \frac{\Gamma^2}{4} + \frac{|\Omega_1^c(\mathbf{r}_0)|^2}{2}} + \frac{\Delta - 2\mu_0 \omega_r}{(\Delta - 2\mu_0 \omega_r)^2 + \frac{\Gamma^2}{4} + \frac{|\Omega_1^c(\mathbf{r}_0)|^2}{2}} \right) \quad (7.27)$$

$$\approx 2\hbar \frac{\Omega_0^2}{\Delta} \frac{\xi_0}{w_0} e^{-2\xi_0^2} = 4\hbar \Omega_0 \frac{\xi_0}{w_0} e^{-2\xi_0^2} = -\partial_\varrho V_{\text{dip}}(x=0, \varrho)|_{\varrho_0}. \quad (7.28)$$

<sup>5</sup> The optical Bloch equations can be derived straightforwardly from the master equation (3.22) with one operator  $\hat{C} = \sqrt{\Gamma} \hat{\sigma}$ . A detailed derivation for a three-level system is given for the Raman velocity filter for hot calcium ions in Section 10.3.2, which can be easily reduced to the two-level approach.

In Eq. (7.27) the initial velocity of the atoms is expressed with  $v_0 = \mu_0 \hbar k_L / M$  using the recoil frequency  $\omega_r$  (4.23), for first-order Bragg diffraction  $\mu_0 = -1$ . Regarding the separation of frequency scales  $\omega_r \ll \Gamma \ll \Omega_0 \ll \Delta$  (5.36), the approximation (7.28) can be made, demonstrating the negative parity of the force concerning  $\varrho_0$  as well as the detuning  $\Delta$ . In addition, it reveals  $4\hbar\Omega/w_0$  as the spring constant, resulting also from the gradient of the optical dipole potential  $V_{\text{dip}}(x, \varrho) = \hbar\Omega_0^2 \exp(-2\xi^2)/\Delta$  for two counterpropagating collimated laser beams [cf. Eqs. (5.38), (7.23)].

This force acting during the interaction time  $T$  leads to a transverse momentum with the same parity and with linear time dependency for a rectangular pulse<sup>6</sup> (6.3)

$$\langle \hat{k}_\varrho^{c,st} \rangle|_{\varrho_0} = \frac{1}{\hbar} \int_0^T dt \langle \hat{F}_\varrho^{c,st} \rangle|_{\varrho_0} = \frac{T}{\hbar} \langle \hat{F}_\varrho^{c,st} \rangle|_{\varrho_0}. \quad (7.29)$$

In the deep-Bragg regime for a mirror  $\pi$ -pulse of width  $\tau_{R\pi}(\Omega^c(\mathbf{r}_0))$  (6.8) the interaction time is  $T_\pi = \pi/|\Omega^c(\mathbf{r}_0)|$  and Eq. (7.29) simplifies to

$$\langle \hat{k}_{\varrho,\pi}^{c,st} \rangle|_{\varrho_0} = \frac{\Omega}{|\Omega|} \frac{4\pi\xi_0}{w_0} \leq \frac{\Omega}{|\Omega|} \frac{4\pi}{w_0}, \quad \text{for } \xi_0 = \frac{\varrho_0}{w_0} \leq 1. \quad (7.30)$$

Here, the local two-photon Rabi frequency  $\Omega^c(\mathbf{r}_0) = \Omega \exp(-2\varrho_0^2/w_0^2)$  at the initial position  $\mathbf{r}_0 = (x_0, \varrho_0)$  [cf. (7.2)] is considered. Clearly, it shows a negative parity with respect to the detuning  $\Delta$  included in the two-photon Rabi frequency  $\Omega = |\Omega_0|^2/2\Delta$  (5.43). In addition, its maximum is even  $2\pi$  times larger than the maximum transverse momentum kick at  $x = x_R$  due to wavefront curvature (7.18).

Finally, in the impact approximation, the mean force and resulting momentum kick to an entire atomic wavepacket is given by spatially averaging over the initial density  $n(t=0, \mathbf{r})$  (7.3), assuming a population completely in the ground state

$$\langle \hat{F}_\varrho^{c,st} \rangle = \int d^3r \langle \hat{F}_\varrho^{c,st} \rangle|_\varrho \frac{n(0, \mathbf{r})}{N^A} = \frac{4\hbar\Omega}{N^A w_0} \int d^3r \xi e^{-2\xi^2} n(0, \mathbf{r}), \quad (7.31)$$

$$\langle \hat{k}_\varrho^{c,st} \rangle = \frac{T}{\hbar} \langle \hat{F}_\varrho^{c,st} \rangle. \quad (7.32)$$

### Time-dependent force

Using the collimated (c) beam approximation (7.23), the spatial dependent Rabi frequency for two (2) exactly counterpropagating laser beams, with equal amplitude is approximately

$$\Omega_2(\mathbf{r}) \approx \Omega_2^c(\mathbf{r}) = \Omega_1^c(x, \varrho) + \Omega_1^c(-x, \varrho) = 2\Omega_0 e^{-\xi^2} \cos(k_L x) = 2\Omega_0^c(\xi) \cos(k_L x). \quad (7.33)$$

This leads to the force operator and its local time-dependent expectation value

$$\hat{F}_\varrho^c(\mathbf{r}) = \hbar \frac{\xi}{w_0} \Omega_2^c(\mathbf{r}) (\hat{\sigma}^\dagger + \hat{\sigma}), \quad \langle \hat{F}_\varrho^c(t, \mathbf{r}) \rangle = \hbar \frac{\xi}{w_0} \Omega_2^c(\mathbf{r}) [\rho_{eg}(t, \mathbf{r}) + \rho_{ge}(t, \mathbf{r})]. \quad (7.34)$$

The matrix elements of the density operator are defined with the time-dependent solution of the Schrödinger equation<sup>7</sup>  $\rho_{ij} = \psi_i \psi_j^*$ . Making use of the adiabatic elimination of the excited

<sup>6</sup> In the steady-state approximation, the transferred momentum depends only on the pulse area, but not on the pulse shape. This applies approximately also for the full numerical results. Therefore, rectangular pulses are studied, providing the shortest computational times.

<sup>7</sup> Only pure states are considered and because of the extremely large detuning  $\Delta \gg \Gamma$  spontaneous emission can be neglected.

state (cf. Sec. 5.5.1), itself and thus the density matrix elements can be expressed in terms of the ground-state wavefunction

$$\psi_e = \frac{\Omega_0^c(\xi)}{\Delta} \cos(k_L x) \psi_g(t, \mathbf{r}), \quad \rho_{ge} = \rho_{eg} = \frac{\Omega_0^c(\xi)}{\Delta} \cos(k_L x) n(t, \mathbf{r}). \quad (7.35)$$

Therefore, the force and the momentum expectation value of the atomic wavepacket read

$$\langle \hat{F}_\rho^c(t) \rangle = \frac{8\hbar\Omega}{N^A w_0} \int d^3r \xi e^{-2\xi^2} \cos^2(k_L x) n(t, \mathbf{r}) \approx \frac{4\hbar\Omega}{N^A w_0} \int dy \int dz \xi e^{-2\xi^2} n(t, y, z), \quad (7.36)$$

$$\langle \hat{k}_\rho^c \rangle = \frac{1}{\hbar} \int_0^T dt \langle \hat{F}_\rho^c(t) \rangle \approx \int_{\tau_i}^{\tau_f} d\tau \frac{\Omega}{N^A w_0} \int dy \int dz \xi e^{-2\xi^2} n(\tau, y, z). \quad (7.37)$$

For wavepackets with sizes larger than the wavelength  $\sigma_x > \lambda_L$ , the interference term  $\cos^2(k_L x)$  vanishes with averaging over one wavelength. Then, for  $t = 0$  the result coincides with the impact approximation (7.31), which was derived from the steady-state solutions of the interaction with one laser.

### Transverse momentum kick

The approximative results for collimated laser beams  $\langle k_\rho^c \rangle$  (7.37) and additionally using the steady-state solution  $\langle k_\rho^{c, st} \rangle$  (7.32) are compared to the full numerical expectation value  $\langle \hat{k}_\rho \rangle$  (7.4) for different beamwaists and displacements  $\rho_0$  of the initial state.

The transverse intensity variations of the laser field are maximum at the minimal beamwaist. Therefore, a vanishing distance  $\ell = (0, 0, 0)$  between the laser origins is chosen, coinciding with the atomic initial position in propagation direction  $x_0 = 0$ . The initial state is a time expanded Gaussian wavepacket with symmetrical width in position  $\sigma_x = 1.25 \mu\text{m}$  and momentum space  $\sigma_k = 0.1 k_L$ . To address the deep-Bragg regime the Rabi frequency  $\Omega(\rho_0 = 0) = 2\omega_r$  is used to apply rectangular  $\pi$ -pulses of widths  $\tilde{\tau}_{R\pi}(\Omega(\mathbf{r}_0))$  (6.32) considering the local Rabi frequency at the initial position  $\mathbf{r}_0 = (x_0, y_0, z_0)$  (7.2). The displacement is  $x_0 = z_0 = 0$ ,  $y_0 = \rho_0 = \xi_0 w_0$  with  $\xi = \{0.1, 0.5, 1\}$ . The results are depicted in Fig. 7.8.

As predicted from the steady-state approximation (7.30), the transverse momentum kick reduces with increasing the beamwaist and in contrast, it increases for larger atomic displacements. However, while this approximation has a negative parity for the detuning, the numerical results show, that also the absolute value of the momentum kick depends on the sign of  $\Delta$ . This cannot be described with the steady-state approximation, not even without making use the separation of frequencies, i.e. using Eq. (7.27). Applying Eq. (7.27) leads to relative differences  $< 10^{-7}$  in comparison to Eq. (7.28), which are negligible, because the relative differences between the numerical results and the steady-state approximation are in the range of  $10^{-1}$ . The deviation to the analytical approximation (7.30) is quantified with comparing the numerical slope  $m$  of  $\langle k_y \rangle \approx m/w_0$  (for  $w_0 > 10 \mu\text{m}$ ) with the analytical slope  $m_\pi = \text{sgn}(\Delta) 4\pi \xi_0$  of  $\langle k_{\rho, \pi}^{c, st} \rangle|_{\rho_0} = m_\pi/w_0$ . Comparing the ratio  $\zeta_{\xi_0}^{\text{sgn}(\Delta)} = m/m_\pi$  for different atomic displacements  $\xi_0$  as well as a positive and negative detuning  $\Delta$  reveals

$$\zeta_{\xi_0}^{\text{sgn}(\Delta)} \equiv \frac{m}{m_\pi} \approx \frac{\langle k_y \rangle}{\langle k_{\rho, \pi}^{c, st} \rangle|_{\rho_0}}, \quad \zeta_{0.1}^\pm = 1 \mp 0.123, \quad \zeta_{0.5}^\pm = 1 \mp 0.075, \quad \zeta_1^\pm = 1 \mp 0.017. \quad (7.38)$$

Here,  $m_\pi = [m(\Delta > 0) + m(\Delta < 0)]/2$  gives indeed exactly the mean of the numerical slopes for positive and negative detuning. For small ratios  $\sigma_x/w_0 \lesssim 1/10$  the spatial variations over

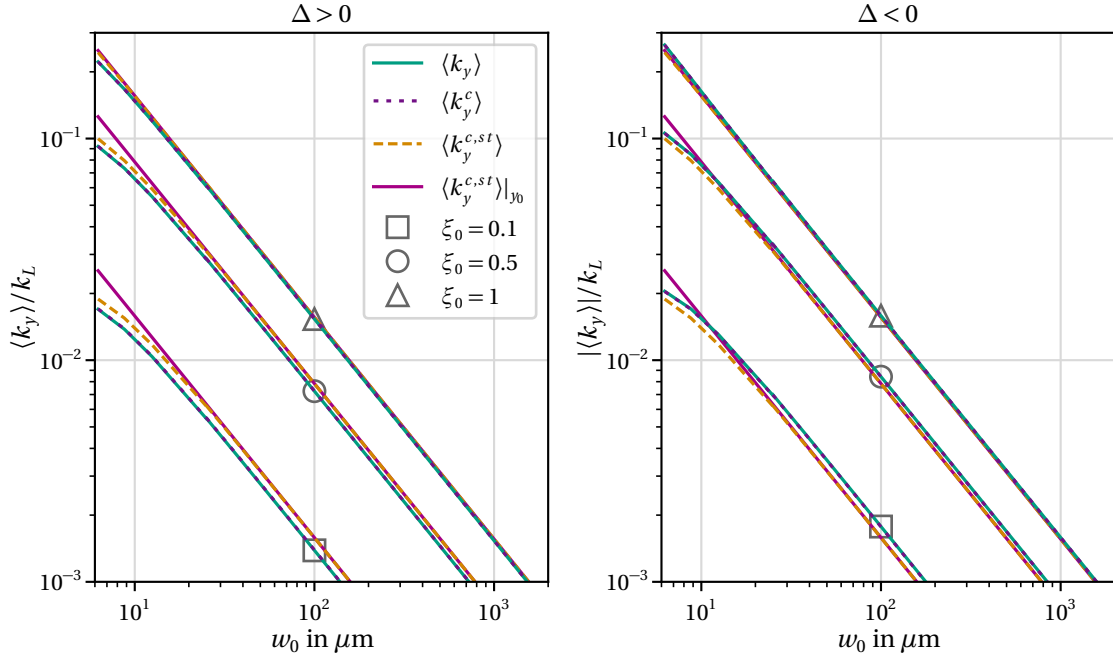


Figure 7.8: Momentum kick in  $y$ -direction due to the reactive force, depending on the beamwaist, for different atomic initial positions  $y_0 = \xi_0 w_0$  and blue detuned lasers (left) respectively red detuning (right). The numerical results for Laguerre-Gaussian beams including wavefront curvature  $\langle k_y \rangle$  (7.4) are compared to the results for collimated laser beams  $\langle k_y^c \rangle$  (7.37), the spatially averaged steady-state approximation  $\langle k_y^{c, st} \rangle$  (7.32) and the local value of the steady-state approximation  $\langle k_y^{c, st} \rangle|_{y_0}$  (7.29). A rectangular  $\pi$ -pulse of width  $\tilde{\tau}_{R\pi}(\Omega(\mathbf{r}_0))$  is applied with  $\Omega = 2\omega_r$ , using the atom and laser parameters of Tables A.1 and A.2.

the expansion of the atomic wavepacket becomes relevant. Therefore, the results differ from the linear behaviour. The spatial average  $\langle k_y^{c, st} \rangle$  (7.32) qualitatively confirms this. Its absolute value gives the mean of the numerical results for  $\Delta > 0$  and  $\Delta < 0$ . As expected, it coincides with the local value  $\langle k_y^{c, st} \rangle|_{y_0}$  (7.29) as long as the beamwaist is much larger than the atomic size  $\sigma_x/w_0 \lesssim 1/15$ .

The collimated beam approximation, calculated with the reactive force, shows no visible difference to the results taking wavefront curvature into account. The maximum difference is in the range of some per mille for extremely small beamwaists and decreases rapidly for increasing  $w_0$ . For beamwaists in the range of millimetres the transverse momentum kick, even if it is much larger than the momentum kick due to wavefront curvature, it is rather small. Only for a displacement  $y_0 \gtrsim 0.7 w_0$  the component reaches one per mille of the laser photon momentum  $k_L$ .

To analyse further the dependency on the displacement, the results for one beamwaist  $w_0 = 25 \mu\text{m}$  but different  $\sigma_x = \{1.25, 2.5, 5\} \mu\text{m}$  are depicted in Fig. 7.9. For smaller ratios  $\sigma_x/w_0$  the numerical results confirm the linear behaviour  $\langle k_\varrho \rangle \propto \varrho$  as predicted by the local steady-state approximation  $\langle k_\varrho^{c, st} \rangle|_{\varrho_0}$ . For larger ratios, the difference of the momentum kicks over the spatial expansion size of the wavepacket cannot be neglected any longer. The averaged steady-state approximation can describe this behaviour, deviating from the linear relation. However, its absolute value gives furthermore *only* the mean value of the numerical results

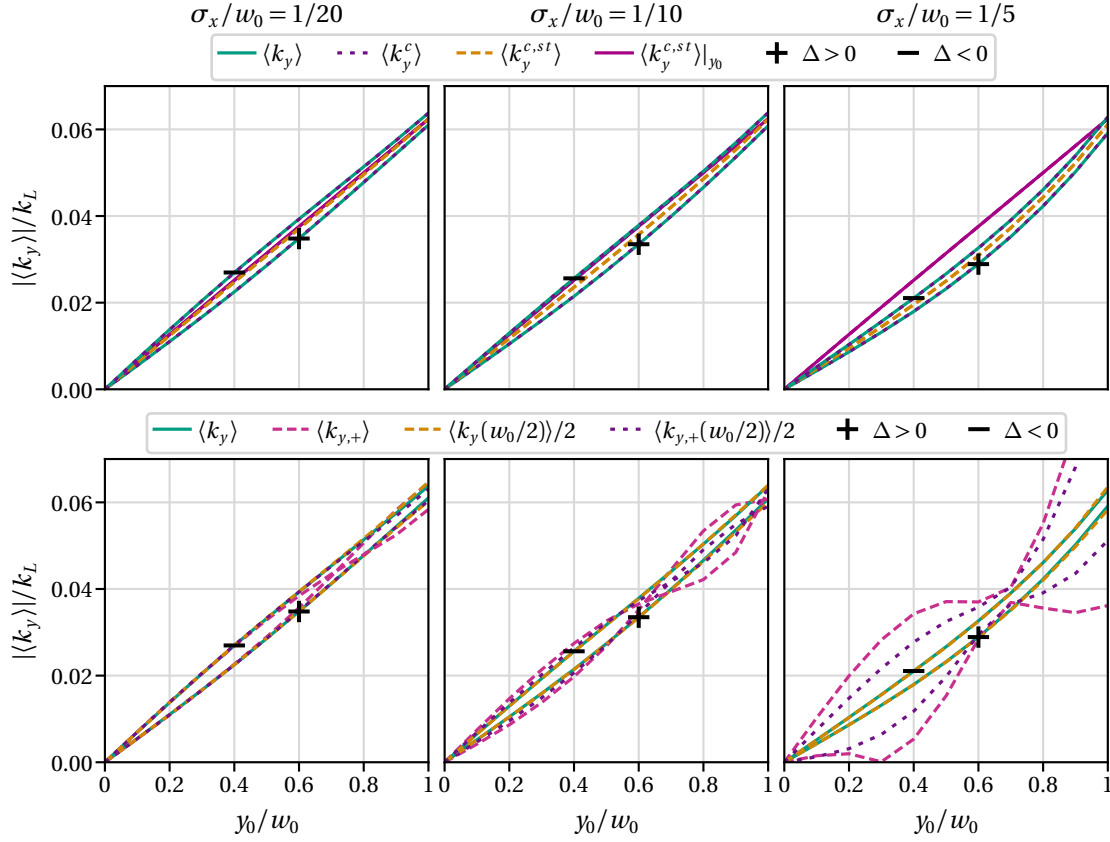


Figure 7.9: Momentum kick in  $y$ -direction due to the reactive force, depending on the atomic initial positions  $y_0$  for a beamwaist  $w_0 = 25\mu\text{m}$  and symmetrical atomic initial states (2.59) of width  $\sigma_x = \{1.25, 2.5, 5\}\mu\text{m}$  (from left to right) and  $\sigma_k = 0.1k_L$ . The plus marks the results for  $\Delta > 0$  and the minus respectively  $\Delta < 0$ . A rectangular  $\pi$ -pulse of width  $\tilde{\tau}_{R,\pi}(\Omega(\mathbf{r}_0))$  (6.32) with  $\Omega = 2\omega_r$  is applied, using the atom and laser parameters of Tables A.1 and A.2. Top: The numerical results for Laguerre-Gaussian beams including wavefront curvature  $\langle k_y \rangle$  (7.4) are compared to the results for collimated laser beams  $\langle k_y^c \rangle$  (7.37), the spatially averaged steady-state approximation  $\langle k_y^{c,st} \rangle$  (7.32) and the local value of the steady-state approximation  $\langle k_y^{c,st} \rangle|_{y_0}$  (7.29). Bottom: The mirror-momentum  $\langle k_{y,+} \rangle$  (7.4) differs from the total transverse momentum  $\langle k_y \rangle$ . The latter can be approximated by the scaled result for  $w'_0 = 12.5\mu\text{m}$  according to  $\langle k_y(w_0) \rangle = \langle k_y(w'_0) \rangle w'_0/w_0$  (7.30).

for positive and negative detuning. Here, the deviations to the approximated analytical slope  $m_\pi = 4\pi/w_0$  of  $\langle k_{\rho,\pi}^{c,st} \rangle|_{\rho_0} = m_\pi \xi_0$  (7.30) due to large atomic expansions are

$$\zeta_{w_0/\sigma_x}^{\text{sgn}(\Delta)} \equiv \frac{m}{m_\pi}, \quad \zeta_{20}^+ = 0.88, \quad \zeta_{20}^- = 1.10, \quad \zeta_{10}^+ = 0.84, \quad \zeta_{10}^- = 1.04, \quad \zeta_5^+ = 0.69, \quad \zeta_5^- = 0.83, \quad (7.39)$$

where  $m$  is the slope of a linear approximation of  $\langle \hat{k}_y \rangle = m\xi_0$  up to  $y_0 = 0.2w_0$ . The momentum kick of the *mirror-state*  $\langle k_{y,+} \rangle$  (7.4) is also shown in Fig. 7.9. It depends strongly on the beamsplitter efficiency and therefore it deviates from the total momentum kick  $\langle k_y \rangle$ . The apparent oscillations arise due to the changing gradient of the lasers' transverse intensity modulations. This is why those increase for larger initial states. The actual value of  $\langle k_{y,+} \rangle$  depends on the individual values of  $\sigma_x$  and  $w_0$ . In contrast, the total kick  $\langle k_y \rangle$  is approximately scalable according to  $\langle k_y \rangle = \langle k'_y \rangle w'_0/w_0$  (7.30).



### Transverse momentum stretching

In addition to the centre-of-mass momentum kick, the spatial dependence of the dipole force leads to a stretching or squeezing of the wavepacket's momentum distribution  $\sigma_k = \sqrt{\langle k^2 \rangle - \langle k \rangle^2}$  as depicted in Fig. 7.10. Obviously, the effects increase for larger ratios  $\sigma_x/w_0$ . The momentum width in  $z$ -direction is stretched for  $\Delta > 0$  and squeezed for  $\Delta < 0$ , but is mainly independent of the transverse displacement  $y_0$ . For small displacements  $y_0$ , this applies also for the displacement direction  $y$ , but it can reverse due to the varying intensity gradient of the lasers' spatial envelopes. For the total momentum width  $\sigma_{k_y}$ , the behaviour is approximately symmetric around the initial value  $\sigma_k(0) = 0.1 k_L$  for changing the sign of the detuning. In contrast, the momentum width of the *mirror*-wavepacket shows a clearly asymmetric characteristic. While the shown effect are considerable for these small beamwaists, they stay qualitatively similar for larger beamwaists but quantitatively they are much smaller.

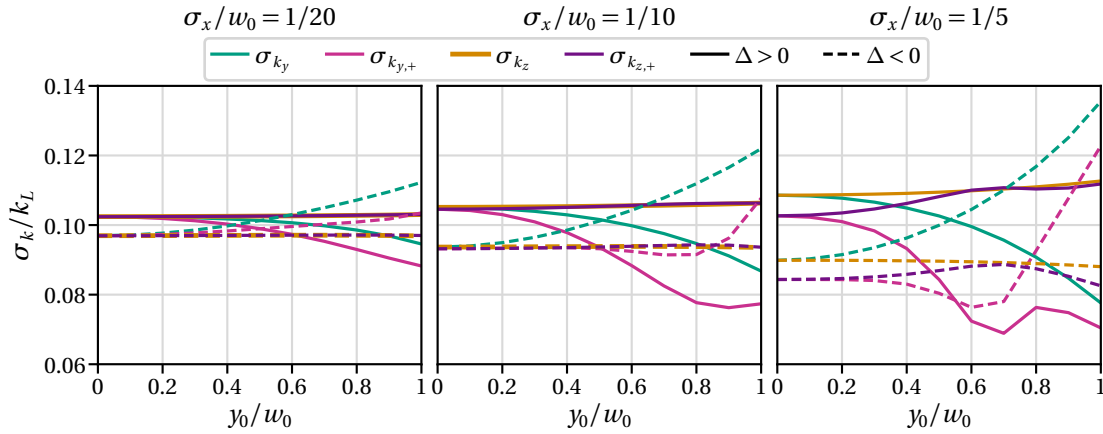


Figure 7.10: Stretching of the momentum width (initially  $\sigma_k = 0.1 k_L$ ) of the  $y$ - and  $z$ -direction, depending on the atomic initial positions  $y_0$  for a beamwaist  $w_0 = 25 \mu\text{m}$ , different ratios  $\sigma_x/w_0$  and positive as well as negative detuning. A rectangular  $\pi$ -pulse of width  $\tilde{\tau}_{R\pi}(\Omega(\mathbf{r}_0))$  is applied with  $\Omega = 2\omega_r$ , using the atom and laser parameters of Tables A.1 and A.2.

**2D APPROXIMATION** It is worth mentioning, that also for these large ratios  $\sigma_x/w_0 \leq 1/10$  and small beamwaists  $w_0 \sim (10^1 - 10^2) \mu\text{m}$ , 2D simulations provide useful predictions for the transverse momentum kick as well as momentum stretching. This saves an enormous amount of computational time, while differing from the full 3D solution only in the range of  $\lesssim 2\%$  for  $\sigma_x/w_0 = 1/10$  and even  $< 10\%$  for  $\sigma_x/w_0 = 1/5$  (besides the results for  $\langle k_{y,+} \rangle$ ).

**CONCLUSION** The investigation on the radiation force shows that the main effects of the spatial variations of the LG-beams are reasoned by the dipole force, actually by the intensity variation  $e^{-2\rho^2/w_0^2}$ . This causes the transfer of transverse momentum components, leading also to variations of the atomic density and phase distributions, visible in the momentum space after applying a  $\pi$ -pulse in Fig. 7.3. Especially in Subfig. (d) around the initial value  $k_x = -k_L$ , the significant shape deviations of the density and the phase are indeed caused by the linear LG-intensity gradient at the atomic initial location  $\rho_0 = w_0/2$  inside the laser region.

## 7.4 REDUCED BEAMSPLITTING PERFORMANCE

Beamsplitters perform best, if an atomic cloud is well localised within the beamwaist. The radiative force reveals that the transversal dipole forces are stronger than the forces along the

propagation direction  $x$  [cf. Sec. 7.3 and Eqs. (7.11), (7.12)]. For a Bragg mirror the fidelity  $F$  (5.34) and diffraction efficiency  $\bar{\eta}$  (5.32) results are depicted in Fig. 7.11.

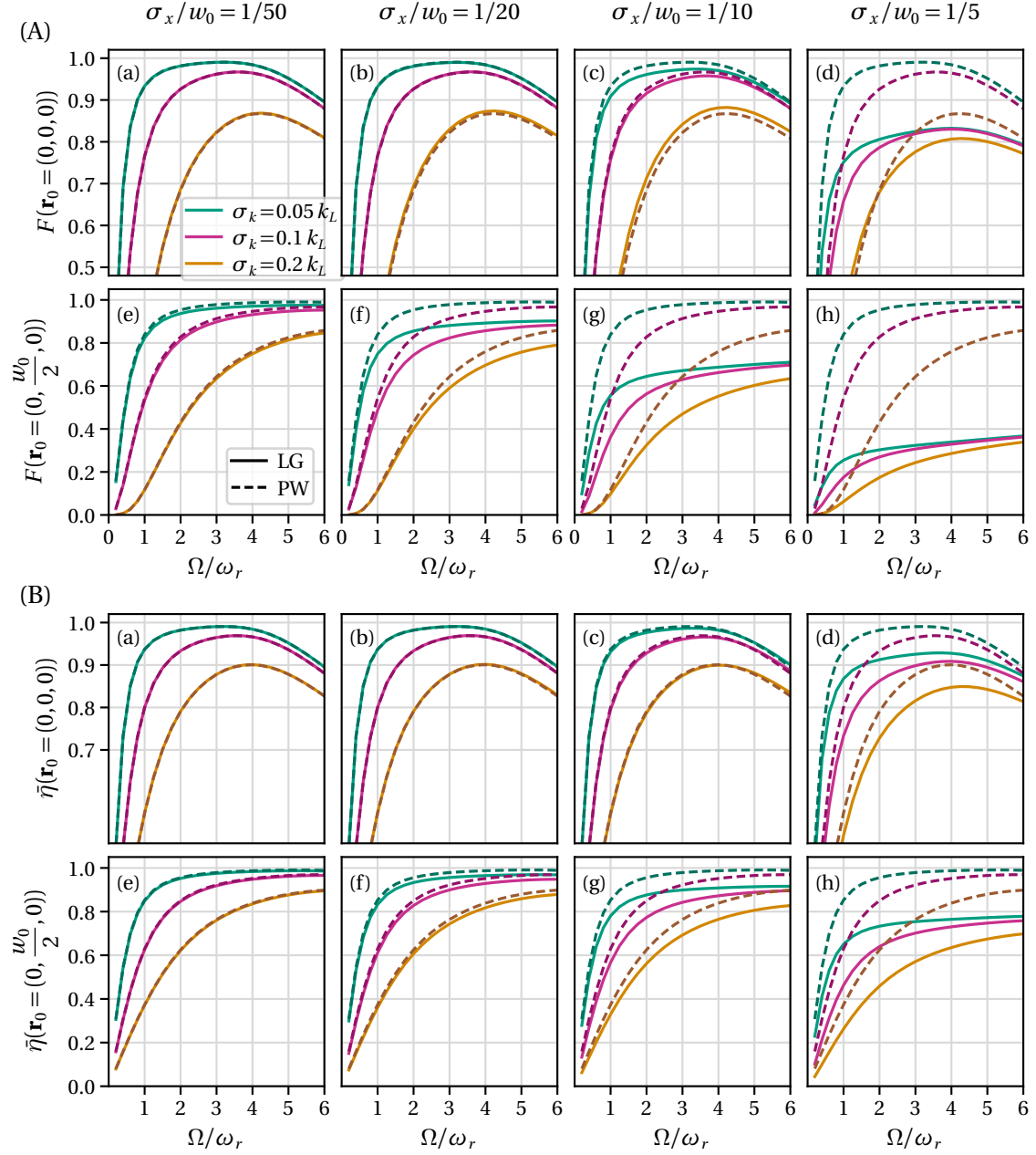


Figure 7.11: (A) Fidelity  $F(\Omega, \sigma_k, \sigma_x)$  (5.34) and (B) diffraction efficiency  $\bar{\eta}$  (5.32) versus two-photon Rabi frequency  $\Omega = \Omega \omega_{2r}$  for different atomic initial momentum widths  $\sigma_k$  of a 3D ballistically expanded Gaussian wavepacket (2.56) for Laguerre-Gaussian beams (solid) in comparison to plane waves (dashed), using the (3+1)D numerical integration (2.59). Connecting the momentum width with a temperature via Eq. (2.89) results in  $T_{a=x,y,z}(\sigma_k) = \{1, 4, 14\}$  nK for  $\sigma_k = \{0.05, 0.1, 0.2\} k_L$  and using the root mean square of the total momentum width in three dimensions  $T(\sigma_k) = T_a/3 = \{0.3, 1.2, 4.8\}$  nK. Blackman temporal envelopes with  $\Delta\tau = 2\pi\tilde{\tau}_{B\pi}$  (6.32) are applied. In columns different ratios  $\sigma_x/w_0$  between spatial expansion size of the initial state  $\sigma_x$  and the beamwaist  $w_0$  are compared and in the bottom rows the atomic initial state is displaced in the radial direction of the LG-laser beams  $\varrho_0 = y_0 = w_0/2$ . Further parameters are given in Tables A.1 and A.2.



Indeed, small clouds centred at the symmetry point  $\mathbf{r}_0 = 0$  will feel the least degradation of  $F$  and  $\bar{\eta}$  in Fig. 7.11 (a) and (b) due to dipole forces. Displacing the initial cloud transversely to  $\mathbf{r}_0 = (0, w_0/2, 0)$  leads to larger aberrations [cf. Fig. 7.11 (e)-(h)].

For the depicted simulation results, Blackman  $\pi$ -pulses of width  $\tilde{\tau}_{B\pi}(\Omega(\mathbf{r}_0))$  (6.32) are applied, for different Rabi frequencies  $\Omega = \Omega \omega_{2r}$ . To estimate the effective  $\pi$ -pulse time the local Rabi frequency  $\Omega(\mathbf{r}_0)$  (7.2) at the atomic initial position  $\mathbf{r}_0$  is considered. The results for *realistic* LG-laser beams are gauged to the PW-idealisation, using the local density approach (7.2). Ballistically expanded 3D Gaussian wavepackets (2.59) are considered as initial states with different momentum widths  $\sigma_k$ . In addition, different relations between the spatial initial expansion size  $\sigma_x$  to the beamwaist  $w_0$  are studied. As in the experiment (cf. Table A.2) a longitudinal laser displacement  $\ell_x = 0.1 x_R$  is considered.

For atoms located at the centre of the LG-laser beams, the spatial inhomogeneity leads to significant aberrations only for large atomic wavepackets [cf. Fig. 7.11 (c) and (d)]. By contrast, even small, but displaced wavepackets show a significant reduction of the fidelity in *realistic* LG-beams compared to ideal plane waves. It is detrimental for large wavepackets [cf. Fig. 7.11 (e) - (h)]. Overall, the phase sensitive fidelity is more sensitive to aberrations due to LG-modes. However, they are also significant for the phase insensitive diffraction efficiency, but for point-particle like wavepackets  $\sigma_x/w_0 \leq 1/50$  the PW-approximation is exact.

It is remarkable, that without a displacement, for large momentum widths and especially for large wavepackets, the LG-laser beams improve the Bragg diffraction performance at least for certain two-photon Rabi frequencies. In general, the LG-laser beams reduce a bit the losses into higher diffraction orders. Without any other negative effects, this would increase the diffraction efficiency as well as the fidelity, in general. In addition, the on-resonance transfer efficiency from initially  $\mathbf{k} = (-k_L, 0, 0)$  to  $\mathbf{k}' = (+k_L, 0, 0)$  decreases for larger ratios  $\sigma_x/w_0$  but the larger the momentum width the slower it is reduced. Therefore, in some parameter regimes the on-resonance efficiency for  $\sigma_k = 0.2k_L$  is even higher than for  $\sigma_k = 0.1k_L$ , while it is independent of  $\sigma_x/w_0$  and almost independent of  $\sigma_k$  for plane laser waves. This is assumed to be the main reason, why LG-laser beams can improve the diffraction in certain cases.

Please note, that for the applied parameters the simulation results of the fidelity and the diffraction efficiency for LG-beams only depend on the ratio  $\sigma_x/w_0$  (cf. App. B.3), not on their individual values. The results for plane laser waves, without transversal intensity variations, are of course independent of  $\sigma_x$  and  $w_0$ . In contrast, the transferred transverse momentum component as well as the stretching of the momentum width, due to the transverse intensity gradient of the LG-laser beams, depends on the individual values of  $\sigma_x = 1.25\mu\text{m}$  and  $w_0$ . The results after a  $\pi$ -pulse for transversely displaced atoms  $\mathbf{r}_0 = (0, w_0/2, 0)$  are shown in Fig. 7.12.

For plane laser waves (PW) without transverse momentum kick  $\langle k_y^{\text{PW}} \rangle = 0$ , the momentum width  $\sigma_{k_y, \pi}^{\text{PW}}/\sigma_{k_y, 0} = 1$  remains constant. For LG-laser beams the normalised momentum kick  $\langle k_y^{\text{LG}} \rangle / \langle k_{y, \pi}^{c, st} \rangle|_{y_0}$  shows an approximately linear dependence on the two-photon Rabi frequency, where the slope decreases for larger beamwaists  $w_0$ . However, the absolute deviation to the impact approximation increases for larger ratios  $\sigma_x/w_0$  as already seen in Fig. 7.9. In addition, the transverse momentum component of the mirror wavepacket  $\langle k_{y, +} \rangle$  shows again larger deviations. As expected, for extremely small wavepackets the momentum width is almost unaffected (e), (f) but for larger ratios (c), (d) the total momentum width  $\sigma_{k_{y, \pi}}$  is increased due to the positive detuning  $\Delta > 0$  and the initial position  $\mathbf{r}_0 = (0, w_0/2, 0)$  (cf. Fig. 7.10). The momentum width of the mirror wavepacket  $\sigma_{k_{y, +}, \pi}$  can be stretched but also squeezed depending on the actual simulation parameters (cf. Fig. 7.10, 7.12).

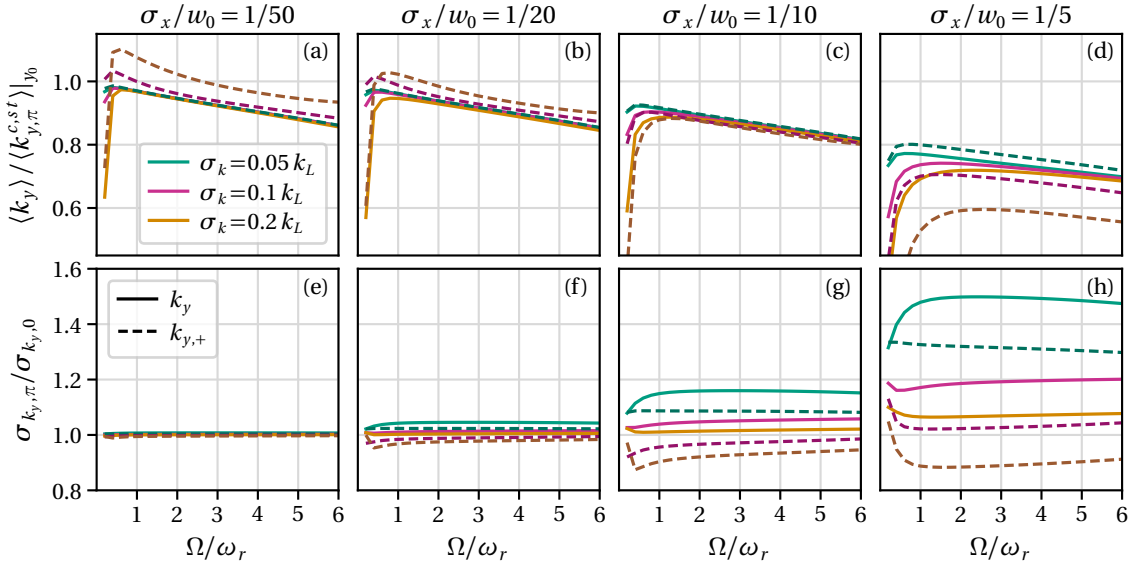


Figure 7.12: Top: Transverse momentum kick  $\langle k_y \rangle$  (solid) and  $\langle k_{y,+} \rangle$  (dashed) (7.4) normalised to the result of the impact approximation for collimated lasers  $\langle k_{y,\pi}^{c,s,t} \rangle_{y_0}$  (7.30). Bottom: Momentum width  $\sigma_{k_y,\pi}$  (solid),  $\sigma_{k_{y,+},\pi}$  (dashed) normalised to the initial momentum width  $\sigma_{k_y,0} = \sigma_k$ . Everything depending on the two-photon Rabi-frequency  $\Omega$  for different initial momentum widths  $\sigma_k$  and ratios  $\sigma_x/w_0$ . The parameters are equal to the parameters used for the results of Fig. 7.11 with the atomic initial position  $\mathbf{r}_0 = (0, w_0/2, 0)$ .

## 7.5 MISALIGNMENT

Misalignment of the laser beams, building the optical grating for the atomic diffraction, is defined by a transversal displacement and a tilt. For displacements, the intensity maxima of both lasers no longer coincide, and for tilts, the lasers are no longer exactly in opposite directions. Effectively, this leads to a reduction of the diffraction efficiency and the transfer of transverse momentum components to the atomic wavepacket.

### 7.5.1 Spatial profile of misaligned laser beams

The misalignment is parametrised in relation to the orientation of laser 1, shown in Fig. 7.13.

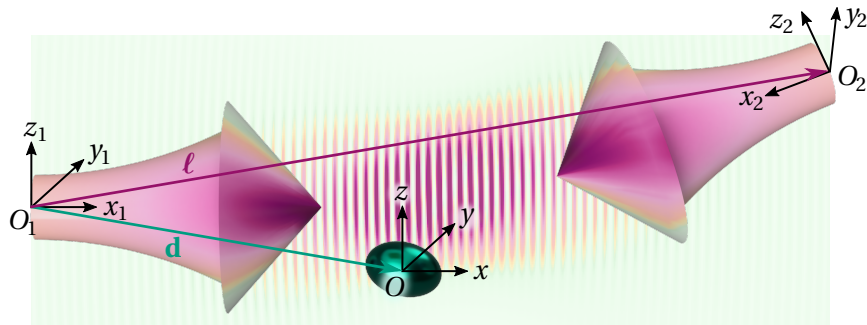


Figure 7.13: Two counterpropagating Laguerre-Gaussian laser beams, with their intrinsic reference frames  $S_{l=1,2}$ , build a standing light field, interacting with an atomic cloud (green). The reference frame  $S$ , used for the theoretical description, is centred at the atomic centre-of-mass position and orientated like laser 1. The distance between the origins  $O$  and  $O_1$  is  $|d|$  and the distance between  $O_1$  and  $O_2$  is  $|l|$ .

The spatio-temporal profiles [cf. Eq. (2.23)] of the misaligned laser beams  $l = \{1, 2\}$  are defined by

$$\mathcal{O}_l = \Omega_l(t, \mathbf{r}) e^{-i\phi_l(t, x)} = \Omega_{0,l} f(t) u(\mathbf{r}_l) e^{-i\phi_l(t, x)}, \quad \phi_l = \omega_l t - k_l x_l, \quad (7.40)$$

with the time-dependent phase of a plane wave  $\phi_l$ . The intrinsic coordinates  $\mathbf{r}_l = M_l^{-1} \mathbf{r}$  are defined by the geometrical transformations  $M_l$  from the intrinsic laser frame  $S_l$  to the simulation frame  $S$  (cf. Sec. 3.4.2). While for plane waves there are no spatial variations with  $u_l^{\text{PW}}(\mathbf{r}_l) = 1$ , the spatial envelope of a LG-beam reads (cf. Sec. 2.2.2)

$$u_l^{\text{LG}}(\mathbf{r}_l) = \frac{w_0}{w(x_l)} \exp\left[-\frac{y_l^2 + z_l^2}{w(x_l)^2}\right] \exp\left[ik_l \frac{y_l^2 + z_l^2}{2R(x_l)} - i\zeta(x_l)\right]. \quad (7.41)$$

**AFFINE TRANSFORMATIONS** The origin of laser 1 is shifted with a translation  $M_1 = T_1 = T(\mathbf{d})$  [cf. Eq. (3.54)], where  $\mathbf{d}$  is the distance between the origins of the coordinate systems  $S$  and  $S_1$ . For laser 2 the reflection  $(S_{yz})_{ij} = (-1)^{ij} \delta_{ij}$  on the  $yz$ -plane serves for the counter-propagation. Now, a tilt is taken into account with the rotation  $R(\alpha, \beta, 0)$  (3.57), with intrinsic rotations around the  $z$ -,  $y'$ -,  $x''$ -axis. In addition to the shift  $\mathbf{d}$  the distance between both laser origins  $\ell$  is considered in  $T_2 = T(\mathbf{d} - \ell)$ . In combination this results in the transformation matrix  $M_2 = T(\mathbf{d} - \ell) \cdot R(\alpha, \beta, 0) \cdot S_{yz}$ . For  $\alpha$  and  $\beta$  the small-angle approximation (3.59) with  $\cos(\theta) \approx 1$  and  $\sin(\theta) \approx \theta$  is appropriate for realistic scales of tilts in the range of few degrees, even for  $\theta < 8^\circ$  the relative errors are less than one percent. Therefore, the coordinates of the intrinsic laser frames read

$$x_1 = x + d_x, \quad y_1 = y + d_y, \quad z_1 = z + d_z. \quad (7.42a)$$

$$x_2 = -\tilde{x} - \alpha \tilde{y} + \beta \tilde{z}, \quad y_2 = \tilde{y} - \alpha \tilde{x}, \quad z_2 = \tilde{z} + \beta \tilde{x} + \alpha \beta \tilde{y}, \quad (7.42b)$$

using the abbreviation  $\tilde{a} = a_1 - \ell_a$ ,  $a \in \{x, y, z\}$ .

**GALILEAN TRANSFORMATION** Beneath the static transformations (7.42), the transformation into a comoving, rotating frame, similar to the transformation in Sec. 5.3.1, needs to be considered. Within the active Galilean transformation  $|\psi(t)\rangle = \hat{G}|\psi'(t)\rangle$  the Rabi frequencies are shifted (3.51)

$$\Omega'_l(t, \hat{\mathbf{r}}) = \Omega_l(t, \hat{\mathbf{r}}_l + \mathbf{r}(t)), \quad \mathbf{r}(t) = v_g t \mathbf{e}_x. \quad (7.43)$$

Therefore, the Doppler shifted plane-wave laser phases  $\phi'_l = \omega_l t - k_l(\hat{x}_l + v_g t)$ ,

$$\phi'_1 = \omega_1 t - k_1(\hat{x} + v_g t + d_x) = \omega_L t - k_1(\hat{x} + d_x), \quad (7.44a)$$

$$\phi'_2 = \omega_2 t + k_2(\tilde{x} + v_g t + \alpha \tilde{y} - \beta \tilde{z}) = \omega_L t + k_2(\hat{x} + d_x - \ell_x + \alpha \tilde{y} - \beta \tilde{z}), \quad (7.44b)$$

still oscillate synchronously with  $\omega_L = (\omega_1 + \omega_2)[1 - (v_g/c)^2]/2 \approx (\omega_1 + \omega_2)/2$  (5.20).

**COROTATING FRAME** The additional local frame transformation  $|\psi'\rangle = \hat{F}|\psi''\rangle$  with

$$\hat{F}(t) = \exp\left[-i\omega_g t - i\omega_L t \hat{\sigma}_e + \frac{i}{2}(\mathbf{k}_{12} \hat{\mathbf{r}} - \chi_{12}) \hat{\sigma}_z\right], \quad (7.45)$$

eliminates the rapid temporal oscillations. Applying

$$\mathbf{k}_{12} = \frac{1}{2} \left[ \Delta k, -\alpha \left( k_L - \frac{\Delta k}{2} \right), \beta \left( k_L - \frac{\Delta k}{2} \right) \right], \quad (7.46)$$

$$\chi_{12} = -\frac{k_2}{2} [\ell_x + \alpha(d_y - \ell_y) - \beta(d_z - \ell_z)] - \frac{\Delta k d_x}{2}, \quad (7.47)$$

with  $\Delta k = k_1 - k_2$ , symmetrises the phases to

$$\phi_1'' = -\phi_2'' = -k_L \left( \hat{x} + d_x - \frac{\ell_x}{2} \right) - \frac{\alpha}{2} k_L \tilde{y} + \frac{\beta}{2} k_L \tilde{z} + \frac{\Delta k}{2} \left( \alpha \tilde{y} - \beta \tilde{z} - \frac{\ell_x}{2} \right). \quad (7.48)$$

Here, all terms scaling with  $\Delta k$  can be safely neglected, because  $\Delta k \ll k_L$ , establishing again the single spatial period  $\lambda_L = 2\pi/k_L$ . However, the additional momentum  $\mathbf{k}_{12}$  appears in the transformed Schrödinger equation  $i\hbar\partial_t|\psi''\rangle = \hat{H}''|\psi''\rangle$  within

$$\begin{aligned} \hat{H}'' = & \frac{(\hat{\mathbf{p}} + \frac{1}{2}\hbar\mathbf{k}_{12}\hat{\sigma}_z)^2}{2M} - \hbar\Delta\hat{\sigma}_e + \frac{\hbar}{2}\hat{\sigma}^\dagger \left( \Omega_1(t)u(\hat{\mathbf{r}}_1 + \mathbf{r}(t))e^{-i\phi_1''(\hat{\mathbf{r}})} \right. \\ & \left. + \Omega_2(t)u(\hat{\mathbf{r}}_2 + \mathbf{r}(t))e^{i\phi_1''(\hat{\mathbf{r}})} \right) + \text{h.c.} \end{aligned} \quad (7.49)$$

Without a relative tilt  $\alpha = \beta = 0$  the momentum  $\mathbf{k}_{12} = (\frac{\Delta k}{2}, 0, 0)$  is negligible. In addition, for idealised plane waves, with  $u(\mathbf{r}) = 1$ ,  $\mathbf{k}_{12}(\alpha, \beta)$  (7.46) can be neglected also for small misalignments  $\alpha, \beta \leq 8^\circ$ . In contrast, for LG-beams, due to their spatial envelope,  $\mathbf{k}_{12}(\alpha, \beta)$  is only negligible for almost vanishing tilts. Therefore, another local frame transformation  $\hat{F}$  (7.45) with

$$\mathbf{k}_{12} = \left( \frac{\Delta k}{2}, 0, 0 \right), \quad \chi_{12} = -\frac{k_2\ell_x + \Delta k d_x}{2} \quad (7.50)$$

is more reasonable. This results in the antisymmetric phases

$$\phi_1'' = -k_L \left( \hat{x} + d_x - \frac{\ell_x}{2} \right) - \frac{\Delta k \ell_x}{4} \approx -k_L \left( \hat{x} + d_x - \frac{\ell_x}{2} \right), \quad (7.51a)$$

$$\phi_2'' = k_L \left( \hat{x} + d_x - \frac{\ell_x}{2} + \alpha \tilde{y} - \beta \tilde{z} \right) + \frac{\Delta k}{2} \left( \frac{\ell_x}{2} - \alpha \tilde{y} + \beta \tilde{z} \right) \approx k_L \left( \hat{x} + d_x - \frac{\ell_x}{2} \right) + k_L \alpha \tilde{y} - k_L \beta \tilde{z}. \quad (7.51b)$$

However, without tilts they are again symmetric.

As already explained for LG-laser beams without misalignment (cf. Sec. 5.3.1), the time dependence of the spatial envelope is negligible  $u_G(\mathbf{r}_l + \mathbf{r}(t)) \approx u_G(\mathbf{r}_l)$  for  $\mathbf{r}(t) = v_g t \mathbf{e}_x$ , as long as  $w_0 > \sigma_x > \lambda_L > v_g t$ . For the group velocity  $v_g = \omega_{2r}/2k_L$  and mirror times in the quasi Bragg regime of the order  $t_\pi \sim 1/\omega_{2r}$ , the distance  $v_g t$  is of the order  $1/2k_L \approx 0.1 \mu\text{m}^{-1} < \lambda_L$ . Therefore,  $\mathbf{r}(t)$  can be safely neglected in the slowly varying beam parameters  $w_l = w(x_l)$ ,  $R_l = R(x_l)$  and  $\zeta_l = \zeta(x_l)$  of the spatial envelope  $u_l^{\text{LG}}(\mathbf{r}_l)$  (7.41). Finally, the spatio-temporal Rabi frequencies of both LG-laser beams read

$$\Omega_l(t, \mathbf{r}) \equiv \Omega_l''(t, \mathbf{r}) = \Omega_{0,l} f(t) \frac{w_0}{w_l} e^{-\frac{y_l^2 + z_l^2}{w_l^2}} e^{-i\Phi_l}, \quad \Phi_l = \phi_l'' - k_L \frac{y_l^2 + z_l^2}{2R_l} + \zeta_l. \quad (7.52)$$

Collimated beams with  $x_R \gg w_0 \gg \lambda_L$  can be approximated with

$$\Omega_l^c(t, \mathbf{r}) = \Omega_{0,l} f(t) e^{-\frac{y_l^2 + z_l^2}{w_0^2}} e^{-i\phi_l''}, \quad (7.53)$$

because in this case, for relevant propagation distances  $w_l \approx w_0$ ,  $\zeta_l \approx 0$  and  $R_l \rightarrow \infty$ .

Including a shifted coordinate origin  $\mathbf{r}_0 = (\chi_1 - \chi_2)/2k_L + \ell_x/2 - d_x - \Delta k \ell_x/4k_L$  in the Galilean transformation  $\mathbf{r}(t) = \mathbf{r}_0 + v_g t \mathbf{e}_x$  (7.43) for the proper gauge  $\chi_{12} = (\chi_1 + \chi_2 - k_2 \ell_x - \Delta k d_x)/2$  possible global laser phases  $\chi_l$  vanish. This simplifies the corotating phases for  $\alpha = \beta = 0$  to  $\phi_1'' = -\phi_2'' = -k_L \hat{x}$ . However, the shift  $\mathbf{r}_0$  must be considered for the location of the atomic cloud  $\mathbf{r}'_0 = \mathbf{r}_0 + \mathbf{r}_0 \mathbf{e}_x$ . For reasonable numerical grid sizes  $x_{\text{max}} \sim 5\sigma_x \sim 10 \mu\text{m} - 1 \text{ mm}$ , just covering the spatial extent of the initial state, the shifts  $(\chi_1 - \chi_2)/2k_L \leq 0.4 \mu\text{m}$  and  $\Delta k \ell_x/4k_L \lesssim 10^{-6} \mu\text{m}$  can be easily taken into account. The latter is generally negligible. In contrast,  $\ell_x/2 - d_x$  vanishes for symmetrical setups  $d_x = \ell_x/2$  but it can also be in the range of centimetres. Therefore, it is advisable to keep  $\mathbf{r} = 0$  for the common case of vanishing global laser phases.

### 7.5.2 Aberrations due to misalignment

The aberration analysis is restricted to misalignments in two dimensions. Still, there are plenty possibilities of misaligning the laser beams. However, many of them can be categorised within three types of scenarios, depicted in Fig. 7.14.

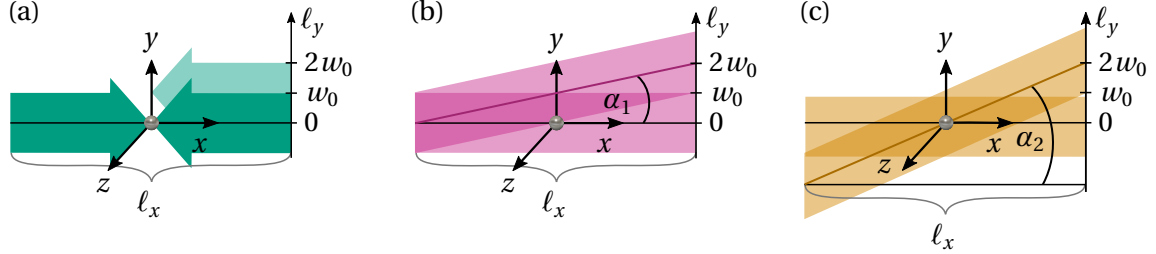


Figure 7.14: Different scenarios of laser misalignment. The lasers are symmetrically displaced in  $x$ -direction to  $\pm \ell_x$  and the atoms (grey) are located at the origin. (a) Laser 2 is misaligned with a transversal displacement  $\ell_y$ . Additionally, laser 2 is tilted by the angles (b)  $\tan \alpha_1 = \ell_y / \ell_x$  and (c)  $\tan \alpha_2 = 2\ell_y / \ell_x$ .

First of all, one laser origin can be transversally displaced by  $\ell_y$  in relation to the other laser origin. Secondly, this shift can be *compensated* by a tilt, wherefore at the origin of laser 1 both lasers overlap perfectly, resulting in the tilt angle  $\tan \alpha_1 = \ell_y / \ell_x$ . At least, a shift of laser 2 can also be *compensated* by a tilt  $\tan \alpha_2 = 2\ell_y / \ell_x$ , wherefore both lasers overlap perfectly at the position of the atoms, here longitudinally exactly in the middle between both laser origins. A longitudinal displacement of the atoms is not studied, because the variations of the radiative force are negligible in this direction for relevant displacements (cf. Eq. 7.11).

The maximum transversal displacement is expected as  $\ell_y \leq 2w_0$ . In this case the two intensity maxima can be distinguished experimentally, revealing the misalignment. Therefore, the maximum tilt angles result in  $\tan \alpha_j \leq 2jw_0 / \ell_x$ . Regarding a longitudinal distance between both lasers of  $\ell_x = 0.1x_R = 0.1\pi w_0^2 / \lambda_L$  the angles are  $\tan \alpha_j \leq 2j\lambda_L / (0.1\pi w_0)$  for typical laser parameters (cf. Tab. A.2) smaller than one degree. However, it is worth mentioning that the simulations can be used as long as the small-angle approximation (3.59) is appropriate. Therefore,  $\tan \alpha_j \approx \alpha_j \leq 8^\circ$  requests  $w_0 \geq 70\mu\text{m}$ . The simulation results are depicted in Fig. 7.15.

The initial states are represented by ballistically expanded isotropic Gaussian wavepackets (2.59) with different expansion sizes  $\sigma_x = \{1/50, 1/20\} w_0 = \{1.4, 3.5\} \mu\text{m}$  for  $w_0 = 70\mu\text{m}$  and momentum widths  $\sigma_k = \{0.05, 0.1, 0.2\} k_L$ , centred at  $\mathbf{r}_0 = (0, 0, 0)$ . Blackman mirror-pulses of width  $\tilde{\tau}_{B\pi}(\Omega)$  (6.32) and total interaction time  $\Delta\tau = 2\pi\tilde{\tau}_{B\pi}(\Omega)$  are analysed, considering a two-photon Rabi frequency  $\Omega = 4\omega_r$ . The results for realistic LG-laser beams are gauged to the idealised case with plane laser waves. Here, without any misalignment in  $z$ -direction, the momentum properties  $\langle k_z \rangle$  and  $\sigma_{k_z}$  of the final wavepacket stay unaffected.

Without a tilt [cf. Fig. 7.15 (a)] the results for plane waves, taking no spatial confinement at all into account corresponding to  $w_0 \rightarrow \infty$ , are obviously independent of the transversal laser shift  $\ell_y$ . In addition, as expected no transverse momentum is transferred and the momentum width is unaffected. For LG-laser beams, both the fidelity  $F$  and the diffraction efficiency  $\bar{\eta}$  are reduced and even vanish for large transversal laser displacements  $\ell_y$ . The similar behaviour of  $F$  and  $\bar{\eta}$  indicates, that the main reason therefore is the reduced Rabi frequency (7.52) of laser 2 at the location of the atomic cloud. That is the reason why the pulse width  $\tilde{\tau}_{B\pi}$  is no longer optimal. In contrast to plane waves, there is indeed a transverse momentum kick (practically independent of the initial momentum width) and stretching of the momentum width, but both are negligibly small. Besides the modification of the momentum width, the fidelity, efficiency and momentum kick is nearly independent of the ratio  $\sigma_x / w_0$ .

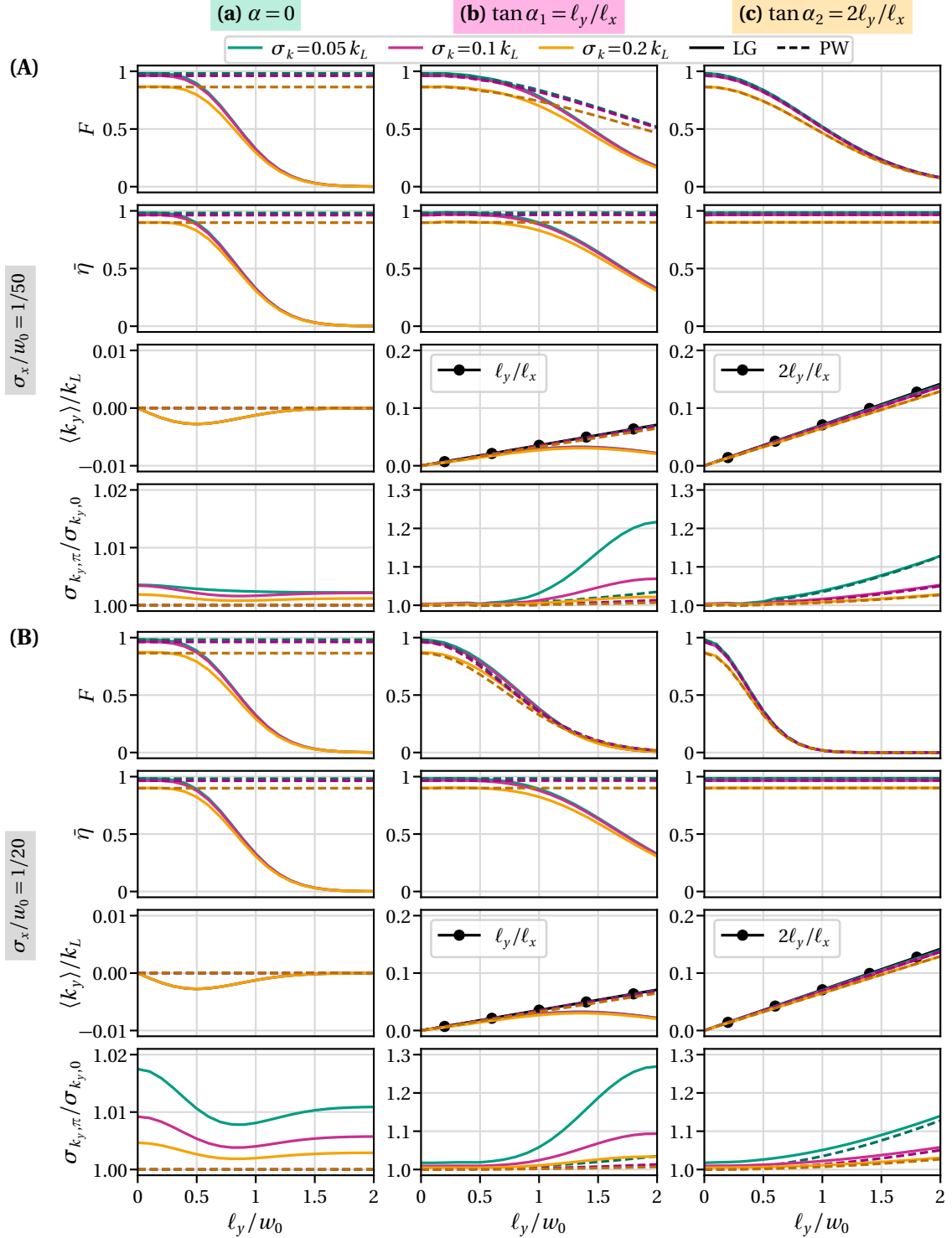


Figure 7.15: Fidelity  $F$  (5.34), diffraction efficiency  $\bar{\eta}$  (5.32), transverse momentum  $\langle k_y \rangle$  (7.4) and normalised transverse momentum width  $\sigma_{k_y,\pi}/\sigma_{k_y,0}$  depending on the transverse shift  $\ell_y$  of laser 2 for different tilts (a)  $\alpha = 0$ , (b)  $\tan \alpha_1 = \ell_y/\ell_x$  and (c)  $\tan \alpha_2 = 2\ell_y/\ell_x$ . The atomic initial states are 3D ballistically expanded Gaussian wavepackets (2.59) centred at  $\mathbf{r}_0 = (0, 0, 0)$ ,  $\mathbf{k}_0 = (-k_L, 0, 0)$  with expansions (A)  $\sigma_x = w_0/50 = 1.4 \mu\text{m}$ , (B)  $\sigma_x = w_0/20 = 3.5 \mu\text{m}$  and momentum widths  $\sigma_k = \{0.05, 0.1, 0.2\} k_L$ . Blackman  $\pi$ -pulses of width  $\bar{\tau}_{B\pi}$  (6.32) are applied with two-photon Rabi frequency  $\Omega = 4\omega_r$  for Laguerre-Gaussian beams ( $w_0 = 70 \mu\text{m}$ ,  $\ell_x = 0.1 x_R$ ) in comparison to plane waves. Further parameters are given in Tabs. A.1, A.2.



For the tilt  $\alpha_1$  [cf. Fig. 7.15 (b)] the diffraction efficiency for plane waves remains constant, while the fidelity is reduced for increasing  $\ell_y$ . For LG-beams the efficiency is less reduced than for  $\alpha = 0$ , due to the larger effective two-photon Rabi frequency at the atomic position. The fidelity is also less reduced, but it differs clearly from the diffraction efficiency due to the transverse momentum kick. In the PW-approximation this kick follows, almost independently of the widths  $\sigma_x, \sigma_k$ , the linear relation  $\langle k_y \rangle / k_L = \sin[\arctan(\ell_y / \ell_x)] \approx \ell_y / \ell_x$ . For LG-beams the momentum kick deviates from the linear relation for  $\ell_y > w_0$ , due to the additional kick due to the intensity variation of laser 2 at the atomic position (cf. Sec. 7.3.2).

Finally, for the tilt  $\alpha_2$  [cf. Fig. 7.15 (c)] the local two-photon Rabi frequency at the atomic position is approximately the same as without misalignment. Therefore, the diffraction efficiency is almost independent of the transversal laser displacement  $\ell_y$ . In contrast, the fidelity is even more impaired as for the half angle  $\alpha_1 = \alpha_2/2$  (b), due to the larger transverse momentum kick. Additionally, this reduction depends strongly on the ratio  $\sigma_x / w_0$ . In this scenario (c), also for LG-beams the momentum kick shows the linear behaviour  $\langle k_y \rangle / k_L = \sin[\arctan(2\ell_y / \ell_x)] \approx 2\ell_y / \ell_x$ , almost independent of the widths  $\sigma_x, \sigma_k$ . The momentum stretching is also almost independent of the spatial extent  $\sigma_x$  and in total less than for  $\alpha_1$  (b). On the whole, for the tilt angle  $\alpha_2$  (c) the results for LG-beams are well described in the PW-approximation as long as  $\sigma_x / w_0 \leq 1/20$ ; only for the momentum stretching a difference is visible to the eye. It is worth mentioning, that for all scenarios the smaller the initial momentum width the stronger it is relatively affected.

### 7.5.3 Comparison with on-ground experiments

To verify the predictions of the simulations of misaligned laser beams, they are gauged to experimentally measured [1] first-order diffraction efficiencies in the deep-Bragg regime (6.56) of partially condensed clouds (cf. Sec. 6.6.2).

#### *Experimental scenario*

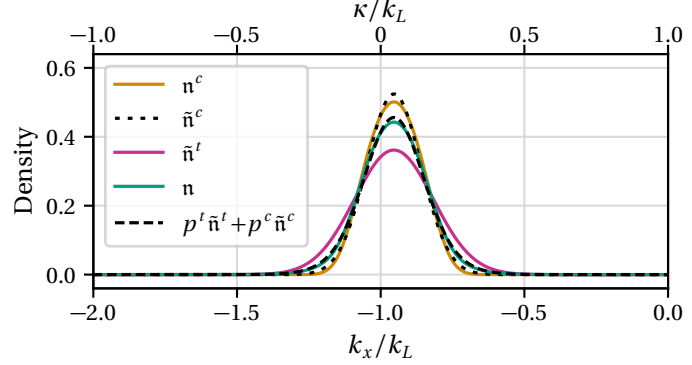
In general, the experimental setup complies with that one to verify the Demkov-Kunike model in Section 6.6.1. For the misalignment measurements, the atom chip apparatus prepares Bose-condensed  $^{87}\text{Rb}$  atoms, with a condensate fraction of  $N^c = (15 \pm 1) \times 10^3$  and a quantum depletion of  $N^t = (11 \pm 1) \times 10^3$  atoms. The trap frequencies are still  $[\omega_x, \omega_y, \omega_z] = 2\pi \times [46(2), 18(1), 31(1)] \text{ Hz}$ . The wavelength is slightly but irrelevantly different  $\lambda_L = 780.0451 \text{ nm}$ .

Bimodal fits (2.90) of TOF-measurements lead to the thermal cloud temperature  $T \leq (10.5 \pm 3.0) \text{ nK}$  (cf. App. E.2.1). Two different TOF = {12, 19} ms before the diffraction pulses are compared, during which the atoms fall vertically towards nadir. Therefore, the atoms are located at  $z_0 = (0.75 \pm 0.03) \omega_r = (1040 \pm 48) \mu\text{m}$ , respectively  $z_0 = (-0.02 \pm 0.03) \omega_r = (-24 \pm 48) \mu\text{m}$  as identified in App. E.2.2. The related widths  $\sigma_x \lesssim 20 \mu\text{m} \ll w_0 = 1386 \mu\text{m}$  are again negligible and the PW-approximation is appropriate.

**MOMENTUM DISTRIBUTION OF THE PARTLY CONDENSED CLOUD** The momentum distribution of the condensate is determined by Jan Teske with solving the (3+1)D Gross-Pitaevskii equation (2.68) for the given parameters of Table A.1 and the different TOF before the diffraction pulses (cf. Sec. 2.3.5). The doubly-integrated momentum density distribution of the BEC at the beginning of the diffraction pulses  $n_i^c(\kappa, \bar{\kappa}) \approx \tilde{n}^c(\kappa, \bar{\kappa})$  (6.67), can be approximated

with a Gaussian distribution (6.71) of width  $\sigma_k^c = (0.094 \pm 0.001)k_L$   $[(0.096 \pm 0.001)k_L]^8$  for TOF = 12 ms [19 ms], as depicted in Fig. 7.16. The thermal cloud is approximately a Gaussian distribution, where the marginal, one-dimensional momentum width is independent of the TOF  $\sigma_k^t = (0.137 \pm 0.003)k_L$  (cf. App. E.2.1). The central momentum  $\bar{\kappa}$  is derived in the following.

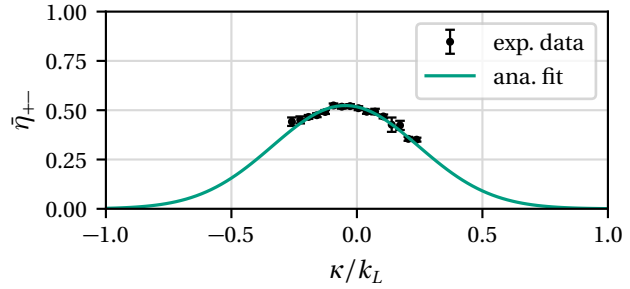
Figure 7.16: One-dimensional density  $n = p^c n^c + p^t n^t$  (6.60), with  $p^c = 0.58$ ,  $p^t = 0.52$ , versus momentum  $k_x$ , respectively momentum detuning  $\kappa$ . The thermal cloud  $n^t$  as well as the condensate  $n^c$ , can be approximated with a Gaussian distribution  $n^{a=\{c,t\}} \approx \tilde{n}^a$  (6.71). The distributions  $n^c$  for different TOF are almost identical, here it is TOF = 12 ms.



## Results

In Fig. 7.17 the velocity dispersion of the diffraction efficiency (6.56) is depicted for temporal Gaussian pulses ( $P_\Delta = (8.4 \pm 0.8)$  mW,  $t_G = \tau_G/\omega_{2r} = 200 \mu s$ ), assuming an ideal laser alignment. A fit with the analytical model (6.72) uncovers a residual horizontal atomic initial momentum  $\bar{\kappa}^S = (0.046 \pm 0.012)k_L$  and determines the two-photon Rabi frequency  $\Omega_\Delta = (1.15 \pm 0.01)\omega_r$ . For both, the 0.95 confidence interval defines the uncertainty. It is worth mentioning, that the fitted Rabi frequency disagree with that one given by the laser power (cf. Table 7.1). The reason for that is provided further on in the text.

Figure 7.17: Velocity dispersion of the diffraction efficiency  $\tilde{\eta}_{+-}$  (6.56) versus detuning  $\bar{\kappa}$  of the initial central momentum  $\langle \hat{p}_x(\tau_i) \rangle = (-1 + \bar{\kappa}^S + \bar{\kappa})\hbar k_L$ , where  $\bar{\kappa}^S = \bar{\kappa}^S k_L = 0.046 k_L$  is a small initial velocity of the atoms in the laboratory frame S and  $\bar{\kappa} = \delta\omega/\omega_{2r}$ . The experimental data is modelled with Eq. (6.72). The parameters are given in Tables 7.1, A.1 and A.2.



The influence of laser misalignment to the Rabi oscillations of the diffraction efficiency is studied for rectangular pulses<sup>9</sup>. Sketches of the laser alignment together with the diffraction results are depicted in Fig. 7.18. The parameters are listed in Table 7.1. For transversally *optimal* laser alignment (a), the experiment for  $P_\Delta \approx 8$  mW shows a shift of the oscillation period at the pulse length  $\Delta t = 180 \mu s$ . Therefore, two numerical simulations with different two-photon Rabi frequencies are depicted, matching the experimental data up to the first maxima (light magenta) and the whole flow (magenta), respectively. However, both differ tremendously from the experimental value, just as for the fit of the velocity dispersion (cf. Table 7.1). This can be explained by an atomic displacement  $y_0$  and/or a distance  $\ell_y$  between the lasers. Although both are realistic, the atomic displacement will cause the main contribution. Together with the TOF-scans (cf. App. E.2.2), three independent measurements constitutes a two-photon Rabi

<sup>8</sup> For the fit of the numerical (3+1)D GP result with the Gaussian distribution (6.71) the flanks are stronger weighted to match the  $1/e$  width of the simulation results.

<sup>9</sup> Unfortunately no data for Gaussian pulses were recorded, which could have been modelled with Eq. (6.72).



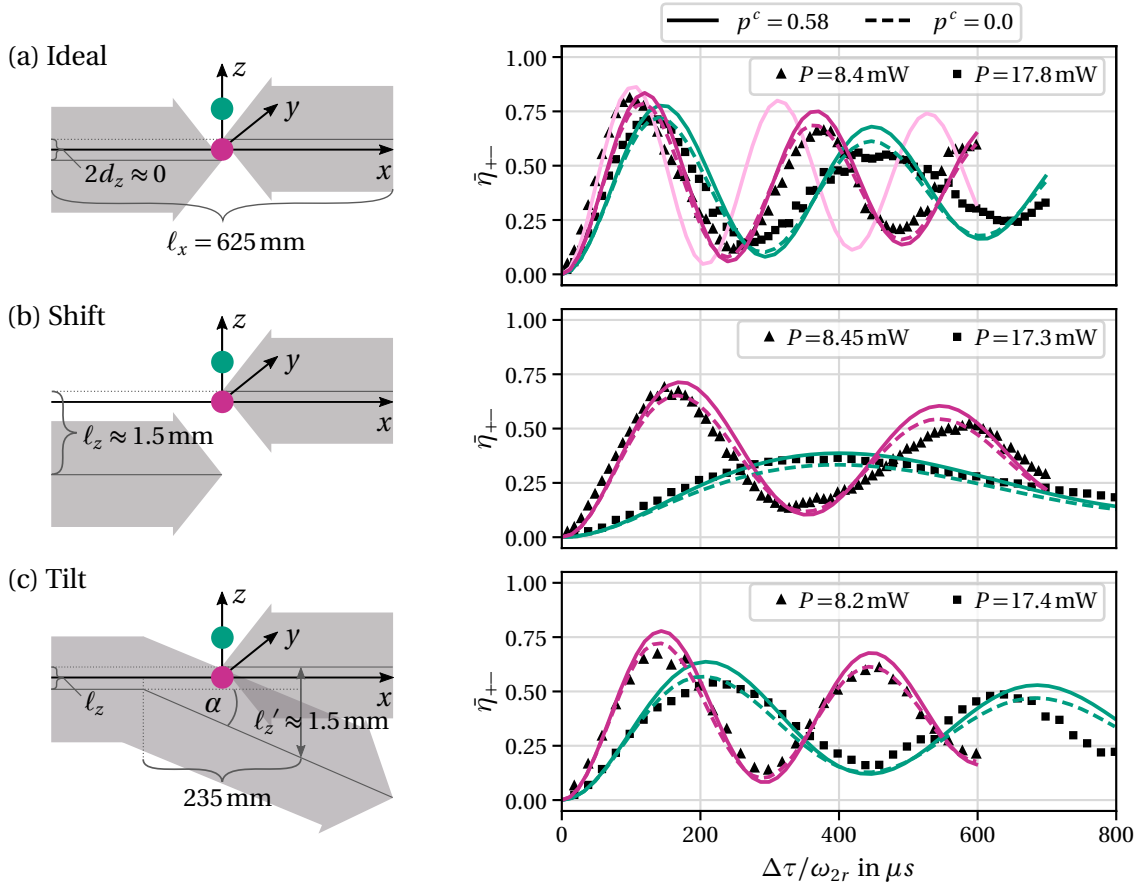


Figure 7.18: Left: Laser set-ups. Right: Rabi oscillations of the diffraction of the experimental diffraction efficiency  $\tilde{\eta}_{+-}$  (6.56) (black) and numerical simulations (coloured). Rectangular pulses with different laser powers are applied to partially condensed clouds, located at different positions  $z_0 \approx 0$  (magenta),  $z_0 \approx 0.75 w_0$  (green). In (a) the lasers are approximately perfectly aligned, while in (b) one laser is shifted, respectively tilted in (c). The parameters are given in Tables 7.1, A.1 and A.2.

frequency  $\Omega_{\blacktriangle} = (1.10 \pm 0.15) \omega_r$  for  $P_{\blacktriangle} = 8 \text{ mW}$ , explaining the deviation as systematic bias. With the relation  $\Omega'(P') = P'/P\Omega(P)$ , the expectation for  $P_{\blacksquare} = 17.8 \text{ mW}$ , namely  $\Omega_{\blacksquare} = (2.45 \pm 0.41) \omega_r$  is also confirmed by the numerical result listed in Table 7.1. Keeping  $\ell_y = 0$  this supposes an atomic displacement  $y_0 \approx 0.66 w_0$ .

The comparison with the misalignment results [cf. Fig. 7.18 (b), (c)] reveal that the laser beams are slightly misaligned in  $z$ -direction as depicted on the left in Fig. 7.18. Even in the *ideal* case (a) there could be a transversal shift  $\ell_z = 2d_z = 0.5 \text{ mm}$ , assumed to be symmetric for simplicity. Assuming such a misalignment is appropriate, due to the generally large experimental uncertainty of the laser distance  $\Delta\ell_z \approx 0.5 \text{ mm}$ . However, this affects the results for the *ideal* reference (a) and the TOF-scans to determine the atomic initial position only within the uncertainty range. In contrast, for the misalignment it is crucial. For  $d_z = 0$  the results can be simulated only with vastly different Rabi frequencies, while they are consistent for  $2d_z = 0.5 \text{ mm}$ . As expected for a shift, the effective Rabi frequency at the atomic location is reduced, leading to a larger oscillation period in (b). For collimated laser beams, the minimal tilt angle in (c) corresponds essentially to a shift. Therefore, the oscillation period of the diffraction results lies correctly in between the results of (a) and (b), because at  $x = 0$  this shift in (c) is smaller than the shift in (b).

For some simulations the damping of the amplitude due to the finite momentum widths  $\sigma_k$  and the initial momentum detuning  $\bar{\kappa}^S$  is under estimated. However, assuming for example the same momentum width for the condensate as for the thermal cloud, which is similar to taking  $p^c = 0$  can reduce the maxima of the Rabi oscillations. In total, the simulations can describe the experimental data quite well.

		$P_{\blacktriangle} \approx 8 \text{ mW}$	$P_{\blacksquare} \approx 18 \text{ mW}$	
	$p^c$	$0.58 \pm 0.04$		
	$\sigma_k^c$	$(0.096 \pm 0.001) k_L$	$(0.094 \pm 0.001) k_L$	
	$\sigma_k^t$	$(0.137 \pm 0.003) k_L$		
Velocity dispersion with Gaussian pulses (Fig. 7.17)				
exp.	$P$	$(8.4 \pm 0.8) \text{ mW}$		
	$\Omega$ (2.13), (5.43)	$(2.77 \pm 0.28) \omega_r$		
	$\Delta t = 8\tau_G/\omega_{2r}$	$200 \mu\text{s}$		
ana.	$\Omega$	$(1.15 \pm 0.01) \omega_r$		
	$\bar{\kappa}^S$	$(0.046 \pm 0.015) k_L$		
Rabi oscillations with rectangular pulses (Fig. 7.18)				
exp.	$z_0$	$(-0.02 \pm 0.03) w_0$	$(0.75 \pm 0.03) w_0$	
	$d_z$	$(0.0 \pm 2.5) \text{ mm}$		
num.	$z_0$	$-0.02 w_0$	$0.72 w_0$	
	$d_z$	$0.25 \text{ mm}$		
(a)	exp.	$P$	$(8.4 \pm 0.8) \text{ mW}$	$(17.8 \pm 1.8) \text{ mW}$
		$\Omega$ (2.13), (5.43)	$(2.77 \pm 0.28) \omega_r$	$(5.87 \pm 0.59) \omega_r$
		$\ell_z$	$(0.0 \pm 0.5) \text{ mm}$	
	num.	$\Omega$	$\{1.1, 1.3\} \omega_r$	$2.5 \omega_r$
		$\ell_z$	$0.5 \text{ mm}$	
(b)	exp.	$P$	$(8.45 \pm 0.85) \text{ mW}$	$(17.3 \pm 1.7) \text{ mW}$
		$\Omega$ (2.13), (5.43)	$(2.79 \pm 0.28) \omega_r$	$(5.70 \pm 0.57) \omega_r$
		$\ell_z$	$(1.5 \pm 0.5) \text{ mm}$	
	num.	$\Omega$	$1.1 \omega_r$	$2.5 \omega_r$
		$\ell_z$	$1.2 \text{ mm}$	
(c)	exp.	$P$	$(8.2 \pm 8.2) \text{ mW}$	$(17.4 \pm 1.7) \text{ mW}$
		$\Omega$ (2.13), (5.43)	$(2.70 \pm 0.27) \omega_r$	$(5.74 \pm 0.57) \omega_r$
		$\ell_z$	$(0.0 \pm 0.5) \text{ mm}$	
		$\ell_z'$	$(1.5 \pm 0.5) \text{ mm}$	
		$\alpha$	$0.37^\circ \pm 0.17^\circ$	
	num.	$\Omega$	$1.0 \omega_r$	$2.5 \omega_r$
		$\ell_z$	$0.5 \text{ mm}$	
		$\ell_z'$	$1.1 \text{ mm}$	
		$\alpha$	$0.15^\circ$	

Table 7.1: Parameters of the results in Fig. 7.18 for the experiment (exp.), the numerical simulation (num.) and the analytical approximation (6.72) (ana.): condensate fraction  $p^c$ , momentum width of the condensate  $\sigma_k^c$  and the quantum depletion  $\sigma_k^t$ , laser power  $P$ , maximum two-photon Rabi frequency  $\Omega$ , total interaction time  $\Delta t$ , initial atomic momentum in  $x$ -direction  $\hbar \bar{\kappa}^S$ , initial atomic position  $z_0$ , laser shift  $d_z$  and distance between lasers  $\ell_z$  in  $z$ -direction, tilt angle  $\alpha$  and laser distance due to the tilt  $\ell_z'$ .

## (3 + 1)D BRAGG DIFFRACTION: SPONTANEOUS EMISSION

Spontaneous emission [14] constitutes an incoherent aberration, diminishing the coherent Bragg diffraction. For an extremely large laser detuning  $\Delta \gg \Gamma$  the excited state stays practically unpopulated, which is why spontaneous emission is negligible, because the probability  $\delta p = \delta t \Gamma p_e$  (3.30) of a quantum jump is proportional to the excited state population  $p_e$ . For the so far studied Bragg diffraction mirror pulses  $\Delta \approx 16000\Gamma$ , wherefore  $p_e \sim 10^{-7}$ , while  $\delta t \Gamma \sim 1$ . This leads to  $\delta p \sim 10^{-7}$  and quantum jumps virtually do not occur.

However, in general, spontaneous emission is ubiquitous. For that reason, the effect of spontaneous emission is studied for resonant diffraction ( $\Delta = 0$ ) with only one laser beam in Section 8.1 and for far detuned atomic Bragg diffraction in Section 8.2. Therefore, the Quantum Monte Carlo wavefunction method, derived in Section 3.3.1, is used. It provides a stochastic solution of the Schrödinger equation, respecting the incoherent effects, rather than solving explicitly the master equation, which also takes dissipation into account.

### 8.1 RESONANT DIFFRACTION WITH SPONTANEOUS EMISSION

To demonstrate the potentially tremendous impact, resonant diffraction with one laser beam, propagating exactly in  $x$ -direction, is studied. Here, the impact of the radiation pressure  $F_{\text{rp}}$ , i.e.

$$F_{\text{rp}} \equiv \langle \hat{F} \rangle = \frac{\Gamma}{2} \frac{s}{1+s} \hbar k_L, \quad s = \frac{|\Omega_0|^2}{2(\Delta_D^2 + \Gamma^2/4)}, \quad (8.1)$$

can be easily observed by the transferred longitudinal momentum expectation value, defined in the impact approximation by  $\Delta p = F \Delta t$  resulting in

$$k_{\text{rp}} = \frac{T}{\hbar} F_{\text{rp}} = k_L T \frac{\Gamma}{2} \frac{|\Omega_0|^2/2}{|\Omega_0|^2/2 + \Delta_D^2 + \Gamma^2/4}, \quad (8.2)$$

for rectangular pulses with pulse duration  $T$ . The radiation pressure (8.1) results from the radiative force operator (7.9), considering only the radiation pressure component in  $x$ -direction  $\beta_x \approx -k_L$  (7.10), (7.12) for collimated laser beams. To estimate the force expectation value, the impact approximation in the semiclassical limit (cf. Sec. 7.3.2) is used with the solution (7.24) leading straightforward to the result  $F_{\text{rp}}$  (8.1). Please note that an atomic initial velocity  $\mathbf{v}_0$  is considered within the Doppler-shifted detuning  $\Delta_D = \Delta - \mathbf{k}_L \mathbf{v}_0$ .

As usual, the initial state is an expanded isotropic coherent Gaussian wavepacket (2.59) purely in the ground state, centred at  $\mathbf{r}_0 = (0, 0, 0)$ ,  $\mathbf{k}_0 = (-k_L, 0, 0)$  with widths  $\sigma_x = 1.5 \mu\text{m}$ ,  $\sigma_k = 0.1 k_L$ . It interacts with a LG-laser beam that propagates exactly in  $x$ -direction, with

$w_0 = 30 \mu\text{m}$ , and therefore  $\sigma_x/w_0 = 1/20$ . Rectangular pulses with one-photon Rabi frequencies  $\Omega_0 = \{0.5, 1\} \Gamma$  are applied. In Fig. 8.1 the results of the quantum Monte-Carlo simulation (cf. Sec. 3.3.1) are depicted, averaging over 100 trajectories.

For the simulations with LG-laser beams 135 [302] quantum jumps occur for  $\Omega_0 = 0.5 \Gamma$  [ $\Omega_0 = 1 \Gamma$ ] and for the plane-wave approximation 120 [304]. The population of the excited state increases rapidly, reaching a significant equilibrium. The momentum expectation value  $\langle k_x \rangle$  grows approximately according to the linear model of the radiation pressure  $k_{\text{rp}}$  (8.2). In the transversal directions the momentum expectation values  $\langle k_y \rangle \approx \langle k_z \rangle \approx 0$  oscillate around zero, due to the randomly directed emission of photons. The standard deviation of the momentum  $\sigma_{k_a} = \sqrt{\langle k_a^2 \rangle - \langle k_a \rangle^2}$  of all dimensions  $a = \{x, y, z\}$  increases due to *heating*<sup>1</sup> the atomic initial state, here a single coherent state at temperature  $T = 0 \text{ K}$ . The coherent diffraction processes in  $x$ -direction additionally promote the growth of the momentum width  $\sigma_{k_x}$  due to acceleration. Due to the short interaction time  $t_{\text{max}} = 0.26 \mu\text{s}$ , the initial and final density distributions in the position space are practically identical. In contrast, the momentum density distribution demonstrates the large expansion to larger momenta due to the radiation pressure.

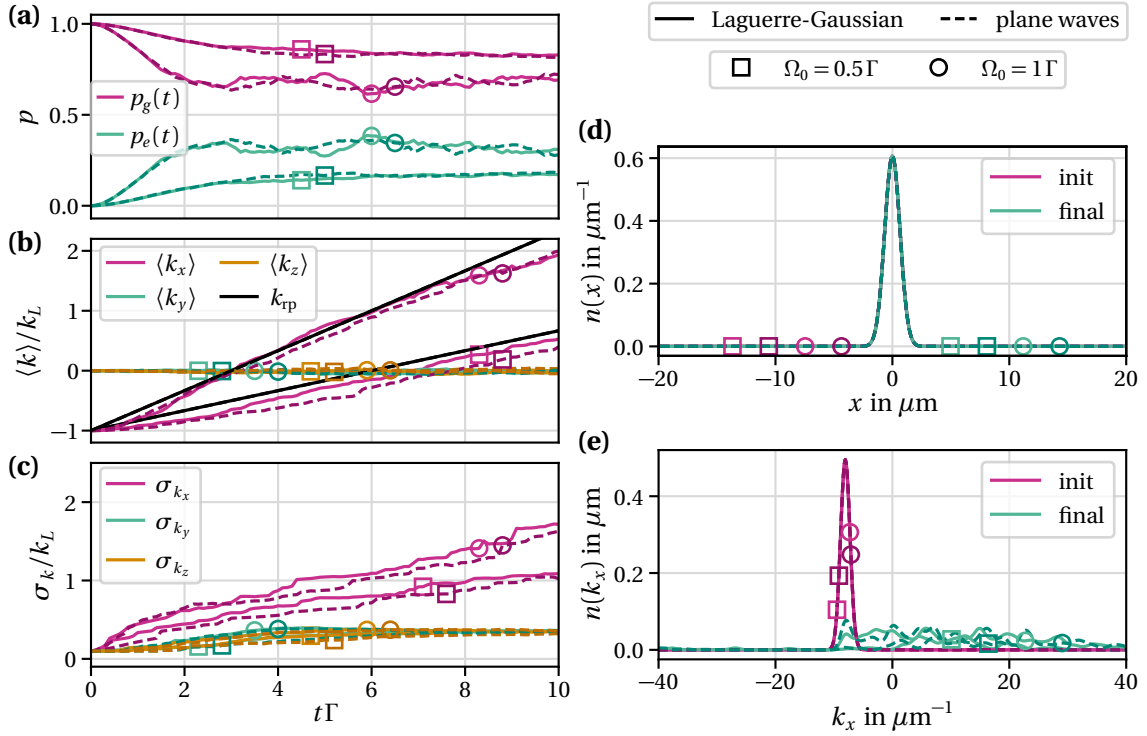


Figure 8.1: Quantum Monte Carlo calculations of the resonant diffraction with one laser beam under consideration of spontaneous emission, with averaging over 100 quantum trajectories. Left: (a) Population  $p$ , (b) momentum expectation value  $\langle k \rangle$  and (c) momentum width  $\sigma_k$  versus time  $t$ . Right: Column integrated density (7.3) [normalised with  $N_r = N_k = 1$ , cf. (7.3)] in position (d) and momentum space (e). All results are depicted for  $\Delta = 0$  but two Rabi frequencies  $\Omega_0 = \{0.5, 1\} \Gamma$ . The results for Laguerre-Gaussian laser beams with  $w_0 = 30 \mu\text{m}$  are compared to the plane-wave approximation. The atomic initial state is an expanded Gaussian wavepacket located at  $\mathbf{r}_0 = (0, 0, 0)$ ,  $\mathbf{k}_0 = (-k_L, 0, 0)$  of width  $\sigma_x = 1.5 \mu\text{m}$ ,  $\sigma_k = 0.1 k_L$ .

<sup>1</sup> In order to simulate laser-cooling, the initial states for the different trajectories must be sampled from a thermal ensemble. While this is not the intention here, the simulation methods can actually be used for this purpose.

## 8.2 BRAGG DIFFRACTION WITH SPONTANEOUS EMISSION

In order to include spontaneous emission as an aberration to Bragg diffraction, here a second, exactly counterpropagating LG-laser beam is considered. Moderate detunings  $\Delta_B = 900\Gamma$  and  $\Delta_C = 300\Gamma$ , while maintaining  $\Delta_{B,C} \gg \Omega_0, \Gamma$ , are compared to the experimentally given extremely large value  $\Delta_A \approx 16000\Gamma$  and the idealisation without any spontaneous emission ( $\Delta \rightarrow \infty$ ).

Again the atomic initial state is an expanded isotropic coherent Gaussian wavepacket (2.59) purely in the ground state, centred at  $\mathbf{r}_0 = (0, 0, 0)$ ,  $\mathbf{k}_0 = (-k_L, 0, 0)$  with widths  $\sigma_x = 1.5\mu\text{m}$ ,  $\sigma_k = 0.1k_L$ . A ratio  $\sigma_x/w_0 = 1/20$  with beamwaist  $w_0 = 30\mu\text{m}$  is considered. The distance between both laser origins is  $\ell_x = 0.1x_R$ , but otherwise the lasers are perfectly aligned with  $\ell_y = \ell_z = 0$ ,  $\alpha = \beta = 0$ .

The simulation results for a rectangular pulses with two-photon Rabi frequency  $\Omega = 2\omega_r$  are depicted in Fig. 8.2.

For  $\Delta_A \approx 16000\Gamma$  not a single quantum jump occurs during the interaction time of the mirror pulse  $\tilde{\tau}_{R\pi}(\Omega = 2\omega_r)$  (6.32). Therefore, spontaneous emission is indeed not an issue and as expected, the results are identical to the simulation of a single wavefunction without spontaneous emission. This results in the diffraction efficiency  $\bar{\eta}_A = \bar{\eta}_\infty = 0.9303$  and the fidelity  $F_A = F_\infty = 0.9284$ . For  $\Delta_C = 300\Gamma$  only five quantum jumps happen for all trajectories, but the diffraction efficiency and the fidelity are already reduced by a few percent to  $\bar{\eta}_C = 0.9044$  and  $F_C = 0.8906$ . However, for  $\Delta_B = 900\Gamma$  just one single photon is spontaneously emitted, but leading to  $\bar{\eta}_B = 0.9250$  and  $F_B = 0.9192$ .

However, in general, the results for the different detunings  $\Delta_A$ ,  $\Delta_B$  and  $\Delta_C$  mostly look quite similar in Fig. 8.2, due to the equal two-photon Rabi frequency. For all detunings, the excited state population is extremely small, but it becomes a bit more populated the smaller the detuning with  $p_{e,C}^{\max} = 3 \times 10^{-5}$ ,  $p_{e,B}^{\max} = 9 \times 10^{-6}$ , while  $p_{e,A}^{\max} = 3 \times 10^{-7}$  [cf. Fig. 8.2 (a)]. The momentum transfer from  $-k_L$  to  $k_L$  shows no significant difference for the different detunings [cf. Fig. 8.2 (b)]; only for  $\Delta_C$  a really small difference is apparent. In contrast, there is a visible but still small difference for the momentum width, especially for  $\Delta_C$  [cf. Fig. 8.2 (c)]. Further, the momentum density distribution uncovers rogue momentum components also apart from the populations around  $mk_L$ ,  $m \in \mathbb{N}$  [cf. Fig. 8.2 (f)], which force the aberrations. Therefore, also the density distributions in the position space [cf. Fig. 8.2 (e)] differ, but only for  $\Delta_C$  this is significant. Please note, that these results depend strongly on the actual number of quantum jumps, which is subject to stochastic fluctuations.

To summarise, if the detuning is extremely large  $\Delta \gg \Gamma$ , indeed, spontaneous emission effects can be neglected safely. However, the diffraction efficiency suffers significantly even from one single quantum jump.

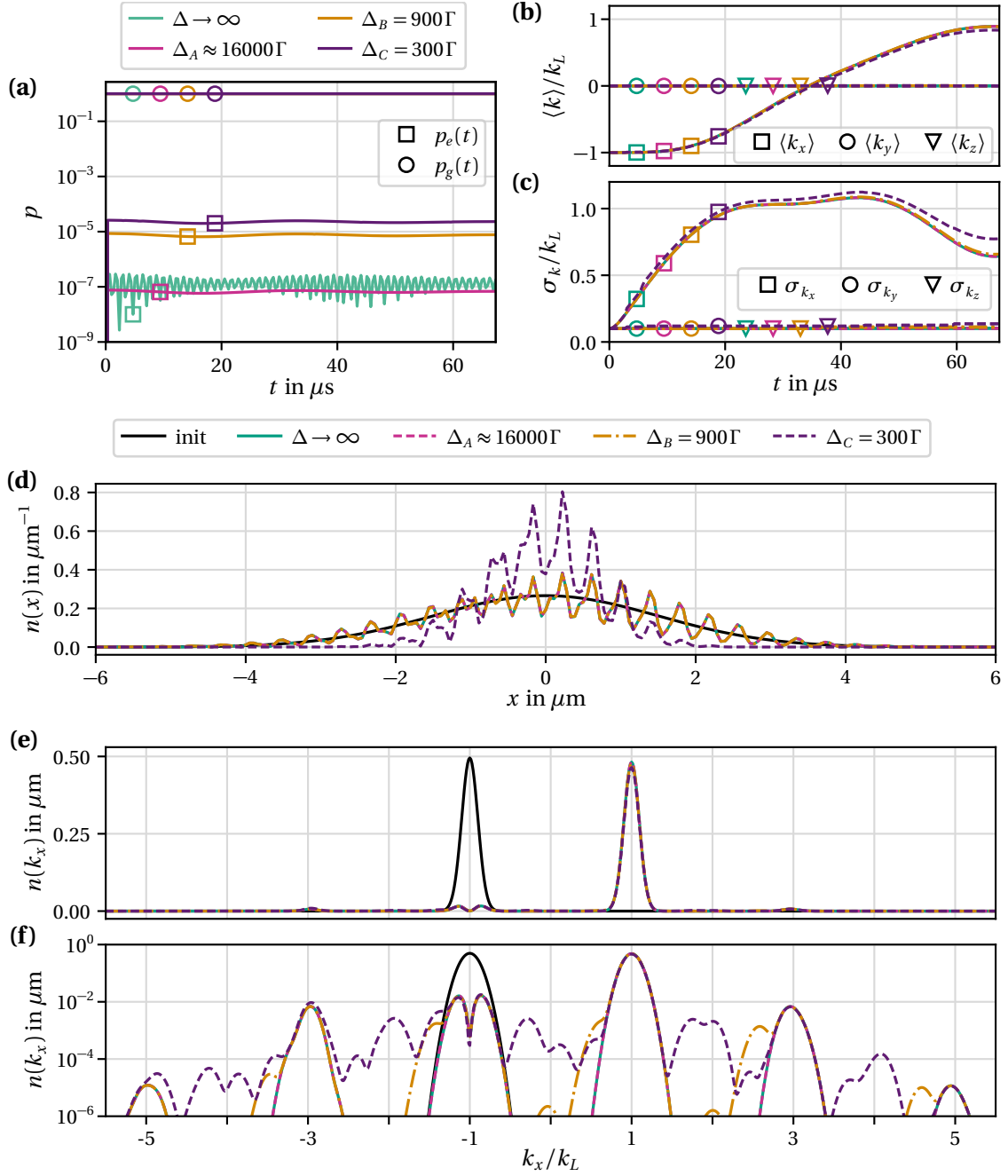


Figure 8.2: Quantum Monte Carlo calculations of a Bragg mirror under consideration of spontaneous emission, with averaging over 100 quantum trajectories. (a) Population  $p$ , (b) momentum expectation value  $\langle k \rangle$  and (c) momentum width  $\sigma_k$  versus time  $t$ . Column integrated density (7.3) (normalised with  $N_r = N_k = 1$ ) in position (d) and momentum space [(e): linear, (f) logarithmic]. The two-photon Rabi frequency is always  $\Omega = 2\omega_r$  but different laser detunings  $\Delta$  are compared. The atomic initial state is an expanded Gaussian wavepacket located at  $\mathbf{r}_0 = (0, 0, 0)$ ,  $\mathbf{k}_0 = (-k_L, 0, 0)$  of width  $\sigma_x = 1.5\mu\text{m}$ ,  $\sigma_k = 0.1k_L$ . The laser beamwaists are  $w_0 = 30\mu\text{m}$

---

## SUMMARY OF THE ABERRATIONS OF ATOMIC BRAGG DIFFRACTION

---

A full three-dimensional simulation of atomic Bragg diffraction as well as straightforward analytical approximations were demonstrated in the last Chapters 5-8. Thereby, several kinds of ubiquitous imperfections are included and characterised, like the velocity dispersion and the population losses into higher, off-resonantly coupled diffraction orders. Temporal as well as spatial envelopes of the laser beams, including misalignment, are considered and finally spontaneous emission was also taken into account.

### 9.1 QUANTIFY ABERRATIONS WITH SUSCEPTIBILITIES

To quantify and compare the influence of different aberrations several linear susceptibilities are estimated. The influence of varying relevant parameters to force aberrations is complex. Therefore, all parameters are kept constant, while the effect of slightly changing one parameter is studied in first order - according to a Latin square. The quality of the Bragg diffraction is defined by observables of interest. The phase dependent fidelity  $F$  (5.34) defines the overall quality, responding most sensitively to all parameters. The diffraction efficiency  $\bar{\eta}_{+-}$  (5.33) is experimentally easy to observe but less sensitive. The transverse momentum component and width, here  $\langle k_y \rangle$  (7.4) and  $\sigma_{k_y}$ , provides insights into reasons why the fidelity shows deviations to the diffraction efficiency.

**REFERENCE PARAMETERS** Common, intermediate parameters define the starting point of the analysis. Therefore, temporal Blackman pulses with mirror pulse widths  $\tilde{\tau}_{B\pi}$  are considered, with a moderate interaction strength  $\Omega = 4\omega_r$ . The laser wavelength and derivative quantities are given in Table A.2. The beamwaists are  $w_0 = 70\mu\text{m}$ , the distance between both laser origins is  $\ell_x = 0.1x_R$ , but otherwise the lasers are perfectly aligned with  $\ell_y = \ell_z = 0$ ,  $\alpha = \beta = 0$  (cf. 7.5.1). The initial state is an expanded isotropic Gaussian wavepacket (2.59) with size  $\sigma_x = w_0/20 = 3.5\mu\text{m}$  and momentum width  $\sigma_k = 0.1k_L$ , initially localised exactly in between the lasers  $\mathbf{r}_0 = (0, 0, 0)$  with initial momentum  $\mathbf{k}_0 = (-k_L, 0, 0)$ . The atomic parameters are given in Table A.1.

**LINEAR SUSCEPTIBILITY** The linear susceptibility  $\chi_p^\phi$  of the observable  $\phi$  and the variation parameter  $p$  is defined via

$$\frac{\Delta\phi}{\phi_0} = \chi_p^\phi \frac{\Delta p}{p_0}, \quad \forall \phi_0, p_0 \neq 0, \quad (9.1)$$



where the index 0 indicates the reference value. The relation (9.1) follows from the Taylor expansion

$$\phi = f(p) = f(p_0) + f'(p_0)(p - p_0) + \dots \quad (9.2)$$

with

$$\frac{\Delta\phi}{\phi_0} \equiv \frac{\phi - f(p_0)}{\phi_0} = \chi_p^\phi \frac{p - p_0}{p_0}, \quad \chi_p^\phi \equiv \frac{f'(p_0)p_0}{\phi_0}. \quad (9.3)$$

Assuming the following variation of the parameters, with respecting explicitly the sign of  $p - p_0$

$$p_\pm = p_0 \pm \Delta p, \quad \Delta p > 0, \quad (9.4)$$

the related susceptibilities are defined with

$$\frac{\Delta\phi}{\phi_0} = \chi_{p_\pm}^\phi \frac{\Delta p}{p_0}, \quad \chi_{p_\pm}^\phi \equiv \pm \frac{f'_\pm(p_0)p_0}{\phi_0}. \quad (9.5)$$

Therefore, a positive  $\chi$  describes a growing of the observable with increasing the absolute value of the variation parameter, and corresponding a negative  $\chi$  a decrease. The numerical results are summarised in Table 9.1.

For non-vanishing reference parameters  $p_0 \neq 0$ , the parameters are varied with  $\Delta p = 0.1 p_0$ . This corresponds for example to the power uncertainty in the experiments (cf. Sec. 6.6, 7.5.3) and is assumed for  $\Omega$ ,  $\sigma_k$ ,  $\sigma_x$ ,  $w_0$ ,  $\ell_x$  and  $k_{x,0}$ . If the reference observable  $\phi_0$  or parameter  $p_0$  vanishes, they cannot be used as normalisation and the susceptibilities get a physical dimension, which needs to be considered. In addition, for  $p_0 = 0$ , the variation  $\Delta p$  is defined by 10% of the *maximally reasonable* deviation, i.e.  $\Delta k_{y,0} = \pm 0.1 k_L$ ,  $\Delta x_0 = \pm 0.1 \ell_x$ ,  $\Delta y_0 = \pm 0.1 w_0$ ,  $\Delta \ell_y = \pm 0.1 w_0$ . For tilted laser beams, a small tilt  $\Delta \alpha_1 = \pm 0.1 \times 2 w_0 / \ell_x$  is compared to  $\Delta \alpha_2 = \pm 0.1 \times 4 w_0 / \ell_x$  with simultaneously  $\Delta \ell_y = \pm 0.1 \times 4 w_0$  according to scenario (c) in Fig. 7.14. In particular for these parameters with  $p_0 = 0$ , it is of special interest to study the sign of the variation  $p_\pm = p_0 \pm \Delta p$ , because in general, susceptibilities for the same parameter can show different parities for the observables or even diverse amplitudes.

As listed, there are several parameters, which can force aberrations.

Large two-photon Rabi frequencies  $\Omega$  lead to losses into higher diffraction orders, showing significant but interestingly almost equal susceptibilities  $\chi_\Omega^F \approx \chi_\Omega^{\tilde{\eta}_{+-}}$ . Please note, that the pulse widths were kept constant while varying  $\Omega$ . Therefore, the  $\pi$ -pulse condition for a mirror pulse (cf. Sec. 5.4) is missed for  $\Omega \neq 4 \omega_r$ , why the diffraction efficiency is reduced for both, increasing and decreasing  $\Omega$ . However, for larger  $\Omega$  the losses into higher diffraction orders become relevant. For that reason, it is  $|\chi_{\Omega+}^{F,\tilde{\eta}_{+-}}| > |\chi_{\Omega-}^{F,\tilde{\eta}_{+-}}|$ .

Wavepackets with large momentum distributions  $\sigma_k$  suffer from the velocity dispersion of the Bragg diffraction with moderate susceptibilities, but the LG-laser beams compress the transversal momentum width a bit.

For large expansions  $\sigma_x$  aberrations due to the intensity variations of LG-beams become significant, but for  $\sigma_x \ll w_0$  the effects are rather small. As expected, the susceptibilities for  $\sigma_x$  and  $w_0$  have an opposite sign. The variation of the ratios  $\sigma_x / w_0$  for  $\chi_{\sigma_x}^\phi$  and  $\chi_{w_0}^\phi$  differ a little, wherefore  $|\chi_{\sigma_x}^\phi| \neq |\chi_{w_0}^\phi|$  but they are indeed on the same order. Contrary to expectations the fidelity and diffraction efficiency improves slightly with increasing the ratio  $\sigma_x / w_0$ . However, this appears only locally for small variations, here in the regime where already approximately the optimum is reached for  $\sigma_x \ll w_0$ . For large ratios  $\sigma_x / w_0 \gtrsim 1/10$  the efficiency is reduced tremendously (cf. Fig. 7.11).



$\chi_{p\pm}^{\circ} \backslash \circ$	$p$	$F$	$\bar{\eta}_{+-}$	$\langle k_y \rangle$	$\sigma_{k_y}$
$\Omega$	+	-0.2552	-0.2550	0	0.0067
	-	-0.1575	-0.1575	0	-0.0071
$\sigma_k$	+	-0.0557	-0.505	0	0.9996
	-	0.0500	0.0460	0	-0.9998
$\sigma_x$	+	0.0013	0.0001	0	0.0090
	-	-0.0020	-0.0004	0	-0.0091
$w_0$	+	-0.0016	-0.0003	0	-0.0156
	-	0.0011	0.0001	0	0.0210
$x_0$	+	0.0001 $\ell_x^{-1}$	0.0001 $\ell_x^{-1}$	0	0.0003 $\ell_x^{-1}$
	-	0.0001 $\ell_x^{-1}$	0.0001 $\ell_x^{-1}$	0	-0.0004 $\ell_x^{-1}$
$y_0$	+	-0.0306 $w_0^{-1}$	-0.0041 $w_0^{-1}$	0.0183 $k_L w_0^{-1}$	-0.0036 $w_0^{-1}$
	-	-0.0306 $w_0^{-1}$	-0.0041 $w_0^{-1}$	-0.0183 $k_L w_0^{-1}$	-0.0036 $w_0^{-1}$
$\ell_x$	$\pm$	0	0	0	0
$\ell_y$	+	-0.0047 $w_0^{-1}$	0.0017 $w_0^{-1}$	-0.0089 $k_L w_0^{-1}$	-0.0023 $w_0^{-1}$
	-	-0.0047 $w_0^{-1}$	0.0017 $w_0^{-1}$	0.0089 $k_L w_0^{-1}$	-0.0023 $w_0^{-1}$
$\alpha_1$	+	-0.4942	0.0017	0.0780 $k_L$	-0.0014
	-	-0.4942	0.0017	-0.0780 $k_L$	-0.0014
$\alpha_2$	+	-1.1872	-0.0135	0.1210 $k_L$	-0.0008
	-	-1.1872	-0.0135	-0.1210 $k_L$	-0.0008
$k_{x,0}$	+	-0.2561	-0.2409	0	0.0070
	-	-0.2615	-0.2404	0	-0.0072
$k_{y,0}$	+	-0.0159 $k_L^{-1}$	0	1.0001	0
	-	-0.0159 $k_L^{-1}$	0	-1.0001	0
$\Delta^*$	$\pm$	0	0	0	0

Table 9.1: Linear susceptibilities  $\chi_{p\pm}^{\circ}$  (9.5) quantify the diminishing influence of different parameters  $p$  to the performance of a Bragg mirror, which is characterised by the observables  $\circ$ . A positive (+) and negative (-) variation  $p_{\pm} = p_0 \pm \Delta p$  is compared. For vanishing reference parameters  $p_0 = 0$  or observables  $\circ_0 = 0$ , the susceptibilities get a physical dimension. \*For varying  $\Delta$ , the Rabi frequency  $\Omega_0$  is adjusted to keep the two-photon Rabi frequency  $\Omega$  (5.43) constant.

Spatial variations and misalignment are further important drivers of aberrations. However, the effects in the longitudinal direction, probed by a displacement  $x_0$  of the initial state and the distance  $\ell_x$  between the lasers are negligible. The transverse effects are probed with  $y_0$ ,  $\ell_y$  and the tilt angles  $\alpha_{1,2}$ . Due to the rotational symmetry of the LG-laser beams, it is sufficient to study therefore the  $y$ -direction. Here, transverse momentum transfers occur intuitively due to the transverse component of the tilted laser wavenumber. This reasons the sharply different behaviour of the fidelity and the diffraction efficiency. While the population can be still transferred very efficiently to momentums around  $k_x = +k_L$  the fidelity (5.34) is reduced drastically, because the ideal final state is still defined with  $|\psi_{\text{ideal}}\rangle = e^{2ik_L \hat{x}} |\psi_i\rangle$ , as for optimally aligned lasers. As expected  $\chi_{y_0, \ell_y}^{F, \bar{\eta}_{+-}}$  are negative, because  $y_0, \ell_y \neq 0$  changes the local effective Rabi frequency, reducing the diffraction efficiency. In contrast,  $\chi_{y_0, \ell_y}^{\langle k_y \rangle}$  show a negative parity for  $\langle k_y \rangle$ , revealing the linear relations  $\langle k_y \rangle \propto y_0$  and  $\langle k_y \rangle \propto -\ell_y$ . The analytical local impact approximation (7.30) confirms approximately  $\chi_{y_0 \pm}^{\langle k_y \rangle} \approx \langle \hat{k}_{\varrho, \pi}^{c, st} \rangle|_{y_0 = \pm 0.1 w_0} / (0.1 w_0) = \pm 0.0223 k_L w_0^{-1}$ . The small deviation complies with the results of Sec. 7.3.2 (cf. Fig. 7.9), where

Eq. (7.30) gives the mean of the numerical results for positive and negative laser detuning  $\Delta$ . For this atomic displacement  $y_0$  the effective Rabi frequency at the location of the atoms is slightly reduced, due to the reduced intensity of both LG-laser beams. Therefore, with keeping the interaction time constant, the  $\pi$ -pulse condition is not matched exactly, which reduces the diffraction efficiency. For a distance  $\ell_y$  the intensity of only one laser changes at the position of the atoms, wherefore  $\chi_{\ell_y}^{F, \tilde{\eta}_{+-}} < \chi_{y_0}^{F, \tilde{\eta}_{+-}}$  and  $\chi_{y_0}^{(k_y)} \approx -2\chi_{\ell_y}^{(k_y)}$ . Here, the definition of  $\ell_y$  (cf. Sec. 3.4.2) reasons the negative sign.

For tilted laser beams the effective beamsplitter wavenumber gets a transverse momentum component transferred to the final wavepacket. Therefore, the fidelity suffers enormously from increasing the tilt angle, while the diffraction efficiency is almost unaffected. Even, it increases for small angles  $\alpha_1$ , essentially because losses into higher diffraction orders are suppressed, due to a stronger off-resonance. For increasing  $\alpha_2$  the efficiency decreases mainly because the diffraction efficiency for initial transverse momentum components of the wavepacket is reduced.

The impact of a residual atomic initial velocity in  $x$ -direction is tremendous, demonstrating the strong velocity dispersion, slightly depending on the sign of the initial momentum detuning. Small transversal momentum components reduces the fidelity while the diffraction efficiency stays constant. Of course, the parity for  $\langle k_y \rangle$  is negative, but due to the intensity variations an additional, outward ( $\Delta > 0$  cf. Sec. 7.3.2) kick occurs.

For a laser detuning in the range of the reference detuning  $\Delta \gg \Gamma$ , aberrations due to spontaneous emission are not an issue. Therefore, the variation of  $\Delta$  is irrelevant for the beamsplitter performance, as long as the two-photon Rabi frequency  $\Omega = -|\Omega_0|^2/2\Delta$  is kept constant.

## 9.2 MINIMISING ABERRATIONS OF BRAGG DIFFRACTION

To conclude, Bragg scattering from standing waves is efficient only for narrow velocity spreads of the atomic cloud, where the width is much less than the photon recoil velocity. Thereby, the laser frequency detuning must match the resonance condition for a certain atomic initial velocity. The spatial expansion must be much smaller than the laser beamwaist and the cloud should be centred transversally in the laser region, a moderate longitudinal displacement is bearable. Smooth temporal pulse shapes can optimise the diffraction in comparison to rectangular pulses. A misalignment of the lasers should be avoided. However, this is particularly important only for small laser beamwaists. For the applied extremely large detuning of the laser frequencies to the atomic resonance, spontaneous emission is not an issue. In combination of the detuning with the laser power, the resulting two-photon Rabi frequency needs to be chosen carefully to reach the optimal working regime, which depends strongly on the momentum width of the atomic cloud. Finally, the pulse width must be precisely coordinated with the Rabi frequency to hit the aimed pulse area.

## Part III

---

RAMAN VELOCITY FILTER FOR HOT IONS

---



---

## RAMAN VELOCITY FILTER

---

The knowledge gained by the diffraction processes of ultracold, neutral atoms can be applied to other kinds of light-matter interactions, like the interaction of alkali-like ions with classical laser light, as introduced in Chapter 2.4. In this Part III of the thesis, the transfer and application of the previous findings to the topic of a Raman velocity filter as a new tool for collinear laser spectroscopy is presented. While the main content follows [102], some points are described in more detail, here.

There is a considerable interest in the investigation of a Raman velocity filter for collinear laser spectroscopy. In particular, the promising benefits of using Raman transitions for the scope of ultra-precise optical high-voltage measurements establish a link between accelerator physics to the world of quantum optics.

The corresponding comprehensive theoretical studies are based on an experiment performed in the research group of Prof. Dr. W. Nörtershäuser at the Technische Universität Darmstadt, which is shortly introduced in Section 10.2. More details can be found in the dissertation of Dr. Kristian König [184]. The describing theoretical model is derived in Section 10.3. Finally, the results of numerical and analytical studies, presented in the frequency domain in Chapter 11 and in the time domain in Chapter 12, give rise for a possible realisation of optical high-voltage measurements with spectroscopic precision.

### 10.1 RAMAN FILTER AS TOOL TO MEASURE HIGH VOLTAGES

Measuring high voltages with very high precision on the ppm (parts-per-million) level and below represents a current challenge. Using Doppler velocimetry promises to be a suitable tool. Therefore, the ions must be prepared with an exactly known, very narrow velocity distribution, achieved by applying stimulated Raman transitions as velocity filter.

#### 10.1.1 Present spectroscopic high-voltage measurements

Recently, it was demonstrated that an accuracy  $s = \Delta U/U$  of at least a few ppm can be reached for high voltages up to 20 kV [185] in laser spectroscopic high-voltage measurements. This is very close to the performance of the world's best high-voltage dividers [186, 187]. In the corresponding measurements two transitions in calcium ( $^{40}\text{Ca}^+$  ions), shown in Fig. 10.1, have been employed: The  $|g = (4s^2S_{1/2})\rangle \rightarrow |e = (4p^2P_{3/2})\rangle$  resonance transition was first used to transfer population from the ionic ground level into the metastable level  $|m = (3d^2D_{5/2})\rangle$  via a sequential stimulated absorption and spontaneous emission cycle. For this process the pump laser is counterpropagating to the ion beam and the laser frequency determines the longitudinal velocity of the ions required to match the Doppler-shifted resonance condition. Afterwards, the ions are accelerated and the velocity of those ions that are in the metastable

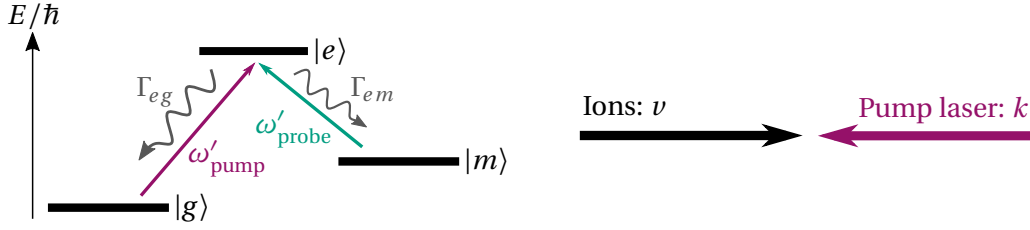


Figure 10.1: Left: Three-level energy diagram for  $^{40}\text{Ca}^+$ . Stimulated absorption and spontaneous transmission transfers population from  $|g\rangle$  to  $|m\rangle$ , which is probed afterwards by resonant excitation. Only ion velocities that match the Doppler-shifted laser frequencies ( $\omega'_{\text{pump}}$ ,  $\omega'_{\text{probe}}$ ) are addressed. Right: The laser is counterpropagating to the ion beam.

state is determined with a probe laser tuned to the Doppler-shifted  $|m\rangle \rightarrow |e\rangle$  transition. The resonance is observed using the fluorescence light emitted in the subsequent decay into the ground state. The frequencies in the laboratory frame of both lasers are measured with a frequency comb and are used to calculate the shift in frequency and the corresponding acceleration voltage.

While an  $s = 5$  ppm uncertainty level has been achieved by now, one of the critical issues is the remaining transverse emittance of the  $\text{Ca}^+$  ionic beam. Due to the 23-MHz width of the resonance transition, ions with small angles relative to the laser beam direction, might also be excited and the angle with respect to the laser beam might be changed during the acceleration with the high-voltage to be measured. Even though measures to avoid this have been taken: The ion optics of the acceleration region has been designed to suppress such effects by accelerating in the focal region and shaping the beam afterwards again into a beam with similar parameters (size and opening angle) as before. A second point is that several excitations are often needed to transfer the ion from the ground state to the metastable state, which is accompanied by uncontrollable recoil effects due to the momentum transfer in absorption and emission.

### 10.1.2 Raman velocimetry

Using Raman transitions between the ground  $|g\rangle$  and the metastable state  $|m\rangle$  by applying a co- and a counterpropagating laser beam, as depicted in Fig. 1.5, promises even higher accuracy for optical high-voltage measurements. In addition, corresponding uncertainties with the existing excitation scheme can be reduced. The advantage is that the selectivity of the narrow Raman transition with respect to the atoms' initial velocity as well as to the angle between the laser direction and the atoms' movement is considerably higher than for the allowed dipole transitions used so far. This will provide better control of the initial conditions of the atoms prepared in the metastable state before the acceleration.

In the framework of this thesis, the influence of interaction time, atomic velocity, laser linewidth and laser intensity on the efficiency of the population transfer are investigated. The results suggest that Raman transitions can be used with available laser beams to considerably improve the measurement accuracy with  $\text{Ca}^+$  ions for high-voltage measurements. This approach will be tested experimentally in the near future by the group of Prof. Dr. W. Nörter-shäuser and might become the basis for further improvements of laser-based high-voltage measurements, which is of great interest for several applications like, e.g., the neutrino mass measurement at the KATRIN experiment [186–188].

## 10.2 EXPERIMENTAL CONDITIONS

The developed theoretical treatment is based on the experimental boundary conditions at the ‘Collinear Apparatus for Laser spectroscopy and Applied Sciences’, short COALA, at the Technische Universität Darmstadt, where the previous high-voltage measurements were performed in the group of Prof. Dr. W. Nörtershäuser. Therefore, this Section 10.2 contains the experimental conditions, that are necessary in the framework of this thesis. For more detailed information, please see [184]. However, the later derived models are universally applicable to three level  $\Lambda$ -systems together with fast atomic motion.

The Raman spectroscopy is formed with two counterpropagating laser beams that interact with  $^{40}\text{Ca}^+$ , moving with velocity  $v$  in the same direction as laser 2, as depicted in Fig. 10.2.



Figure 10.2: Two counterpropagating lasers with wavevectors  $\mathbf{k}_1 = -k_1 \mathbf{e}_x$  and  $\mathbf{k}_2 = k_2 \mathbf{e}_x$  interact with the ions, which move with velocity  $\mathbf{v} = v \mathbf{e}_x$  parallel to laser 2. Wavenumbers and scalar velocities are positive quantities  $k_i, v > 0$ .

### 10.2.1 Ionic velocity distribution

In the beamline, ions get accelerated by a high voltage  $U$ . For the typical value  $U = 14 \text{ kV}$ , the mean velocity  $\bar{v}$  can be estimated from energy conservation

$$eU = \frac{M \bar{v}^2}{2}. \quad (10.1)$$

For singly charged  $^{40}\text{Ca}^+$ , one finds  $\bar{v} = 260 \text{ km/s} = 8.7 \times 10^{-4} c$ , which is much smaller than the speed of light  $c$  and justifies a nonrelativistic treatment.

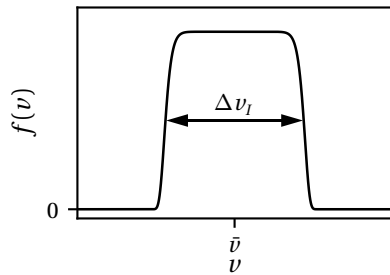


Figure 10.3: Ionic initial velocity distribution  $f(v)$  with mean velocity  $\bar{v}$  and width  $\Delta v_I$ . Note that the velocity distribution emerging from the accelerator is rather flat topped.

Due to technical reasons, the ensemble emerges with an artificial velocity distribution  $f(v)$ , which is depicted in Fig. 10.3. It exhibits an initial residual velocity spread  $\Delta v_I = (10 - 100) \text{ m/s}$  (full width half maximum, short FWHM). The spectroscopy is performed in an interaction zone of length  $L = 1.2 \text{ m}$ . This gives a mean transit time

$$\bar{t} = L / \bar{v} = 4.62 \mu\text{s}. \quad (10.2)$$

Due to the velocity spread, an interaction time spread  $\Delta t / \bar{t} = \Delta v_I / \bar{v}$  arises. For the maximal ion velocity width  $\Delta v_I = 100 \text{ m/s}$ , one finds a time spread  $\Delta t = 1.7 \text{ ns}$ , which can be neglected.

For the determined interaction time, the particle flux of  $100 \text{ pA}$  generates  $N \approx 3000$  calcium ions. The interaction volume is approximated with the laser region, which is assumed to be cylindrical and defined by the length  $L$  and the radius of the laser beam, given by the beamwaist  $w_0 = 1.7 \text{ mm}$ , and resulting in  $V = \pi w_0^2 L \approx 11 \text{ cm}^3$ . Finally, the very low particle



density is at most  $n = N/V \approx 3 \times 10^2/\text{cm}^3$ , as long as all ions are inside this region. Therewith, the mean inter-particle distance is approximately  $\bar{r} \approx 1/n^{1/3} = 1.6 \text{ mm}$ . In this dilute distribution and the short time of the spectroscopy pulse, binary interactions or other charge effects are negligible.

Due to the large momentum uncertainty  $M \Delta v_I \gg \hbar k_i$  compared to the photon momentum recoil, in this theoretical treatment mechanical light effects are disregarded (c.f. 10.3). Therefore, the position  $x$  and the momentum of the particle  $p = M v$  can be treated as parameters. Consequently, observables are obtained by static averaging over the initial phase-space distribution. Hence, the proportion of the total velocity distribution that is transferred into the metastable state is given by the incoherent average of the metastable-state population across the velocity distribution.

### 10.2.2 Spatial inhomogeneities

The laser beams as well as the ion beam have spatial intensity variations. The lasers are described with Laguerre-Gaussian (LG) laser beams, exhibiting intensity variations in transversal  $r = \sqrt{y^2 + z^2}$  as well as in propagation direction  $x$

$$I(x, r) = I_0 \left( \frac{w_0}{w(x)} \right)^2 e^{-2r^2/w(x)^2}, \quad (10.3)$$

with beamwaist  $w(x) = w_0 \sqrt{1 + x^2/x_R^2}$  and Rayleigh length  $x_R = \pi w_0^2/\lambda$ . For collimated laser beams, one can approximate  $w(x) \approx w_0$ , getting rid of the longitudinal intensity variations and the spatial-dependent Rabi frequency reads

$$\Omega(r) = \Omega_0 e^{-r^2/w_0^2}. \quad (10.4)$$

The spatial distribution of the ion beam is also assumed to be Gaussian of width  $\sigma$

$$g(r) = \frac{1}{2\pi\sigma^2} e^{-r^2/(2\sigma^2)}. \quad (10.5)$$

As for the velocity distribution, observables are obtained by static averaging over these spatial distributions.

If the ion beam is much smaller than the laser beams  $\sigma \ll w_0$ , the spatial inhomogeneities are negligible. Therefore, the theoretical treatment starts with this idealised scenario, showing the essential concepts. In Sec. 12.3.3 this is rectified, when spatial inhomogeneities are explicitly taken into account.

### 10.2.3 Parameters

Relevant spectroscopic data for  $^{40}\text{Ca}^+$  ions are given in Table 10.1, together with the characteristic properties of the applied velocity distribution. The laser parameters are specified in Table 10.2. Three different sets are compared in the further discussion. Parameter set (A) differs from (B) mainly in the laser frequencies, while (B<sub>1</sub>) and (B<sub>2</sub>) provide different laser powers. The beam waist as well as the laser linewidths stay the same for all cases.

Quantity	Symbol	Value	Ref.
Mass	$M$	39.962 042 286(22) u	[A, B]
Transition frequency	$\omega_{eg}$	$2\pi \times 761.905\,012\,599(82)$ THz	[C]
Natural linewidth (FWHM)	$\Gamma_{ge}$	$2\pi \times 23.396$ MHz	[B]
Lifetime	$\tau_{ge} = \Gamma_{ge}^{-1}$	6.8 ns	
Transition dipole matrix element	$\langle J=\frac{1}{2}    e\mathbf{r}    J'=\frac{3}{2} \rangle$	$2.301\,129 \times 10^{-29}$ C m	
Transition frequency	$\omega_{em}$	$2\pi \times 350.862\,882\,823(82)$ THz	[C, D]
Natural linewidth (FWHM)	$\Gamma_{me}$	$2\pi \times 1.576$ MHz	[B]
Lifetime	$\tau_{me} = \Gamma_{me}^{-1}$	101 ns	
Transition dipole matrix element	$\langle J=\frac{5}{2}    e\mathbf{r}    J'=\frac{3}{2} \rangle$	$1.250\,998 \times 10^{-29}$ C m	
Acceleration voltage	$U$	14 kV	
Mean velocity	$\bar{v}$	260 km/s	
Initial width of velocity distribution (FWHM)	$\Delta v_I$	(10 - 100) m/s	

Table 10.1: Parameters for  $^{40}\text{Ca}^+$  transitions between the states  $|g\rangle$ ,  $|e\rangle$  and  $|m\rangle$ , of the configurations  $4s^2S_{1/2}$ ,  $4p^2P_{3/2}$ , and  $3d^2D_{5/2}$ , taken from [A]: [189], [B]:[190], [C]:[191], [D]:[192]. The parameters  $U$ ,  $\bar{v}$ ,  $\Delta v$  are applied in the simulations, being experimentally accessible.

Quantity	Symbol	Value		
Laser 1 (anti collinear)		Parameter set (A)	Parameter set (B <sub>1</sub> )	Parameter set (B <sub>2</sub> )
Frequency	$f_1$	761.243 795 50 THz	— 761.241 765 92 THz	—
Wavelength	$\lambda_1$	393.8192 nm	— 393.8203 nm	—
Wavenumber	$k_1$	$15.954490\,\mu\text{m}^{-1}$	— $15.954448\,\mu\text{m}^{-1}$	—
Power	$P_1$	3.29 mW	10 mW	30 mW
Rabi frequency	$\Omega_1$	$2\pi \times 14.828$ MHz	$2\pi \times 25.852$ MHz	$2\pi \times 44.777$ MHz
Beamradius	$w_0$	—	1.7 mm	—
Linewidth	$\Gamma_{gg}$	—	300 kHz	—
Laser 2 (collinear)		Parameter set (A)	Parameter set (B <sub>1</sub> )	Parameter set (B <sub>2</sub> )
Frequency	$f_2$	351.166 422 00 THz	— 351.164 388 90 THz	—
Wavelength	$\lambda_2$	853.7048 nm	— 853.7097 nm	—
Wavenumber	$k_2$	$7.359904\,\mu\text{m}^{-1}$	— $7.359861\,\mu\text{m}^{-1}$	—
Power	$P_2$	11.13 mW	33 mW	500 mW
Rabi frequency	$\Omega_2$	$2\pi \times 14.827$ MHz	$2\pi \times 25.531$ MHz	$2\pi \times 99.379$ MHz
Beamradius	$w_0$	—	1.7 mm	—
Linewidth	$\Gamma_{mm}$	—	300 kHz	—

Table 10.2: Experimentally accessible laser parameters used for the simulations.

### Rabi frequencies

The Rabi frequencies, defining the interaction strength and listed in Table 10.2, can be calculated with the total laser power  $P$  and the effective dipole moment  $\mathcal{D}_{\text{eff}}$  via Eq. (2.13). Due to the non-existent nuclear spin of the considered level configurations, there is no hyperfine splitting and consequently the lasers interact with the  $J \rightarrow J'$  transition. It is worth mentioning, that any Zeeman splitting of the fine structure is neglected, assuming the absence of static magnetic fields. The lasers are linearly polarised, wherefore they interact only with

one of three components of the dipole operator and the effective coupling strength is given by  $|\mathcal{D}_{\text{eff}}|^2 = |\mathcal{D}|^2/3$ , with the reduced dipole matrix element  $\mathcal{D} = \langle J || e \mathbf{r} || J' \rangle$  [cf. Table 10.1, Eq. (2.14)] [109, 193].

### 10.3 THEORETICAL MODEL

The essential electronic structure of the ions is assumed to be a closed three-level system, consisting of the ground-state manifold  $4s^2S_{1/2}$ , the excited state  $4p^2P_{3/2}$ , and the metastable state  $3d^2D_{5/2}$ , depicted in Fig. 10.4. The lifetime  $\tau_{mg} = 1.168(7)\text{s}$  [194] of the metastable state is much longer than the duration of the spectroscopy and therefore it is considered as stable. Further calcium data and laser parameters are provided in Tabs. 10.1, 10.2.

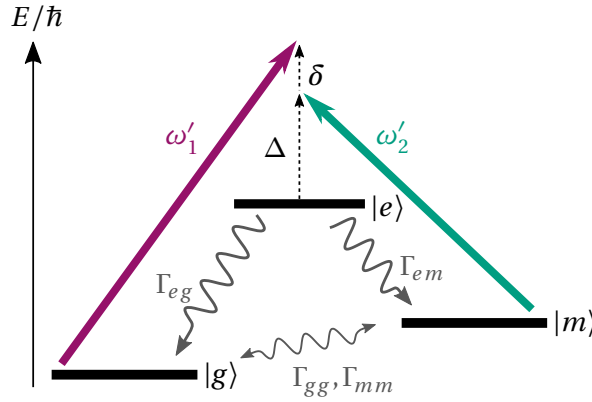


Figure 10.4: Three-level energy diagram for  $^{40}\text{Ca}^+$ . Laser 1 induces  $eg$ -transitions with  $\omega_{eg} = \omega_e - \omega_g$  and laser 2 couples the  $em$ -transition with  $\omega_{em} = \omega_e - \omega_m$ . In the rest frame of the ions, the one-photon detuning is  $\Delta = \omega'_2 - \omega_{em}$  and the two-photon detuning  $\delta = \omega'_1 - \omega'_2 - \omega_{mg}$  with respect to the Doppler-shifted frequencies  $\omega'_1, \omega'_2$  given by Eq. (10.10). The spontaneous decay rates  $\Gamma_{eg}$  and  $\Gamma_{em}$  couple the excited state  $|e\rangle$  to the ground  $|g\rangle$  and metastable state  $|m\rangle$ . Laser noise induces ground-state decoherence with rates  $\Gamma_{gg}, \Gamma_{mm}$ .

#### 10.3.1 Ion-field interaction

The Raman transition is generated with two counterpropagating lasers as shown in Fig. 10.2, with electric fields  $\mathbf{E}_i(\mathbf{r}, t) = \text{Re}[\epsilon_i \mathcal{E}_i e^{i(\mathbf{k}_i \mathbf{r} - \omega_i t)}]$ . The coordinate  $\mathbf{r}$  refers to the laboratory frame  $S$ . Assuming that the ion beam and the lasers are aligned along the  $x$ -direction, the ion velocity  $\mathbf{v} = v \mathbf{e}_x$  and the laser wavevectors  $\mathbf{k}_1 = -k_1 \mathbf{e}_x$  and  $\mathbf{k}_2 = k_2 \mathbf{e}_x$  are specified. During the interaction of the laser pulses, no relevant transversal motion occurs, leading to the reduction to the one-dimensional evolution in the  $x$ -direction.

In the optical domain, the electric dipole interaction in rotating-wave approximation is dominant [140]. Thus, the Hamilton operator of an ion with quantised canonical coordinates  $[\hat{x}, \hat{p}_x] = i\hbar$  is

$$\hat{H}(t) = \frac{\hat{p}_x^2}{2M} + \hbar(\omega_g \hat{\sigma}_{gg} + \omega_m \hat{\sigma}_{mm} + \omega_e \hat{\sigma}_{ee}) + \hbar \left( \hat{\sigma}_{eg} \frac{\Omega_1}{2} e^{i\phi_1} + \hat{\sigma}_{em} \frac{\Omega_2}{2} e^{i\phi_2} + \text{h.c.} \right), \quad (10.6)$$

with the phases of the lasers  $\phi_1 = -k_1 \hat{x} - \omega_1 t$  and  $\phi_2 = k_2 \hat{x} - \omega_2 t$ . It accounts for the kinetic and the internal energy of the ion, where  $\hbar\omega_i$  is the energy of state  $|i\rangle$ . The electronic transition operators are  $\hat{\sigma}_{ij} = |i\rangle\langle j|$ . The strength of the dipole interaction is measured by the Rabi

frequency  $\Omega_i$  (c.f. Sec. 10.2.3). The complete internal and motion state  $\hat{\rho}(t)$  of the ionic beam evolves according to (cf. Sec. 3.2)

$$\dot{\hat{\rho}} = -i[\hat{H}/\hbar, \hat{\rho}]. \quad (10.7)$$

The ballistic evolution is eliminated by the transformation

$$\hat{\rho} = \exp\left(-it \frac{\hat{p}_x^2}{2M\hbar}\right) \hat{\rho}' \exp\left(it \frac{\hat{p}_x^2}{2M\hbar}\right). \quad (10.8)$$

Then, the Liouville-von-Neumann equation  $\dot{\hat{\rho}}' = -i[\hat{H}'/\hbar, \hat{\rho}']$  is defined by the transformed Hamilton operator

$$\hat{H}'(t) = \hbar(\omega_g \hat{\sigma}_{gg} + \omega_m \hat{\sigma}_{mm} + \omega_e \hat{\sigma}_{ee}) + \hbar\left(\hat{\sigma}_{eg} \frac{\Omega_1}{2} e^{i\phi'_1} + \hat{\sigma}_{em} \frac{\Omega_2}{2} e^{i\phi'_2} + \text{h.c.}\right), \quad (10.9)$$

with Doppler-shifted phases  $\phi'_1 = -k_1 \hat{x} - (\omega_1 + k_1 \hat{p}_x/M)t$  and  $\phi'_2 = k_2 \hat{x} - (\omega_2 - k_2 \hat{p}_x/M)t$ . The motional state of the ionic beam smoothly extends over a large phase-space area  $\Delta \hat{x} \Delta \hat{p}_x \gg \hbar/2$ . The photon recoils  $\hbar k_i \ll \Delta \hat{p}_x$  are extremely small compared to the momentum width. In addition, the recoil energy  $\hbar^2(k_1 + k_2)^2/2M \ll \hbar\Gamma_i$ ,  $\hbar\Omega_i$  is extremely small compared to the level shifts or widths, however the Doppler shifts  $k_i \Delta \hat{p}_x \gg \Gamma_i, \Omega_i$  are significant. Hence, the classical approximation  $(\hat{x}, \hat{p}_x) \rightarrow (x, p_x = Mv)$  of kinetic theory [106] can be used. Consequently, the full quantum state  $\hat{\rho}'(t) \rightarrow \hat{\rho}'(t; x, v)$  is replaced by an internal state operator denoting the motional variables to the role of parameters.

Introducing the Doppler-shifted laser frequencies

$$\omega'_i = \omega_i - \mathbf{k}_i \mathbf{v} = \begin{cases} \omega_1 + k_1 v, \\ \omega_2 - k_2 v, \end{cases} \quad (10.10)$$

with the vacuum dispersion  $\omega_i = c k_i$ , the phases read  $\phi'_1 = -k_1 x - \omega'_1 t$  and  $\phi'_2 = k_2 x - \omega'_2 t$ . Then, the Hamilton operator in the classical approximation  $\hat{H}' \rightarrow \hat{\mathcal{H}}'$  is given by

$$\hat{\mathcal{H}}'(t) = \hbar(\omega_g \hat{\sigma}_{gg} + \omega_m \hat{\sigma}_{mm} + \omega_e \hat{\sigma}_{ee}) + \hbar\left(\hat{\sigma}_{eg} \frac{\Omega_1}{2} e^{i\phi'_1} + \hat{\sigma}_{em} \frac{\Omega_2}{2} e^{i\phi'_2} + \text{h.c.}\right). \quad (10.11)$$

Transforming the laboratory frame into the rest frame of an ion moving with velocity  $v$  the remaining optical and spatial oscillations are eliminated by the transformation

$$\hat{\rho}' = \hat{U}(t; x) \hat{\rho} \hat{U}^\dagger(t; x), \quad \hat{U}(t, x) = \exp(-i\omega_e t - i\phi'_1 \hat{\sigma}_{gg} + i\phi'_2 \hat{\sigma}_{mm}). \quad (10.12)$$

This results in the Liouville-von Neumann equation for the semiclassical state  $\dot{\hat{\rho}} = -i[\hat{\mathcal{H}}/\hbar, \hat{\rho}]$ , with the effective  $\Lambda$ -Hamilton matrix

$$\mathcal{H}_{ij} = \hbar \begin{pmatrix} \Delta_1 & \frac{\Omega_1^*}{2} & 0 \\ \frac{\Omega_1}{2} & 0 & \frac{\Omega_2}{2} \\ 0 & \frac{\Omega_2^*}{2} & \Delta_2 \end{pmatrix}, \quad (10.13)$$

where the basis states are sorted as  $i \in \{g, e, m\}$ . The detuning of laser 1 ( $\Delta_1$ ) and laser 2 ( $\Delta_2$ ) define the one- ( $\Delta$ ) and two-photon detuning ( $\delta$ ), according to the energy diagram in Fig. 10.4 and resulting in

$$\Delta_1 = \omega_1 + k_1 v - \omega_{eg} = \Delta_{1,0} + k_1 v, \quad \delta \equiv \Delta_1 - \Delta_2, \quad \delta_0 \equiv \Delta_{1,0} - \Delta_{2,0}, \quad (10.14a)$$

$$\Delta_2 = \omega_2 - k_2 v - \omega_{em} = \Delta_{2,0} - k_2 v, \quad \Delta \equiv \Delta_2. \quad (10.14b)$$

Here, transition frequencies are denoted as  $\omega_{ij} = \omega_i - \omega_j$ .

### 10.3.2 Optical Bloch equations

An ensemble of ions interacting with lasers in free space establishes an open quantum system and must be described by a master equation (cf. Sec. 3.3) for the semi-classical density operator  $\hat{\rho}(t; x, v)$

$$\dot{\hat{\rho}} = -\frac{i}{\hbar} [\hat{\mathcal{H}}, \hat{\rho}] + (\mathcal{L}_{eg} + \mathcal{L}_{em} + \mathcal{L}_{gg} + \mathcal{L}_{mm})\hat{\rho}, \quad (10.15)$$

with the Lindblad operators

$$\mathcal{L}_\lambda \hat{\rho} \equiv \frac{\Gamma_\lambda}{2} (2\hat{\sigma}_\lambda \hat{\rho} \hat{\sigma}_\lambda^\dagger - \hat{\sigma}_\lambda^\dagger \hat{\sigma}_\lambda \hat{\rho} - \hat{\rho} \hat{\sigma}_\lambda^\dagger \hat{\sigma}_\lambda). \quad (10.16)$$

The first term of the master equation describes the coherent dynamics. The second and third term represent spontaneous transitions to the ground  $|g\rangle$  and metastable state  $|m\rangle$  with decay rates  $\Gamma_{eg}$  and  $\Gamma_{em}$ , respectively. It is worth to mention, that distinguishable radiation from the two transitions is assumed. For indistinguishable radiation  $\sqrt{\Gamma_{eg}\Gamma_{em}}(\hat{\sigma}_{ge}\hat{\rho}\hat{\sigma}_{me}^\dagger + \hat{\sigma}_{me}\hat{\rho}\hat{\sigma}_{ge}^\dagger)$  has to be added in Eq. (10.15). Expecting  $|\omega_1 - \omega_2| \gg \Gamma_{eg/em}$  that term can be neglected. The fourth and fifth term consider ground-state dephasing due to finite laser linewidths  $\Gamma_{gg}$  of laser 1 and  $\Gamma_{mm}$  of laser 2 [89, 106, 195–198]. Please note, with the applied approximation for the Hamiltonian evolution in the last Section 10.3.1, essentially any photon recoil effects are disregarded. One can apply the same arguments to the spontaneous contributions of the Lindblad equation [106].

If one represents the master equation in a basis and arranges the matrix elements of  $\rho = (\rho_{ij})$ , with  $\rho_{ij} = \langle i | \hat{\rho} | j \rangle$ , as a list, one obtains

$$\dot{\rho}(t; v) = L(v)\rho(t; v). \quad (10.17)$$

Explicitly, these optical Bloch equations (OBEs) read

$$\begin{aligned} \dot{\rho}_{ee} &= -\Gamma\rho_{ee} + \frac{i}{2}(\Omega_1^*\rho_{eg} + \Omega_2^*\rho_{em} - \text{h.c.}), \\ \dot{\rho}_{gg} &= \Gamma_{eg}\rho_{ee} + \frac{i}{2}(\Omega_1\rho_{ge} - \Omega_1^*\rho_{eg}), \\ \dot{\rho}_{mm} &= \Gamma_{em}\rho_{ee} + \frac{i}{2}(\Omega_2\rho_{me} - \Omega_2^*\rho_{em}), \end{aligned} \quad (10.18)$$

for the populations and for the coherences  $\rho_{ij} = \rho_{ji}^*$

$$\begin{aligned} \dot{\rho}_{eg} &= (i\Delta_1 - \Gamma_1)\rho_{eg} + \frac{i}{2}[\Omega_1(\rho_{ee} - \rho_{gg}) - \Omega_2\rho_{mg}], \\ \dot{\rho}_{em} &= (i\Delta_2 - \Gamma_2)\rho_{em} + \frac{i}{2}[\Omega_2(\rho_{ee} - \rho_{mm}) - \Omega_1\rho_{gm}], \\ \dot{\rho}_{gm} &= -(i\delta + \gamma)\rho_{gm} + \frac{i}{2}[\Omega_2\rho_{ge} - \Omega_1^*\rho_{em}], \end{aligned} \quad (10.19)$$

with composite rates

$$\Gamma = \Gamma_{eg} + \Gamma_{em}, \quad \gamma = (\Gamma_{gg} + \Gamma_{mm})/2, \quad \Gamma_1 = (\Gamma + \Gamma_{gg})/2, \quad \Gamma_2 = (\Gamma + \Gamma_{mm})/2. \quad (10.20)$$

## RESONANCES IN THE FREQUENCY DOMAIN

Analysing the solution of the optical Bloch equations in the frequency domain, gives physical insights to the relevant underlying processes.

### 11.1 RESONANCE CONDITIONS

The objective for using the stimulated Raman transition is to filter a velocity group  $v_R$  from the ionic ensemble with a resolution far below the natural linewidth. Therefore, population from the ground state is transferred to the metastable state via the strongly velocity selective Raman transition. From energy conservation (cf. Fig. 10.4) and the AC-Stark shifted eigenfrequencies  $\underline{\Delta}$ , one obtains the kinematic condition defining the Raman velocity  $v_R$  for the effective two-photon resonance

$$\underline{\delta}(v = v_R) = \underline{\Delta}_1 - \underline{\Delta}_2 = 0. \quad (11.1)$$

From second order perturbation theory of the Schrödinger equation  $\mathcal{H}\mathbf{w}_i = \hbar \underline{\Delta}_i \mathbf{w}_i$  (10.13), one obtains the AC-Stark shifted eigenfrequencies

$$\underline{\Delta}_1 = \Delta_1 \left(1 + \frac{s_1}{2}\right), \quad \underline{\Delta}_2 = \Delta_2 \left(1 + \frac{s_2}{2}\right), \quad \underline{\Delta}_3 = \Delta_1 + \Delta_2 - \underline{\Delta}_1 - \underline{\Delta}_2 \quad (11.2)$$

to order  $\mathcal{O}(s_1^2, s_2^2)$ . In here, the limit of weakly saturated transitions is considered, conveniently captured by the saturation parameter  $s_i = |\Omega_i|^2 / 2\Delta_i^2 \ll 1$ . Thus, the Doppler shifted laser frequencies must match the AC-Stark shifted transition frequencies of the ground states (11.2). This defines the Raman resonance velocity<sup>1</sup>

$$v_R = -\frac{\delta_0}{k_1 + k_2} + \frac{|\Omega_2|^2 - |\Omega_1|^2}{4(k_1 + k_2)\tilde{\Delta}}, \quad (11.3)$$

where  $v_{R,0} = -\delta_0 / (k_1 + k_2)$  is the dominant contribution, and around the Raman resonance, within the limit of weak saturation, one can approximate

$$\frac{\Omega_i^* \Omega_j}{\Delta_i(\nu)} \approx \frac{\Omega_i^* \Omega_j}{\tilde{\Delta}}, \quad \tilde{\Delta} \equiv \Delta_i(v_{R,0}) = \frac{\Delta_{2,0}k_1 + \Delta_{1,0}k_2}{k_1 + k_2}. \quad (11.4)$$

It is interesting to recognise the magic spot  $|\Omega_1| = |\Omega_2|$ , where second order energy shifts cancel in (11.3) resulting in  $v_R = v_{R,0}$ .

<sup>1</sup> The Raman resonance condition (11.1) is simplified using approximation (11.4). Then  $\underline{\delta}(v_R) = \underline{\Delta}_1(v_R) - \underline{\Delta}_2(v_R) = \Delta_1(v_R) + \frac{|\Omega_1|^2}{4\Delta_1(v_R)} - \Delta_2(v_R) - \frac{|\Omega_2|^2}{4\Delta_2(v_R)} \approx \delta(v_R) + \frac{|\Omega_1|^2 - |\Omega_2|^2}{4\tilde{\Delta}} = \delta_0 + (k_1 + k_2)v_R + \frac{|\Omega_1|^2 - |\Omega_2|^2}{4\tilde{\Delta}} \stackrel{!}{=} 0$  results in (11.3).

There are also two rogue resonances at velocities  $v_1$  and  $v_2$ , where each laser couples individually resonantly to the excited state

$$\underline{\Delta}_1(v_1) = 0, \quad v_1 = -\Delta_{1,0}/k_1, \quad (11.5)$$

$$\underline{\Delta}_2(v_2) = 0, \quad v_2 = \Delta_{2,0}/k_2. \quad (11.6)$$

Depending on the laser parameters and the ion velocity, all three resonances can be far apart from each other or even coincide.

## 11.2 CONTRIBUTIONS OF THE RESONANCES

Width and strength of the resonances are determined by the Bloch equations (10.17). Representing the master equation (10.15) in the sorted basis  $\{|g\rangle, |e\rangle, |m\rangle\}$  and arranging the matrix elements as linear arrays  $\rho = (\rho_g, \rho_e, \rho_m)$  with  $\rho_i = (\rho_{ig}, \rho_{ie}, \rho_{im})$ , one finds the Bloch matrix

$$L = i \begin{pmatrix} 0 & \frac{\Omega_1}{2} & 0 & -\frac{\Omega_1^*}{2} & -i\Gamma_{eg} & 0 & 0 & 0 & 0 \\ \frac{\Omega_1^*}{2} & i\Gamma_1 - \Delta_1 & \frac{\Omega_2^*}{2} & 0 & -\frac{\Omega_1^*}{2} & 0 & 0 & 0 & 0 \\ 0 & \frac{\Omega_2}{2} & i\gamma - \delta & 0 & 0 & -\frac{\Omega_1^*}{2} & 0 & 0 & 0 \\ -\frac{\Omega_1}{2} & 0 & 0 & \Delta_1 + i\Gamma_1 & \frac{\Omega_1}{2} & 0 & -\frac{\Omega_2}{2} & 0 & 0 \\ 0 & -\frac{\Omega_1}{2} & 0 & \frac{\Omega_1^*}{2} & i\Gamma & \frac{\Omega_2^*}{2} & 0 & -\frac{\Omega_2}{2} & 0 \\ 0 & 0 & -\frac{\Omega_1}{2} & 0 & \frac{\Omega_2}{2} & \Delta_2 + i\Gamma_2 & 0 & 0 & -\frac{\Omega_2}{2} \\ 0 & 0 & 0 & -\frac{\Omega_2^*}{2} & 0 & 0 & \delta + i\gamma & \frac{\Omega_1}{2} & 0 \\ 0 & 0 & 0 & 0 & -\frac{\Omega_2^*}{2} & 0 & \frac{\Omega_1^*}{2} & i\Gamma_2 - \Delta_2 & \frac{\Omega_2^*}{2} \\ 0 & 0 & 0 & 0 & -i\Gamma_{em} & -\frac{\Omega_2^*}{2} & 0 & \frac{\Omega_2}{2} & 0 \end{pmatrix}. \quad (11.7)$$

It exhibits the block structure of two coupled two-level systems

$$L = \begin{pmatrix} L_{gg} & L_{ge} & 0 \\ L_{eg} & L_{ee} & L_{em} \\ 0 & L_{me} & L_{mm} \end{pmatrix}. \quad (11.8)$$

The Bloch equations define an initial value problem, where the whole population starts in the ground state  $\rho(t=0) = (\rho_g^0, \rho_e^0, \rho_m^0) = (1, 0, 0, 0, 0, 0, 0, 0, 0)$ . The Laplace transform

$$\varrho(s) = \int_0^\infty dt e^{-st} \rho(t), \quad (11.9)$$

is ideally suited to transform the system of differential equations with initial values to an algebraic equation

$$\begin{pmatrix} \mathcal{G}_g^{0-1} & -L_{ge} & 0 \\ 0 & \mathcal{G}_e^{0-1} & -L_{em} \\ 0 & 0 & \mathcal{G}_m^{0-1} \end{pmatrix} \begin{pmatrix} \varrho_g \\ \varrho_e \\ \varrho_m \end{pmatrix} = \begin{pmatrix} \rho_g^0 \\ L_{eg} \varrho_g \\ L_{me} \varrho_e \end{pmatrix}, \quad (11.10)$$



where  $\mathcal{G}_\lambda^0(s) = (s - L_{\lambda\lambda})^{-1}$  is the resolvent matrix. The formal inversion of the Bloch matrix is facilitated by the block structure and by backward substitution. This leads to the explicit solution

$$\begin{aligned}\varrho_g(s) &= \mathcal{G}_g(s) \rho_g^0, & \mathcal{G}_g^{-1} &= \mathcal{G}_g^{0-1} - L_{ge} \mathcal{G}_e L_{eg}, \\ \varrho_e(s) &= \mathcal{G}_e(s) L_{eg} \varrho_g(s), & \mathcal{G}_e^{-1} &= \mathcal{G}_e^{0-1} - L_{em} \mathcal{G}_m L_{me}, \\ \varrho_m(s) &= \mathcal{G}_m(s) L_{me} \rho_e(s), & \varrho_i &= (\rho_{ig}, \rho_{ie}, \rho_{im}).\end{aligned}\quad (11.11)$$

One finds the stationary solution using the final value theorem of the Laplace transformation

$$\rho_{mm}^\infty \equiv \lim_{t \rightarrow \infty} \rho_{mm}(t) = \lim_{s \rightarrow 0} s \varrho_{mm}(s). \quad (11.12)$$

In addition, the Laplace transform can be used to approximate the initial growth rate of the population of the metastable state  $\dot{\rho}_{mm}(t=0)$ . This provides insights into the contributions of different processes of population transfer. Therefore, in Fig. 11.1 the processes generating population in  $|m\rangle$  are schematically visualised.

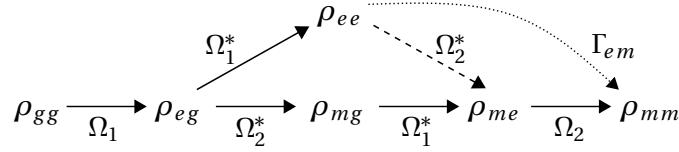


Figure 11.1: Linkage pattern for two-photon transitions connecting the ground state  $|g\rangle$  with the metastable state  $|m\rangle$ .

From this linkage pattern, one obtains three pathways to reach state  $|m\rangle$ , starting at  $|g\rangle$ . Perturbatively, one obtains the Laplace transform, considering only the initial processes (cf. App. F1), denoted with  $\tilde{\varrho}_{mm}$

$$\tilde{\varrho}_{mm}(s) = G_{mm} \left[ \left( \Gamma_{em} + \frac{|\Omega_2|^2}{2} \text{Re}[G_{me}] \right) \tilde{\varrho}_{ee}(s) + \frac{|\Omega_2|^2 |\Omega_1|^2}{8} \text{Re}[G_{me} G_{mg} G_{eg}] G_{gg} \right], \quad (11.13)$$

$$\tilde{\varrho}_{ee}(s) = \frac{|\Omega_1|^2}{2} G_{ee} \text{Re}[G_{eg}] G_{gg}, \quad (11.14)$$

with

$$\begin{aligned}G_{gg}^{-1} &= s, & G_{ee}^{-1} &= s + \Gamma, & G_{eg}^{-1} &= s - i\Delta_1 + \Gamma_1, \\ G_{mm}^{-1} &= s, & G_{gm}^{-1} &= s + i\delta + \gamma, & G_{em}^{-1} &= s - i\Delta_2 + \Gamma_2.\end{aligned}\quad (11.15)$$

In equation (11.13) the three different population processes, following the scheme in Fig. 11.1, are apparent. The first two terms lead to population in the excited state, followed by spontaneous emission (dotted path in the linkage pattern) for the first term or stimulated emission (dashed) for the second term respectively into the metastable state. The third term represents the Raman transition, without generating population in the excited state (full solid path from  $\rho_{gg}$  to  $\rho_{mm}$  in Fig. 11.1). The initial growth rate of the metastable state's population is then given by  $r_m = \lim_{s \rightarrow 0} s^2 \tilde{\varrho}_{mm}(s)$

$$r_m = \frac{\Gamma_1 s_1}{\Gamma} \left[ \Gamma_{em} + \Gamma_2 s_2 \left\{ 1 + \frac{\Gamma \delta}{2(\gamma^2 + \delta^2)} \left( \frac{\Delta_1}{\Gamma_1} - \frac{\Delta_2}{\Gamma_2} \right) + \frac{\Gamma \gamma}{2(\gamma^2 + \delta^2)} \left( 1 + \frac{\Delta_1 \Delta_2}{\Gamma_1 \Gamma_2} \right) \right\} \right]. \quad (11.16)$$

Here, the saturation parameter is generalised from the coherent limit to  $s_i = |\Omega_i|^2 / 2(\Gamma_i^2 + \Delta_i^2)$ , now broadening the resonances with the linewidths  $\Gamma_i$ . The first two resonances occur spontaneously at  $\Delta_1 = 0$  and  $\Delta_2 = 0$ , while the last two describe the stimulated Raman process at  $\delta = 0$ . Due to laser noise, it acquires the finite linewidth  $\gamma$ .

This growth rate  $r_m$  is schematically depicted in Fig. 11.2 together with the stationary solution  $\rho_{mm}^\infty$  (11.12). The narrow stimulated Raman resonance at  $\nu_R$ , is clearly distinguishable from the resonance of laser 1 at  $\nu_1$ , where  $|e\rangle$  gets populated followed by spontaneous emission into  $|m\rangle$ . This incoherent process limits the velocity determination, due to the broad tail. Therefore, it is called the rogue resonance in the further course. In contrast to the initial rate  $r_m$ , the stationary solution  $\rho_{mm}^\infty$  suppresses the resonance at  $\nu_2$ , because stimulated emission is compensated with stimulated absorption. Conclusively, it is import to take the rogue resonance of laser 1 into account, while that one of laser 2 will have a much smaller impact.

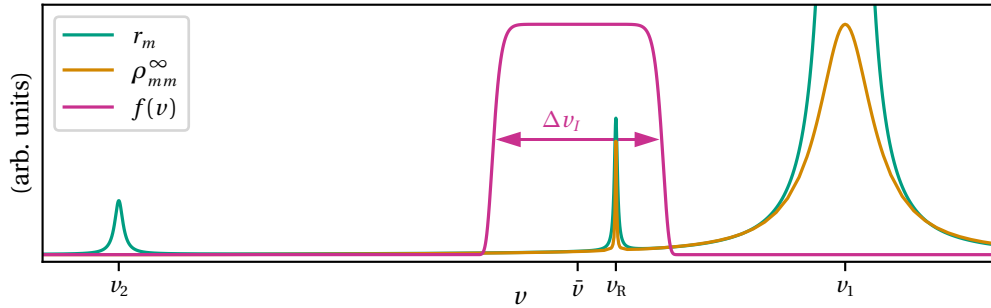


Figure 11.2: The initial growth rate  $r_m$  (11.16) of the metastable state's population and the exact stationary solution  $\rho_{mm}^\infty$  (11.11, 11.12) exhibit resonances at  $\nu_1$ ,  $\nu_2$  and  $\nu_R$ . The ionic initial velocity distribution  $f(v)$  is defined by its mean velocity  $\bar{\nu}$  and width  $\Delta \nu_l$ . Note that the velocity distribution emerging from the accelerator is rather flat topped.

### 11.3 ISOLATING RESONANCES

The positions of the resonances are controlled by the laser frequencies. Obviously, the Raman resonance at  $\nu_R$  should be within the ion velocity distribution, also depicted in Fig. 10.3. In contrast, the rogue resonances should be spread far apart. Therefore, optimal laser frequencies are defined by maximising the resonance separations

$$\beta_i = \frac{v_i - \nu_{R,0}}{c}. \quad (11.17)$$

First, for a given Raman resonance velocity  $\nu_{R,0}$  (11.3), one obtains a linear frequency relation

$$\omega_2(\omega_1; \nu_{R,0}) = \frac{\omega_1 \alpha_+ - \omega_{mg}}{\alpha_-}, \quad \alpha_{\pm} = 1 \pm \frac{\nu_{R,0}}{c}, \quad (11.18)$$

where AC-frequency shifts are deliberately disregarded. Second, the distances between the resonances are now functions of  $\omega_1$

$$\beta_1(\omega_1) = \frac{\omega_{eg}}{\omega_1} - \alpha_+, \quad \beta_2(\omega_1) = \alpha_- \left( 1 - \frac{\omega_{em}}{\omega_1 \alpha_+ - \omega_{mg}} \right), \quad (11.19)$$

which is depicted in Fig. 11.3. The requirement of positive laser frequencies  $\omega_2(\omega_1) > 0$ , leads

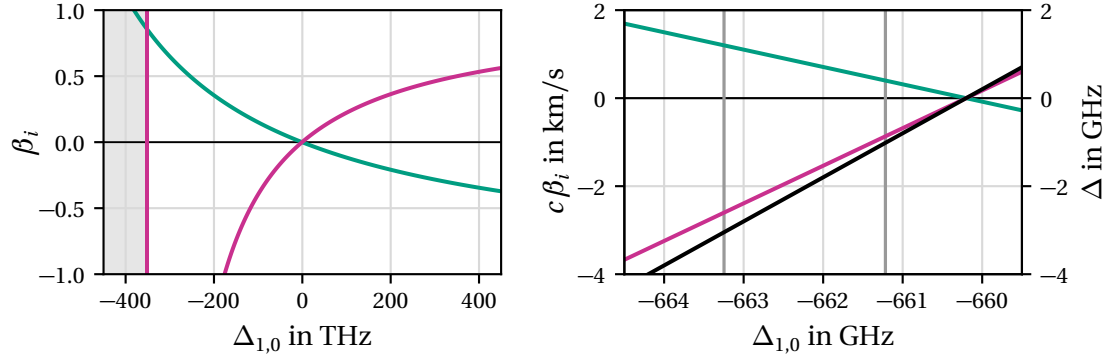


Figure 11.3: Velocity distance  $\beta_1$  (magenta) and  $\beta_2$  (green) between the Raman resonance and the rogue resonances versus detuning  $\Delta_{1,0}$ . The inadmissible range  $\omega_2 < 0$ , is shaded in grey (left). On the right, real velocities  $c\beta_i$  and the Doppler shifted one-photon detuning  $\Delta$  (black) are shown on a small scale. Here, the detunings for parameter set (A) and (B) (cf. Table 10.2) are highlighted (grey).

to a lower limit for  $\omega_1 > \omega_{mg}/\alpha_+$ . For positive laser frequencies the Raman resonance lies always between the rogue resonances  $\nu_1$  and  $\nu_2$ . Therefore, the distances  $\beta_1$  and  $\beta_2$  show opposite signs. Obviously, the zero crossing of  $\beta_i$  represents the worst scenario, when all three resonances occur simultaneously and interfere. The related detuning  $\Delta_{1,0}(\beta_i = 0)$  depends on  $\nu_{R,0}$  and lies between  $\Delta_{1,0}(\beta_i = 0) = 0$  for  $\nu_{R,0} = 0$  m/s and  $\Delta_{1,0}(\beta_i = 0) = -\omega_{eg}/2$  for  $\nu_{R,0} = c$ . For ultraviolet to near-infrared laser frequencies, viz.  $\nu_{R,0} \ll c$ , the relation  $|\beta_2| > |\beta_1|$  holds. Therefore, only the distance  $\beta_1$  needs to be maximised, lying within the range  $-\alpha_+ < \beta_1 < \alpha_+ \omega_{em}/\omega_{mg}$ . For detunings  $|\Delta_{1,0}| < 1$  THz, the hyperbolic shape of the distance

$$\beta_1(\Delta_{1,0}) = -\frac{\nu_{R,0}}{c} - \frac{\Delta_{1,0}}{\omega_{eg}} + \frac{\Delta_{1,0}^2}{\omega_{eg}^2} + \dots \quad (11.20)$$

is almost linear. Then, the maximal distance of  $\beta_1$  is only limited by the available laser powers and interaction time. The time should last at least for one  $\pi$ -pulse  $t_\pi$  (12.13) of a Raman transition, where maximal population transfer is achieved. This time will be derived in the next Chapter 11 and is proportional to the Doppler shifted one-photon detuning  $\Delta$  and anti-proportional to the laser power. Therefore,  $\Delta$  is also depicted in Fig. 11.3 (right) and the values of  $\Delta_{1,0}$  for the parameter set (A) and (B), (cf. Table 10.2) are highlighted. These parameter sets lead to two distinct velocity distances  $c\beta_1^{(A)} = 400$  m/s,  $c\beta_1^{(B)} = 1200$  m/s, keeping  $\Delta$  small enough for the experimentally given interaction time and provided laser power.

Due to the approximately linear behaviour of  $\beta_1$  there is only a very little difference between a red- and blue detuning  $\Delta_{1,0}$ . However, regarding the gradient

$$\frac{d\beta_1}{d\omega_1} = -\frac{\omega_{eg}}{\omega_1^2} \quad (11.21)$$

its absolute value is larger for  $\omega_1 < \omega_{eg}$ , demonstrating the benefit of choosing negative detunings  $\Delta_{1,0}$ .

For the sake of completeness, the distances to the resonance of laser 2 are  $c\beta_2^{(A)} = 867$  m/s and  $c\beta_2^{(B)} = 2601$  m/s.



---

## TIME RESOLVED POPULATION TRANSFER

---

The principal aim is the optimisation of the time- and velocity-dependent population transfer from the initial state  $|g\rangle$  to the metastable state  $|m\rangle$ , where the population of  $|m\rangle$  is denoted with  $m$ . Therefore, the velocity averaged quantum expectation value of the observable  $\hat{\sigma}_{mm}$

$$\langle m(t, v) \rangle_v = \int_0^\infty dv f(v) \text{Tr}\{\hat{\sigma}_{mm} \hat{\rho}(t; v)\} \quad (12.1)$$

should be maximised. In addition, the uncertainty of the voltage measurement should be minimised simultaneously, which is defined by the logarithmic derivative of Eq. (10.1)

$$s = \frac{\Delta U}{U} = \frac{2\Delta v}{v_R}. \quad (12.2)$$

The smallest uncertainties are obtained for minimal final velocity widths of the metastable-state population, denoted with  $\Delta v$ .

Both objectives require the solution of the Bloch equations (10.17) for each velocity  $v$  within the distribution  $f(v)$ . Formally, the solution of this initial value problem

$$\rho(t; v) = V(v) e^{\Lambda(v)t} V(v)^{-1} \rho(t=0; v), \quad (12.3)$$

$$L(v) V(v) = V(v) \Lambda(v), \quad (12.4)$$

is determined from the knowledge of the eigenvalues  $\Lambda_i$  and the eigenmatrix  $V(v)$  of the Liouvillian matrix  $L(v)$ . A numerical procedure is implemented to solve these equations for all velocities, obtaining averages as physical observables. This is referred to as the exact solution. However, in order to get insights on the underlying physical mechanisms, a simple approximation is derived that matches the exact solution very well. In the following, different approximations emphasise the relevance of the individual processes contributing cumulatively to the exact result. Therefore, a good separation of all resonances, analysed in the last Section 11.3, is assumed. In addition to physical insights, these approximations provide tremendous reduction in computational effort in comparison to the exact numerical solution.

### 12.1 STIMULATED RAMAN TRANSITION

For far detuned lasers  $|\Delta| \gg \Gamma_i$ , taking the Doppler-shifts into account, the excited state stays nearly unpopulated, wherefore spontaneous emission is not an issue. Hence, in a small regime around the resonant velocity  $v_R$ , the dynamics can be approximated by an effective two-level system, consisting of the ground and metastable states. This describes the pure process of the stimulated Raman transition, neglecting the influence of any rogue resonance. Therefore, it corresponds to the ideal solution.

The experimental parameters provide laser linewidths  $\gamma \sim 10^2$  kHz, much larger Rabi frequencies  $\Omega_i \sim 10^2$  MHz and even larger one-photon detunings  $\Delta_{0,i} \sim (10^2 - 10^3)$  GHz. In addition, around the Raman resonance, the two-photon detuning  $\delta$  is by definition very small. Therefore, the separation of frequency scales

$$\boxed{\gamma, \delta \ll \Gamma, \Omega_i \ll \Delta_i} \quad (12.5)$$

will be frequently used to simplify the following approximations.

### 12.1.1 Coherent dynamics

The ideal coherent dynamics, assuming infinitely sharp laser linewidths ( $\gamma=0$ ), are described by the Schrödinger equation

$$i\hbar\partial_t|\psi\rangle = (\hat{\mathcal{H}} - \hbar\varpi)|\psi\rangle, \quad (12.6)$$

with  $|\psi\rangle = \psi_g|g\rangle + \psi_e|e\rangle + \psi_m|m\rangle$  and the Hamilton matrix (10.13). In order to apply the standard adiabatic elimination methods [150] to eliminate the extremely small excited state population, one needs to transform to another frame. This is accomplished by introducing the constant frequency shift  $\varpi = \Delta + \delta/2$ , leading only to an unobservable, global, dynamical phase. With  $\partial_t\psi_e \ll \Delta\psi_e$  the usual way to eliminate the excited state consists in claiming  $\partial_t\psi_e(t) = 0$ . Thus, the resulting effective two-level system reads

$$i\partial_t \begin{pmatrix} \psi_g \\ \psi_m \end{pmatrix} = \begin{pmatrix} \frac{\delta}{2} + \omega_{AC1} & \frac{\Omega_R}{2} \\ \frac{\Omega_R^*}{2} & -\frac{\delta}{2} + \omega_{AC2} \end{pmatrix} \begin{pmatrix} \psi_g \\ \psi_m \end{pmatrix}, \quad (12.7)$$

with the Raman Rabi frequency  $\Omega_R$  and the AC-Stark shifts  $\omega_{ACi}$ . They can be simplified to

$$\Omega_R = \frac{\Omega_1^*\Omega_2}{2\Delta} + \mathcal{O}\left(\frac{\delta}{\Delta}\right), \quad \omega_{ACi} = \frac{|\Omega_i|^2}{4\Delta} + \mathcal{O}\left(\frac{\delta}{\Delta}\right), \quad (12.8)$$

with taking advantage of the separation of the frequency scales (12.5) with  $\delta/\Delta \ll 1$ . The two-level dynamics (12.7) can be solved analytically by diagonalisation, equivalent to Eqs. (12.3), (12.4). For the initial condition  $\psi_g(t=0) = 1$ , the metastable-state population reads

$$m_0(t, \nu) = |\psi_m(t, \nu)|^2 = \frac{|\Omega_R|^2}{\Omega^2} \sin^2\left[\frac{\Omega t}{2}\right], \quad \Omega = \sqrt{|\Omega_R|^2 + \underline{\delta}^2}, \quad (12.9)$$

where the index indicates  $\gamma = 0$  and the effective detuning is simplified according to  $\omega_{ACi}$ , i.e.

$$\underline{\delta} = \underline{\Delta}_1 - \underline{\Delta}_2 = \delta + \frac{|\Omega_1|^2 - |\Omega_2|^2}{4\Delta} + \mathcal{O}\left(\frac{\delta}{\Delta}\right). \quad (12.10)$$

In the limit of weak saturation the solution  $m_0(t, \nu)$  (12.9) can be simplified with

$$\Omega_R \approx \tilde{\Omega}_R \equiv \frac{\Omega_1^*\Omega_2}{2\Delta}, \quad \underline{\delta} \approx d \equiv (k_1 + k_2)(\nu - \nu_R), \quad (12.11)$$

approximating the velocity-dependent Rabi frequencies with their on-resonance values (11.4). Finally, the velocity averaged population is given by Eq. (12.1) and an explicit ionic velocity distribution  $f(\nu)$ . In the calcium experiment, the ions emerge from the accelerator with a flat top velocity distribution

$$f(\nu) = \begin{cases} 1/\Delta\nu_I, & |\nu| \leq \Delta\nu_I/2, \\ 0, & \text{else,} \end{cases} \quad (12.12)$$

introducing the relative velocity  $\nu = \nu - \bar{\nu}$ .

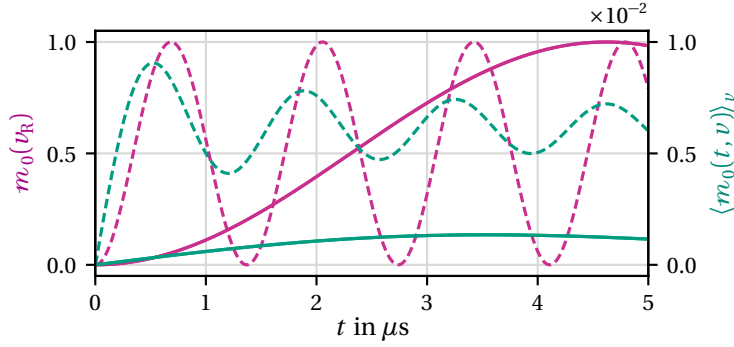


Figure 12.1: Rabi oscillations of the metastable-state population  $m_0(t, \nu_R)$  (magenta) for the resonant velocity, together with the velocity averaged population  $\langle m_0(t, \nu) \rangle_\nu$  (green) for an initial ion velocity width  $\Delta \nu_I = 50 \text{ m/s}$ . The parameter sets (A), (B<sub>1</sub>) (solid) and (B<sub>2</sub>) (dashed) (Table 10.2) are compared.

Figure 12.1 shows Rabi oscillations of the metastable-state population for the resonant velocity  $m_0(t, \nu = \nu_R)$  together with its velocity average  $\langle m_0(t, \nu) \rangle_\nu$ . Three different laser-parameter sets, listed in Table 10.2, are compared, demonstrating the essential impact of different laser frequencies and powers. Parameter sets (A) and (B<sub>1</sub>) generate a  $\pi$ -pulse for the experimental transit time  $\bar{t} = 4.62 \mu\text{s}$  (10.2), where a complete population transfer is achieved for the resonant velocity  $d(\nu = \nu_R) = 0$ . Applying the approximations for the Raman Rabi frequency and the effective detuning (12.11) to the metastable-state population  $m_0(t, \nu)$  (12.9), the  $\pi$ -pulse duration can be easily derived

$$t_{\pi,0} \equiv t_\pi(\gamma = 0) = \frac{\pi}{|\tilde{\Omega}_R|}. \quad (12.13)$$

Parameter sets (A) and (B) differ in the laser frequencies, resulting in vastly different distances between the stimulated and the spontaneous Raman resonances  $\beta_1^{(B_1)} > \beta_1^{(A)}$ , as mentioned in Section 11.3. However, this does not affect the Rabi oscillations and  $\langle m_0(t, \nu) \rangle_\nu$  in Fig. 12.1, because for the purely coherent population transfer via the Raman transition, the spontaneous population transfer is not at all taken into account. Hence, for (A) and (B<sub>1</sub>) there is no difference in the Rabi oscillations and  $\langle m_0(t, \nu) \rangle_\nu$  apparent. The parameter set (B<sub>2</sub>) provides the same laser frequencies as (B<sub>1</sub>), while the maximum laser power, available in the experiment, is applied. Therefore,  $\langle m_0(t, \nu) \rangle_\nu$  is slightly enlarged, effectively due to power broadening. This becomes clear in Fig. 12.2, depicting the velocity dispersion of the metastable-state population after a  $\pi$ -pulse. Using approximations (12.11) and the expression for the  $\pi$ -pulse time (12.13), this population can be approximated with

$$m_0(t_{\pi,0}, \nu) = \frac{\pi^2}{4} \text{sinc}^2\left(\frac{\pi \tilde{\Omega}}{2|\tilde{\Omega}_R|}\right), \quad \text{sinc}(x) = \sin(x)/x. \quad (12.14)$$

This approximation is exemplary plotted for (B<sub>2</sub>), matching the exact analytical solution (12.9). The  $\text{sinc}^2$ -behaviour is the typical response to constant interaction. For smooth temporal

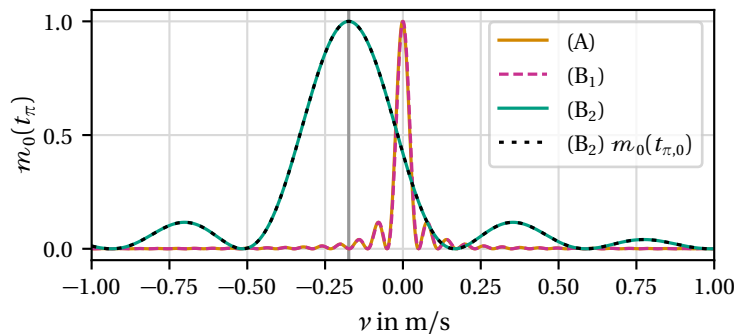


Figure 12.2: The velocity-dependent metastable-state population  $m_0(t_\pi)$  after applying a  $\pi$ -pulse ( $t_\pi^{(A)} = t_\pi^{(B_1)} = 4.62 \mu\text{s}$ ,  $t_\pi^{(B_2)} = 0.68 \mu\text{s}$ ) is indiscernible for parameter sets (A) and (B<sub>1</sub>). For maximal laser power (B<sub>2</sub>) the resonance is broadened as well as shifted. The approximation  $m_0(t_{\pi,0})$  (12.14) matches the full solution.



envelopes the side maxima vanish. Again, the results for (A) and (B<sub>1</sub>) show no difference. For (B<sub>2</sub>), due to the differing Rabi frequencies of both lasers  $\Omega_1^{(B_2)} \neq \Omega_2^{(B_2)}$ , the resonance is AC-Stark shifted to  $\nu_R^{(B_2)} = \nu_R - \bar{\nu} = -0.17$  m/s as predicted by (11.3).

**UNCERTAINTY OF THE VOLTAGE MEASUREMENTS** Finally, the velocity width of  $m_0$  (12.14) characterises the uncertainty of the voltage measurement (12.2), aiming the ppm level. The FWHM of  $m_0$  is defined by the first zero of the sinc-function resulting in

$$\Delta \nu_0(t_{\pi,0}) = \sqrt{3} \frac{|\tilde{\Omega}_R|}{k_1 + k_2}. \quad (12.15)$$

For maximal laser power this width increases from  $\Delta \nu^{(B_1)}(t_{\pi,0} = 4.62 \mu\text{s}) = 0.05$  m/s [0.05 m/s] to  $\Delta \nu^{(B_2)}(t_{\pi,0} = 0.68 \mu\text{s}) = 0.32$  m/s [0.34 m/s], where the results of approximation (12.15) are displayed in square brackets, providing very good predictions. Obviously parameter set (A) provides the same width as (B<sub>1</sub>). The sensitivity is then given by  $s^{(A),(B_1)} = 0.4$  and  $s^{(B_2)} = 2.4$  respectively, reaching even the sub-ppm level for (A), (B<sub>1</sub>).

### 12.1.2 Finite laser linewidths

Considering finite laser linewidths, the ground- and metastable-state decoherences must be taken into account. Adiabatic elimination of the fast coherences  $\rho_{ge}$  and  $\rho_{me}$  in addition to neglecting population of the excited state ( $\rho_{ee}(t) \rightarrow 0$ ) in the OBEs (10.18) and (10.19) leads to the following equations of motion in matrix representation  $\dot{\rho} = L\rho$  with  $\rho = (\rho_{gg}, \rho_{gm}, \rho_{mg}, \rho_{mm})$  and

$$L = \begin{pmatrix} -2\Gamma_1 \frac{|\Omega_1|^2}{|d_1|^2} & i \frac{\Omega_1 \Omega_2^*}{2d_1^*} & -i \frac{\Omega_1^* \Omega_2}{2d_1} & 0 \\ i \frac{\Omega_1^* \Omega_2}{2d_1^*} & -\gamma - i \left( \delta + \frac{|\Omega_1|^2}{2d_2} - \frac{|\Omega_2|^2}{2d_1^*} \right) & 0 & -i \frac{\Omega_1^* \Omega_2}{2d_2} \\ -i \frac{\Omega_1 \Omega_2^*}{2d_1} & 0 & -\gamma + i \left( \delta + \frac{|\Omega_1|^2}{2d_2^*} - \frac{|\Omega_2|^2}{2d_1} \right) & i \frac{\Omega_1 \Omega_2^*}{2d_2^*} \\ 0 & -i \frac{\Omega_1 \Omega_2^*}{2d_2} & i \frac{\Omega_1^* \Omega_2}{2d_2^*} & -2\Gamma_1 \frac{|\Omega_2|^2}{|d_2|^2} \end{pmatrix}, \quad (12.16)$$

with the effective detuning  $d_i = 2(\Delta_i + i\Gamma_i)$ . Making use of the frequency scale separation (12.5), it can be approximated

$$2\Gamma_i \frac{|\Omega_i|^2}{|d_i|^2} \approx 0, \quad d_i \approx 2\Delta_i. \quad (12.17)$$

Therewith, the system of equations simplifies enormously, resulting in

$$L = \begin{pmatrix} 0 & i \frac{\Omega_R^*}{2} & -i \frac{\Omega_R}{2} & 0 \\ i \frac{\Omega_R}{2} & -\gamma - i \underline{\delta} & 0 & -i \frac{\Omega_R}{2} \\ -i \frac{\Omega_R^*}{2} & 0 & -\gamma + i \underline{\delta} & i \frac{\Omega_R^*}{2} \\ 0 & -i \frac{\Omega_R^*}{2} & i \frac{\Omega_R}{2} & 0 \end{pmatrix}, \quad (12.18)$$

with employing the definition of the Raman Rabi frequency  $\Omega_R$  (12.8) as well as the effective detuning  $\underline{\delta}$  (12.10). The corresponding initial value problem can be solved analytically. Applying  $\rho_{gg}(t=0) = 1$  leads to the solution for the population of the metastable state

$$m_R(t, \nu) = \frac{1}{2} + e^{-\theta t} [A \cos(\theta t) + B \sin(\theta t)] - e^{2(\theta - \gamma)t} C. \quad (12.19)$$

Here, the stationary solution approaches  $\lim_{t \rightarrow \infty} m_R = 1/2$ . The complex, velocity-dependent frequency  $\theta$  and damping rate  $\vartheta$  as well as the coefficients  $A, B, C$  define damped oscillations. Their exact expression are given in App. E2 but turn out to be uninspiring. Depending on the parameters, these oscillations can be under- to overdamped.

### ***The $\pi$ -pulse for underdamped oscillations***

For  $\eta = \sqrt{3}|\tilde{\Omega}_R|/\gamma > 1$  the solution (12.19) is in the regime of underdamping. Here, one finds that the coefficient  $C(v_R) = 0$  vanishes. In addition, the oscillation frequency  $\theta$  and damping rate  $\vartheta$  are real. In order to maximise the population transfer, the  $\pi$ -pulse time  $t_\pi$  for the resonant velocity  $v = v_R$  is defined by the condition  $\dot{m}_R(t_\pi, v_R) = 0$ , resulting in

$$t_\pi = \frac{1}{\theta} \cos^{-1} \left( \frac{A\theta + B\vartheta}{\sqrt{(A^2 + B^2)(\theta^2 + \vartheta^2)}} \right) \approx \frac{\pi}{\theta} = \frac{2\sqrt{3}\pi\xi}{\gamma(\xi^2 - 1 + \eta^2)}, \quad \eta > 1 \quad (12.20)$$

$$\xi = \left[ 1 - \frac{\eta^2}{2} (1 - \sqrt{4\eta^2 - 3}) \right]^{1/3},$$

using again the approximations for the Raman Rabi frequency  $\Omega_R \approx \tilde{\Omega}_R$  and the effective detuning  $\underline{\delta} \approx d$  (12.11). In the limit  $\gamma = 0$ ,  $t_{\pi,0}$  (12.13) can be recovered.

For  $t_\pi$ , an upper bound for the velocity width of  $m_R(t_\pi, v)$  is given by the FWHM of

$$e^{2(\vartheta - \gamma)t_\pi} C \approx \frac{1}{2} \frac{d^2}{\zeta^2 + d^2} \exp \left( \frac{D t_\pi}{1 + E d^2} \right), \quad (12.21)$$

where  $\zeta^2 = \gamma^2(\eta^2 - 1)/3$  and  $D$  and  $E$  are velocity-independent functions, given in App. E2. With this approximation the width reads

$$\Delta v_R(t_\pi) = \frac{2}{k_1 + k_2} \sqrt{p + \sqrt{p^2 + q}}, \quad p = \frac{\zeta^2 E - D t_\pi - \ln(2)}{2 \ln(2) E}, \quad q = \frac{\zeta^2}{\ln(2) E} \quad (12.22)$$

using  $\ln(d^2 + \zeta^2) = \ln(d^2) + \zeta^2/d^2 + \mathcal{O}((\zeta^2/d^2)^2)$ . Together with the lower bound, provided by the limit of vanishing laser linewidths  $\Delta v_0$  (12.15), the velocity width of  $m(t_\pi)$  is constrained by

$$\Delta v_0(t_\pi) \leq \Delta v(t_\pi) \leq \Delta v_R(t_\pi), \quad (12.23)$$

for arbitrary  $\eta > 1$ .

### ***Limit of large laser linewidths and long interaction times***

In the limit  $t \gg 1/\gamma$  of large laser linewidths and long interaction times, the populations of the ground and metastable state can be approximated with the solutions of the rate equations

$$\partial_t \begin{pmatrix} \rho_{gg} \\ \rho_{mm} \end{pmatrix} = \mathbf{r} \begin{pmatrix} -1 & 1 \\ 1 & -1 \end{pmatrix} \begin{pmatrix} \rho_{gg} \\ \rho_{mm} \end{pmatrix}, \quad (12.24)$$

derived from the two-level OBEs (12.18) with adiabatic elimination, using  $\dot{\rho}_{gm} \ll \gamma \rho_{gm}$ . The decay rate  $\mathbf{r} = \gamma |\tilde{\Omega}_R|^2 / (\gamma^2 + d^2) < r_0 \equiv \mathbf{r}(d = 0)$  involves the approximations  $\Omega_R \approx \tilde{\Omega}_R$  and  $\underline{\delta} \approx d$  (12.11). Therefore, the solution reads

$$m_{RE}(t, v) = \frac{1}{2} (1 - e^{-\mathbf{r}t}). \quad (12.25)$$

The velocity width of  $m_{\text{RE}}$  follows with

$$\Delta v_{\text{RE}}(t) = \frac{2\gamma}{k_1 + k_2} \sqrt{\frac{r_0 t}{\ln(1 + \tanh \frac{r_0 t}{2})}} - 1, \quad (12.26)$$

where  $\Delta v_{\text{RE}}(t) \geq \gamma/(k_1 + k_2) \forall r_0, t$ . The presented rate-equation limit is a good approximation when the transient part of the general solution  $m_{\text{R}}$  (12.19) vanishes, which is the case if  $\gamma t \gg 1$ , because  $\gamma/2 \leq \vartheta < \gamma$ .

### ***The $\pi$ -pulse for overdamped oscillations***

For  $\eta < 1$ , the solution (12.25) is overdamped with  $m(t) < 1/2 \forall t$ . Therefore, the saturation of  $m$  defines a  $\pi$ -pulse with several decay times  $t_\pi = n/r_0$ ,  $n > 1$ . For a continuous  $\pi$ -pulse time,  $n$  is defined by the condition  $\lim_{\eta \rightarrow 1-} n/r_0 = \lim_{\eta \rightarrow 1+} t_\pi$  with  $t_\pi(\eta > 1)$  from Eq. (12.20), leading to  $n = 2\pi/\sqrt{3}$  and

$$t_\pi = \frac{2\pi\gamma}{\sqrt{3}|\tilde{\Omega}_{\text{R}}|^2}, \quad 0 < \eta \leq 1. \quad (12.27)$$

## 12.2 SPONTANEOUS RAMAN TRANSITION

The atomic transition between the ground and the excited state can be coupled resonantly, depending on the frequency of laser 1 and the ion velocity. In this limit, the population transferred into the metastable state can be approximated with the solution of the rate equations for ground, excited and metastable state, assuming the steady state of all coherences ( $\dot{\rho}_{ij} \rightarrow 0$ ,  $i \neq j$ ). Additionally,  $\rho_{gm}(t) \approx 0$  can be approximated, being important only for the transfer via the stimulated Raman transition. Therewith, the OBEs (10.18) and (10.19) simplify to

$$\partial_t \begin{pmatrix} \rho_{gg} \\ \rho_{mm} \\ \rho_{ee} \end{pmatrix} = \begin{pmatrix} -R_1 & 0 & \Gamma_{eg} + R_1 \\ 0 & -R_2 & \Gamma_{em} + R_2 \\ R_1 & R_2 & -\Gamma - R_1 - R_2 \end{pmatrix} \begin{pmatrix} \rho_{gg} \\ \rho_{mm} \\ \rho_{ee} \end{pmatrix}, \quad (12.28)$$

with rates  $R_i = \Gamma_i |\Omega_i|^2 / (4\Delta_i^2 + \Gamma_i^2)$ . Applying the initial condition  $\rho_{gg}(t=0) = 1$ , for  $t > 1/\Gamma$  the population of the metastable state reads

$$m_{\text{sp}}(t, v) = \frac{\frac{\Gamma_{em}}{R_2} + 1}{\frac{\Gamma_{em}}{R_2} + \frac{\Gamma_{eg}}{R_1} + 3} (1 - e^{-\nu' t}), \quad \nu' = \frac{R_1 \Gamma_{em} + R_2 (\Gamma_{eg} + 3R_1)}{\Gamma + 2(R_1 + R_2)}. \quad (12.29)$$

**ONE LASER LIMIT** As long as the resonances at  $\nu_{\text{R}}$  and  $\nu_1$  are spread far apart from each other, the population transfer around  $\nu_1$  is primarily defined by the resonant coupling of laser 1, populating the excited state followed by spontaneous emission into the metastable state. The far off-resonant coupling of laser 2, leading to stimulated emission into  $|m\rangle$  is only of secondary importance. Therefore, in the limit  $\Omega_2 \rightarrow 0$ , solution (12.29) simplifies to

$$m_1(t, v) \equiv m_{\text{sp}}(t, v; \Omega_2 = 0) = 1 - e^{-\nu' t}, \quad \nu' = \nu(\Omega_2 = 0) = \frac{\Gamma_{em}}{2 + \frac{\Gamma}{R_1}}. \quad (12.30)$$

This represents the experiment [185] mentioned in Section 10.1.1, leading to a sensitivity of the voltage measurement of a few ppm for high voltages up to 20 kV and motivating this topic of the thesis. The sensitivity  $s$  (12.2) is characterised by the velocity width of the metastable-state population (12.30), which can be given for example after applying a  $\pi$ -pulse. Therefore, a

$\pi$ -pulse time is defined similar to the last Section 12.1.2, when  $m_1(t_\pi, v_1)$  is saturated, with  $t_\pi = n/r'_0$  and  $r'_0 \equiv r'(v = v_1)$ . The FWHM of the metastable-state population around the spontaneous resonance after  $t_\pi$  reads

$$\Delta v_1(t_\pi) = \frac{\sqrt{(2\Gamma_1)^2 + 2\Omega_1^2 \frac{2\Gamma_1}{\Gamma}}}{k_1} \sqrt{\frac{n}{\ln\left(\frac{2e^n}{1+e^n}\right)} - 1}. \quad (12.31)$$

In the limit of short times  $n \rightarrow 0$ , a lower bound of the width is given by

$$\lim_{n \rightarrow 0} \Delta v_1(t_\pi, \gamma = 0) = \frac{\sqrt{\Gamma^2 + 2\Omega_1^2}}{k_1} \leq \Delta v_1(t_\pi), \quad (12.32)$$

which corresponds to the natural linewidth for a vanishing laser power  $\Omega_1 \rightarrow 0$ . For parameters (B) the resulting width is

$$s = \frac{\Delta U}{U} = \frac{2\Delta v_1}{v_1} \gtrsim \frac{2\Gamma}{k_1 v_1} = 75 \text{ ppm}. \quad (12.33)$$

Please note that the width of the distribution does not represent the ultimate limit of the determination of the resonance velocity  $v_1$  and therewith of the sensitivity  $s$ . The central velocity of the final distribution, here  $v_1$  can be determined much more precisely, characterised by the statistical uncertainty. In the experiment velocities are measured with laser frequencies and statistical uncertainties less than 400 kHz (cf. Chap. 4 in [184]). Therefore, even lower  $s$  are achievable. In [185] sensitivities of around  $\pm 5$  ppm could be reached.

## 12.3 MAXIMISING THE POPULATION TRANSFER

After studying the individual population transfers into the metastable state via the stimulated Raman transition  $m_R$  (12.19) and the spontaneous population transfer  $m_{sp}$  (12.29) separately, now the total population transfer is discussed. Therefore, it is assumed, that both processes can be combined incoherently, as long as they do not interfere. The ad-hoc analytical ansatz

$$m_{ana}(t, v) = \frac{1}{w} m_R(t, v) + m_{sp}(t, v), \quad w = m_R(t_{\pi,0}, v_R) + m_{sp}(t_{\pi,0}, v_R), \quad (12.34)$$

superposes the populations such that  $m_{ana}(t_{\pi,0}, v_R) = 1$ . Therefore, the introduced weight  $w$  prevents non-physical populations  $m_{ana}(t, v) > 1$ .

### 12.3.1 Vanishing laser linewidths

The numerical solutions of the OBEs (10.18) and (10.19) provide the population distributions over a wide velocity range, depicted in Fig. 12.3 after applying a  $\pi$ -pulse. The approximation  $m_{ana}$  (12.34) clearly matches the numerical results. The rogue resonance of spontaneous population transfer, located at  $v_1^{(A)} = 400 \text{ m/s}$  respectively  $v_1^{(B)} = 1200 \text{ m/s}$ , is clearly distinguishable from the narrow Raman resonance at  $v_R^{(A)} = v_R^{(B_1)} \approx v_R^{(B_2)} \approx 0 \text{ m/s}$ . Due to the larger  $\pi$ -pulse time  $t_{\pi,0}^{(B_1)} = 4.62 \mu\text{s} \gg t_{\pi,0}^{(B_2)} = 0.68 \mu\text{s}$  the rouge resonances of parameter set (B<sub>1</sub>) is broader than for (B<sub>2</sub>). More cycles of near-resonant stimulated absorption followed by spontaneous emission can happen, which cannot be compensated by the far off-resonant laser 2. Obviously parameter sets (B) are more favourable, because with larger resonance distances  $\beta_1$  it can be ensured that for wider ionic velocity distributions the population of  $|m\rangle$  originates

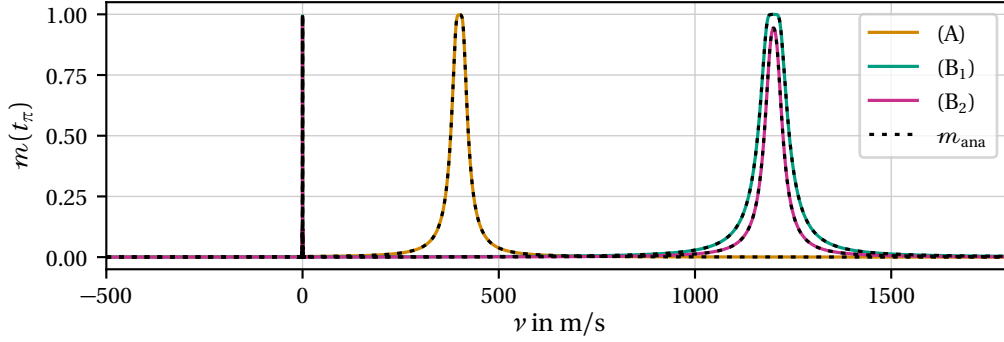


Figure 12.3: Velocity-dependent population of the metastable state after applying a  $\pi$ -pulse  $m(t_\pi)$ , conforming with the analytical approximation  $m_{\text{ana}}$  (12.34). The narrow Raman resonance at  $v_R \approx 0$  m/s (whose details are quasi identical to Fig. 12.2) and the broad resonance of laser 1 at  $v_1^{(A)} = 400$  m/s and  $v_1^{(B)} = 1200$  m/s are apparent.

(almost) exclusively from the coherent Raman transition. Thus, it remains less influenced by the tail of the rogue resonance as for (A). However, for all parameter sets there is a small contribution from the rogue resonance to the population at the Raman resonance, visualised in Fig. 12.4.

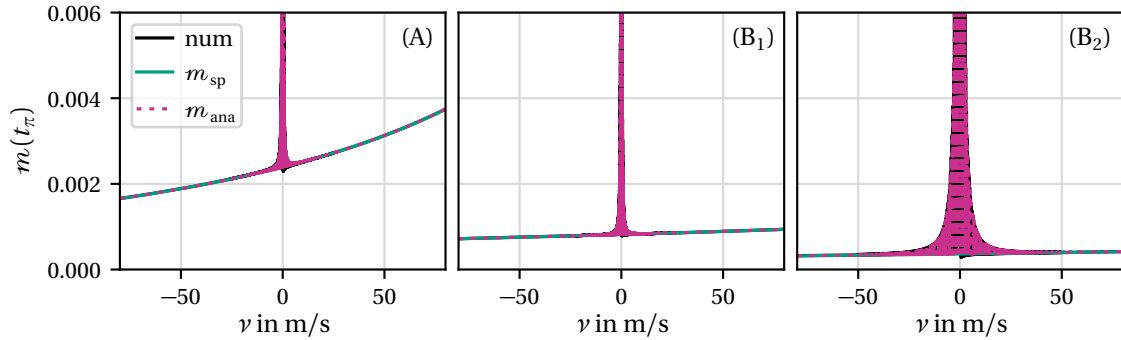


Figure 12.4: The numerical solution of the velocity-dependent population of the metastable state around the Raman Resonance consists of a roughly constant offset, provided by the tail of the spontaneous resonance (12.29) and the velocity dispersion is defined by the purely coherent Raman resonance (12.19). Both processes are incoherently combined in the analytical ad-hoc ansatz (12.34), matching the numerical results very well.

The ad-hoc ansatz (12.34) works very well. While the contribution of the spontaneous resonance (12.29) provides a roughly constant offset, the velocity dispersion is defined by the analytic approximation of the Raman resonance (12.19). Its shape in details is quasi identical to the purely coherent transfer (c.f. Fig. 12.2). However, as indicated in Fig. 12.4, there is indeed a small deviation to the reference (12.19), considering exclusively the coherent transfer via the Raman transition. To compare all parameter sets, this difference is depicted in Fig. 12.5 for a small velocity range around the Raman resonance. For (A) the deviation and especially the roughly constant offset besides the Raman resonance is clearly larger than for (B<sub>1</sub>) and (B<sub>2</sub>), due to  $\beta_1^{(A)} < \beta_1^{(B)}$ . However, with enlarging the laser power (B<sub>2</sub>), especially the reduction exactly on the Raman resonance is as expected slightly enlarged again. Nevertheless, the velocity width of the transferred population is quasi purely defined by the width of the Raman transition  $\Delta v_{\text{ana}} = \Delta v_R$ , showing no differences to the results of Section 12.1.1 (cf.  $\Delta v_0(t_{\pi,0})$  (12.15) and Fig. 12.2).

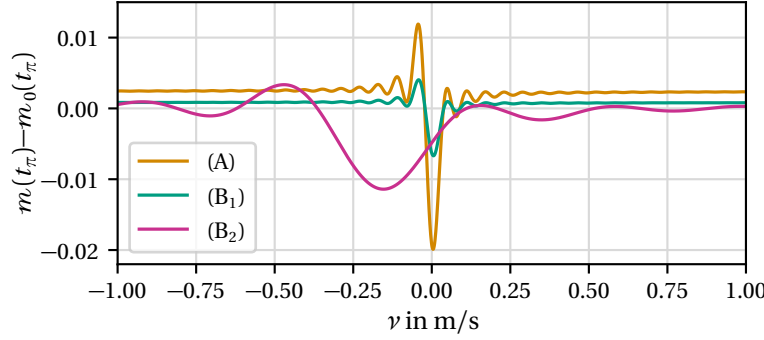


Figure 12.5: Velocity-dependent difference between the metastable state's population, considering ( $m$ ) and neglecting ( $m_0$ ) spontaneous emission effects, after  $t_\pi$ .

The negative impact of *small* distances  $\beta_1$  between the Raman and the spontaneous resonance is also apparent from the velocity averaged population  $\langle m(t, v) \rangle_v$  (12.1), shown in Fig. 12.6. Already for the as narrow as possible initial ion velocity distribution with  $\Delta v_I = 10$  m/s the effect of the incoherent population transfer is discernible for (A). For  $\Delta v_I = 50$  m/s and (A) the total transferred population (solid) is more than twice of the population, transferred via the Raman transition (dotted). So for (A) this regime is already unsuitable to properly determine the ion velocity. However, the major portion of  $\langle m(t, v) \rangle_v$  for (B<sub>1</sub>) and (B<sub>2</sub>) results still from the narrow Raman transition. In addition, the necessary, larger Rabi frequencies are still reachable, viz. this represents a good working regime for a reachable ion velocity width.

For parameter sets (A) and (B<sub>1</sub>) the analytical approximation  $m_{\text{ana}}$  (12.34) (dashed) describes exactly the numerical results. Only for the maximum laser power within (B<sub>2</sub>) there are very little deviations after the first  $\pi$ -pulse.

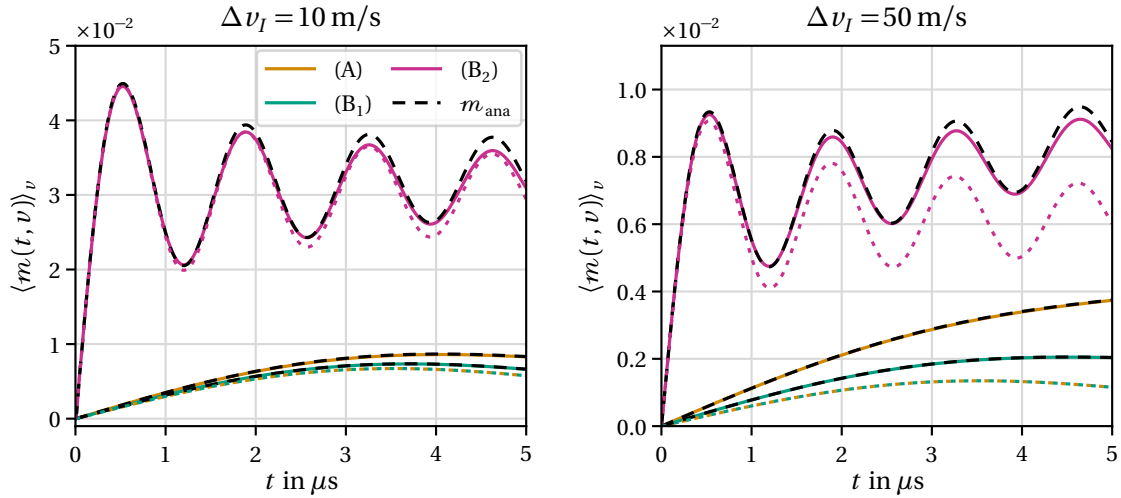
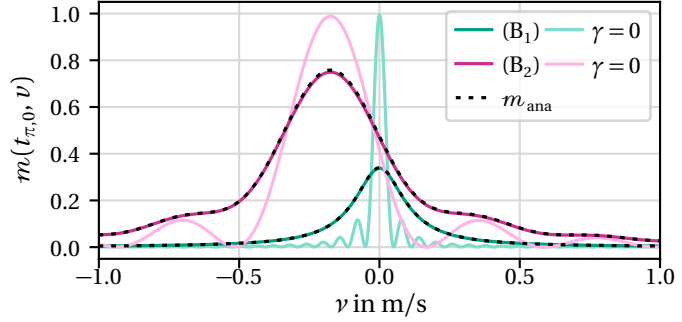


Figure 12.6: Time evolution of the velocity averaged metastable-state population  $\langle m(t, v) \rangle_v$  for two initial ion velocity widths:  $\Delta v_I = 10$  m/s (left) and  $\Delta v_I = 50$  m/s (right). The numerical solutions considering incoherent effects (solid), well predicted by the analytical approximation  $m_{\text{ana}}$  (12.34) (black dashed), are compared to the analytical ones, indicating the transferred population purely due to the Raman transition  $m_R$  (12.9) (dotted).

### 12.3.2 Finite laser linewidths

Taking into account a non-vanishing laser linewidth ( $\gamma = \Gamma_{gg} = \Gamma_{mm} = 300$  kHz) the velocity selectivity of the Raman transition is significantly affected. On the one hand, as expected, their width is enlarged, so the velocity determination is less exact. On the other hand, even on the resonance  $\nu_R$  the maximum transfer efficiency of almost 100% for  $t_\pi$  cannot be reached any longer. Both effects are visible in Fig. 12.7, depicting the velocity dependent population of

Figure 12.7: Velocity-dependent population of the metastable state after  $t_{\pi,0}$ . Considering finite laser linewidths  $\gamma = 300$  kHz is compared to  $\gamma = 0$ . The analytic approximation  $m_{\text{ana}}$  (12.34) matches the numerical simulation results.



the metastable state after time  $t_{\pi,0}$ . However, the Raman resonance is still clearly discernible and just as for  $\gamma = 0$  the analytic approximation  $m_{\text{ana}}$  (12.34) can predict the numerical, exact solution. The Lorentzian shape of the velocity dispersion for parameter set (B<sub>1</sub>) indicates the overdamped regime, which is achieved for (B<sub>1</sub>) with  $\gamma \geq \sqrt{3}|\tilde{\Omega}_R|$ . In contrast, applying the maximal laser powers with (B<sub>2</sub>), shows underdamping, resulting in the crossover from the sinc<sup>2</sup> shape for no damping ( $\gamma = 0$ ) to the Lorentzian shape for overdamping. The results for (A) are not plotted in Fig. 12.7, because they are very similar to (B<sub>1</sub>). However, the differences are not negligible, becoming apparent in Fig. 12.8, where the velocity average  $\langle m(t, v) \rangle_v$  is visualised.

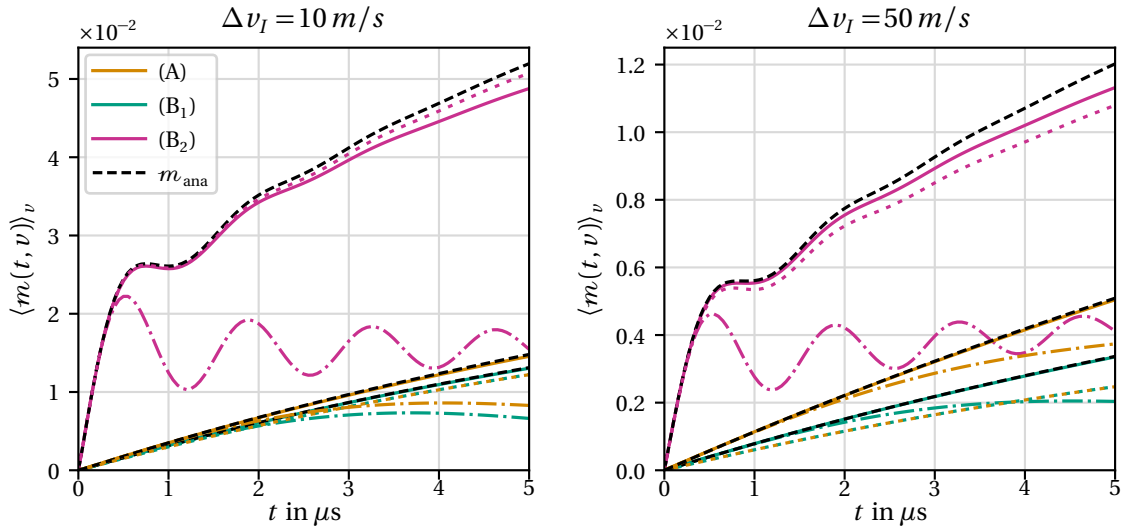


Figure 12.8: Time evolution of the metastable-state population summed over a certain velocity width:  $\Delta v_I = 10$  m/s (left) and  $\Delta v_I = 50$  m/s (right). The numerical results for  $\gamma = 300$  kHz (solid) are well predicted by the analytic approximation for the full solution  $m_{\text{ana}}$  (12.34) (dashed black). The analytic approximation  $m_R$  (12.19) (dotted) gives the populations purely transferred via the Raman transition. The numerical solutions for  $\gamma = 0$  (dash-dotted) are given for the sake of completeness. The results for (B<sub>2</sub>) are scaled with a factor of 0.5.

Again the analytic approximation  $m_{\text{ana}}$  (12.34) gives reliable predictions; only for the maximum laser power and longer times very little deviations are visible. Here, the disappearance of Rabi oscillations indicates, that the applied laser linewidths together with the interaction time are sufficient to yield the rate equation limit. Only for (B<sub>2</sub>) the time of a  $\pi$ -pulse is discernible with  $t_{\pi}^{(\text{B}_2)} = 0.70 \mu\text{s}$ , slightly different from  $t_{\pi,0}^{(\text{B}_2)} = 0.68 \mu\text{s}$ . The width of the velocity dispersion after this  $\pi$ -pulse time is  $\Delta v(t_{\pi}) = 0.42$  m/s, where the analytical approximations  $\Delta v_0(t_{\pi,0})$  (12.15) and  $\Delta v_R(t_{\pi})$  (12.22) provide an appropriate range  $\Delta v(t_{\pi}) \in [\Delta v_0(t_{\pi,0}), \Delta v_{\text{ana}}(t_{\pi})] =$



$[0.34, 0.60]$  m/s. The  $\pi$ -pulse times for the other parameter sets  $t_{\pi}^{(A)} \approx t_{\pi}^{(B_1)} = 14.8 \mu\text{s}$  are much larger than  $t_{\pi,0}^{(A)} = t_{\pi,0}^{(B_1)} = \bar{t} = 4.62 \mu\text{s}$ , demonstrating again the overdamping for (A) and (B<sub>1</sub>) with  $\gamma = 300$  kHz. Hence, the velocity width after the experimental interaction time  $\bar{t}$  is of major interest. These are  $\Delta v(\bar{t}) = \{0.22, 0.22, 1.34\}$  m/s for  $\{(A), (B_1), (B_2)\}$ , demonstrating the broadening of the Raman transition due to finite laser linewidths. They are well predicted by the analytical approximation  $\Delta v_{\text{RE}}(\bar{t}) = \{0.21, 0.21, 1.38\}$  m/s, because even though (B<sub>2</sub>) is in the regime of underdamping with  $\gamma \bar{t} = 9 \gg 1$ , the rate equation limit is a reasonable approximation for the solution after  $\bar{t}$ . Due to this broadening, in particular for (B<sub>2</sub>), the total amount of the metastable-state population is substantially enlarged. At the same time, the ratio  $\mu$  of population transferred into the metastable state via the Raman transition to the whole population

$$\mu = \frac{\langle m_{\text{R}}(t, v, r) \rangle_{v,r}}{\langle m_{\text{ana}}(t, v, r) \rangle_{v,r}}, \quad (12.35)$$

depicted in Fig. 12.9, remains larger in comparison to the simulations with  $\gamma = 0$ .

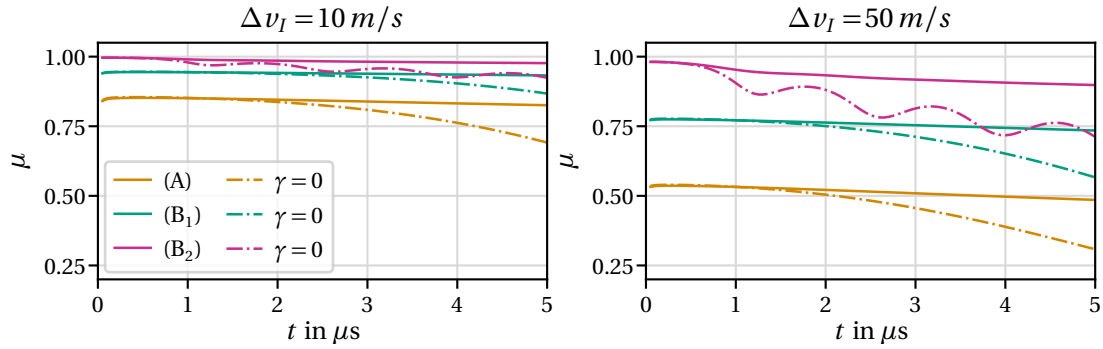


Figure 12.9: Time-dependent ratio  $\mu$  (12.35) of the population transferred into the metastable state via the Raman transition to the whole transferred population, including spontaneous population transfer. Two initial, ionic velocity widths  $\Delta v_I$  are compared, as well as considering a finite laser linewidth  $\gamma = 300$  kHz to neglecting it.

The comparison of the parameter sets demonstrates the compelling necessity of a careful choice of laser frequencies, providing a sufficiently large distance  $\beta_1$  between Raman and rogue resonance, especially for wider initial velocity distributions of the ions. It is worth mentioning that the ratio  $\mu$  decreases with time. This reduction is much more crucial for the idealised scenario with  $\gamma = 0$ . However, it is also apparent for  $\gamma \neq 0$ . Therefore, it is important to carefully choose the interaction time in combination to the laser powers, achieving a significant absolute population amount and simultaneously keep a reliable ratio, optimally  $\mu \rightarrow 1$  but at least  $\mu > 0.5$ .

To identify the maximum laser powers to reach a prescribed maximum uncertainty of the velocity determination, the widths after applying a  $\pi$ -pulse  $\Delta v(t_{\pi})$  as well as after the experimental transit time  $\Delta v(\bar{t})$  are depicted in Fig. 12.10. Please note the different scales of  $\Delta v$  for  $t_{\pi}$  and  $\bar{t}$ . Again, the quality of the analytical approximation  $m_{\text{ana}}(t, v)$  (12.34) is demonstrated, because their width  $\Delta v_{\text{ana}}$  describes the numerical, exact solution  $\Delta v_{\text{num}}$  very well. In addition,  $\Delta v_{\text{R}}(t_{\pi})$  (12.22) provides an upper bound for  $\Delta v(t_{\pi})$  as stated in Section 12.1.2. Due to  $\gamma \bar{t} = 9 \gg 1$ ,  $\Delta v_{\text{RE}}(\bar{t})$  (12.26) matches completely the actual results  $\Delta v_{\text{ana}}(\bar{t})$ . For  $t_{\pi}$  the border between under- and overdamping is indicated, demonstrating that parameters (B<sub>1</sub>) are in the regime of overdamping, while (B<sub>2</sub>), with the maximal laser powers  $P_1 = 30$  mW and  $P_2 = 500$  mW, is located far inside the underdamped regime.

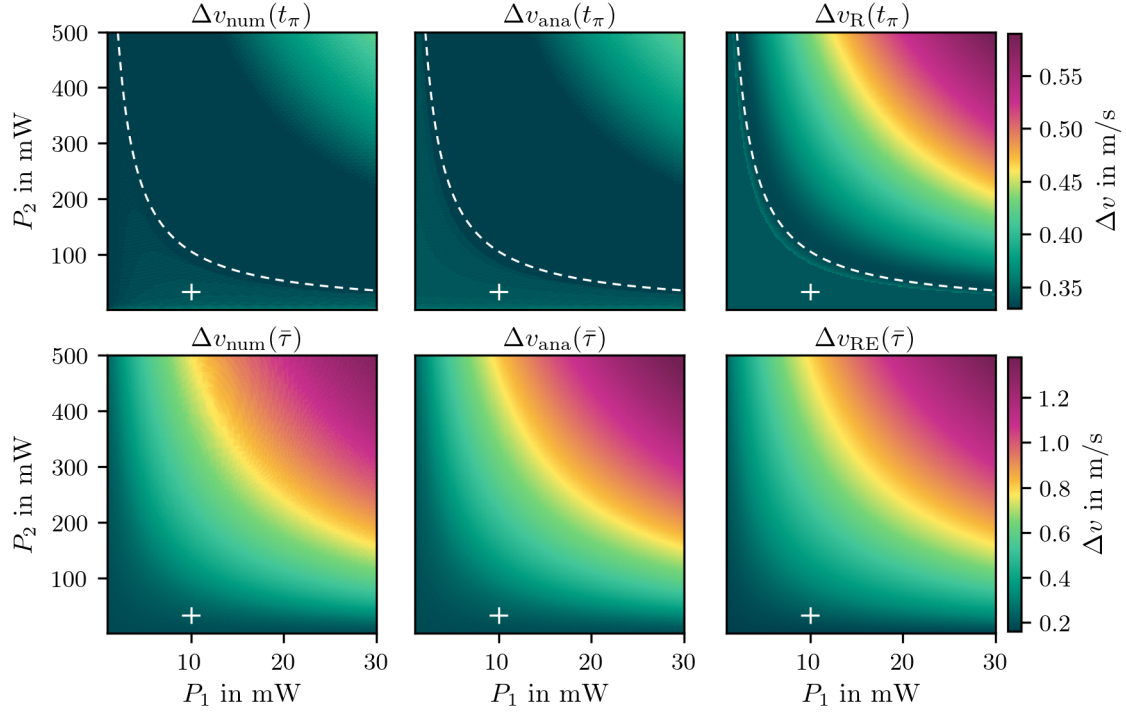


Figure 12.10: Velocity width  $\Delta v$  (FWHM) of the metastable-state population for parameters (B), depending on the laser powers  $P_1$  and  $P_2$  for different times. Top: after applying a  $\pi$ -pulse and bottom:  $\bar{t} = 4.62 \mu\text{s}$ . The FWHM of the exact numerical solution  $\Delta v_{\text{num}}$  is compared to the FWHM of  $m_{\text{ana}}$ , i.e.  $\Delta v_{\text{ana}}$  (12.34) and the approximations  $\Delta v_{\text{R}}$  (12.22) and  $\Delta v_{\text{RE}}$  (12.26). The pluses highlight the laser powers used with parameter set (B<sub>1</sub>) and the border between under- and overdamping is also indicated (dashed white).

### 12.3.3 Spatial intensity variations

So far the lasers were approximated as plane waves with no spatial dependencies. In reality, they are collimated LG-laser beams with beamwaist  $w_0$  (c.f. (10.4)). The spatial distribution of the ions is also assumed to be Gaussian with width  $\sigma$  (c.f. (10.5)). The metastable state population observable is obtained by incoherent averaging over the cross-sectional area of the ion and the laser beams, assuming that the respective maxima of all are perfectly overlapped

$$\langle m(t, v, r) \rangle_r = 2\pi \int_0^\infty dr r g(r) m(t, v, r). \quad (12.36)$$

This integral can be solved numerically with Gauss-Laguerre-Quadrature [199]. Finally, the population of  $|m\rangle$  can be additionally averaged over the velocity distribution according to (12.1). In the following, three scenarios are compared, where the results are depicted in Figs. 12.11 and 12.12.

- For  $\sigma \ll w_0$ , the ion beam is much narrower than the laser beam, corresponding to the case we assumed so far, all ions experience the same Rabi frequency [Subfigures (a)].
- For  $\sigma = w_0/2$ , the ion beam width is of comparable size to the laser beam width [Subfigures (b)].
- For  $\sigma = w_0$ , the ion beam is broader than the laser beam, thus some ions are not affected at all, representing the current experimental scenario [Subfigures (c)].

The idealised results, neglecting spatial inhomogeneities from Sections 12.3.1, 12.3.2 are again depicted in Figs. 12.11 and 12.12, to compare them to the results, taking spatial inhomogeneities into account. Essentially,  $\langle m(t_{\pi,0}, v, r) \rangle_r$  (Fig. 12.11) and  $\langle m(t, v, r) \rangle_{v,r}$  (Fig. 12.12) are reduced overall. Further away from the centre  $r = 0$ , the Rabi frequencies are reduced and therewith  $v_R$  is shifted. This effect is more crucial, the larger  $\Omega_2$ . Averaging over the results for different  $r$ , for (B<sub>2</sub>) the velocity of maximum transfer efficiency is shifted from  $v_R = -0.17$  m/s to  $v_R = -0.12$  m/s for  $\sigma = w_0/2$  and to  $v_R = -0.11$  m/s for  $\sigma = w_0$ . However, the resonance of the Raman transition is still visible. In addition, the considered spatial intensity variations lead to a small reduction of the ratio  $\mu$  (12.35), primarily for (A) and (B<sub>1</sub>).

To conclude, even with taking the aberrations due to finite laser linewidths and spatial inhomogeneities into account, a narrow velocity class of ions can be transferred from the ground to the metastable state with a sufficiently large population proportion.

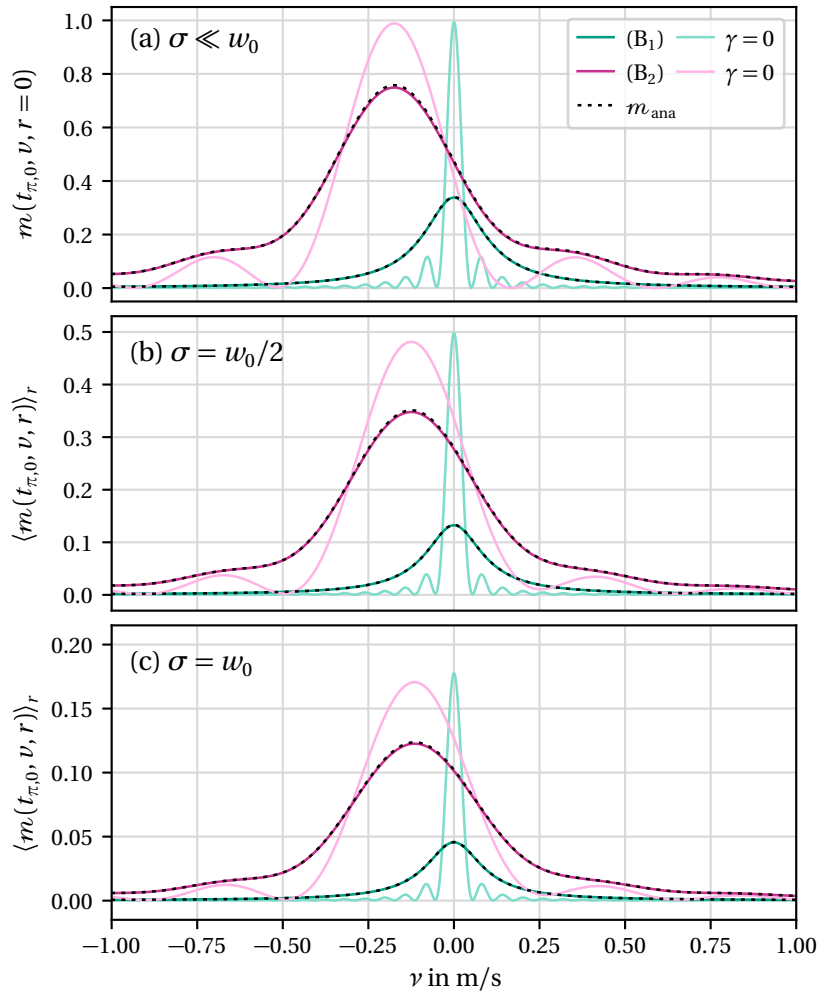


Figure 12.11: Velocity-dependent population of the metastable state after  $t_{\pi,0}$  for different spatial distributions: (a) no intensity variations according to  $\sigma \ll w_0$ , and averaged over the spatial intensity variations for an ion beam width (b)  $\sigma = w_0/2$ , respectively (c)  $\sigma = w_0$ . Considering finite laser linewidths  $\gamma = 300$  kHz is compared to the idealisation with vanishing laser linewidths  $\gamma = 0$ . The analytic approximation  $m_{\text{ana}}$  (12.34) matches the simulation results.

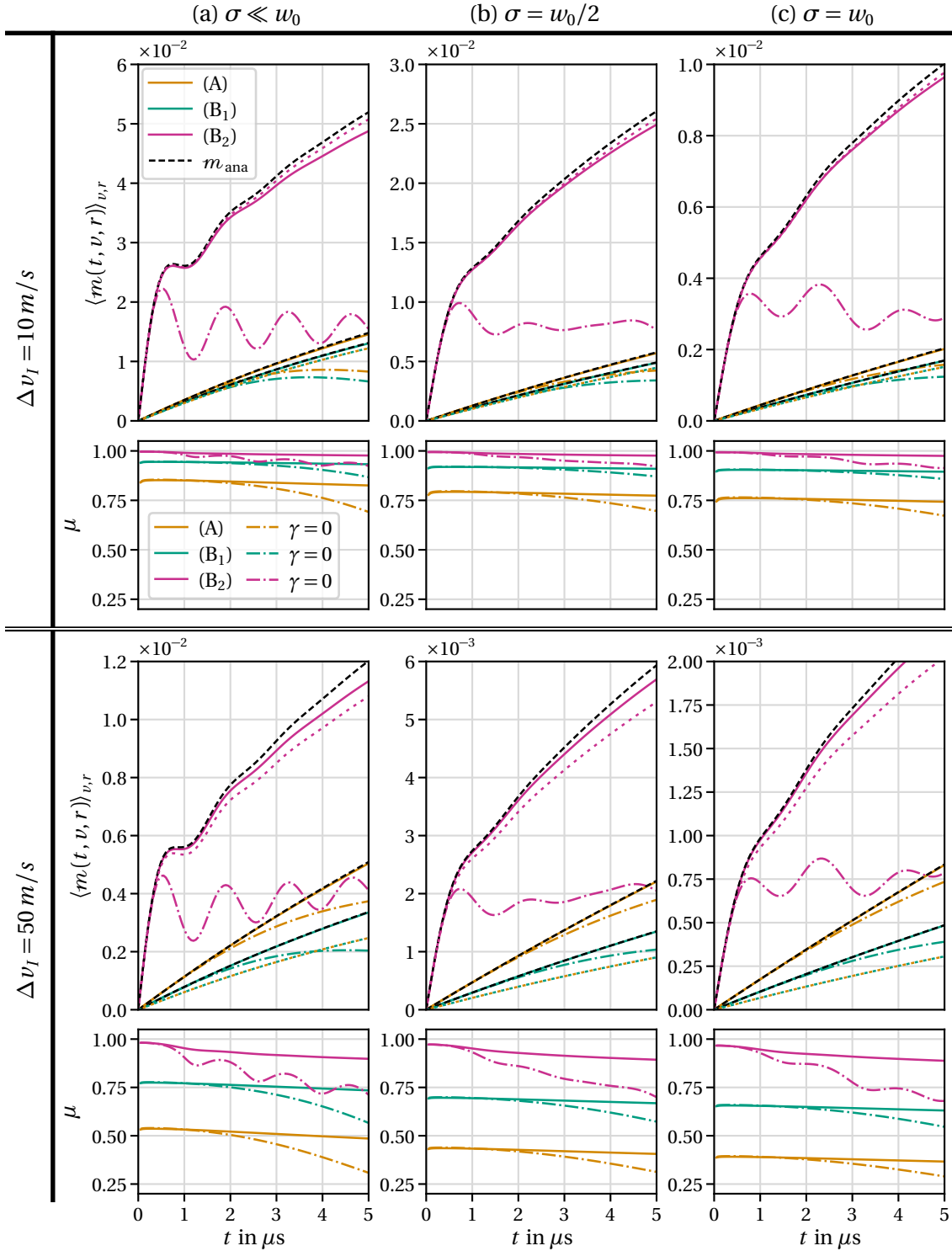


Figure 12.12: Time evolution of the velocity averaged metastable-state population and of the ratio  $\mu$  (12.35) of the population transferred into the metastable state via the Raman transition to the whole transferred population. The considered initial ionic velocity widths are:  $\Delta v_I = 10$  m/s (top) and  $\Delta v_I = 50$  m/s (bottom). Three spatial scenarios are analysed: (a) no intensity variations with  $\sigma \ll w_0$  and averaged over the spatial distributions with ion beam widths (b)  $\sigma = w_0/2$  and (c)  $\sigma = w_0$ . The results of  $\langle m(t, v, r) \rangle_r$  for  $(B_2)$  are scaled with a factor of 0.5. The numerical results for  $\gamma = 300$  kHz (solid) are well predicted by the analytical approximation  $m_{\text{ana}}$  (12.34) (dashed black). The population transferred via the Raman transition  $m_R$  (12.19) (dotted) and the numerical solutions for  $\gamma = 0$  (dash-dotted) are also depicted.

# Part IV

---

## CONCLUSION

---



---

## SUMMARY AND OUTLOOK

---

This thesis presents an extensive study of the aberrations of atomic diffraction. Thereby a wide spectrum of atomic initial states is considered: From single coherent quantum states at zero temperature, over multi particle coherent ultracold Bose-Einstein condensates and thermal clouds as statistical mixtures at nanokelvin temperatures ending with hot ions with temperatures up to the Kelvin regime. Ultracold atoms represent the optimal test states for `ATOMIC BRAGG DIFFRACTION` within matter-wave interferometry for high precision rotation and acceleration measurements. Hot ions can be used with a `RAMAN VELOCITY FILTER` to prepare optimal initial conditions for high precision collinear laser spectroscopy to measure high voltages on the sub-ppm level.

### 13.1 RAMAN VELOCITY FILTER

The results of Part III show, that ion velocity classes with widths as low as 0.2 m/s can be transferred into the metastable state via the Raman transition, achieving a significant population proportion  $\langle m(t, v, r) \rangle_{v,r} = 10^{-3} - 10^{-2}$ . This velocity width is related to voltage widths on the sub-ppm level. To achieve such impressive resolutions, it is important to carefully choose the laser frequency combination. One needs to ensure that the transferred population into the metastable state originates mainly from the coherent Raman process and not from incoherent spontaneous emission processes, when laser 1 couples resonantly the ground state to the excited state. This also supports an initially narrow ion velocity distribution.

The idealised case of infinitely sharp laser linewidths ( $\gamma = 0$ ) and an ion beam much smaller than the laser beams defines the smallest reachable FWHMs of the ion velocity distribution in the metastable state with  $\Delta v(t_{\pi,0}) = \{0.05, 0.05, 0.32\}$  m/s, for parameter sets  $\{(A), (B_1), (B_2)\}$ . This results in voltage widths  $s = \{0.4, 0.4, 2.4\}$  ppm on the sub-ppm level for (A) and (B<sub>1</sub>). The derived analytic expressions for the resonance velocity of the Raman transition  $v_R$  (11.3), the population of the metastable state after applying a  $\pi$ -pulse  $m_0(t_{\pi,0}, v)$  (12.14) as well as the corresponding FWHM  $\Delta v_0(t_{\pi,0})$  (12.15) give reliable predictions.

Considering finite laser linewidths, the analytic approximation for the velocity- and time-dependent metastable-state population  $m_{\text{ana}}$  (12.34) still matches the full numerical solution very well. In addition, the approximations for the velocity width for both, after applying a  $\pi$ -pulse  $\Delta v_R(t_\pi)$  (12.22) and in the rate equation limit  $\Delta v_{\text{RE}}(t)$  (12.26), are also suitable models. Thereby, almost exact results for large parameter regimes are predicted while requiring simultaneously small computational efforts. Moreover, the presented analytical models lead to physical insights, verified by the numerical results.

Finite laser linewidths lead to a significant broadening of the Raman transition. With  $\gamma = 300$  kHz the velocity width of  $m$  is enlarged to  $\Delta v(t_{\pi,0}) = \{0.22, 0.22, 0.43\}$  m/s, leading to  $s = \{1.7, 1.7, 3.3\}$  ppm, still on the ppm level. Note that this width of the distribu-



tion does not represent the ultimate limit of the determination of the resonance velocity  $v_R$  and thereby of the sensitivity  $s$ . The centre velocity of the final distribution, here  $v_R$ , can be determined much more precisely, characterised by the statistical uncertainty. In the experiment velocities are measured with laser frequencies and statistical uncertainties less than 400 kHz (cf. Chap. 4 in [184]) are achieved. Therefore, sub-ppm high-voltage measurements are still attainable. This becomes apparent in the related width in the frequency domain  $\Delta f = (k_1 + k_2)\Delta v/(2\pi) = \{0.8, 0.6, 1.6\}$  MHz, which is much smaller than the natural linewidth  $\Gamma_{eg} = 23.396$  MHz. The Raman transition has therefore the potential to provide a significant reduction in uncertainty. Moreover, it avoids additional uncertainties caused by varying and unknown momentum transfers in multiple resonant excitations along the  $4s \rightarrow 4p$  transition and the subsequent spontaneous decay in the current measurement scheme. The momentum transfer during the Raman transition is very small and exactly defined as  $\hbar(k_1 + k_2)^2/2m = 69$  kHz in direction of laser 2. Therefore, it can be taken into account in the analysis process.

In addition, with the velocity acceptance of the Raman transition, the maximum angle between ion and laser beams can be approximated. Within this angle ions can be just transferred into the metastable state, even though their absolute velocity value does not match the Raman condition. By demanding that this discrepancy of the longitudinal ion velocity component must be smaller than  $\Delta v/2$  the resulting angle is  $\alpha \leq \arccos[(v_R - \Delta v/2)/(v_R + \Delta v/2)] \approx 6$  mrad for  $\Delta v_I = 10$  m/s and all parameter sets. Consequently, this transverse emittance is mainly defined by the initial velocity width of the ions. However, in comparison, the natural linewidth induces a much larger angle  $\alpha' \leq \arccos[(v_1 - \Gamma_{eg}/(2k_1))/(v_1 + \Delta v_I/2)] = 11$  mrad. Therefore, the use of Raman spectroscopy indeed reduces the transverse emittance, improving one of the critical issues in the experiment applying spontaneous population transfer with only one laser [185].

The main effect of spatial intensity variations of both the laser beams and the ion beam is a small reduction of the transfer efficiency for all velocities (less than one order of magnitude). Thereby, the velocity width of the transferred population is approximately not affected. Note, that for maximum laser powers the velocity of maximum population transfer is slightly shifted in comparison to infinitely large laser beams. Therefore, the central velocity differs from the Raman velocity for infinite large lasers. In order to avoid systematic errors, this shift must be taken into account when deriving specific velocity values and thus voltages. However, this can easily be accomplished by incoherent averaging over the different Raman velocities (11.3), according to the varying Rabi frequencies in the Laguerre-Gaussian laser beams.

Despite these experimental imperfections, the resonance of the Raman transition is still clearly identifiable. Therefore, the presented theoretical study of aberrations to Raman velocity filters for hot ions demonstrates the feasibility of high-voltage measurements using coherent Raman spectroscopy on the ppm level, under realistic conditions. Besides provisioning a deep physical understanding of Raman velocity filters, the gained findings pave the way for further promising experiments to realise high precision measurements of high voltages, pointing out important conditions for experimental parameters.

## 13.2 ATOMIC BRAGG DIFFRACTION

Bragg scattering from moving standing waves provides the opportunity to realise highly efficient matter-wave beamsplitters and mirrors, which are the central components of atom interferometers. However, they suffer from a multitude of aberration sources. Especially for challenging space experiments these aberrations must be considered and quantified to provide realistic predictions and to demonstrate possible optimisation approaches. Therefore, full three-dimensional simulations and analytical models of atomic beamsplitters with different spatio-temporal envelopes are studied in Part II.

Several kinds of ubiquitous imperfections, like the velocity dispersion and the population losses into higher, off-resonant coupled diffraction orders are characterised. The influence of four common pulse shapes (rectangular, Gaussian, Blackman, hyperbolic secant) is compared. For a rectangular pulse, explicit higher order diffraction results are obtained from Kato's degenerate perturbation theory, which provide insight in the quasi-Bragg regime. Due to a renormalisation of the effective Rabi frequency in the beamsplitter manifold, one finds a significant stretching of the optimal  $\pi$ -pulse time (6.32), which has been seen experimentally [167]. It is assumed to be universal, because it is found for all considered pulse shapes.

Clearly, the diffraction efficiency and the fidelity benefit from Fourier-limited, smooth envelopes. Thereby, much insight is gained from the analytical Demkov-Kunike model (6.42) of a beamsplitter pulse, which assumes hyperbolic secant pulses. It reveals the explicit dependence on the multitude of physical parameters. It describes very accurately one of the most important aberrations, i.e. the velocity dispersion. Additionally, with the extended model (6.52) also losses into the neighbouring diffraction orders are considered. Due to its similarity with a Gaussian pulse, the diffraction efficiency for sech pulses (6.44) can be adapted to Gaussian pulses (6.54). Thereby, an analytical model (6.72) of the diffraction efficiency of partially condensed clouds can be derived for large, collimated Laguerre-Gaussian laser beams with temporal Gaussian envelopes, considering also laser frequency mismatches and rouge atomic initial velocity components. The model is verified experimentally [1] for a large parameter regime, matching the velocity dispersion and the even more sensitive Rabi oscillations of the diffraction efficiency.

In contrast to smooth temporal envelopes, smooth spatial variations diminish the diffraction performance. Comparing Laguerre-Gaussian laser beams with plane waves almost always reduces the diffraction efficiency and transfer fidelity. In particular, the beam inhomogeneity becomes relevant for *large* atomic clouds of width  $\sigma_x$  in comparison to the laser beam waist  $w_0$  with ratios  $\sigma_x \geq w_0/10$ . However, even for smaller but decentred clouds, the phase sensitive fidelity suffers significantly.

The detailed study of the radiative force, composed by the radiation pressure and the dipole force, reveals the most important aberration sources for this worsening, namely the transfer of transverse momentum components as well as an increase in the momentum width. For these transverse effects, the radiation pressure is negligibly small. However, a simple analytical model (7.18) for the effectively transferred momentum, quantifies its maximum contribution very precisely, giving advice in which situations it could be still important to take it into account. In contrast, while on relevant scales the dipole force in longitudinal direction is negligible, its transversal effects can be tremendous. A simple impact approximation (7.30), using the classical approximation of the Ehrenfest theorem, predicts sufficiently well the transferred momentum, even taking into account only the centre-of-mass position of the atomic states. Averaging over the spatial extent of the atomic cloud (7.31)-(7.32) is appropriate

even for *large* atomic sizes  $\sigma_x/w_0 \geq 1/10$ . However, the numerical simulations show a small systematic deviation. In contrast to the expectation, the transferred momentum has no exact negative parity for the laser detuning. To account for this effect, the dipole force should be studied in more detail, beyond the classical impact approximation of the Ehrenfest theorem.

In addition, laser misalignment forces a variation of the laser beam intensities and significant transverse momentum components are transferred to the atoms. However, this is only relevant for large misalignments or focussed laser beams. It is worth mentioning, that especially for laser misalignment the fidelity is much more sensitive to aberrations than the diffraction efficiency. The simulation results and the predictions for the effectively transferred momentum due to misaligned laser beams are again verified experimentally [1].

Spontaneous emission as an incoherent aberration source can be taken into account, using a Quantum Monte Carlo method. As expected, for extremely large laser detunings to the atomic resonance, spontaneous emission effects can be neglected safely. However, even one quantum jump, during the atomic diffraction, reduces the beamsplitter performance significantly in the percent regime.

In total, the beamsplitter quality depends on and is defined by a variety of observables. Therefore, linear susceptibilities make the diminishing effect of a multitude of aberration sources comparable. Regarding moderate but realistic beamsplitter parameters, these susceptibilities quantify the influence of different aberrations. This confirms that the velocity dispersion is one of the most important aberration source. To realise efficient matter-wave devices, it is equally important to match the pulse area conditions of a  $\pi/2$ - (beamsplitter) and  $\pi$ -pulse (mirror) exactly by adjusting the laser power and the pulse width. Rogue transferred transverse momentum components reduce the fidelity enormously, but leave the diffraction efficiency mostly unharmed.

While the derived analytical models provide deep physical insights into the characteristic properties of atomic Bragg diffraction, the full (3+1)-dimensional numerical simulation possesses realistic predictions as well as the clear advantage that it can be applied straightforward to different problems. For instance, one could think of Double Bragg diffraction [200], comparing even more temporal pulse shapes than indicated within this thesis and different intensity distributions, considering for example damaged optical devices.

Obviously, the next step is to combine the characterised matter-wave devices, based on atomic Bragg diffraction, with realistic (partially) condensed and expanded atomic clouds as initial states. Along with free expansion simulations, the ultimate objective of building a full matter-wave interferometer under realistic conditions, viz. taking plenty of aberrations into account, can be accomplished.

# Part V

---

## APPENDIX

---



## FUNDAMENTAL PARAMETERS

### A.1 ATOMIC BRAGG DIFFRACTION

For experiments with ultracold atoms the  $D_2$ -line of rubidium-87 atoms serves optimal conditions, accessible for common optical devices. Table A.1 lists fundamental parameters as well as parameters mostly used for the simulations and the compared experiments.

Quantity	Symbol	Value	Ref.
Number of atoms in BEC	$N^c$	$10(1) \times 10^3$	
Number of atoms in thermal cloud	$N^t$	$7(1) \times 10^3$	
Atomic mass	$M$	86.909 180 520(15) u	[A]
Transition frequency	$\omega_0$	$2\pi \times 384.230\,484\,468\,5(62)$ THz	[B]
Lifetime	$\tau$	26.2348(77) ns	[C]
Decay rate	$\Gamma$	$2\pi \times 6.0666(18)$ MHz	
Dipole matrix element	$\mathcal{D}$	$3.58424(52) \times 10^{-29}$ Cm	
Scattering length	$a_s$	$98.96 a_0$	[D]
Trap frequencies	$[\omega_x, \omega_y, \omega_z]$	$2\pi \times [46(2), 18(1), 31(1)]$ Hz	
Thomas-Fermi radii inside trap	$[r_x, r_y, r_z]$	$[4.2, 10.8, 6.2] \mu\text{m}$	

Table A.1: Set of **rubidium-87 atom parameters** of the  $D_2$  ( $5^2S_{1/2} \rightarrow 5^2P_{3/2}$ ) transition line, used in the experiments and simulations, taken from [A]: [201], [B]: [202], [C]: [203–206], [D]: [207].

The laser parameters mostly used for the atomic Bragg beamsplitter simulations and experiments are provided in Table A.2.

Quantity	Symbol	Value	Ref.
Wavelength	$\lambda_L$	780.024 500 015 nm	
Wavenumber	$k_L$	$8.056 \mu\text{m}^{-1}$	
Detuning to atomic resonance	$\Delta = \omega_L - \omega_0$	+97.875 GHz	
Beamwaist	$w_0$	1.386 mm	[208]
Rayleigh length	$x_R$	7.7 m	
Total interaction time	$\Delta t$	$(10^2 \dots 10^3) \mu\text{s}$	
Temporal Gaussian pulse width (6.4)	$t_G$	$\Delta t / 8$	
Distance between laser origins	$\ell_x$	$\sim 0.1 x_R$	

Table A.2: Set of **laser parameters**, used in this thesis for the experiments and simulations for atomic Bragg diffraction, with the mean wavenumber  $2k_L = k_1 + k_2$ .

## A.2 RAMAN VELOCITY FILTER

Relevant spectroscopic data for  $^{40}\text{Ca}^+$  ions are given in Table A.3, together with the characteristic properties of the applied velocity distribution. The laser parameters for the simulations of the Raman velocity filter are specified in Table A.4. Three different sets are compared in Part III. Parameter set (A) differs from (B) mainly in the laser frequencies, while (B<sub>1</sub>) and (B<sub>2</sub>) provide different laser powers. The beam waist as well as the laser linewidths stay the same for all cases.

Quantity	Symbol	Value	Ref.
Mass	$M$	39.962 042 286(22) u	[A, B]
Transition frequency	$\omega_{eg}$	$2\pi \times 761.905\,012\,599(82)$ THz	[C]
Natural linewidth (FWHM)	$\Gamma_{ge}$	$2\pi \times 23.396$ MHz	[B]
Lifetime	$\tau_{ge} = \Gamma_{ge}^{-1}$	6.8 ns	
Transition dipole matrix element	$\langle J = \frac{1}{2}    e \mathbf{r}    J' = \frac{3}{2} \rangle$	$2.301\,129 \times 10^{-29}$ C m	
Transition frequency	$\omega_{em}$	$2\pi \times 350.862\,882\,823(82)$ THz	[C, D]
Natural linewidth (FWHM)	$\Gamma_{me}$	$2\pi \times 1.576$ MHz	[B]
Lifetime	$\tau_{me} = \Gamma_{me}^{-1}$	101 ns	
Transition dipole matrix element	$\langle J = \frac{5}{2}    e \mathbf{r}    J' = \frac{3}{2} \rangle$	$1.250\,998 \times 10^{-29}$ C m	
Acceleration voltage	$U$	14 kV	
Mean velocity	$\bar{v}$	260 km/s	
Initial width of velocity distribution (FWHM)	$\Delta v_I$	(10 - 100) m/s	

Table A.3: **Parameters for  $^{40}\text{Ca}^+$  transitions** between the states  $|g\rangle$ ,  $|e\rangle$  and  $|m\rangle$ , of the configurations  $4s^2S_{1/2}$ ,  $4p^2P_{3/2}$ , and  $3d^2D_{5/2}$ , taken from [A]: [189], [B]:[190], [C]:[191], [D]:[192]. The parameters  $U$ ,  $\bar{v}$ ,  $\Delta v$  are applied in the simulations, being experimentally accessible.

Quantity	Symbol	Value		
Laser 1 (anti collinear)		Parameter set (A)	Parameter set (B <sub>1</sub> )	Parameter set (B <sub>2</sub> )
Frequency	$f_1$	761.243 795 50 THz	—	761.241 765 92 THz —
Wavelength	$\lambda_1$	393.8192 nm	—	393.8203 nm —
Wavenumber	$k_1$	$15.954490 \mu\text{m}^{-1}$	—	$15.954448 \mu\text{m}^{-1}$ —
Power	$P_1$	3.29 mW	10 mW	30 mW
Rabi frequency	$\Omega_1$	$2\pi \times 14.828$ MHz	$2\pi \times 25.852$ MHz	$2\pi \times 44.777$ MHz
Beamradius	$w_0$	—	1.7 mm	—
Linewidth	$\Gamma_{gg}$	—	300 kHz	—
Laser 2 (collinear)		Parameter set (A)	Parameter set (B <sub>1</sub> )	Parameter set (B <sub>2</sub> )
Frequency	$f_2$	351.166 422 00 THz	—	351.164 388 90 THz —
Wavelength	$\lambda_2$	853.7048 nm	—	853.7097 nm —
Wavenumber	$k_2$	$7.359904 \mu\text{m}^{-1}$	—	$7.359861 \mu\text{m}^{-1}$ —
Power	$P_2$	11.13 mW	33 mW	500 mW
Rabi frequency	$\Omega_2$	$2\pi \times 14.827$ MHz	$2\pi \times 25.531$ MHz	$2\pi \times 99.379$ MHz
Beamradius	$w_0$	—	1.7 mm	—
Linewidth	$\Gamma_{mm}$	—	300 kHz	—

Table A.4: Experimentally accessible **laser parameters** used for the Raman simulations.

## NUMERICAL METHODS

### B.1 DISCRETE FOURIER TRANSFORM ON PERIODIC LATTICES

Using discrete Fourier transformations there are fixed relations between the grid size in the real  $\mathbf{r} = (r_x, r_y, r_z)$  and the reciprocal  $\mathbf{k} = (k_x, k_y, k_z)$  space. Regarding in the three dimensions  $a \in \{x, y, z\}$  a number of  $N_a$  grid points and an extent of the grid  $r_a \in [-L_a, L_a]$ , respectively  $k_a \in [-K_a, K_a]$ , the discrete grid values are defined with

$$r_l \equiv r_{x_l} = \frac{2lL_x}{N_x}, \quad l \in \left[-\frac{N_x}{2}, \frac{N_x}{2}\right), \quad k_o \equiv k_{x_o} = \frac{o\pi}{L_x}, \quad o \in \left[-\frac{N_x}{2}, \frac{N_x}{2}\right), \quad (\text{B.1})$$

$$r_m \equiv r_{y_m} = \frac{2mL_y}{N_y}, \quad m \in \left[-\frac{N_y}{2}, \frac{N_y}{2}\right), \quad k_p \equiv k_{y_p} = \frac{p\pi}{L_y}, \quad p \in \left[-\frac{N_y}{2}, \frac{N_y}{2}\right), \quad (\text{B.2})$$

$$r_n \equiv r_{z_n} = \frac{2nL_z}{N_z}, \quad n \in \left[-\frac{N_z}{2}, \frac{N_z}{2}\right), \quad k_q \equiv k_{z_q} = \frac{q\pi}{L_z}, \quad q \in \left[-\frac{N_z}{2}, \frac{N_z}{2}\right). \quad (\text{B.3})$$

The relations between the increments read

$$\Delta a = \frac{2L_a}{N_a}, \quad K_a = \frac{\pi}{\Delta a} = \frac{\pi N_a}{2L_a}, \quad \Delta k_a = \frac{2K_a}{N_a} = \frac{2\pi}{N_a \Delta a} = \frac{\pi}{L_a}. \quad (\text{B.4})$$

Periodical boundary conditions are considered with

$$\psi_l = \psi_{l+N_x}, \quad \psi_m = \psi_{m+N_y}, \quad \psi_n = \psi_{n+N_z}, \quad (\text{B.5})$$

which are equivalent to the continuous boundary conditions  $\psi(r_a + 2L_a) = \psi(r_a)$ .

#### B.1.1 Wavefunctions

The wavefunctions are defined with the discrete Fourier transform in the position space by

$$\psi_{lmn} \equiv \psi(r_l, r_m, r_n) = \sum_{o=-\frac{N_x}{2}}^{\frac{N_x}{2}-1} \sum_{p=-\frac{N_y}{2}}^{\frac{N_y}{2}-1} \sum_{q=-\frac{N_z}{2}}^{\frac{N_z}{2}-1} \frac{e^{ik_o r_l}}{\sqrt{2L_x}} \frac{e^{ik_p r_m}}{\sqrt{2L_y}} \frac{e^{ik_q r_n}}{\sqrt{2L_z}} \Psi(k_o, k_p, k_q) \quad (\text{B.6})$$

and in the reciprocal momentum space by

$$\Psi_{opq} \equiv \Psi(k_o, k_p, k_q) = \frac{V}{\bar{N}} \sum_{l=-\frac{N_x}{2}}^{\frac{N_x}{2}-1} \sum_{m=-\frac{N_y}{2}}^{\frac{N_y}{2}-1} \sum_{n=-\frac{N_z}{2}}^{\frac{N_z}{2}-1} \frac{e^{-ik_o r_l}}{\sqrt{2L_x}} \frac{e^{-ik_p r_m}}{\sqrt{2L_y}} \frac{e^{-ik_q r_n}}{\sqrt{2L_z}} \psi(r_l, r_m, r_n). \quad (\text{B.7})$$



Here,  $\tilde{N} = N_x N_y N_z$  is the total number of grid points and  $V = 8L_x L_y L_z$  the volume of the orthorhombic grid. The norm of the wavefunction  $\|\psi\|$  is defined by the discrete scalar product

$$(\psi, \psi) = \sum_{l,m,n} |\psi_{lmn}|^2 = \frac{1}{V}, \quad (\text{B.8})$$

Choosing here the normalisation of the wavefunction to the volume  $V$ , the value in the continuous case  $\langle\psi|\psi\rangle$  is defined simultaneously to

$$\|\psi\|^2 = \langle\psi|\psi\rangle = \int_V d^3r |\psi(\mathbf{r})|^2 = \frac{1}{\tilde{N}}. \quad (\text{B.9})$$

Therefore, it is worth mentioning that the continuous scalar product  $\langle\cdot|\cdot\rangle$  give a different result than the discrete scalar product  $(\cdot, \cdot)$ . In addition, there is the relation

$$\sum_{l,m,n} |\psi_{lmn}|^2 = \frac{\tilde{N}}{V} \sum_{o,p,q} |\Psi_{opq}|^2 \quad (\text{B.10})$$

between the discrete representation in real and reciprocal space.

Please note, that numerical fast Fourier transforms (FFTs) methods use the following definition of the Fourier and inverse Fourier transform (in one dimension  $x$ )

$$\psi_l^{\text{FFT}} = \frac{1}{N_x} \sum_{o=0}^{N_x-1} e^{i2\pi o l / N_x} \Psi_o^{\text{FFT}}, \quad \Psi_o^{\text{FFT}} = \sum_{l=0}^{N_x-1} e^{-i2\pi o l / N_x} \psi_l^{\text{FFT}}. \quad (\text{B.11})$$

It is a shifted wavefunction in phase space. J.W. Cooley and J.W. Tukey developed the algorithm of FFTs [209], based on splitting the sum into one for the even and a second sum for the odd indices, while C.F. Gauß invented an algorithm similar to the FFT for the computation of the coefficients of a finite Fourier series [210]. In this way the computational complexity is reduced from  $\mathcal{O}(l^2)$  to  $\mathcal{O}(l \log l)$ . The discrepancy of the wavefunctions defined by the discrete Fourier transform (B.6), (B.7) to that one applying FFTs (B.11), i.e.

$$\Psi_{opq} = \frac{\sqrt{V}}{\tilde{N}} e^{i\pi o} e^{i\pi p} e^{i\pi q} \Psi_{opq}^{\text{FFT}}, \quad (\text{B.12})$$

needs to be kept in mind. More general details to discrete Fourier methods can be found e.g. in [211] and also more specific in Chapter 7 of the master thesis of Micha Ober [212].

### B.1.2 Expectation values

Physically observable expectation values  $\langle\hat{A}\rangle_\psi$  for pure states  $|\psi\rangle$ , respectively  $\langle\hat{A}\rangle_\rho$  for mixed states  $\hat{\rho}$  (3.20), are defined by

$$\langle\hat{A}\rangle_\psi = \frac{\langle\psi|\hat{A}|\psi\rangle}{\langle\psi|\psi\rangle}, \quad \langle\hat{A}\rangle_\rho = \text{Tr}\{\hat{\rho}\hat{A}\} = \frac{\sum_i p_i \langle\psi_i|\hat{A}|\psi_i\rangle}{\sum_i p_i \langle\psi_i|\psi_i\rangle} = \sum_i p_i \langle\hat{A}\rangle_{\psi_i}. \quad (\text{B.13})$$

Here, the square of the norm  $\|\psi\| = \sqrt{\langle\psi|\psi\rangle}$  of the wavefunction can be separated into the population of all internal states  $|\varsigma\rangle$  with

$$\|\psi\|^2 = \langle\psi|\psi\rangle = \sum_{\varsigma} \|\psi_{\varsigma}\|^2, \quad \|\psi_{\varsigma}\|^2 = \int d^3r |\psi_{\varsigma}(\mathbf{r})|^2, \quad \psi_{\varsigma} = \langle\varsigma|\psi\rangle. \quad (\text{B.14})$$

The total energy of the system

$$\langle \hat{H} \rangle = \frac{\langle \psi | \hat{H} | \psi \rangle}{\langle \psi | \psi \rangle} = \frac{\langle \psi | \hat{T} | \psi \rangle}{\langle \psi | \psi \rangle} + \frac{\langle \psi | \hat{V} | \psi \rangle}{\langle \psi | \psi \rangle}, \quad (\text{B.15})$$

contains the potential energy, which can be evaluated in real space

$$\langle \psi | \hat{V}(t, \mathbf{r}) | \psi \rangle = \int d^3r \psi^*(\mathbf{r}) \hat{V}(t, \mathbf{r}) \psi(\mathbf{r}), \quad (\text{B.16})$$

and the kinetic energy, using the Fourier transform into the momentum space  $\Psi(\mathbf{k})$

$$\langle \psi | \hat{T} | \psi \rangle = \langle \psi | \frac{\hat{\mathbf{p}}^2}{2M} | \psi \rangle = \frac{\hbar^2}{2M} \langle \psi | \hat{\mathbf{k}}^2 | \psi \rangle = \frac{\hbar^2}{2M} \int d^3k \mathbf{k}^2 |\Psi(\mathbf{k})|^2. \quad (\text{B.17})$$

The position and momentum moments of order  $s \in \mathbb{Z}_+$  for a certain direction  $a \in \{x, y, z\}$  are essential. In the continuous case, they read

$$\langle \hat{r}_a^s \rangle = \frac{\int d^3r r_a^s |\psi(\mathbf{r})|^2}{\int d^3r |\psi(\mathbf{r})|^2}, \quad \langle \hat{k}_a^s \rangle = \frac{\int d^3k k_a^s |\Psi(\mathbf{k})|^2}{\int d^3k |\Psi(\mathbf{k})|^2}, \quad (\text{B.18})$$

and in the discrete case, exemplary for the  $x$ -direction they are

$$\langle \hat{r}_x^s \rangle = V \sum_l r_l^s \sum_{m,n} |\psi_{lmn}|^2 = V \sum_l r_l^s \sum_{m,n} |\psi_{lmn}^{\text{FFT}}|^2, \quad (\text{B.19})$$

$$\langle \hat{k}_x^s \rangle = \bar{N} \sum_o k_o^s \sum_{p,q} |\Psi_{opq}|^2 = \frac{V}{N_x} \sum_o k_o^s \sum_{p,q} |\Psi_{opq}^{\text{FFT}, o}|^2, \quad (\text{B.20})$$

analogue in the remaining directions. In Eq. (B.20) the partial FFT for the  $x$ -axis ( $o$ ) occurs. The expectation value  $\langle \hat{\mathbf{k}}^2 \rangle = \langle \hat{k}_x^2 + \hat{k}_y^2 + \hat{k}_z^2 \rangle$  required for the kinetic energy is given by

$$\langle \hat{\mathbf{k}}^2 \rangle = \bar{N} \sum_{o,p,q} (k_o^2 + k_p^2 + k_q^2) |\Psi_{opq}|^2 = \frac{V}{\bar{N}} \sum_{o,p,q} (k_o^2 + k_p^2 + k_q^2) |\Psi_{opq}^{\text{FFT}}|^2. \quad (\text{B.21})$$

### B.1.3 Conserved quantities

For closed systems, where no population is lost into unobserved states, consequently the norm (B.14) is conserved with  $\|\psi\|^2 = \text{const.}$  In addition, for time-independent potentials  $\hat{V}(t, \mathbf{r}) = \hat{V}(0, \mathbf{r})$  the total energy of the system (B.15) remains constant  $\langle \hat{H} \rangle = \text{const.}$

## B.2 NUMBER OF SIMULATION TIMESTEPS

Naturally, the precision of the numerical simulation increases for smaller integration timesteps. Thus, the number of timesteps needs to be increased, claiming a longer computational time. Therefore, tools are required to identify a proper number of timesteps, keeping it as small as reasonable. Specifying a required accuracy of the norm and energy conservation, characterises a maximal time-step size for the numerical integration. It is worth mentioning, that the energy conservation is much more sensitive than the norm conservation. The exemplary results of the quality of energy conservation using symplectic integrators (cf. Sec. 3.1.1) with different splitting orders are visualised in Fig. 3.1.

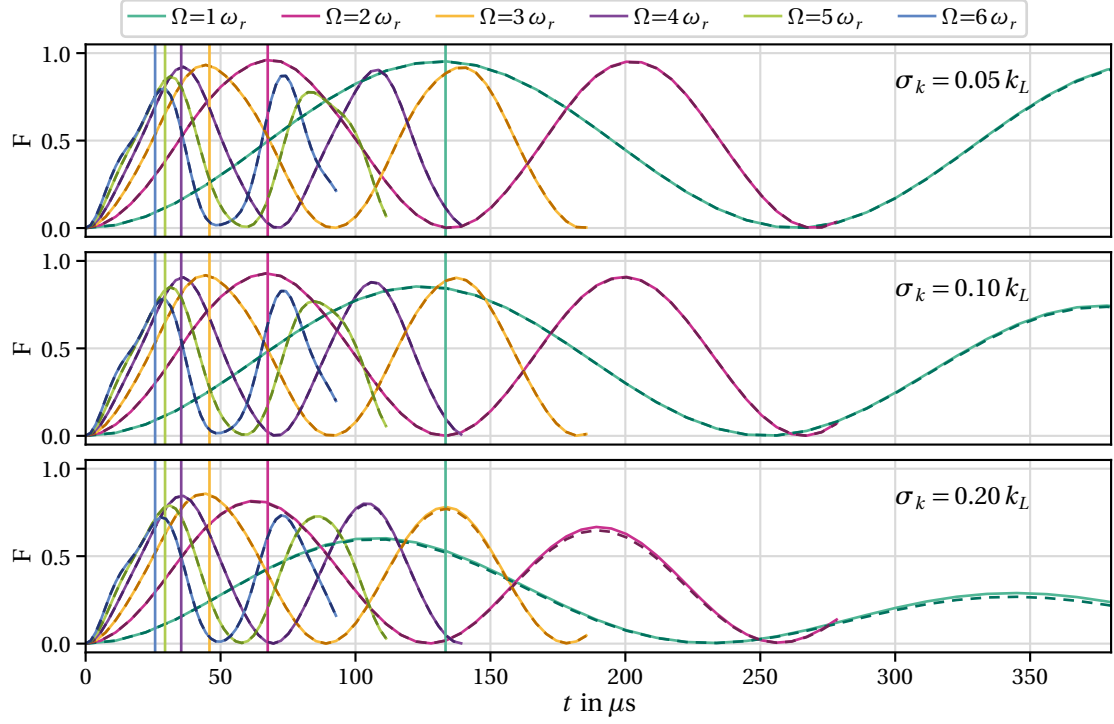
### B.3 SCALING OF THE NUMERICAL SIMULATIONS

To consider losses into higher diffraction orders in the quasi-Bragg regime (cf. Part II) a grid size of  $K_x \gtrsim 6k_L \approx 50\mu\text{m}^{-1}$  in the propagation direction  $x$  of the lasers is required for resonant first-order diffraction. Therefore, considering additionally a spatial extent in the range of the laser beamwaist  $w_0$  with  $L \sim w_0 \sim \text{mm}$  leads to a giant number of grid points  $\tilde{N} = N_x \times N_y \times N_z > 2^{30}$  for simulations in three dimensions. For discrete Fourier transformations, there are fixed relations between the grid size in the real  $\mathbf{r}$ - and the reciprocal  $\mathbf{k}$ -space, as mentioned in App. B.1. Therefore, with  $K \propto 1/L$  and  $\Delta k \propto 1/\Delta x$ , it is not possible to expand the  $x$ - and the  $k$ -size simultaneously without increasing the number of grid points. However, if the diffraction results can be scaled in the real space, the number of grid points can be kept in a practicable range. Therefore, large atomic clouds in large laser fields must be approximable with small atomic clouds in small laser fields, thus the diffraction efficiency must depend only on the ratio  $\sigma_x/w_0$ , not on the individual values of the laser beamwaist  $w_0$  and the size of the atomic cloud  $\sigma_x$ . Indeed, this is the case for an appropriate size  $\sigma_x$  with  $w_0 > \sigma_x > \lambda_L$ , as demonstrated in Fig. B.1 and Fig. B.2.

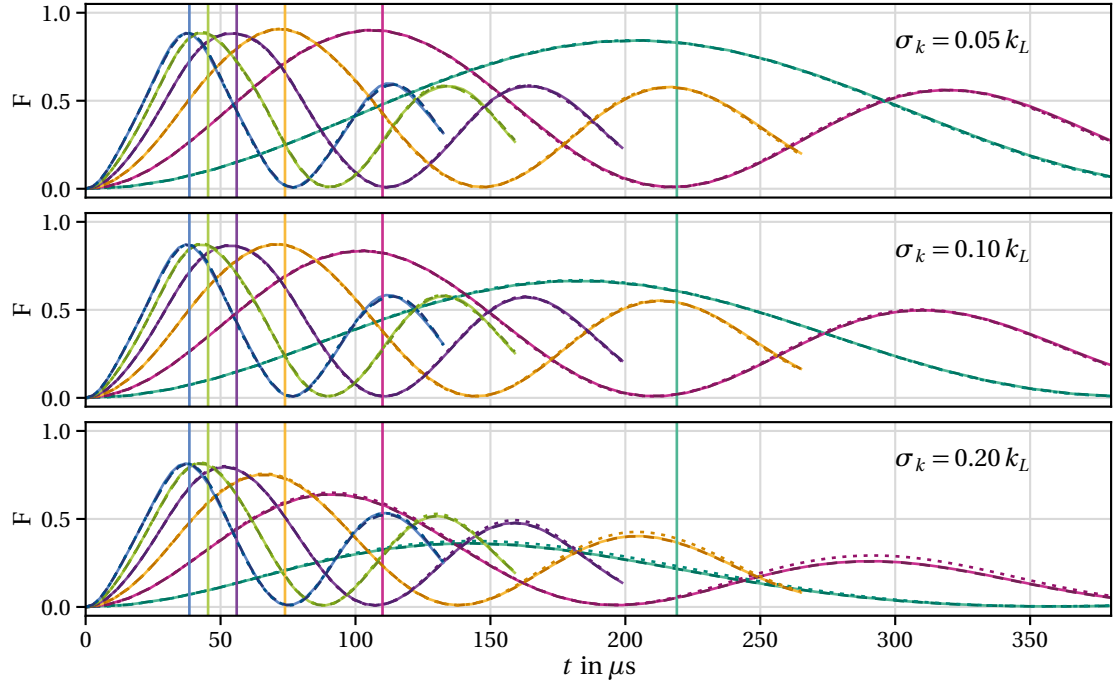
The phase sensitive fidelity  $F$  (5.34) depending on the pulse width represents the most sensible observable. Therefore, the Rabi oscillations of  $F$  for rectangular pulses with Laguerre-Gaussian spatial envelopes (cf. Sec. 2.2.2 and Chap. 7) are compared for different sizes of  $\sigma_x$  and  $w_0$  keeping the ratio  $\sigma_x/w_0$  constant. Different ratios  $\sigma_x/w_0$ , two-photon Rabi frequencies  $\Omega$ , momentum widths  $\sigma_k$  and atomic initial positions  $\mathbf{r}_0$  are considered.

In Fig. B.1 the ratio  $\sigma_x/w_0 = 1/25$  is studied. The results show, that indeed large atomic clouds [ $\sigma_x = 16\mu\text{m}$  (a),  $\sigma_x = 8\mu\text{m}$  (b)] in large laser fields [ $w_0 = 400\mu\text{m}$  (a),  $w_0 = 200\mu\text{m}$  (b)] can be approximated with small atomic clouds ( $\sigma_x = 2\mu\text{m}$ ) in small laser fields ( $w_0 = 50\mu\text{m}$ ). Even 2D simulations (simply skipping the third dimension with  $N_z = 1$ ,  $z = 0$ ) give exact results for  $\sigma_k \leq 0.1 k_L$ , only for  $\sigma_k = 0.2 k_L$  there are small deviations to the simulations in 3D. For (a) the size  $\sigma_x = 16\mu\text{m}$  is marginal too large for the grid size, causing very little deviations to the simulations with  $\sigma_x = 2\mu\text{m}$  especially for long interaction times, larger than the mirror times. The simulations show, that the larger the momentum width, the shorter is the effective  $\pi$ -pulse time, deviating from the analytical prediction (6.32) especially for small Rabi frequencies and large momentum widths. With displacing the initial state transversally the experienced effective Rabi frequency  $\Omega(\mathbf{r})$  is reduced. Therefore, the oscillation periods increases and the mismatch between the time of maximum population transfer and the analytical effective  $\pi$ -pulse time (6.32) is more crucial than for centrally located atoms.

In Fig. B.2 a large expansion with the ratio  $\sigma_x/w_0 = 1/5$  is studied. The results demonstrate again the spatial scalability of the atomic diffraction. Here, 2D simulations are not exact even for small momentum widths, but they give approximate predictions. In addition, for small Rabi frequencies or rather displaced atoms, the mismatch between the time of maximum population transfer and the analytical effective  $\pi$ -pulse time (6.32) increases further. However, for moderate effective Rabi frequencies it still gives reliable predictions.

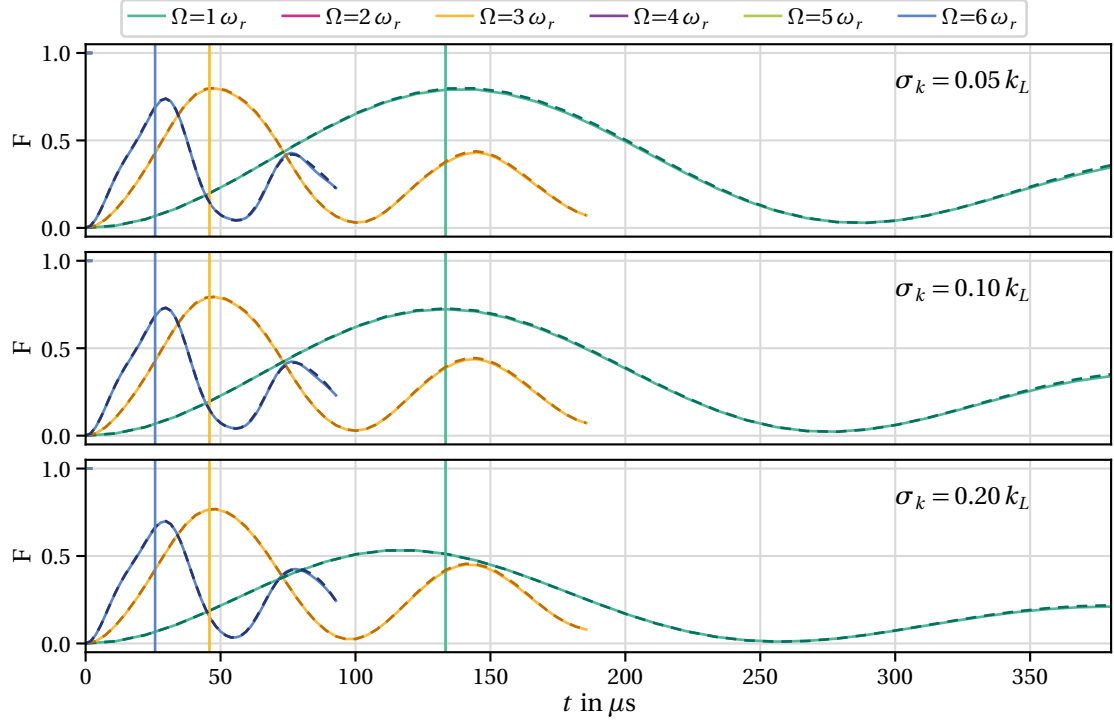


(a)  $\mathbf{r}_0 = (0, 0, 0)$ . Solid:  $\sigma_x = 16 \mu\text{m}$  with  $N_x = 2^{11}$ ,  $N_{i=y,z} = 2^8$ ,  $L_x = \sqrt{\pi N_x/2}$ ,  $L_{i=y,z} = 2\sqrt{\pi N_i/2}$ . Dashed:  $\sigma_x = 2 \mu\text{m}$  with  $N_x = 2^{11}$ ,  $N_y = N_z = 2^6$ ,  $L_i = \sqrt{\pi N_i/2}$ .

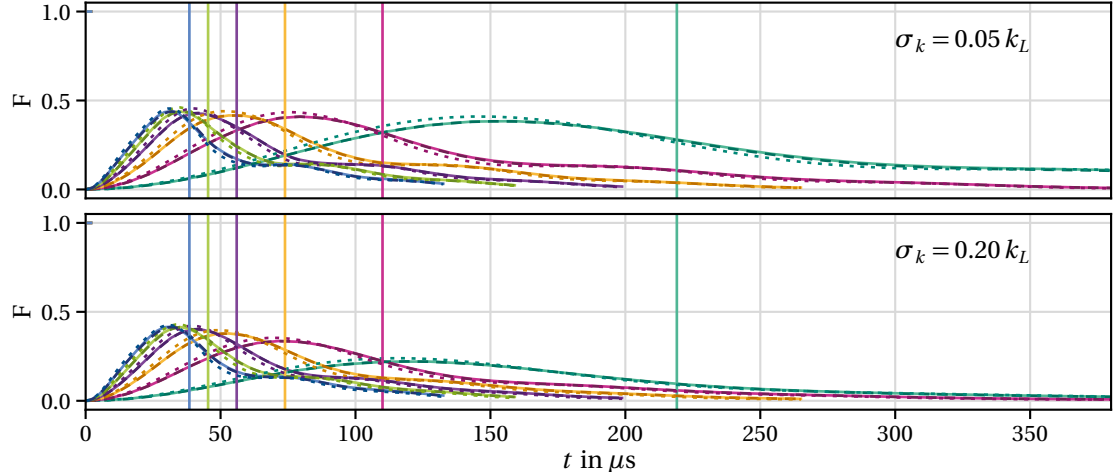


(b)  $\mathbf{r}_0 = (0, w_0/2, 0)$ . Solid:  $\sigma_x = 8 \mu\text{m}$  with  $N_x = 2^{10}$ ,  $N_{i=y,z} = 2^7$ ,  $L_x = \sqrt{\pi N_x/2}$ ,  $L_{i=y,z} = \sqrt{\pi N_i/2}$ . Dashed:  $\sigma_x = 2 \mu\text{m}$  with  $N_x = 2^{10}$ ,  $N_{i=y,z} = 2^7$ ,  $L_x = \sqrt{\pi N_x/2}$ ,  $L_{i=y,z} = \sqrt{\pi N_i/2}$ . Dotted:  $\sigma_x = 2 \mu\text{m}$  with  $N_x = 2^{10}$ ,  $N_y = 2^6$ ,  $N_z = 0$ ,  $L_i = \sqrt{\pi N_i/2}$ .

Figure B.1: Rabi oscillations of the fidelity  $F(t)$  (5.34), for ballistically expanded isotropic Gaussian wavepackets (5.26) as atomic initial states with a ratio  $\sigma_x/w_0 = 1/25$ , located at  $\mathbf{r}_0 = (0, 0, 0)$  (a) and  $\mathbf{r}_0 = (0, w_0/2, 0)$  (b). Different Rabi frequencies  $\Omega$ , momentum widths  $\sigma_k$  and spatial widths  $\sigma_x$  are considered. The analytical mirror times  $2\tilde{\tau}_{R\pi\omega_{2r}}$  (6.32) are highlighted.



(a)  $\mathbf{r}_0 = (0, 0, 0)$ . Solid:  $\sigma_x = 8\mu\text{m}$  with  $N_x = 2^{10}$ ,  $N_{i=y,z} = 2^7$ ,  $L_x = \sqrt{\pi N_x/2}$ ,  $L_{i=y,z} = 2\sqrt{\pi N_i/2}$ . Dashed:  $\sigma_x = 2\mu\text{m}$  with  $N_x = 2^{11}$ ,  $N_y = N_z = 2^6$ ,  $L_i = \sqrt{\pi N_i/2}$ .



(b)  $\mathbf{r}_0 = (0, w_0/2, 0)$ . Solid:  $\sigma_x = 8\mu\text{m}$  with  $N_x = 2^{10}$ ,  $N_{i=y,z} = 2^7$ ,  $L_x = \sqrt{\pi N_x/2}$ ,  $L_{i=y,z} = 2\sqrt{\pi N_i/2}$ . Dashed:  $\sigma_x = 1.25\mu\text{m}$  with  $N_x = 2^{10}$ ,  $N_{i=y,z} = 2^6$ ,  $L_i = \sqrt{\pi N_i/2}$ . Dotted:  $\sigma_x = 1.25\mu\text{m}$  with  $N_x = 2^{10}$ ,  $N_y = 2^6$ ,  $N_z = 0$ ,  $L_i = \sqrt{\pi N_i/2}$ .

Figure B.2: Rabi oscillations of the fidelity  $F(t)$  (5.34), for ballistically expanded isotropic Gaussian wavepackets (5.26) as atomic initial states with a ratio  $\sigma_x/w_0 = 1/5$ , located at  $\mathbf{r}_0 = (0, 0, 0)$  (a) and  $\mathbf{r}_0 = (0, w_0/2, 0)$  (b). Different Rabi frequencies  $\Omega$ , momentum  $\sigma_k$  and spatial widths  $\sigma_x$  are considered. The analytical mirror times  $2\tilde{\tau}_{R\pi}\omega_{2r}$  (6.32) are highlighted.

---

## DISENTANGLING AN EXPONENTIAL: $SU(2)$ ALGEBRA

---

The disentangling of the exponential  $\exp[-i\hat{V}\tau/\hbar]$  belonging to the spin operator algebra  $SU(2)$  represents one key method of the numerical simulations, which are developed and used within this work. Therefore, its derivation is described here in more detail, taken from [134].

In general, the disentangled expansion of an exponential of a sum of non-commutative operators  $\hat{X}_i$  is finite if all  $\hat{X}_i$  belong to a finite-dimensional Lie algebra generated by  $\hat{X}_1, \dots, \hat{X}_n$ ,  $n \in \mathbb{Z}_+$ , leading to

$$e^{\theta \sum_{i=1}^n \alpha_i \hat{X}_i} = e^{f_1(\theta) \hat{X}_1} \dots e^{f_n(\theta) \hat{X}_n}, \quad f_i(0) = 0. \quad (\text{C.1})$$

The Pauli spin operators couple the ground  $|g\rangle$  and the excited  $|e\rangle$  state of a two-level system

$$\hat{\sigma} = |g\rangle\langle e|, \quad \hat{\sigma}^\dagger = |e\rangle\langle g|, \quad \mathbb{1} = |g\rangle\langle g| + |e\rangle\langle e|, \quad (\text{C.2})$$

$$\hat{\sigma}_x = \hat{\sigma} + \hat{\sigma}^\dagger, \quad \hat{\sigma}_y = i(\hat{\sigma} - \hat{\sigma}^\dagger), \quad \hat{\sigma}_z = |e\rangle\langle e| - |g\rangle\langle g|. \quad (\text{C.3})$$

They obey the commutator relation  $[\hat{\sigma}_i, \hat{\sigma}_j] = 2i\epsilon_{ijk}\hat{\sigma}_k$ , and in a standard matrix representation they read

$$\sigma_x = \begin{pmatrix} 0 & 1 \\ 1 & 0 \end{pmatrix}, \quad \sigma_y = \begin{pmatrix} 0 & -i \\ i & 0 \end{pmatrix}, \quad \sigma_z = \begin{pmatrix} 1 & 0 \\ 0 & -1 \end{pmatrix}, \quad \sigma^\dagger = \begin{pmatrix} 0 & 1 \\ 0 & 0 \end{pmatrix}, \quad \sigma = \begin{pmatrix} 0 & 0 \\ 1 & 0 \end{pmatrix}. \quad (\text{C.4})$$

The imaginary multiples  $i\hat{\sigma}_j$ ,  $j \in \{x, y, z\}$  are elements of the  $SU(2)$  algebra, therefore the achievements for the disentangling of an exponential for the  $SU(2)$  algebra derived in [134] is applicable. Thus, the matrix exponential with arbitrary complex factors, possibly with spatial but no temporal dependency,  $\alpha_\pm$ ,  $\alpha_z$ , can be entangled with

$$e^{i\tau(\alpha_+\hat{\sigma}^\dagger + \alpha_z\hat{\sigma}_z + \alpha_-\hat{\sigma})} = e^{f_+(\tau)\hat{\sigma}^\dagger} e^{f_z(\tau)\hat{\sigma}_z} e^{f_-(\tau)\hat{\sigma}}. \quad (\text{C.5})$$

The determination of the complex functions  $f_\pm$  and  $f_z$  works as follows: Differentiating equation (C.5) with respect to  $\tau$  and the subsequent multiplication with the inverse of equation (C.5) leads to

$$i(\alpha_+\hat{\sigma}^\dagger + \alpha_z\hat{\sigma}_z + \alpha_-\hat{\sigma}) = \dot{f}_+\hat{\sigma}^\dagger + \underbrace{\dot{f}_z e^{f_+\hat{\sigma}^\dagger} \hat{\sigma}_z e^{-f_+\hat{\sigma}^\dagger}}_A + \underbrace{\dot{f}_- e^{f_+\hat{\sigma}^\dagger} \hat{\sigma} e^{-f_+\hat{\sigma}^\dagger}}_B. \quad (\text{C.6})$$

Using following relations derived from the commutator relations of the  $SU(2)$  algebra

$$e^{\frac{i\theta}{2}\hat{\sigma}} \hat{\sigma}_z e^{-\frac{i\theta}{2}\hat{\sigma}} = \hat{\sigma}_z + i\theta\hat{\sigma}, \quad e^{\frac{i\theta}{2}\hat{\sigma}_z} \hat{\sigma} e^{-\frac{i\theta}{2}\hat{\sigma}_z} = e^{-i\theta}\hat{\sigma}, \quad (\text{C.7})$$

$$e^{\frac{i\theta}{2}\hat{\sigma}^\dagger} \hat{\sigma}_z e^{-\frac{i\theta}{2}\hat{\sigma}^\dagger} = \hat{\sigma}_z - i\theta\hat{\sigma}^\dagger, \quad e^{\frac{i\theta}{2}\hat{\sigma}_z} \hat{\sigma}^\dagger e^{-\frac{i\theta}{2}\hat{\sigma}_z} = e^{i\theta}\hat{\sigma}^\dagger, \quad (\text{C.8})$$

the marked sandwich terms simplify to

$$A \equiv e^{f_+ \hat{\sigma}^\dagger} \hat{\sigma}_z e^{-f_+ \hat{\sigma}^\dagger} = \hat{\sigma}_z - 2f_+ \hat{\sigma}^\dagger, \quad B \equiv e^{f_z \hat{\sigma}_z} \hat{\sigma}^{-f_z \hat{\sigma}_z} = e^{-2f_z} \hat{\sigma}. \quad (\text{C.9})$$

With inserting this into the full equation

$$i(\alpha_+ \hat{\sigma}^\dagger + \alpha_z \hat{\sigma}_z + \alpha_- \hat{\sigma}) = \dot{f}_+ \hat{\sigma}^\dagger + \dot{f}_z \hat{\sigma}_z - 2f_+ \dot{f}_z \hat{\sigma}^\dagger + \dot{f}_- e^{-2f_z} \underbrace{e^{f_+ \hat{\sigma}^\dagger} \hat{\sigma} e^{-f_+ \hat{\sigma}^\dagger}}_C, \quad (\text{C.10})$$

one last sandwich term  $C$  needs to be determined. Applying the similarity transformation

$$\hat{A}(\theta) \equiv e^{-\theta \hat{P}} \hat{A} e^{\theta \hat{P}} = \hat{A} - \theta [\hat{P}, \hat{A}] + \frac{\theta^2}{2!} [\hat{P}, [\hat{P}, \hat{A}]] + \frac{\theta^3}{3!} [\hat{P}, [\hat{P}, [\hat{P}, \hat{A}]]] + \dots, \quad (\text{C.11})$$

$C$  reads

$$C \equiv e^{f_+ \hat{\sigma}^\dagger} \hat{\sigma} e^{-f_+ \hat{\sigma}^\dagger} = \hat{\sigma} + f_+ [\hat{\sigma}^\dagger, \hat{\sigma}] + \frac{f_+^2}{2!} [\hat{\sigma}^\dagger, [\hat{\sigma}^\dagger, \hat{\sigma}]] - \frac{f_+^3}{3!} [\hat{\sigma}^\dagger, [\hat{\sigma}^\dagger, [\hat{\sigma}^\dagger, \hat{\sigma}]]] + \dots \quad (\text{C.12})$$

Taking advantage of the commutator relations  $[\hat{\sigma}^\dagger, \hat{\sigma}] = \hat{\sigma}_z$ ,  $[\hat{\sigma}_z, \hat{\sigma}] = 2\hat{\sigma}$  and  $[\hat{\sigma}_z, \hat{\sigma}^\dagger] = 2\hat{\sigma}^\dagger$  the finitude of this expansion becomes apparent with

$$[\hat{\sigma}^\dagger, [\hat{\sigma}^\dagger, \hat{\sigma}]] = [\hat{\sigma}^\dagger, \hat{\sigma}_z] = -2\hat{\sigma}^\dagger, \quad (\text{C.13})$$

$$[\hat{\sigma}^\dagger, [\hat{\sigma}^\dagger, [\hat{\sigma}^\dagger, \hat{\sigma}]]] = [\hat{\sigma}^\dagger, [\hat{\sigma}^\dagger, \hat{\sigma}_z]] = -2[\hat{\sigma}^\dagger, \hat{\sigma}^\dagger] = 0. \quad (\text{C.14})$$

Comparing the pre-factors of  $\hat{\sigma}$ ,  $\hat{\sigma}^\dagger$  and  $\hat{\sigma}_z$  in the final expression

$$i(\alpha_+ \hat{\sigma}^\dagger + \alpha_z \hat{\sigma}_z + \alpha_- \hat{\sigma}) = \dot{f}_+ \hat{\sigma}^\dagger + \dot{f}_z \hat{\sigma}_z - 2f_+ \dot{f}_z \hat{\sigma}^\dagger + \dot{f}_- e^{-2f_z} (\hat{\sigma} + f_+ \hat{\sigma}_z - f_+^2 \hat{\sigma}^\dagger), \quad (\text{C.15})$$

results in non-linear differential equations, defining  $f_\pm$ ,  $f_z$  with

$$i\alpha_+ = \dot{f}_+ - 2\dot{f}_z f_+ - \dot{f}_- f_+^2 e^{-2f_z}, \quad (\text{C.16})$$

$$i\alpha_z = \dot{f}_z + \dot{f}_- f_+ e^{-2f_z}, \quad (\text{C.17})$$

$$i\alpha_- = \dot{f}_- e^{-2f_z}. \quad (\text{C.18})$$

Inserting (C.18) into (C.16), (C.17) and eliminating  $\dot{f}_z$  afterwards, yields the Riccati [213] equation

$$0 = i\dot{f}_+ + 2\alpha_z f_+ - f_+^2 \alpha_- + \alpha_+, \quad (\text{C.19})$$

which can be solved with

$$f_\pm = \frac{i\alpha_\pm \sin(\Gamma_1 \tau)}{\Gamma_1 F_z}, \quad f_z = -\ln(F_z), \quad F_z = \cos(\Gamma_1 \tau) - \frac{i\alpha_z}{\Gamma_1} \sin(\Gamma_1 \tau), \quad \Gamma_1^2 = \alpha_+ \alpha_- + \alpha_z^2, \quad (\text{C.20})$$

where  $f_-$  and  $f_z$  are calculated with the solution  $f_+$  in combination with (C.17), (C.18). With these solutions the disentangled exponential (C.5) is completely defined and can be written in matrix representation, applying the matrix representations of the Pauli spin operators (C.4). With  $\hat{\sigma}^2 = (\hat{\sigma}^\dagger)^2 = 0$ <sup>1</sup> the Taylor expansions  $\exp[f_- \hat{\sigma}] = 1 + f_- \hat{\sigma}$  and equivalently  $\exp[f_+ \hat{\sigma}^\dagger] = 1 + f_+ \hat{\sigma}^\dagger$  are exact and because  $\hat{\sigma}_z$  is diagonal the exponential of the diagonal elements can be directly taken, leading to

$$\begin{aligned} e^{f_+ \hat{\sigma}^\dagger} e^{f_z \hat{\sigma}_z} e^{f_- \hat{\sigma}} &= (1 + f_+ \hat{\sigma}^\dagger) e^{f_z \hat{\sigma}_z} (1 + f_- \hat{\sigma}) = \left( \mathbb{1} + \begin{pmatrix} 0 & f_+ \\ 0 & 0 \end{pmatrix} \right) \begin{pmatrix} e^{f_z} & 0 \\ 0 & e^{-f_z} \end{pmatrix} \left( \mathbb{1} + \begin{pmatrix} 0 & 0 \\ f_- & 0 \end{pmatrix} \right) \\ &= \begin{pmatrix} e^{f_z} + f_+ f_- e^{-f_z} & f_+ e^{-f_z} \\ f_- e^{-f_z} & e^{-f_z} \end{pmatrix} = \begin{pmatrix} F_z^{-1} + f_+ f_- F_z & f_+ F_z \\ f_- F_z & F_z \end{pmatrix}. \end{aligned} \quad (\text{C.21})$$

<sup>1</sup> The excited state cannot be excited further and the ground state cannot be further lowered.

## MODELS FOR (1+1)D ATOMIC BRAGG DIFFRACTION

### D.1 KATO MODEL

The Kato model rectifies the Pendellösung (6.11) for the Bragg diffraction of plane laser waves with rectangular pulse shapes with contributions from higher order diffraction (cf. Sec. 6.2.2). The full solution of the Schrödinger equation with the Kato Hamiltonian (6.15) results in (6.27)

$$\mathbf{g}^K(\tau) = \frac{\tilde{\mathbf{g}}^K(\tau)}{|\tilde{\mathbf{g}}^K(\tau)|}, \quad \tilde{\mathbf{g}}^K(\tau) = \sum_{i=\{1,3\}} \sum_{j=\{+,-\}} c_{i,j} e^{-i\omega_{i,j}(\tau-\tau_i)} \mathbf{v}_{i,j}. \quad (\text{D.1})$$

The eigenvalues  $\omega_{i,j}$  are given by the Eqs. (6.23), (6.25) and the normalised eigenvectors by

$$\mathbf{v}_{i,j} = \frac{P_i \mathbf{v}_{i,j}^{(0)}}{|P_i \mathbf{v}_{i,j}^{(0)}|}, \quad \mathbf{v}_{1,j}^{(0)} = (0, (\mathbf{v}_{1,j}^{(0)})_1, (\mathbf{v}_{1,j}^{(0)})_2, 0), \quad \mathbf{v}_{3,j}^{(0)} = ((\mathbf{v}_{3,j}^{(0)})_1, 0, 0, (\mathbf{v}_{3,j}^{(0)})_2), \quad (\text{D.2})$$

with the projections  $P_i$  (6.26) and eigenvectors of the reduced  $2 \times 2$  systems  $\mathbf{v}_{i,j}^{(0)}$  (6.23), (6.25). The integration constants  $c_{i,j}$  with  $\mathbf{c} \equiv (c_{1,+}, c_{1,-}, c_{3,+}, c_{3,-})$  are defined by the initial condition  $\tilde{\mathbf{g}}^K(\tau_i) = (0, 1, 0, 0)$  via

$$\mathbf{c} = A^{-1} \cdot \tilde{\mathbf{g}}^K(\tau_i), \quad A = (\mathbf{v}_{1,+}, \mathbf{v}_{1,-}, \mathbf{v}_{3,+}, \mathbf{v}_{3,-})^T. \quad (\text{D.3})$$

### D.2 DEMKOV-KUNIKE MODEL

The full Demkov-Kunike propagator  $G_{\mp}$  (6.40), for the Bragg diffraction of plane laser waves with sech-pulse shapes (cf. Sec. 6.3) results in bulky expressions. Especially for the extended DK-model (6.51), (6.52) it is useful to simplify  $G_{\mp}$  approximately as follows.

#### D.2.1 Demkov-Kunike propagator

With  $a = \Omega\tau_S/2$ ,  $b = -a$  and  $c = (1 + i\kappa\tau_S)/2$  the hypergeometric differential equation simplifies to

$$z(1-z)\gamma'' + (c-z)\gamma' + a^2\gamma = 0, \quad (\text{D.4})$$

and its solution reads

$$g_{-1}(z) = \gamma(z) = A {}_2F_1[-a, a; c, z] + B(-1)^{1-c} z^{1-c} {}_2F_1[\alpha_+, \alpha_-; 2-c, z], \quad (\text{D.5})$$

with  $\alpha_{\pm} = 1 \pm a - c = (1 + \Omega\tau_S - i\kappa\tau_S)/2$ . The solution of  $g_{+1}$  is given by the time derivation (6.35), which transforms in the  $z$ -domain to

$$g_{+1}(z) = \frac{i}{a} \sqrt{z(1-z)} g'_{-1}(z), \quad (\text{D.6})$$



resulting in

$$g_{+1}(z) = -Ai \frac{a\sqrt{z(1-z)}}{c} {}_2F_1[1-a, 1+a; 1+c, z] - Bi \frac{\sqrt{z(1-z)}}{a} (-1)^{-c} z^{-c} \left( (1-c) {}_2F_1[\alpha_-, \alpha_+, 2-c, z] + z \frac{(1+a-c)(a+c-1)}{c-2} {}_2F_1[1+\alpha_-, 1+\alpha_+; 3-c, z] \right). \quad (D.7)$$

The integration constants  $A$  and  $B$  are defined by the initial conditions  $g_{\pm 1,0} = g_{\pm}(z_i)$  with  $z_i = z(\tau_i)$ . Using the limit  $\lim_{\tau_i \rightarrow -\infty} z(\tau_i) = 0$  of a pulse beginning in the remote past, one can identify  $g_{-1}(z=0) = A = g_{-1,0}$ . Unfortunately,  $g_{+1}(z=0) = 0$  is independent of  $B$ . However, evaluating  $g_{-1}(z)$  on resonance for  $c(\kappa=0) = 1/2$ , and  $g_{+1}(z)$  with using again Eq. (D.6), the relation  $g_{+1}(z=0; c=1/2) = -B/(2a)$  can be found, wherefore  $B(\kappa=0) = -2ag_{+1,0}$ . For arbitrary  $\kappa$  the actual initial time  $\tau_i$  needs to be considered, for solving  $g_{+1}(z_i) = g_{+1,0}$  to separate  $B(g_{-1,0}, g_{+1,0}) = \mathfrak{J}g_{-1,0} + \Upsilon g_{+1,0}$ , with the two contributions

$$\mathfrak{J}(z_i) = \frac{(-1)^{1+c} a^2 z_i^c}{c} \frac{{}_2F_1[1-a, 1+a; 1+c, z_i]}{a {}_2F_1[\alpha_-, \alpha_+; 2-c, z_i] + \alpha_- {}_2F_1[1+\alpha_-, \alpha_+; 2-c, z_i]}, \quad (D.8)$$

$$\Upsilon(z_i) = \frac{i(-1)^c a z_i^c}{\sqrt{z_i(1-z_i)}} \frac{1}{a {}_2F_1[\alpha_-, \alpha_+; 2-c, z_i] + \alpha_- {}_2F_1[1+\alpha_-, \alpha_+; 2-c, z_i]}. \quad (D.9)$$

To fulfil the condition  $f(\tau_i) \approx 0$ , it is required  $n \gtrsim 3$  for  $\tau_i = -n\tau_G = n\tau_S \sqrt{2/\pi}$ . Then the limit of infinite boundaries ( $n \rightarrow \infty$ ) is appropriate and again profitable, because  $\lim_{z_i \rightarrow 0} \mathfrak{J} = 0$ . In addition, using the identity  ${}_2F_1[a, b; c, 0] = 1$ , it can be simplified

$$\Upsilon(z_i) \approx \frac{i(-1)^c a z_i^c}{(1-c)\sqrt{z_i(1-z_i)}} \Rightarrow \Upsilon(\tau_i) = \Upsilon(z(\tau_i)) = \frac{ia2^{1-c}}{1-c} \cosh\left(\frac{\tau_i}{\tau_s}\right) \left[-1 + \tanh\left(\frac{\tau_i}{\tau_s}\right)\right]^c, \quad (D.10)$$

where in the time domain the facts  $\tau_i < 0$  and  $\tau_s > 0$  are applied. Transforming back into the  $z$ -domain, results finally in

$$\Upsilon(z_i) = \frac{2ia(-z_i)^c}{(1-c)\sqrt{1-(1-2z_i)^2}}. \quad (D.11)$$

For  $c(\kappa=0) = 1/2$  this reduces to  $\Upsilon(z_i; c=1/2) = -2a/\sqrt{1-z_i}$ , verifying in the limit  $z_i \rightarrow 0$  the previous finding  $B(\kappa=0) = -2ag_{+1,0}$ . In general  $c = (1 + i\kappa\tau_s)/2$ , why  $\Upsilon$  depends strongly on the actual initial datum  $z_i$ , respectively  $\tau_i \propto \tau_s$ .

Now, with the integration constants  $A = g_{-1,0}$  and  $B \approx \Upsilon g_{+1,0}$  the time-dependent DK-Pendellösung is defined by the simplified Demkov-Kunike  $\tilde{G}$ -matrix

$$\mathbf{g}(\tau) = \tilde{G}(z(\tau)) \mathbf{g}(\tau_i), \quad (D.12)$$

with the matrix elements  $\tilde{G}_{ij}$  in the  $z$ -domain

$$\tilde{G}_{11} = {}_2F_1[a, -a; c, z], \quad (D.13)$$

$$\tilde{G}_{12} = \Upsilon(-1)^{1-c} z^{1-c} {}_2F_1[\alpha_-, \alpha_+; 2-c, z], \quad (D.14)$$

$$\tilde{G}_{21} = -i \frac{a}{c} \sqrt{z(1-z)} {}_2F_1[1-a, 1+a; 1+c, z], \quad (D.15)$$

$$\tilde{G}_{22} = -i\Upsilon \frac{(-1)^{-c} z^{-c} \sqrt{z(1-z)}}{a} \left\{ a {}_2F_1[\alpha_-, \alpha_+; 2-c, z] + \alpha_- {}_2F_1[1+\alpha_-, \alpha_+; 2-c, z] \right\}. \quad (D.16)$$

Please keep in mind, that this is only applicable for  $|\tau_i| \gtrsim 3\tau_G$  and that  $\tilde{G}_{12}$  and  $\tilde{G}_{22}$  depend strongly on  $\tau_i$ , because they are proportional to  $\Upsilon$ . However, for initially  $\mathbf{g}(\tau_i) = (1, 0)$ , one obtains Eqs. (6.42), which are independent of  $\Upsilon$ .

### D.2.2 Extended Demkov-Kunike model

Losses into higher diffraction orders can be taken into account with a time-dependent perturbation theory. Therefore, the integrals of the propagator  $G(\tau, \tau_i) \equiv G_0 + G_1 + G_2$  (6.52) need to be solved. The most important loss channels are the neighboring states  $\mu = \pm 3$ . In the quasi-Bragg regime the losses into even higher orders  $\mu = \pm 5$  can be neglected approximately. The integrals of  $G_1$  and  $G_2$  can be solved analytically, with approximating the matrix elements  $\tilde{G}_{ij}(z)$  with a weighted sum of a power series and Puiseux series (Taylor series in  $(z - z_0)^{1/p}$ ) expansions at the interval limits  $z_0 = 0$  and  $z_0 = 1$

$$\tilde{G}_{ij}(z) \approx (1-z) \sum_n c_n z^n + z \sum_i c_i (1-z)^{\alpha_i}. \quad (\text{D.17})$$

At these boundaries the series expansions describe the full solution very well and with the weighted sum they are suitably continued to the centre  $z(\tau = 0) = 1/2$ .

With the second order approximation of  $G(\tau, \tau_i)$  (6.52) the losses into  $\mu = \pm 3$  are overestimated within  $G_1$ . This would be compensated with taking the next two iterations  $G_3$  and  $G_4$  into account. However, it can be found that a simple scaling of the  $\mu = \pm 3$  contributions, using  $G(\tau, \tau_i) \approx G_0 + 0.77G_1 + G_2$  is sufficient to approximate this compensation. Due to the additional couplings in  $\mathcal{H}_1$  the solution  $\mathbf{g} = G(\tau, \tau_i)\mathbf{g}(\tau_i)$  needs to be normalised to achieve a final analytical expression for  $\mathbf{g} = (g_{-3}, g_{-1}, g_{+1}, g_{+3})$ .

#### Series expansion of the Demkov-Kunike Pendellösung

The matrix elements  $\tilde{G}_{ij}(z)$  (D.13) are approximated with

$$\tilde{G}_{11} \approx (1-z) \left( 1 - \frac{a^2}{c} z \right) + \frac{z}{\sin(c\pi)} \left( \frac{\pi \Gamma(c)[1-c-a^2(1-z)]}{\Gamma(2-c)\Gamma_+\Gamma_+} + \frac{a}{c} \sin(a\pi)(1-z)^c \right), \quad (\text{D.18a})$$

$$\tilde{G}_{12} \approx (-1)^{-2c} z \Upsilon \left[ (-1)^{c+1} (1-z) z^{-c} + [i + \cot(c\pi)] \left( \frac{7\pi(1-z)^c [c+1(c^2-a^2)(1-z)] \Gamma[2-c]}{8\Gamma(\alpha_-)\Gamma(\alpha_+)\Gamma(2+c)} + \frac{[c-1+a^2(1-z)] \sin(a\pi)}{a} \right) \right], \quad (\text{D.18b})$$

$$\tilde{G}_{21} \approx -i \frac{a}{c} (1-z) \sqrt{z} + \frac{iz\sqrt{1-z}}{2\sin(c\pi)} \left( \frac{a\pi[4-2a^2(1-z)-c(1+z)]\Gamma(c)}{\Gamma(3-c)\Gamma_+\Gamma_+} + \frac{e^{-ic\pi}(-1+z)^{c-1} \sin(a\pi)}{c} [(2c^2-2a^2)(1-z)+c(1+z)] \right), \quad (\text{D.18c})$$

$$\tilde{G}_{22} \approx (1-z) \frac{(-1)^{-c} \Upsilon}{a} \left( z^{\frac{1}{2}-c} \left[ \frac{T}{8\sqrt{2}\pi^{3/2}} - i(1-c) \right] + z^{\frac{3}{2}-c} \frac{i[2a^2-1+(3-2c)c]}{2} \right) - z \Upsilon [1 + i \cot(c\pi)] \left( -\sqrt{1-z} \sin(a\pi) + (1-z)^{-\frac{1}{2}+c} \frac{\pi \Gamma(2-c)}{a \Gamma(\alpha_-)\Gamma(\alpha_+)\Gamma(c)} \right), \quad (\text{D.18d})$$

with  $\Gamma_{\pm} = \Gamma(c \pm a)$ ,  $\alpha_{\pm} = 1 \pm a - c$  and  $a = \Omega\tau_S/2$ ,  $c = (1 + i\kappa\tau_S)/2$ . These approximations approach the matrix elements (D.13) very well, as visualised exemplary for  $\tilde{G}_{11}$  in Fig. D.1.

Here, also the single expansions around  $z_0 = 0$  and  $z_0 = 1$  are shown. For  $\kappa = 0$ , obviously the approximation is dominated by the expansion at  $z_0 = 1$ , with  $c(\kappa = 0) = 1/2$  resulting in

$$\tilde{G}_{11}(\kappa = 0) \approx 2a \sin(a\pi) \sqrt{1-z} + \cos(a\pi)[1 - 2a^2(1-z)]. \quad (\text{D.19})$$

However, for  $\kappa \neq 0$  the expansion at  $z = 0$  needs to be considered.

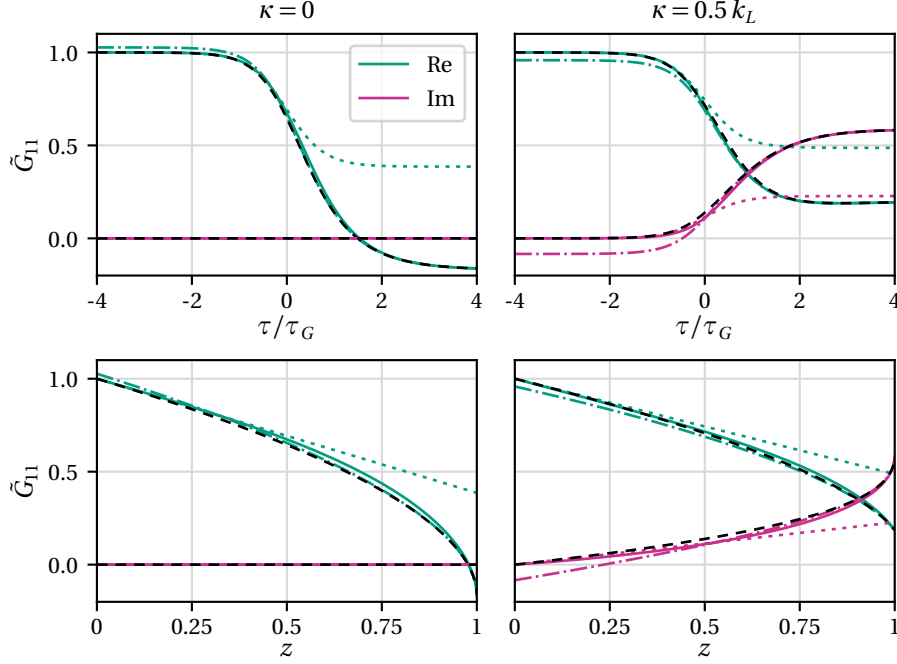


Figure D.1: Time-dependence (top:  $z(\tau)$  (6.37), bottom:  $\tau$ ) of the matrix element  $\tilde{G}_{11}$  of the time evolution matrix of the Demkov-Kunike Pendellösung (D.12). The approximation (D.18a) (solid), composed of the expansions at  $z_0 = 0$  (dotted) and  $z_0 = 1$  (dash-dotted), is compared to the exact solution (D.13) (dashed). Two different momentum detunings  $\kappa = 0$  (left) and  $\kappa = 0.5 k_L$  (right) are depicted for  $\Omega = 5 \omega_r$  and total interaction time  $\Delta\tau = 8 \tau_{G\pi}$ .

## COMPARISON WITH EXPERIMENTS

### E.1 VERIFICATION OF THE DEMKOV-KUNIKE MODEL

#### E.1.1 Expansion of the thermal cloud

Time-of-flight (TOF) measurements of a free expanding thermal cloud provide informations about their momentum distributions via the expansion velocity. For partially condensed clouds, as present in the experiment (cf. Sec. 6.6.1), a bimodal function (2.90) is fitted to the spatial one-dimensional density distributions as mentioned in Section 2.3.7. In Fig. E.1 the time-dependent widths of the quantum depletion are depicted for the experimentally accessible directions  $x$  and  $z$ . Linear fits of  $\sigma^2(t^2) = \sigma^2(0) + \sigma_v^2 t^2$  result with Eq. (2.89) in momentum widths  $\sigma_{k_x}^t = (1.91 \pm 0.12) \mu\text{m}^{-1} = (0.237 \pm 0.015) k_L$  and  $\sigma_{k_z}^t = (1.34 \pm 0.14) \mu\text{m}^{-1} = (0.166 \pm 0.017) k_L$ , related to the temperatures  $T_x = (20.4 \pm 2.5) \text{nK}$  and  $T_z = (10.0 \pm 1.9) \text{nK}$ . The uncertainties are given by the confidence interval to the confidence level 0.95. The resulting one-dimensional momentum distribution of the quantum depletion in  $x$ -direction is depicted in Fig. 6.12.

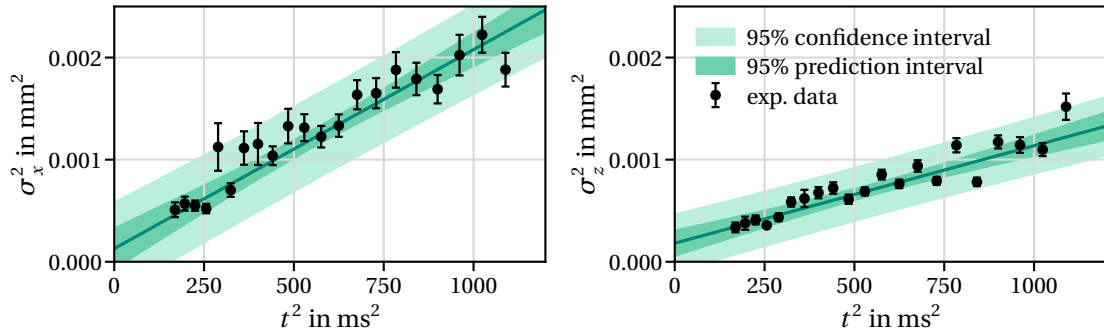
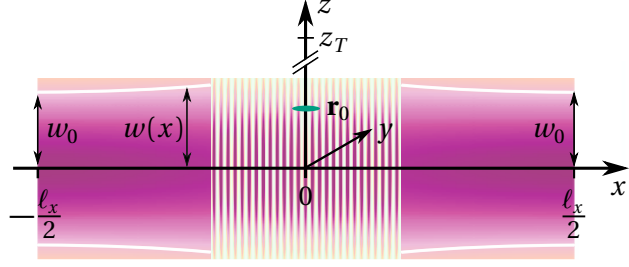


Figure E.1: Time-of-flight measurements [1] of the time-dependent width  $\sigma(t)$  of the doubly-integrated density of the quantum depletion in  $x$ - (left) and  $z$ -direction (right).

#### E.1.2 Location of the atoms

The location of the atoms  $\mathbf{r}_0$  is given by the experimental setup, depicted in Fig. E.2. In the propagation direction  $x$  of the lasers, the atoms are located at  $x_0 \approx 0$  and the lasers at  $\pm \ell_x/2$ . However, these positions are approximately irrelevant, because the lasers are collimated with  $w(x) \approx w_0 \gg \lambda_L$ . In contrast, a displacement of the atoms in the transverse  $\varrho$ -direction

Figure E.2: Two counterpropagating, collimated Laguerre-Gaussian laser beams (magenta) build the intensity pattern of a standing wave. The atoms (green) are located at  $\mathbf{r}_0 \approx (0, 0, z_0)$ . The distance between the two beamwaists  $w_0$  is  $\ell_x$ . However, for collimated beams  $w_0 \gg \lambda_L$  this is approximately irrelevant with  $w(x) \approx w_0$ .



affects, according to the Gaussian envelope of the lasers (2.24), tremendously the effective local two-photon Rabi frequency

$$\Omega(\mathbf{r}_0) \approx \Omega u(\mathbf{r}_0)^2, \quad u(\mathbf{r}_0)^2 = \exp(-2\rho_0^2/w_0^2). \quad (\text{E.1})$$

The transversal displacement is  $\rho_0 = \sqrt{y_0^2 + z_0^2}$ . While  $y_0 \approx 0$ ,  $z_0$  is defined by the distance between the trap  $z_T$  and the laser symmetry axis  $z = 0$  and the time-of-flight (TOF) before the beamsplitter pulses, during which the atoms fall into the interaction region

$$z_0(\text{TOF}) = z_T - \frac{1}{2}g\text{TOF}^2, \quad (\text{E.2})$$

with the gravitational acceleration  $g$  and assuming no initial velocity in the  $z$ -direction.

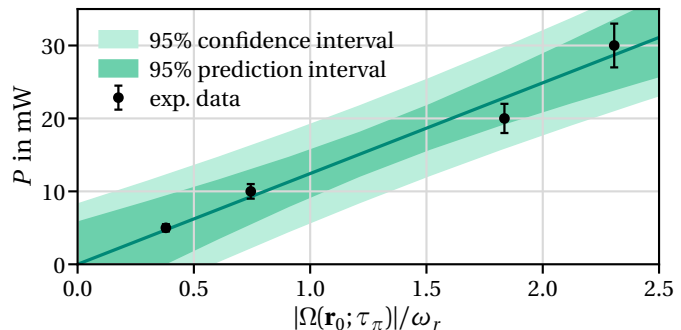
Without knowing the exact value of  $z_T$ , nevertheless  $z_0$  can be estimated. Therefore, it is assumed that the trap and laser positions do not change and additionally the TOF stays constant and can be measured very precisely resulting in a well-defined  $z_0$ .

From the Rabi oscillations of the diffraction efficiency (6.56) for different total laser powers  $P$ , depicted in Fig. 6.13, one can read out the experimental mirror pulse widths  $\tau_\pi(P)$  as time of the first maxima. Together with the analytical relations  $|\Omega(\mathbf{r}_0)| = \pi/2\tau_{R\pi}$  for rectangular pulses and  $|\Omega(\mathbf{r}_0)| = \sqrt{\pi/2}/\tau_{G\pi}$  for Gaussian pulses in the deep-Bragg regime [cf. Eq. (6.8)], one finds a linear dependency  $P = m|\Omega(\mathbf{r}_0; \tau_\pi)|$ , as depicted in Fig. E.3. In addition, the local two-photon Rabi frequency is also proportional to the laser power  $|\Omega(\mathbf{r}_0)| = \mu u(\mathbf{r}_0)^2 P$  [cf. Eqs. (2.13), (5.43), (E.1)]. Together, the slopes  $m$  and  $\mu$  define the location of the atoms with

$$u(\mathbf{r}_0)^2 = \frac{1}{m\mu}, \quad \frac{\rho_0^2}{w_0^2} = \frac{1}{2} \ln(m\mu); \quad (\text{E.3})$$

for  $x_0 = y_0 = 0$  one gets  $z_0 = (0.84 \pm 0.04)w_0 = (1165 \pm 50)\mu\text{m}$ . Therefore, a power uncertainty  $\Delta P = 0.1 P$  was estimated and the fit in Fig. E.3 results in  $m = (12.4 \pm 1.5)\text{mW}/\omega_r$ , where the 0.95-confidence interval is taken as uncertainty of  $m$ .

Figure E.3: Laser power  $P$  versus local two-photon Rabi frequency  $|\Omega(\mathbf{r}_0; \tau_\pi)|$ , which is derived via Eq. (6.8) from the  $\pi$ -pulse width  $\tau_{R\pi}$  of rectangular pulses [ $P = \{5, 10\} \text{ mW}$ ] and  $\tau_{G\pi}$  of Gaussian pulses [ $P = \{20, 30\} \text{ mW}$ ].



It is worth mentioning that the approximations (6.8) for the  $\pi$ -pulse widths are less exact the smaller the Rabi frequencies and the larger the momentum widths  $\sigma_k$  (cf. Fig. B.1). However, for the experimental parameters (cf. Table 6.1), the deviations are still small and therefore covered by the *large* uncertainty limit  $\Delta m$ .

There is an additional experimental method providing information about the location of the atoms, for experiments on ground and an experimental setup as depicted in Fig. E.2. Varying the TOF, the atoms scan the transversal beam profile according to Eq. (E.2), which is apparent in the diffraction efficiency of subsequent diffraction pulses, where the interaction time as well as the laser power are kept constant. This position dependent diffraction efficiency is depicted in Fig. E.4. Here, the number of maxima is defined by the maximum pulse area  $\theta_{j=R,G,\dots}$  (6.55). For  $\theta_j \leq \pi$  there can be only one maxima at  $z = 0$  and for  $(n-1)\pi < \theta_j \leq n\pi$  there are  $n$  local maxima. The central extremum defines the origin  $z = 0$ , due to the reflection symmetry  $\eta(\varrho_0) = \eta(-\varrho_0)$ , motivated by the analytical model (6.72). With Eq. (E.2) this defines the trap position  $z_T$ . The experimental measurements indicate  $z_T = 1.77$  mm resulting in an atomic initial position  $z_0^{\text{TOF}} = z(\text{TOF} = 10 \text{ ms}) = 0.92 w_0 = 1.28$  mm at the beginning of the diffraction pulses analysed in Section 6.6. This is similar to the results  $z_0 = (0.84 \pm 0.04) w_0$  achieved from the Rabi oscillation measurements. However, the TOF-measurements are less precise due to the lower data points, which furthermore for unknown reasons do not show the expected symmetrical behaviour  $\eta(\varrho_0) = \eta(-\varrho_0)$ . Therefore, for the evaluation of the experimental data in Section 6.6.3 the result  $z_0 = (0.84 \pm 0.04) w_0$  is used.

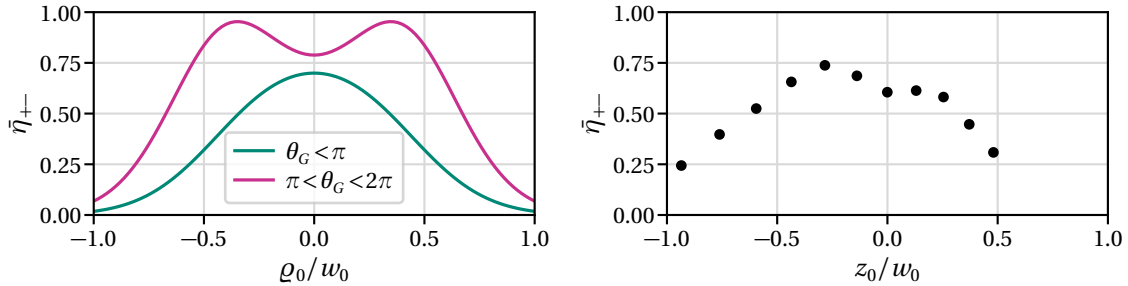


Figure E.4: Diffraction efficiency  $\bar{\eta}_{+-}$  (6.56) versus transversal atomic initial position  $\varrho_0 = \sqrt{y_0^2 + z_0^2}$ . Left: theoretical expectation for two pulse areas  $\theta_G$  using model (6.72). Right: experimental results [1].

## E.2 LASER MISALIGNMENT

### E.2.1 Expansion of the thermal cloud

For the misalignment experiment (cf. Sec. 7.5.3) the results of the TOF-measurements reveal the momentum spread of the thermal cloud (cf. App. E.1.1) and are depicted in Fig. E.5. Linear

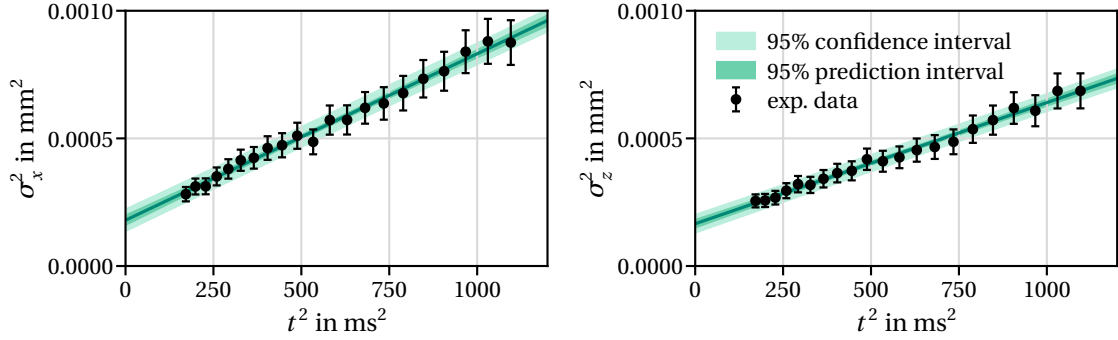


Figure E.5: Time-of-flight measurements [1] of the time-dependent width  $\sigma(t)$  of the doubly-integrated density of the quantum depletion in  $x$ - (left) and  $z$ -direction (right).

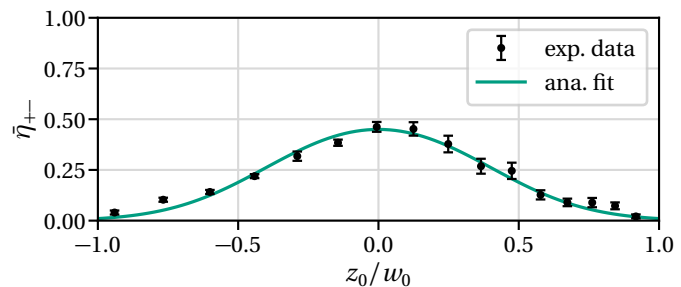
fits determine momentum widths  $\sigma_{k_x}^t = (1.10 \pm 0.03) \mu\text{m}^{-1} = (0.137 \pm 0.003) k_L$  and  $\sigma_{k_z}^t = (0.93 \pm 0.02) \mu\text{m}^{-1} = (0.116 \pm 0.003) k_L$ , related to the *temperatures*  $T_x = (6.81 \pm 0.33) \text{nK}$  and  $T_z = (4.87 \pm 0.24) \text{nK}$ . The uncertainties are given by the confidence interval to the confidence level 0.95. The resulting one-dimensional momentum distribution of the quantum depletion in  $x$ -direction is depicted in Fig. 7.16. In total, the momentum width is significantly smaller (almost half) than for the experiment to verify the Demkov-Kunike model (cf. App. E.1.1).

### E.2.2 Location of the atoms

The location of the atoms  $\mathbf{r}_0$  is given by the experimental setup, depicted in Fig. E.2, like for the verification of the DK-model (cf. App. E.1.2). However, for the misalignment experiment, only the TOF-scans are available, where the atoms scan the transversal beam profile according to Eq. (E.2). The position dependent diffraction efficiency for Gaussian pulses [ $P_1 = P_2 = (8.2 \pm 0.8) \text{mW}$ ] is depicted in Fig. E.6.

Applying the local two-photon Rabi frequency  $\Omega e^{-2(z_0/w_0)^2}$  to the analytical model (6.72) determines the trap position to  $z_T = (1747 \pm 48) \mu\text{m} = (1.26 \pm 0.03) w_0$ . Therefore, the atoms are displaced to  $z_0 = (1040 \pm 48) \mu\text{m} = (0.75 \pm 0.03) w_0$  for TOF = 12 ms, respectively almost perfectly centred with  $z_0 = (-24 \pm 48) \mu\text{m} = (-0.02 \pm 0.03) w_0$  for TOF = 19 ms. For the fit the experimentally given parameters (cf. Sec. 7.5.3)  $p^c = 0.58$ ,  $\sigma_k^c = 0.095$ ,  $\bar{\kappa} = \bar{\kappa}^S = 0.46 k_L$  and  $t_G = \tau_G / \omega_{2r} = 200 \mu\text{s}$  are applied, yielding the trap position  $z_T$  as well as the Rabi frequency  $\Omega = (1.05 \pm 0.04) \omega_r$ .

Figure E.6: Diffraction efficiency  $\bar{\eta}_{+-}$  (6.56) versus transversal atomic initial position  $z_0$ . The experimental data [1] are modelled with Eq. (6.56) using a local two-photon Rabi frequency  $\Omega \rightarrow \Omega e^{-2(z_0/w_0)^2}$ .



## RAMAN VELOCITY FILTER

### F.1 PERTURBATIVE METASTABLE STATE POPULATION

The Laplace transform of the metastable state's population provides insights on the population generating processes. Therefore, the OBEs are solved perturbatively, using Laplace transformations and following the linkage pattern depicted in Fig. 11.1. The whole population starts in the ground state with  $\rho_{gg}(t=0)=1$ . Therefore, initially, the time derivation

$$\dot{\rho}_{gg} = \Gamma_{eg}\rho_{ee} + i\left(\frac{\Omega_1}{2}\rho_{ge} - \frac{\Omega_1^*}{2}\rho_{eg}\right) \quad (\text{F.1})$$

vanishes in perturbation theory and the Laplace transform of the ground-state population  $\tilde{\rho}_{gg}$ , considering only the initial processes results from

$$s\tilde{\rho}_{gg} - \rho_{gg}(0) = 0 \quad \Rightarrow \quad \tilde{\rho}_{gg}(s) = \frac{1}{s} + \mathcal{O}(\Omega_1) = G_{gg}. \quad (\text{F.2})$$

Equivalently, the following processes in the linkage pattern can be calculated. With initially  $\rho_{ij}(0) = 0$ , they result in

$$\dot{\rho}_{eg} = (i\Delta_1 - \Gamma_{eg})\rho_{eg} + i\frac{\Omega_1}{2}(\rho_{ee} - \rho_{gg}) - \frac{\Omega_2}{2}\rho_{mg}, \quad (\text{F.3})$$

$$\underbrace{[s - i\Delta_1 + \Gamma_1]}_{G_{eg}^{-1}}\tilde{\rho}_{eg} = -i\frac{\Omega_1}{2}\tilde{\rho}_{gg} \quad \Rightarrow \quad \tilde{\rho}_{eg} = -\frac{i\Omega_1}{2}G_{eg}G_{gg}, \quad (\text{F.4})$$

$$\dot{\rho}_{ee} = -\Gamma\rho_{ee} + i\frac{\Omega_1^*}{2}\rho_{eg} - i\frac{\Omega_1}{2}\rho_{ge} + i\frac{\Omega_2^*}{2}\rho_{em} - i\frac{\Omega_2}{2}\rho_{me}, \quad (\text{F.5})$$

$$\underbrace{[s + \Gamma]}_{G_{ee}^{-1}}\tilde{\rho}_{ee} = i\frac{\Omega_1^*}{2}\tilde{\rho}_{eg} - i\frac{\Omega_1}{2}\tilde{\rho}_{ge} \quad \Rightarrow \quad \tilde{\rho}_{ee} = \frac{|\Omega_1|^2}{2}G_{gg}\text{Re}(G_{eg})G_{ee}, \quad (\text{F.6})$$

$$\dot{\rho}_{gm} = -(i\delta + \gamma)\rho_{gm} + i\frac{\Omega_2}{2}\rho_{ge} - i\frac{\Omega_1^*}{2}\rho_{em}, \quad (\text{F.7})$$

$$\underbrace{[s + i\delta + \gamma]}_{G_{gm}^{-1}}\tilde{\rho}_{gm} = i\frac{\Omega_2}{2}\tilde{\rho}_{ge} \quad \Rightarrow \quad \tilde{\rho}_{gm} = -\frac{\Omega_1^*\Omega_2}{4}G_{gm}G_{eg}^*G_{gg}, \quad (\text{F.8})$$

$$\dot{\rho}_{em} = (i\Delta - \Gamma_2)\rho_{em} + i\frac{\Omega_2}{2}(\rho_{ee} - \rho_{mm}) - i\frac{\Omega_1}{2}\rho_{gm}, \quad (\text{F.9})$$

$$\underbrace{[s - i\Delta + \gamma_2]}_{G_{em}^{-1}}\tilde{\rho}_{em} = i\frac{\Omega_2}{2}\tilde{\rho}_{ee} - i\frac{\Omega_1}{2}\tilde{\rho}_{gm} \quad \Rightarrow \quad \tilde{\rho}_{em} = G_{em}\left(i\frac{\Omega_2}{2}\tilde{\rho}_{ee} - i\frac{\Omega_1}{2}\tilde{\rho}_{gm}\right). \quad (\text{F.10})$$



Finally, for the population of the metastable state, it follows

$$\dot{\rho}_{mm} = \Gamma_{em}\rho_{ee} - i\frac{\Omega_2^*}{2}\rho_{em} + i\frac{\Omega_2}{2}\rho_{me}, \quad (\text{E11})$$

$$\underbrace{s}_{G_{mm}^{-1}}\tilde{\rho}_{mm} = \Gamma_{em}\tilde{\rho}_{ee} - i\frac{\Omega_2^*}{2}\tilde{\rho}_{em} + i\frac{\Omega_2}{2}\tilde{\rho}_{me}, \quad (\text{E12})$$

achieving the result (11.13)

$$\tilde{\rho}_{mm}(s) = G_{mm} \left[ \left( \Gamma_{em} + \frac{|\Omega_2|^2}{2} \text{Re}[G_{me}] \right) \tilde{\rho}_{ee}(s) + \frac{|\Omega_2|^2 |\Omega_1|^2}{8} \text{Re}[G_{me} G_{mg} G_{eg}] G_{gg} \right]. \quad (\text{E13})$$

## E.2 FULL SOLUTION OF THE POPULATION TRANSFER VIA THE RAMAN TRANSITION

The analytic approximation for the velocity- and time-dependent population of the metastable state, transferred via the Raman transition, results in a rather complicated expression (12.19)

$$m_R(t, \nu) = \frac{1}{2} + e^{-\vartheta t} [A \cos(\theta t) + B \sin(\theta t)] - e^{2(\vartheta - \gamma)t} C. \quad (\text{E14})$$

The complex, time-independent but velocity-dependent damping rate and frequency read

$$\vartheta = \frac{1}{12} \left( 8\gamma + x + \frac{y}{x} \right), \quad \theta = \frac{x^2 - y}{4\sqrt{3}x}, \quad (\text{E15})$$

and the also complex and velocity-dependent coefficients are

$$A = \frac{1}{3} \frac{mn + op}{m^2 + o^2}, \quad B = \frac{1}{3} \frac{mp - no}{m^2 + o^2}, \quad C = \frac{36x^2 \underline{\delta}^2 / \gamma^2 + (x(x+2) + y)^2}{6(x^4 + x^2 y + y^2)}. \quad (\text{E16})$$

These include further coefficients

$$m = \sqrt{3}(x^4 - 4y^2), \quad n = \sqrt{3}(y - x^2)[x(x-4) + y], \quad (\text{E17})$$

$$o = (x^2 - y)^2, \quad p = 4xy(x-1) - y^2 + x^2[8(1 + 9\underline{\delta}^2 / \gamma^2) - x(4+x)]. \quad (\text{E18})$$

Finally, the physical parameters within  $\underline{\delta}$  and  $\Omega_R$  are contained in

$$x = \left( z + \sqrt{z^2 - y^3} \right)^{1/3}, \quad y = 4 \left( 1 - 3 \frac{\underline{\delta}^2 + \Omega_R^2}{\gamma^2} \right), \quad z = 8 \left( 1 + 9 \frac{\underline{\delta}^2 - \Omega_R^2 / 2}{\gamma^2} \right). \quad (\text{E19})$$

The corresponding width in the velocity space of  $m_R(t, \nu)$  can be approximated analytically for  $t = t_\pi$  resulting in (12.22)

$$\Delta \nu_R(t_\pi) = \frac{2}{k_1 + k_2} \sqrt{p + \sqrt{p^2 + q}}, \quad p = \frac{\zeta^2 E - D t_\pi - \ln(2)}{2 \ln(2) E}, \quad q = \frac{\zeta^2}{\ln(2) E}. \quad (\text{E20})$$

Here, the following coefficients are introduced

$$D = 3F(d=0), \quad E = \frac{1}{2} \frac{d^2}{dd^2} \frac{9F(d=0)}{3F(d)-2} \bigg|_{\Omega_R = \tilde{\Omega}_R, d=\Gamma}, \quad F = \frac{x^2 + y}{6x} \bigg|_{\underline{\delta}=d}, \quad (\text{E21})$$

depending on  $x, y$  from (F19).

---

## BIBLIOGRAPHY

---

- [1] The experiments were done by Dr. Martina Gebbe, ZARM, Universität Bremen, Am Fallturm, D-28359 Bremen, Germany. (cit. on pp. [iii–iv](#), [8](#), [18](#), [78](#), [85](#), [107](#), [153–154](#), [171](#), [173–174](#)).
- [2] M. H. Anderson, J. R. Ensher, M. R. Matthews, et al., *Observation of Bose-Einstein Condensation in a Dilute Atomic Vapor*, *Science* **269**, 198–201 (1995) (cit. on p. [1](#)).
- [3] K. B. Davis, M. O. Mewes, M. R. Andrews, et al., *Bose-Einstein Condensation in a Gas of Sodium Atoms*, *Phys. Rev. Lett.* **75**, 3969–3973 (1995) (cit. on p. [1](#)).
- [4] C. C. Bradley, C. A. Sackett, J. J. Tollett, et al., *Evidence of Bose-Einstein Condensation in an Atomic Gas with Attractive Interactions*, *Phys. Rev. Lett.* **75**, 1687–1690 (1995) (cit. on p. [1](#)).
- [5] A. Einstein, *Quantentheorie des einatomigen idealen Gases*, *Sitzungsberichte der Preussischen Akademie der Wissenschaften* **22**, 237–244 (1924) (cit. on p. [1](#)).
- [6] A. Einstein, *Quantentheorie des einatomigen idealen Gases: Zweite Abhandlung*, *Sitzungsberichte der Preussischen Akademie der Wissenschaften* **1**, 245–257 (1925) (cit. on p. [1](#)).
- [7] E. A. Cornell and C. E. Wieman, *Nobel lecture: Bose-Einstein condensation in a dilute gas, the first 70 years and some recent experiments*, *Rev. Mod. Phys.* **74**, 875–893 (2002) (cit. on p. [1](#)).
- [8] W. Ketterle, *Nobel lecture: When atoms behave as waves: Bose-Einstein condensation and the atom laser*, *Rev. Mod. Phys.* **74**, 1131–1151 (2002) (cit. on p. [1](#)).
- [9] C. H. Townes, N. G. Basov, and A. M. Prokhorov, *The Nobel Prize in Physics for fundamental work in the field of quantum electronics, which has led to the construction of oscillators and amplifiers based on the maser-laser principle*, 1964 (cit. on p. [1](#)).
- [10] N. Bloembergen, A. L. Schawlow, and K. M. Siegbahn, *The Nobel Prize in Physics to N.B., A.S. for their contribution to the development of laser spectroscopy and to K.S. for his contribution to the development of high-resolution electron spectroscopy*, 1981 (cit. on p. [1](#)).
- [11] S. Chu, C. Cohen-Tannoudji, and W. D. Phillips, *The Nobel Prize in Physics for development of methods to cool and trap atoms with laser light*, 1997 (cit. on p. [1](#)).
- [12] R. J. Glauber, J. L. Hall, and T. W. Hänsch, *The Nobel Prize in Physics to R.G. for his contribution to the quantum theory of optical coherence and to J.H., T.H. for their contributions to the development of laser-based precision spectroscopy, including the optical frequency comb technique*, 2005 (cit. on p. [1](#)).
- [13] A. Ashkin, G. Mourou, and D. Strickland, *The Nobel Prize in Physics for groundbreaking inventions in the field of laser physics*, 2018 (cit. on p. [1](#)).
- [14] A. P. Kazantsev, G. I. Surdutovich, and V. P. Yakovlev, *Mechanical Action of Light on Atoms* (World Scientific, Singapore, 1990) (cit. on pp. [1](#), [51](#), [59](#), [111](#)).
- [15] P. R. Berman, *Atom Interferometry* (Academic Press, San Diego, 1997) (cit. on p. [1](#)).

- [16] A. D. Cronin, J. Schmiedmayer, and D. E. Pritchard, *Optics and interferometry with atoms and molecules*, *Rev. Mod. Phys.* **81**, 1051–1129 (2009) (cit. on pp. 1, 4).
- [17] G. M. Tino and M. A. Kasevich, *Atom Interferometry*, in *Proceedings of the International School of Physics Enrico Fermi*, Vol. 188 (Società Italiana di Fisica and IOS Press, Amsterdam, 2014) (cit. on p. 1).
- [18] S. Abend, M. Gersemann, C. Schubert, et al., *Atom interferometry and its applications*, in *Foundations of Quantum Theory. Proceedings of the International School of Physics Enrico Fermi*, Vol. 197 (IOS Press, 2019), pp. 345–392 (cit. on p. 1).
- [19] S. Fray, C. A. Diez, T. W. Hänsch, et al., *Atomic Interferometer with Amplitude Gratings of Light and Its Applications to Atom Based Tests of the Equivalence Principle*, *Phys. Rev. Lett.* **93**, 240404 (2004) (cit. on p. 1).
- [20] D. Schlippert, J. Hartwig, H. Albers, et al., *Quantum Test of the Universality of Free Fall*, *Phys. Rev. Lett.* **112**, 203002 (2014) (cit. on p. 1).
- [21] L. Zhou, S. Long, B. Tang, et al., *Test of Equivalence Principle at  $10^{-8}$  Level by a Dual-Species Double-Diffraction Raman Atom Interferometer*, *Phys. Rev. Lett.* **115**, 013004 (2015) (cit. on p. 1).
- [22] B. Altschul, Q. G. Bailey, L. Blanchet, et al., *Quantum tests of the Einstein Equivalence Principle with the STE-QUEST space mission*, *Adv. Sp. Res.* **55**, 501–524 (2015) (cit. on p. 1).
- [23] A. Bonnin, N. Zahzam, Y. Bidel, et al., *Characterization of a simultaneous dual-species atom interferometer for a quantum test of the weak equivalence principle*, *Phys. Rev. A* **92**, 023626 (2015) (cit. on p. 1).
- [24] B. Barrett, L. Antoni-Micollier, L. Chichet, et al., *Dual matter-wave inertial sensors in weightlessness*, *Nat. Commun.* **7**, 13786 (2016) (cit. on p. 1).
- [25] J. Williams, S.-w. Chiow, N. Yu, et al., *Quantum test of the equivalence principle and space-time aboard the International Space Station*, *New J. Phys.* **18**, 025018 (2016) (cit. on p. 1).
- [26] C. Overstreet, P. Asenbaum, T. Kovachy, et al., *Effective Inertial Frame in an Atom Interferometric Test of the Equivalence Principle*, *Phys. Rev. Lett.* **120**, 183604 (2018) (cit. on p. 1).
- [27] P. Asenbaum, C. Overstreet, M. Kim, et al., *Atom-Interferometric Test of the Equivalence Principle at the  $10^{-12}$  Level*, *Phys. Rev. Lett.* **125**, 191101 (2020) (cit. on p. 1).
- [28] A. Arvanitaki, S. Dimopoulos, A. A. Geraci, et al., *How to Test Atom and Neutron Neutrality with Atom Interferometry*, *Phys. Rev. Lett.* **100**, 120407 (2008) (cit. on p. 1).
- [29] R. Bouchendira, P. Cladé, S. Guellati-Khélifa, et al., *New Determination of the Fine Structure Constant and Test of the Quantum Electrodynamics*, *Phys. Rev. Lett.* **106**, 080801 (2011) (cit. on p. 1).
- [30] R. H. Parker, C. Yu, W. Zhong, et al., *Measurement of the fine-structure constant as a test of the Standard Model*, *Science* **360**, 191–195 (2018) (cit. on pp. 1, 5–6).
- [31] A. Peters, K. Y. Chung, and S. Chu, *High-precision gravity measurements using atom interferometry*, *Metrologia* **38**, 25–61 (2001) (cit. on p. 1).
- [32] J. M. McGuirk, G. T. Foster, J. B. Fixler, et al., *Sensitive absolute-gravity gradiometry using atom interferometry*, *Phys. Rev. A* **65**, 033608 (2002) (cit. on p. 1).

- [33] D. S. Durfee, Y. K. Shaham, and M. A. Kasevich, *Long-Term Stability of an Area-Reversible Atom-Interferometer Sagnac Gyroscope*, *Phys. Rev. Lett.* **97**, 240801 (2006) (cit. on p. 1).
- [34] S. Dimopoulos, P. W. Graham, J. M. Hogan, et al., *Testing General Relativity with Atom Interferometry*, *Phys. Rev. Lett.* **98**, 111102 (2007) (cit. on p. 1).
- [35] D. Aguilera, H. Ahlers, B. Battelier, et al., *STE-QUEST - Test of the universality of free fall using cold atom interferometry*, *Class. Quantum Grav.* **31**, 115010 (2014) (cit. on p. 1).
- [36] I. Dutta, D. Savoie, B. Fang, et al., *Continuous Cold-Atom Inertial Sensor with 1 nrad/sec Rotation Stability*, *Phys. Rev. Lett.* **116**, 183003 (2016) (cit. on p. 1).
- [37] V. Xu, M. Jaffe, C. D. Panda, et al., *Probing gravity by holding atoms for 20 seconds*, *Science* **366**, 745–749 (2019) (cit. on p. 1).
- [38] W. Ertmer, C. Schubert, T. Wendrich, et al., *Matter wave explorer of gravity (MWXG)*, *Exp. Astron.* **23**, 611–649 (2009) (cit. on p. 1).
- [39] R. Geiger, V. M  noret, G. Stern, et al., *Detecting inertial effects with airborne matter-wave interferometry*, *Nat. Commun.* **2**, 474 (2011) (cit. on p. 1).
- [40] H. M  ntinga, H. Ahlers, M. Krutzik, et al., *Interferometry with Bose-Einstein Condensates in Microgravity*, *Phys. Rev. Lett.* **110**, 093602 (2013) (cit. on pp. 1, 4).
- [41] T. Kovachy, P. Asenbaum, C. Overstreet, et al., *Quantum superposition at the half-metre scale*, *Nature* **528**, 530–533 (2015) (cit. on pp. 1, 5–6).
- [42] T. Schuldt, C. Schubert, M. Krutzik, et al., *Design of a dual species atom interferometer for space*, *Exp. Astron.* **39**, 167–206 (2015) (cit. on p. 1).
- [43] D. Becker, M. D. Lachmann, S. T. Seidel, et al., *Space-borne Bose-Einstein condensation for precision interferometry*, *Nature* **562**, 391–395 (2018) (cit. on pp. 1, 5).
- [44] E. R. Elliott, M. C. Krutzik, J. R. Williams, et al., *NASA’s Cold Atom Lab (CAL): system development and ground test status*, *npj Microgravity* **4**, 16 (2018) (cit. on p. 1).
- [45] G. M. Tino, A. Bassi, G. Bianco, et al., *SAGE: A proposal for a space atomic gravity explorer*, *Eur. Phys. J. D* **73**, 228 (2019) (cit. on p. 1).
- [46] S. L. Kaufman, *High-resolution laser spectroscopy in fast beams*, *Opt. Commun.* **17**, 309–312 (1976) (cit. on pp. 1, 6).
- [47] W. H. Wing, G. A. Ruff, W. E. Lamb, et al., *Observation of the Infrared Spectrum of the Hydrogen Molecular Ion  $HD^+$* , *Phys. Rev. Lett.* **36**, 1488–1491 (1976) (cit. on pp. 1, 6).
- [48] B. Schinzler, W. Klempt, S. L. Kaufman, et al., *Collinear laser spectroscopy of neutron-rich Cs isotopes at an on-line mass separator*, *Phys. Lett. B* **79**, 209–212 (1978) (cit. on pp. 1, 6).
- [49] A. Smekal, *Zur Quantentheorie der Dispersion*, *Naturwissenschaften* **11**, 873 (1923) (cit. on p. 1).
- [50] C. V. Raman and K. S. Krishnan, *A New Type of Secondary Radiation*, *Nature* **121**, 501–502 (1928) (cit. on p. 1).
- [51] C. Raman, *The molecular scattering of light*, in *Nobel lect. phys. 1922-1941* (Elsevier, 1965) (cit. on p. 1).
- [52] J. R. Ferraro, K. Nakamoto, C. W. Brown, et al., *Introductory Raman Spectroscopy*, 2nd ed. (Academic Press, 2003) (cit. on p. 1).

- [53] A. Aspect, E. Arimondo, R. Kaiser, et al., *Laser Cooling below the One-Photon Recoil Energy by Velocity-Selective Coherent Population Trapping*, *Phys. Rev. Lett.* **61**, 826–829 (1988) (cit. on p. 1).
- [54] W. Nernst, *The New Heat Theorem* (Methuen and Co., London, 1926) (cit. on p. 3).
- [55] L. De Broglie, *Recherches sur la théorie des quanta*, PhD thesis (Migration - université en cours d’affectation, Français, 1924) (cit. on pp. 3, 21).
- [56] L. De Broglie, *The wave nature of the electron*, Nobel Lecture, 1929 (cit. on p. 3).
- [57] J. Rudolph, N. Gaaloul, Y. Singh, et al., *Degenerate Quantum Gases in Microgravity*, *Microgravity Sci. Technol.* **23**, 287–292 (2011) (cit. on p. 4).
- [58] A. Vogel, M. Schmidt, K. Sengstock, et al., *Bose-Einstein condensates in microgravity*, *Appl. Phys. B Lasers Opt.* **84**, 663–671 (2006) (cit. on p. 4).
- [59] T. van Zoest, N. Gaaloul, Y. Singh, et al., *Bose-Einstein Condensation in Microgravity*, *Science* **328**, 1540–1543 (2010) (cit. on pp. 4, 78).
- [60] K. Frye, S. Abend, W. Bartosch, et al., *The Bose-Einstein Condensate and Cold Atom Laboratory*, *EPJ Quantum Technol.* **8**, 1–38 (2021) (cit. on p. 5).
- [61] W. Hänsel, P. Hommelhoff, T. W. Hänsch, et al., *Bose-Einstein condensation on a micro-electronic chip*, *Nature* **413**, 498–501 (2001) (cit. on p. 5).
- [62] J. Rudolph, W. Herr, C. Grzeschik, et al., *A high-flux BEC source for mobile atom interferometers*, *New J. Phys.* **17**, 065001 (2015) (cit. on p. 5).
- [63] S.-w. Chiow, T. Kovachy, H. C. Chien, et al.,  *$102\hbar k$  Large Area Atom Interferometers*, *Phys. Rev. Lett.* **107**, 130403 (2011) (cit. on p. 5).
- [64] G. D. McDonald, C. C. N. Kuhn, S. Bennetts, et al.,  *$80\hbar k$  momentum separation with Bloch oscillations in an optically guided atom interferometer*, *Phys. Rev. A* **88**, 053620 (2013) (cit. on pp. 5–6).
- [65] B. Plotkin-Swing, D. Gochnauer, K. E. McAlpine, et al., *Three-Path Atom Interferometry with Large Momentum Separation*, *Phys. Rev. Lett.* **121**, 133201 (2018) (cit. on p. 5).
- [66] M. Gebbe, J.-N. Siemß, M. Gersemann, et al., *Twin-lattice atom interferometry*, *Nat. Commun.* **12**, 2544 (2021) (cit. on pp. 5, 78).
- [67] H. Müller, S.-w. Chiow, and S. Chu, *Atom-wave diffraction between the Raman-Nath and the Bragg regime: Effective Rabi frequency, losses, and phase shifts*, *Phys. Rev. A* **77**, 023609 (2008) (cit. on pp. 5–6, 59, 61).
- [68] H. Müller, S.-w. Chiow, S. Herrmann, et al., *Atom Interferometers with Scalable Enclosed Area*, *Phys. Rev. Lett.* **102**, 240403 (2009) (cit. on p. 5).
- [69] T. Kovachy, S.-w. Chiow, and M. A. Kasevich, *Adiabatic-rapid-passage multiphoton Bragg atom optics*, *Phys. Rev. A* **86**, 011606(R) (2012) (cit. on p. 5).
- [70] H. Ahlers, H. Müntinga, A. Wenzlawski, et al., *Double Bragg Interferometry*, *Phys. Rev. Lett.* **116**, 173601 (2016) (cit. on p. 5).
- [71] M. Gebbe, J.-N. Siemß, M. Gersemann, et al., *Twin-lattice atom interferometry*, 2019 (cit. on p. 5).
- [72] P. J. Martin, B. G. Oldaker, A. H. Miklich, et al., *Bragg scattering of atoms from a standing light wave*, *Phys. Rev. Lett.* **60**, 515–518 (1988) (cit. on p. 5).



- [73] D. M. Giltner, R. W. McGowan, and S. A. Lee, *Atom Interferometer Based on Bragg Scattering from Standing Light Waves*, *Phys. Rev. Lett.* **75**, 2638–2641 (1995) (cit. on p. 5).
- [74] M. K. Oberthaler, R. Abfalterer, S. Bernet, et al., *Atom Waves in Crystals of Light*, *Phys. Rev. Lett.* **77**, 4980–4983 (1996) (cit. on p. 5).
- [75] S. Kunze, S. Dürr, and G. Rempe, *Bragg scattering of slow atoms from a standing light wave*, *Eur. Lett* **34**, 343–348 (1996) (cit. on p. 5).
- [76] M. B. Dahan, E. Peik, J. Reichel, et al., *Bloch Oscillations of Atoms in an Optical Potential*, *Phys. Rev. Lett.* **76**, 4508–4511 (1996) (cit. on p. 5).
- [77] S. R. Wilkinson, C. F. Bharucha, K. W. Madison, et al., *Observation of Atomic Wannier-Stark Ladders in an Accelerating Optical Potential*, *Phys. Rev. Lett.* **76**, 4512–4515 (1996) (cit. on p. 5).
- [78] E. Peik, M. B. Dahan, I. Bouchoule, et al., *Bloch oscillations of atoms, adiabatic rapid passage, and monokinetic atomic beams*, *Phys. Rev. A* **55**, 2989–3001 (1997) (cit. on p. 5).
- [79] P. Cladé, S. Guellati-Khélifa, F. Nez, et al., *Large Momentum Beam Splitter Using Bloch Oscillations*, *Phys. Rev. Lett.* **102**, 240402 (2009) (cit. on p. 5).
- [80] K. E. McAlpine, D. Gochnauer, and S. Gupta, *Excited-band Bloch oscillations for precision atom interferometry*, *Phys. Rev. A* **101**, 023614 (2020) (cit. on p. 5).
- [81] D. M. Giltner, R. W. McGowan, and S. A. Lee, *Theoretical and experimental study of the Bragg scattering of atoms from a standing light wave*, *Phys. Rev. A* **52**, 3966–3972 (1995) (cit. on p. 5).
- [82] S. Gupta, A. E. Leanhardt, A. D. Cronin, et al., *Coherent manipulation of atoms with standing light waves*, *Comptes Rendus l'Académie des Sci. - Ser. IV Physics, Astrophys.* **2**, 479–495 (2001) (cit. on p. 5).
- [83] P. E. Moskowitz, P. L. Gould, S. R. B. Atlas, et al., *Diffraction of an Atomic Beam by Standing-Wave Radiation*, *Phys. Rev. Lett.* **51**, 370–373 (1983) (cit. on p. 6).
- [84] P. L. Gould, G. A. Ruff, and D. E. Pritchard, *Diffraction of Atoms by Light: The near-resonant Kapitza-Dirac Effect*, *Phys. Rev. Lett.* **56**, 827–830 (1986) (cit. on p. 6).
- [85] D. L. Freimund, K. Aflatooni, and H. Batelaan, *Observation of the Kapitza-Dirac effect*, *Nature* **413**, 142–143 (2001) (cit. on p. 6).
- [86] S. S. Szigeti, J. E. Debs, J. J. Hope, et al., *Why momentum width matters for atom interferometry with Bragg pulses*, *New J. Phys.* **14**, 023009 (2012) (cit. on pp. 6, 61).
- [87] H. Müller, S.-w. Chiow, Q. Long, et al., *Atom Interferometry with up to 24-Photon-Momentum-Transfer Beam Splitters*, *Phys. Rev. Lett.* **100**, 180405 (2008) (cit. on p. 6).
- [88] V. Schkolnik, B. Leykauf, M. Hauth, et al., *The effect of wavefront aberrations in atom interferometry*, *Appl. Phys. B Lasers Opt.* **120**, 311–316 (2015) (cit. on p. 6).
- [89] M. R. Sturm, B. Rein, T. Walther, et al., *Feasibility of UV lasing without inversion in mercury vapor*, *J. Opt. Soc. Am. B* **31**, 1964 (2014) (cit. on pp. 6, 128).
- [90] R. Neugart, *Collinear laser spectroscopy on unstable isotopes - A tool of nuclear physics*, *Hyperfine Interact.* **24**, 159–180 (1985) (cit. on p. 6).
- [91] E. W. Otten, *Nuclear Radii and Moments of Unstable Isotopes*, in *Treatise Heavy Ion Science*, Vol. 8 (Plenum Press, New York, 1989) Chap. 7, p. 517 (cit. on p. 6).

- [92] K. Blaum, J. Dilling, and W. Nörtershäuser, *Precision atomic physics techniques for nuclear physics with radioactive beams*, *Phys. Scr.* **T152**, 014017 (2013) (cit. on p. 6).
- [93] P. Campbell, I. D. Moore, and M. R. Pearson, *Laser spectroscopy for nuclear structure physics*, *Prog. Part. Nucl. Phys.* **86**, 127–180 (2016) (cit. on p. 6).
- [94] R. Neugart, J. Billowes, M. L. Bissell, et al., *Collinear laser spectroscopy at ISOLDE: new methods and highlights*, *J. Phys. G Nucl. Part. Phys.* **44**, 064002 (2017) (cit. on p. 6).
- [95] K. Wendt, K. Blaum, B. A. Bushaw, et al., *Recent developments in and applications of resonance ionization mass spectrometry*, *Fresenius. J. Anal. Chem.* **364**, 471–477 (1999) (cit. on p. 7).
- [96] O. Poulsen and E. Riis, *Absolute Determination of High Voltages Using Fast-Beam Laser Velocimetry*, *Metrologia* **25**, 147 (1988) (cit. on p. 7).
- [97] S. Götze, K.-M. Knaak, N. Kotovski, et al., *Test of collinear spectroscopy for precise high-voltage determination*, *Rev. Sci. Instrum.* **75**, 1039–1050 (2004) (cit. on p. 7).
- [98] A. Krieger, C. Geppert, R. Catherall, et al., *Calibration of the ISOLDE acceleration voltage using a high-precision voltage divider and applying collinear fast beam laser spectroscopy*, *Nucl. Instruments Methods Phys. Res. Sect. A* **632**, 23–31 (2011) (cit. on p. 7).
- [99] K. Baczyńska, J. Billowes, P. Campbell, et al., *Nuclear spin determination of  $^{100m}\text{Y}$  by collinear laser spectroscopy of optically pumped ions*, *J. Phys. G Nucl. Part. Phys.* **37**, 105103 (2010) (cit. on p. 7).
- [100] T. P. Dinneen, N. Berrah Mansour, C. Kurtz, et al., *Stimulated Raman measurements of the hyperfine structure in Y II*, *Phys. Rev. A* **43**, 4824–4831 (1991) (cit. on p. 7).
- [101] A. Neumann, M. Gebbe, and R. Walser, *Aberrations in (3+1)-dimensional Bragg diffraction using pulsed Laguerre-Gaussian laser beams*, *Phys. Rev. A* **103**, 043306 (2021) (cit. on pp. 9, 51).
- [102] A. Neumann, R. Walser, and W. Nörtershäuser, *Raman velocity filter as a tool for collinear laser spectroscopy*, *Phys. Rev. A* **101**, 052512 (2020) (cit. on pp. 9, 121).
- [103] C. Cohen-Tannoudji, J. Dupont-Roc, and G. Grynberg, *Photons and Atoms: Introduction to Quantum Electrodynamics* (Wiley, Weinheim, 1989) (cit. on pp. 13–14, 94).
- [104] J. Weiner and P.-T. Ho, *Light-Matter Interaction - Fundamentals and Applications* (Wiley & Sons, Hoboken, 2003) (cit. on p. 13).
- [105] W. T. Hill and C. H. Lee, *Light-Matter Interaction - Atoms and Molecules in External Fields and Nonlinear Optics* (Wiley-VCH, Weinheim, 2007) (cit. on p. 13).
- [106] J. Dalibard and C. Cohen-Tannoudji, *Atomic motion in laser light: connection between semiclassical and quantum descriptions*, *J. Phys. B At. Mol. Phys* **18**, 1661–1683 (1985) (cit. on pp. 14, 127–128).
- [107] W. P. Schleich, *Quantum Optics in Phase Space* (Wiley, Berlin, 2001) (cit. on p. 15).
- [108] D. F. Walls and G. J. Milburn, *Quantum Optics*, 2nd ed. (Springer, Berlin Heidelberg, 2008) (cit. on p. 15).
- [109] B. W. Shore, *The theory of coherent atomic excitation*, Vol. 1 and 2 (Wiley-Interscience, New York, 1990), Chap. 2.6, 20.7, 20.8 (cit. on pp. 15, 126).
- [110] D. A. Steck, *Rubidium 87 D Line Data (revision 2.2.1)*, 2019 (cit. on p. 15).

- [111] A. E. Siegman, *Lasers* (University Science Books, Mill Valley, 1986) (cit. on p. 16).
- [112] B. E. A. Saleh and M. C. Teich, *Fundamentals of Photonics*, 2nd ed. (Wiley, Hoboken, 2007) (cit. on p. 16).
- [113] M. Lax, W. H. Louisell, and W. B. McKnight, *From Maxwell to paraxial wave optics*, *Phys. Rev. A* **11**, 1365–1370 (1975) (cit. on p. 16).
- [114] J.-P. Blaizot and G. Ripka, *Quantum Theory of Finite Systems* (MIT Press, Cambridge, 1986) (cit. on pp. 18–19).
- [115] G. Nandi, A. Sizmann, J. Fortágh, et al., *Number filter for matter waves*, *Phys. Rev. A* **78**, 013605 (2008) (cit. on p. 19).
- [116] F. Dalfovo, S. Giorgini, L. P. Pitaevskii, et al., *Theory of Bose-Einstein condensation in trapped gases*, *Rev. Mod. Phys.* **71**, 463–512 (1999) (cit. on pp. 20, 23–25).
- [117] E. Schrödinger, *Der stetige Übergang von der Mikro- zur Makromechanik*, *Naturwissenschaften* **14**, 664–666 (1926) (cit. on p. 21).
- [118] H. T. C. Stoof, K. B. Gubbels, and D. B. M. Dickerscheid, *Ultracold Quantum Fields*, 2 (Bristol, 2009), pp. 475–485 (cit. on p. 22).
- [119] C. J. Pethick and H. Smith, *The non-interacting Bose gas*, in *Bose-Einstein Condensation in Dilute Gases*, 2nd ed. (Cambridge University Press, Cambridge, 2008) Chap. 2, pp. 17–40 (cit. on pp. 24, 27–28).
- [120] J. Teske, M. R. Besbes, B. Okhrimenko, et al., *Mean-field Wigner function of Bose-Einstein condensates in the Thomas-Fermi limit*, *Phys. Scr.* **93**, 124004 (2018) (cit. on pp. 24–25).
- [121] F. Damon, F. Vermersch, J. G. Muga, et al., *Reduction of local velocity spreads by linear potentials*, *Phys. Rev. A* **89**, 053626 (2014) (cit. on pp. 26, 81).
- [122] Y. Castin and R. Dum, *Bose-Einstein Condensates in Time Dependent Traps*, *Phys. Rev. Lett.* **77**, 5315–5319 (1996) (cit. on pp. 26, 81).
- [123] Y. Kagan, E. L. Surkov, and G. V. Shlyapnikov, *Evolution of a Bose-condensed gas under variations of the confining potential*, *Phys. Rev. A* **54**, R1753–R1756 (1996) (cit. on pp. 26, 81).
- [124] Y. Kagan, E. L. Surkov, and G. V. Shlyapnikov, *Evolution of a Bose gas in anisotropic time-dependent traps*, *Phys. Rev. A* **55**, R18–R21 (1997) (cit. on pp. 26, 81).
- [125] M. Meister, S. Arnold, D. Moll, et al., *Efficient Description of Bose-Einstein Condensates in Time-Dependent Rotating Traps*, in *Advances in Atomic, Molecular, and Optical Physics*, Vol. 66 (Academic Press Inc., 2017), pp. 375–438 (cit. on pp. 26, 81).
- [126] R Walser, *Ground state correlations in a trapped quasi one-dimensional Bose gas*, *Opt. Commun.* **243**, 107–129 (2004) (cit. on p. 27).
- [127] O. Penrose and L. Onsager, *Bose-Einstein Condensation and Liquid Helium*, *Phys. Rev.* **104**, 576–584 (1956) (cit. on p. 27).
- [128] C. N. Yang, *Concept of Off-Diagonal Long-Range Order and the Quantum Phases of Liquid He and of Superconductors*, *Rev. Mod. Phys.* **34**, 694–704 (1962) (cit. on p. 27).
- [129] W. Ketterle, D. S. Durfee, and D. M. Stamper-Kurn, *Making, probing and understanding Bose-Einstein condensates*, in *Bose-Einstein Condensation in Atomic Gases. Proceedings of the International School of Physics Enrico Fermi*, Vol. 140 (1999), pp. 67–176 (cit. on p. 28).



- [130] M. Carey, J. Saywell, D. Elcock, et al., *Velocimetry of cold atoms by matter-wave interferometry*, *Phys. Rev. A* **99**, 023631 (2019) (cit. on p. 28).
- [131] C. Runge, *Ueber die numerische Auflösung von Differentialgleichungen*, *Math. Ann.* **46**, 167–178 (1895) (cit. on p. 32).
- [132] W. Kutta, *Beitrag zur Näherungsweise Integration Totaler Differentialgleichungen*, *Zeit. Math. Phys.* **46**, 435–452 (1901) (cit. on p. 32).
- [133] H. Yoshida, *Construction of higher order symplectic integrators*, *Phys. Lett. A* **150**, 262–268 (1990) (cit. on p. 32).
- [134] R. R. Puri, *Mathematical Methods of Quantum Optics*, Springer Series in Optical Sciences (Springer, Berlin, Heidelberg, 2001) (cit. on pp. 33, 165).
- [135] H. J. Carmichael, *Statistical Methods in Quantum Optics 1: Master Equations and Fokker-Planck Equations*, Vol. 1 (Springer Berlin Heidelberg, Berlin, Heidelberg, 1999) (cit. on p. 34).
- [136] G. Lindblad, *On the generators of quantum dynamical semigroups*, *Commun. Math. Phys.* **48**, 119–130 (1976) (cit. on p. 34).
- [137] K. Mølmer, Y. Castin, and J. Dalibard, *Monte Carlo wave-function method in quantum optics*, *J. Opt. Soc. Am. B* **10**, 524–538 (1993) (cit. on pp. 34–36).
- [138] R. Dum, P. Zoller, and H. Ritsch, *Monte Carlo simulation of the atomic master equation for spontaneous emission*, *Phys. Rev. A* **45**, 4879–4887 (1992) (cit. on p. 35).
- [139] J. Dalibard, Y. Castin, and K. Mølmer, *Wave-function approach to dissipative processes in quantum optics*, *Phys. Rev. Lett.* **68**, 580–583 (1992) (cit. on p. 35).
- [140] C. Cohen-Tannoudji, J. Dupont-Roc, and G. Grynberg, *Atom-Photon Interactions: Basic Process and Applications* (Wiley-VCH, Weinheim, 2004) (cit. on pp. 36, 126).
- [141] L. Devroye, *Non-Uniform Random Variate Generation* (Springer-Verlag, New York, 1986) (cit. on p. 37).
- [142] G. Galilei, *Dialogue Concerning the Two Chief World Systems-Ptolemaic & Copernican (translated by Stillman Drake, foreword by Albert Einstein)*, 2nd ed. (University of California Press, Berkeley, 1967, originally published 1632), p. 187 (cit. on p. 38).
- [143] R. P. Paul, *Robot Manipulators: Mathematics, Programming, and Control* (MIT Press, Cambridge, 1981) (cit. on p. 39).
- [144] C. Cohen-Tannoudji, B. Diu, and F. Laloë, *General study of two-level systems*, in *Quantum Mechanics Vol. 1* (Wiley-Interscience, New York, 1977) Chap. IV C, pp. 405–415 (cit. on p. 44).
- [145] A. F. Bernhardt and B. W. Shore, *Coherent atomic deflection by resonant standing waves*, *Phys. Rev. A* **23**, 1290–1301 (1981) (cit. on p. 51).
- [146] R. G. Newton, *Scattering Theory of Waves and Particles* (Dover Publications, Berlin, Heidelberg, 2002) (cit. on p. 57).
- [147] S. L. McCall and E. L. Hahn, *Pulse-Area-Pulse-Energy Description of a Traveling Wave Laser Amplifier*, *Phys. Rev. A* **2**, 861–870 (1970) (cit. on p. 57).
- [148] L. Allen and J. H. Eberly, *Optical Resonance and Two-level Atoms* (Dover, New York, 1987) (cit. on p. 57).
- [149] P. Meystre and M. Sargent, *Elements of Quantum Optics*, 4th ed. (Springer, Berlin, Heidelberg, 2007) (cit. on p. 59).

- [150] E. Brion, L. H. Pedersen, and K. Mølmer, *Adiabatic elimination in a lambda system*, *J. Phys. A Math. Theor. J.* **40**, 1033–1043 (2007) (cit. on pp. 59, 136).
- [151] F. W. J. Olver, D. W. Lozier, R. F. Boisvert, et al., *NIST Handbook of Mathematical Functions* (National Institute of Standards, Technology, and Cambridge University Press, 2010) (cit. on pp. 59, 72).
- [152] M. Wilkens, E. Schumacher, and P. Meystre, *Band theory of a common model of atom optics*, *Phys. Rev. A* **44**, 3130–3137 (1991) (cit. on p. 59).
- [153] C. Champenois, M. Büchner, R. Delhuelle, et al., *Atomic diffraction by a laser standing wave: Analysis using Bloch states*, *Eur. Phys. J. D* **13**, 271–278 (2001) (cit. on p. 59).
- [154] W. Kohn, *Analytic Properties of Bloch Waves and Wannier Functions*, *Phys. Rev.* **115**, 809–821 (1959) (cit. on p. 60).
- [155] J. Callaway, *Quantum Theory of the Solid State*, 2nd ed. (Academic Press, New York, 1991) (cit. on p. 60).
- [156] M. Grupp, R. Walser, W. P. Schleich, et al., *Resonant Feshbach scattering of fermions in one-dimensional optical lattices*, *J. Phys. B At. Mol. Opt. Phys.* **40**, 2703–2718 (2007) (cit. on p. 60).
- [157] M. R. Sturm, M. Schlosser, R. Walser, et al., *Quantum simulators by design: Many-body physics in reconfigurable arrays of tunnel-coupled traps*, *Phys. Rev. A* **95**, 063625 (2017) (cit. on p. 60).
- [158] R. B. Blackman and J. W. Tukey, *The measurement of power spectra from the point of view of communications engineering*, *Bell Syst. Tech. J.* **37**, 185–282 (1958) (cit. on p. 64).
- [159] E. J. Harris, *On the Use of Windows for Harmonic Analysis with the Discrete Fourier Transform*, *Proc. IEEE* **66**, 51–83 (1978) (cit. on p. 64).
- [160] M. Kasevich and S. Chu, *Laser cooling below a photon recoil with three-level atoms*, *Phys. Rev. Lett.* **69**, 1741–1744 (1992) (cit. on p. 64).
- [161] N. Davidson, H.-J. Lee, M. Kasevich, et al., *Raman cooling of atoms in two and three dimensions*, *Phys. Rev. Lett.* **72**, 3158–3161 (1994) (cit. on p. 64).
- [162] Y. N. Demkov and M. Kunike, *Hypergeometric models of the two-state approximation in the theory of atomic collisions*, *Vestn. Leningr. Univ. Fiz. Khim* **16**, 39 (1969) (cit. on pp. 64, 71).
- [163] K.-A. Suominen and B. M. Garraway, *Population transfer in a level-crossing model with two time scales*, *Phys. Rev. A* **45**, 374–386 (1992) (cit. on pp. 64, 71).
- [164] N. V. Vitanov, *Complete population inversion by a phase jump: an exactly soluble model*, *New J. Phys.* **9**, 58 (2007) (cit. on pp. 64, 71).
- [165] P. P. Ewald, *Zur Begründung der Kristalloptik (Teil III: Die Kristalloptik der Röntgenstrahlen)*, *Ann. Phys.* **24**, 557–597 (1917) (cit. on p. 65).
- [166] A. Zeilinger, *Complementarity in neutron interferometry*, *Phys. B+C* **137**, 235–244 (1986) (cit. on p. 65).
- [167] D. Gochnauer, K. E. McAlpine, B. Plotkin-Swing, et al., *Bloch-band picture for light-pulse atom diffraction and interferometry*, *Phys. Rev. A* **100**, 043611 (2019) (cit. on pp. 66, 75, 153).

- [168] S. Hartmann, J. Jenewein, E. Giese, et al., *Regimes of atomic diffraction: Raman versus Bragg diffraction in retroreflective geometries*, *Phys. Rev. A* **101**, 53610 (2020) (cit. on p. 66).
- [169] T. Kato, *On the Convergence of the Perturbation Method. I*, *Prog. Theor. Phys.* **4**, 514–523 (1949) (cit. on p. 66).
- [170] T. Kato, *Perturbation Theory for Linear Operators* (Springer, Berlin Heidelberg, 1995) (cit. on p. 66).
- [171] A. Galindo and P. Pascual, *Kato's Theory*, in *Quantum mechanics ii* (Springer, Berlin Heidelberg, 1991) Chap. 10.7 (cit. on p. 66).
- [172] D. J. Wales, *Energy Landscapes: Applications to Clusters, Biomolecules and Glasses* (Cambridge University Press, Cambridge, 2004) (cit. on p. 71).
- [173] D. J. Wales and J. P. K. Doye, *Global Optimization by Basin-Hopping and the Lowest Energy Structures of Lennard-Jones Clusters Containing up to 110 Atoms*, *J. Phys. Chem. A* **101**, 5111–5116 (1997) (cit. on p. 71).
- [174] Z. Li and H. A. Scheraga, *Monte Carlo-minimization approach to the multiple-minima problem in protein folding*, *Proc. Natl. Acad. Sci.* **84**, 6611–6615 (1987) (cit. on p. 71).
- [175] D. J. Wales and H. A. Scheraga, *Global Optimization of Clusters, Crystals, and Biomolecules*, *Science* **285**, 1368–1372 (1999) (cit. on p. 71).
- [176] S. Beckett, *Waiting for Godot* (Faber and Faber, London, 1956) (cit. on p. 73).
- [177] D. M. Tong, K. Singh, L. C. Kwek, et al., *Sufficiency Criterion for the Validity of the Adiabatic Approximation*, *Phys. Rev. Lett.* **98**, 150402 (2007) (cit. on p. 74).
- [178] A. I. Akhiezer and S. V. Peletminskii, *Methods of Statistical Physics* (Pergamon Press Ltd., Oxford, 1981) (cit. on p. 79).
- [179] N. Proukakis, S. Gardiner, M. Davis, et al., *Quantum Gases: Finite Temperature and Non-Equilibrium Dynamics*, Cold Atoms (Imperial College Press, London, 2013) (cit. on p. 79).
- [180] R. Walser, J. Cooper, and M. Holland, *Reversible and irreversible evolution of a condensed bosonic gas*, *Phys. Rev. A* **63**, 013607 (2000) (cit. on p. 79).
- [181] C. Cohen-Tannoudji, *Atomic motion in laser light*, in *Fundamental Systems in Quantum Optics* (Elsevier Science Publishers B.V., Les Houches Session LIII, 1992) (cit. on pp. 90, 94).
- [182] P. Ehrenfest, *Bemerkung über die angenäherte Gültigkeit der klassischen Mechanik innerhalb der Quantenmechanik*, *Zeitschrift für Phys.* **45**, 455–457 (1927) (cit. on p. 90).
- [183] L. E. Ballentine, *Quantum Mechanics: A Modern Development*, 2nd ed. (World Scientific, 2014) (cit. on p. 90).
- [184] K. L. König, *Laser-Based High-Voltage Metrology with ppm Accuracy*, PhD Thesis (Technische Universität Darmstadt, 2019) (cit. on pp. 121, 123, 141, 152).
- [185] J. Krämer, K. König, C. Geppert, et al., *High-voltage measurements on the 5 ppm relative uncertainty level with collinear laser spectroscopy*, *Metrologia* **55**, 268–274 (2018) (cit. on pp. 121, 140–141, 152).
- [186] T. Thümmler, R. Marx, and C. Weinheimer, *Precision high voltage divider for the KATRIN experiment*, *New J. Phys.* **11**, 103007 (2009) (cit. on pp. 121–122).

- [187] O. Rest, D. Winzen, S. Bauer, et al., *A novel ppm-precise absolute calibration method for precision high-voltage dividers*, *Metrologia* **56**, 045007 (2019) (cit. on pp. 121–122).
- [188] M. Aker, K. Altenmüller, M. Arenz, et al., *Improved Upper Limit on the Neutrino Mass from a Direct Kinematic Method by KATRIN*, *Phys. Rev. Lett.* **123**, 221802(10) (2019) (cit. on p. 122).
- [189] M. Wang, G. Audi, F. G. Kondev, et al., *The AME2016 atomic mass evaluation (II). Tables, graphs and references*, *Chinese Phys. C* **41**, 030003 (2017) (cit. on pp. 125, 158).
- [190] A. Kramida, Y. Ralchenko, J. Reader, et al., *NIST Atomic Spectra Database (ver. 5.6.1)*, 2018 (cit. on pp. 125, 158).
- [191] C. Shi, F. Gebert, C. Gorges, et al., *Unexpectedly large difference of the electron density at the nucleus in the  $4p^2P_{1/2,3/2}$  fine-structure doublet of  $\text{Ca}^+$* , *Appl. Phys. B* **123**, 2 (2017) (cit. on pp. 125, 158).
- [192] H. Guan, Y. Huang, P. L. Liu, et al., *Precision spectroscopy with a single  $^{40}\text{Ca}^+$  ion in a Paul trap*, *Chinese Phys. B* **24**, 054213 (2015) (cit. on pp. 125, 158).
- [193] D. A. Steck, *Quantum Chaos, Transport, and Decoherence in Atom Optics*, PhD thesis (University of Texas at Austin, 2001) (cit. on p. 126).
- [194] P. A. Barton, C. J. S. Donald, D. M. Lucas, et al., *Measurement of the lifetime of the  $3d^2D_{5/2}$  state in  $^{40}\text{Ca}^+$* , *Phys. Rev. A* **62**, 032503 (2000) (cit. on p. 126).
- [195] S. Marksteiner, R. Walser, P. Marte, et al., *Localization of atoms in light fields: Optical molasses, adiabatic compression and squeezing*, *Appl. Phys. B Laser Opt.* **60**, 145–153 (1995) (cit. on p. 128).
- [196] R. Walser, J. Cooper, and P. Zoller, *Saturated absorption spectroscopy using diode-laser phase noise*, *Phys Rev A* **50**, 4303–4309 (1994) (cit. on p. 128).
- [197] M. Rosenbluh, A. Rosenhouse-Dantsker, A. Wilson-Gordon, et al., *Spectroscopy with diode-laser noise*, *Opt. Commun.* **146**, 158–162 (1998) (cit. on p. 128).
- [198] D. H. McIntyre, C. E. Fairchild, J. Cooper, et al., *Diode-laser noise spectroscopy of rubidium*, *Opt. Lett.* **18**, 1816 (1993) (cit. on p. 128).
- [199] M. Abramowitz and I. A. Stegun, *Handbook of Mathematical Functions With Formulas, Graphs, and Mathematical Tables*, 10th Print (US Government Printing Office, Washington, 1964) (cit. on p. 146).
- [200] E. Giese, A. Roura, G. Tackmann, et al., *Double Bragg diffraction: A tool for atom optics*, *Phys. Rev. A* **88**, 053608 (2013) (cit. on p. 154).
- [201] M. P. Bradley, J. V. Porto, S. Rainville, et al., *Penning Trap Measurements of the Masses of  $^{133}\text{Cs}$ ,  $^{87,85}\text{Rb}$ , and  $^{23}\text{Na}$  with uncertainties  $\leq 0.2$  ppb*, *Phys. Rev. Lett.* **83**, 4510–4513 (1999) (cit. on p. 157).
- [202] J. Ye, S. Swartz, P. Jungner, et al., *Hyperfine structure and absolute frequency of the  $^{87}\text{Rb}$   $5P_{3/2}$  state*, *Opt. Lett.* **21**, 1280 (1996) (cit. on p. 157).
- [203] U. Volz and H. Schmoranzner, *Precision lifetime measurements on alkali atoms and on helium by beam-gas-laser spectroscopy*, *Phys. Scr.*, 48 (1996) (cit. on p. 157).
- [204] J. E. Simsarian, L. A. Orozco, G. D. Sprouse, et al., *Lifetime measurements of the 7p levels of atomic francium*, *Phys. Rev. A* **57**, 2448–2458 (1998) (cit. on p. 157).

- [205] H. M.J. M. Boesten, C. C. Tsai, J. R. Gardner, et al., *Observation of a shape resonance in the collision of two cold  $^{87}\text{Rb}$  atoms*, *Phys. Rev. A - At. Mol. Opt. Phys.* **55**, 636–640 (1997) (cit. on p. 157).
- [206] R. F. Gutterres, C. Amiot, A. Fioretti, et al., *Determination of the  $^{87}\text{Rb}$  5p state dipole matrix element and radiative lifetime from the photoassociation spectroscopy of the  $\text{Rb}_2$   $0_g^-(P_{3/2})$  long-range state*, *Phys. Rev. A* **66**, 024502 (2002) (cit. on p. 157).
- [207] A. Marte, T. Volz, J. Schuster, et al., *Feshbach Resonances in Rubidium 87: Precision Measurement and Analysis*, *Phys. Rev. Lett.* **89**, 283202 (2002) (cit. on p. 157).
- [208] Schäfter+Kirchhoff, *Fiber Collimators 60FC-... for a range of laser beam diameters using variety of attached or integrated optics capabilities*, 2017 (cit. on p. 157).
- [209] J. W. Cooley and J. W. Tukey, *An algorithm for the machine calculation of complex Fourier series*, *Math. Comput.* **19**, 297–297 (1965) (cit. on p. 160).
- [210] C. F. Gauß, *Nachlass, Theoria Interpolationis Methodo Nova Tractata*, in *Carl Friedrich Gauss Werke, Band III* (Königliche Gesellschaft der Wissenschaften zu Göttingen, 1966), pp. 265–330 (cit. on p. 160).
- [211] G. Plonka, D. Potts, G. Steidl, et al., *Numerical Fourier Analysis*, in *Fundamentals of Numerical Mathematics for Physicists and Engineers* (Springer Nature Switzerland, Birkhäuser, 2020), pp. 235–259 (cit. on p. 160).
- [212] M. S. Ober, *Quantum Monte-Carlo wave function simulation*, M.Sc. Thesis, Technische Universität Darmstadt, 2014 (cit. on p. 160).
- [213] D. R. Smith, *A Riccati approach to the Airy equation*, in *Asymptotic and Computational Analysis* (Marcel Dekker, Inc., Winnipeg, Manitoba, 1990), pp. 403–415 (cit. on p. 166).

---

## LIST OF PUBLICATIONS

---

- A. Neumann, M. Gebbe, R. Walser  
*Aberrations in (3+1)-dimensional Bragg diffraction using pulsed Laguerre-Gaussian laser beams*  
Phys. Rev. A **103**, 043306 (2021)  
<https://link.aps.org/doi/10.1103/PhysRevA.103.043306>
- A. Neumann, W. Nörtershäuser, R. Walser  
*Raman velocity filter as a tool for collinear laser spectroscopy*  
Phys. Rev. A **101**, 052512 (2020), Editors' Suggestion <sup>1</sup>  
<https://doi.org/10.1103/PhysRevA.101.052512>
- T. Peters, T.-P. Wang, A. Neumann, S. Simeonov, T. Halfmann  
*Single-photon-level narrowband memory in a hollow-core photonic bandgap fiber*  
Opt. Express **28**, 5340-5354 (2020), Editor's Pick <sup>2</sup>  
<https://doi.org/10.1364/OE.383999>
- A. Neumann, M. Gebbe, R. Walser  
*Aberrations in (3+1)-dimensional Bragg diffraction due to misaligned, pulsed Laguerre-Gaussian laser beams*  
In preparation
- O. Marchukov, A. Neumann, J. Teske, R. Walser  
*Collimation of Bose-Einstein condensates within Bragg-beam splitters applying pulsed Laguerre-Gaussian laser beams*  
In preparation

---

<sup>1</sup> 'A small number of Physical Review A papers that the editors and referees find of particular interest, importance, or clarity.'

<sup>2</sup> 'Editor's Picks serve to highlight articles with excellent scientific quality and are representative of the work taking place in a specific field.'



---

## CONFERENCE CONTRIBUTIONS

---

- **Poster** (canceled due to COVID-19 pandemic)  
*From idealised to 'realistic' atomic beamsplitters*  
DPG Frühjahrstagung, Hannover, Germany (2020)
- **Contributed Talk & Poster**  
*From idealised to 'realistic' atomic beamsplitters*  
Quantum Matter - Out of Equilibrium (Summer School), Granada, Spain (2019)
- **Talk (Q 5.8)**  
*Bragg beamsplitters with misaligned Gaussian laser beams*  
DPG Frühjahrstagung, Rostock, Germany (2019)
- **Interactive Presentation**<sup>3</sup>  
*Realistic 3D simulations of Bragg beamsplitters for matter-wave interferometry under microgravity*  
69th International Astronautical Congress, Bremen, Germany (2018)
- **Poster**  
*Aberrations of Bragg beamsplitters - 3D simulations*  
Frontiers of Matter Wave Optics Conference (Kolymbari) & Summer School (Archanes), Crete, Greece (2018)
- **Talk (Q 22.4)**  
*Aberrations of Bragg beamsplitters - 3D simulations*  
DPG Frühjahrstagung, Erlangen, Germany (2018)
- **Poster**  
*3D simulation of atomic Bragg beamsplitters*  
Fundamental Physics in Space (656th WE-Heraeus-Seminar), Bremen, Germany (2017)
- **Poster (EA-P.4)**  
*3D simulation of atomic Bragg beamsplitters*  
CLEO Europe, München, Germany (2017)
- **Poster (Q 31.26)**  
*Simulation of 3D atomic Bragg beamsplitters*  
DPG Frühjahrstagung, Mainz, Germany (2017)
- **Poster (Q 27.33)**  
*Abberations of atomic beamsplitters*  
DPG Frühjahrstagung, Hannover, Germany (2016)

---

<sup>3</sup> Among the top 20 percent of 341 Interactive Presentations.

---

## DANKSAGUNG

---

An dieser Stelle möchte ich bei all jenen bedanken, die zu meiner Promotion auf ihre Weise beigetragen haben.

An erster Stelle gilt mein Dank meinem Doktorvater Prof. Dr. Reinhold Walser, für die Ermöglichung dieser Promotion und die Überzeugung auf die theoretische Seite der Physik zu wechseln. Danke, für die wissenschaftlichen Auseinandersetzungen und Anregungen und besonders für die Erinnerungen stets das physikalische Verständnis über eine sture mathematische Berechnung hervorzuheben.

Ich danke Prof. Dr. Enno Giese für die Bereitschaft meine Dissertation als Zweitgutachter mit Zeit und Mühe zu unterstützen. Daneben danke ich Prof. Dr. Wilfried Nörtershäuser und Prof. Dr. Thomas Walther für den Einsatz als weitere Prüfer.

Ein elementarer Dank gilt der Unterstützung dieser Arbeit im Rahmen des QUANTUS-Projekts durch das Zentrum für Luft- und Raumfahrt. Damit verbunden, möchte ich mich beim gesamten QUANTUS-Team für die erfolgreiche Zusammenarbeit, interessanten Meetings und den produktiven wissenschaftlichen Austausch bedanken. Insbesondere danke ich Martina Gebbe für die Bereitstellung der experimentellen Daten zur Analyse der Beugungseffizienz von ultrakalten Atomen. Ebenso möchte ich mich für die erfolgreiche Zusammenarbeit und Anregungen im Rahmen des Geschwindigkeitsfilters für heiße Ionen bei Prof. Dr. Wilfried Nörtershäuser, Jörg Krämer und Kristian König bedanken.

Ein herzliches Dankeschön geht an alle aktuellen und ehemaligen Kollegen und Mitglieder des Instituts für Angewandte Physik - Theorie, die mich während meiner Promotion begleitet haben, insbesondere das Büro 01. Dabei danke ich Jan für die lange gemeinsame Zeit als gutes Team in der Uni, auf den Konferenzen und im Sport. Ihm möchte ich zusätzlich für die Simulation der Impulsverteilungen von Bose-Einstein-Kondensaten danken. Martin hatte immer unendlich viel Zeit, um sein weitgreifendes Wissen - über alles was er jemals gehört oder gelesen hat - mit uns zu teilen. Kai ist einer der ordentlichsten Korrekturleser - Danke! Vielen Dank an alle Korrekturleser\*innen: Tine, Franzi, Michaela, Michi, Jan, Oleks, Kai, Nico. Ganz am Anfang war da noch Bogdan, der einfach wirklich wie ein kleiner, aber definitiv nicht nerviger Bruder war. Ganz besonders möchte ich mich bei meiner ersten richtigen und dafür aller besten Fysiker Freundin Franziska Friedrich bedanken. Zum ersten Mal in meinem Physikstudium konnte ich auf eine weibliche Verbündete in jeder Lage zählen.

Danke an alle Freunde für die gemeinsamen Mittagsspaziergänge und abendlichen Aufheiterungen. Zuletzt hat meine Familie für ihre unermessliche Unterstützung ein riesiges Dankeschön verdient. Meine Mutter und meine Schwester für ihr ehrliches Interesse trotz ihrer beruflichen Herkunft aus einer anderen Galaxie aber vor allem für alles abseits des Physikstudiums. Dafür stammt mein Schwiegervater beruflich nicht nur aus derselben Welt wie ich, sondern hat sogar an der TU Darmstadt promoviert. Danke für die wissenschaftliche Unterstützung. Zum Abschluss danke ich meinem Mann Nico für - die Unterstützung bei dem Wechsel zum Physikstudium - das gemeinsame Physikstudium - für den unermüdlichen Beistand bei der Promotion - für alles und für jeden Tag unseres gemeinsamen Lebens.

*Diese Arbeit wurde unterstützt durch das Zentrum für Luft- und Raumfahrt (DLR), mit Geldmitteln bereitgestellt vom Bundesministerium für Wirtschaft und Energie (BMWi) unter den Förderkennzeichen 50WM1557 und 50WM1957.*



---

## ERKLÄRUNG GEMÄSS §9 PROMOTIONSORDNUNG

---

Hiermit versichere ich, dass ich die vorliegende Dissertation selbstständig angefertigt und keine anderen als die angegebenen Quellen und Hilfsmittel verwendet habe. Alle wörtlichen und paraphrasierten Zitate wurden angemessen kenntlich gemacht. Die Arbeit hat bisher noch nicht zu Prüfungszwecken gedient.

*Darmstadt, 07. Mai 2021*

---

Antje Neumann